KARLSRUHER INSTITUT FÜR TECHNOLOGIE

Signal model for the radio emission of inclined cosmic-ray air-showers and energy reconstruction of event candidates for GRAND

Zur Erlangung des akademischen Grades eines
DOKTORS DER NATURWISSENSCHAFTEN (Dr. rer. nat.)

von der KIT-Fakultät für Physik des
Karlsruher Instituts für Technologie (KIT)
angenommene

DISSERTATION

von

M.Sc. Lukas GÜLZOW

Tag der mündlichen Prüfung:
November 7, 2025

Referent:
Prof. Dr. Ralph ENGEL
Korreferent:
Prof. Dr. Olivier MARTINEAU
Betreuer:
Dr. Tim HUEGE

Declaration of Authorship

I, M.Sc. Lukas GÜLZOW, declare that this thesis titled, "Signal model for the radio emission of inclined cosmic-ray air-showers and energy reconstruction of event candidates for GRAND" and the work presented in it are my own. I confirm that:

- This work was done wholly or mainly while in candidature for a research degree at this University.
- Where any part of this thesis has previously been submitted for a degree or any other qualification at this University or any other institution, this has been clearly stated.
- Where I have consulted the published work of others, this is always clearly attributed.
- Where I have quoted from the work of others, the source is always given. With the exception of such quotations, this thesis is entirely my own work.
- I have acknowledged all main sources of help.
- Where the thesis is based on work done by myself jointly with others, I have made clear exactly what was done by others and what I have contributed myself.

Signed:

Date:

Statement on the use of AI

I, M.Sc. Lukas GÜLZOW, declare that I have not used generative AI to generate any text or any of the images included in this thesis titled, "Signal model for the radio emission of inclined cosmic-ray air-showers and energy reconstruction of event candidates for GRAND". In the following, I state the ways I have used AI in the course of this project:

- I have used ChatGPT in early 2023 for code documentation.
- I have used ChatGPT in 2024 to generate bash scripts I used to process CORSIKA simulation results on HoreKa.
- I have occasionally used the AI tool "Writefull", integrated in Overleaf, to suggest synonyms while writing this thesis.
- I have occasionally used the AI tool "Google NotebookLM" to search for information and citations in references.

Signed:

Date:

KARLSRUHER INSTITUT FÜR TECHNOLOGIE

Abstract

Faculty of Physics
Institute for Astroparticle Physics

DOKTORS DER NATURWISSENSCHAFTEN (Dr. rer. nat.)

Signal model for the radio emission of inclined cosmic-ray air-showers and energy reconstruction of event candidates for GRAND

by M.Sc. Lukas GÜLZOW

Ultra-high-energy cosmic rays (UHECRs) originate from the most energetic and mysterious environments in the Universe. When UHECRs reach Earth, they collide with nuclei in the atmosphere, and induce massive particle cascades. Due to their rarity, we can only measure them with large surface detectors. The Giant Radio Array for Neutrino Detection (GRAND) will, next to its main goal of measuring UHE neutrinos, also be especially sensitive to inclined air-showers induced by UHECRs.

I use CoREAS simulations of the radio emission of inclined air-showers to adapt a previously developed signal model for this phenomenon in the 30–80 MHz frequency band to the 50–200 MHz band used by GRAND. I tune the model for the site of the GRAND prototypes GRAND@Auger, located at the Pierre Auger Observatory in Argentina, and GRANDProto300 (GP300) in the Gansu province of China. I reconstruct the geomagnetic radiation energy by fitting a lateral distribution function to the radially symmetric distribution of the energy deposited in the ground. After I correct for the air-density and geomagnetic field dependence, I correlate the radiation energy with the electromagnetic shower energy. The radio emission of air-showers changes significantly depending on parameters like frequency, geomagnetic field, and observation altitude. With the modifications I introduce to the model, I expect it to be viable for any configuration of the geomagnetic field, as well as lower and higher frequency bands by simply retuning the model parameters.

With this work, I provide the first end-to-end event reconstruction for GRAND, including the reconstruction of the electric field from measured data, as well as a solid basis for the analysis of future GRAND measurements. The reconstruction achieves an intrinsic energy resolution better than 5% for the sites of GRAND@Auger and GP300. I benchmark the reconstruction by simulating the sparse antenna layouts of GP300 and GRAND10k, a future stage of GRAND with a 10,000 km^2 detection area. Under realistic measurement conditions, the reconstruction achieves an excellent energy resolution of 7% with vanishing biases for both detectors. The reconstruction shows no inherent dependence on the cosmic-ray primary particle. I successfully apply the energy reconstruction to six of the first GRAND cosmic-ray event candidates, measured by a partial configuration of GP300. The reconstructed energies agree with expectations. Furthermore, I study the detection efficiency of GP300 and GRAND10k. I estimate for both detectors the rate of detected and reconstructed cosmic ray events. I expect GP300 and GRAND10k, respectively, to measure about 2000 and 85,000 cosmic-ray events with energies $> 10^{18}$ eV within one year of exposure time. I predict that a detector like GRAND10k will detect at least 10 UHECR events with energies $> 10^{19.75}$ eV within the same time period.

Contents

List of Figures

List of Tables

List of Abbreviations

ADC	**A**nalogue-to-**D**igital **C**onverter
AERA	**A**uger **E**ngineering **R**adio **A**rray
CR	**C**osmic **R**ay
DU	**D**etection **U**nit
EAS	**E**xtensive **A**ir-**S**hower
GP300	**G**RAND**P**roto**300**
GRAND	**G**iant **R**adio **A**rray for **N**eutrino **D**etection
LDF	**L**ateral **D**istribution **F**unction
LOFAR	**LO**w-**F**requency **AR**ray
NWU	**N**orth-**West**-Vertical/**U**p
PWF	**P**lane-**W**ave **F**ront
RD	AugerPrime **R**adio **D**etector
SNR	**S**ignal-to-**N**oise **R**atio
UHE	**U**ltra-**H**igh **E**nergy
UHECR	**U**ltra-**H**igh **E**nergy **C**osmic **R**ay

Chapter 1

Introduction

At first glance, the term "cosmic rays" may seem misleading. One would think it describes a kind of electromagnetic radiation. This term originates from the early era of cosmic ray research during which this view was the consensus. Cosmic rays (CR) were discovered in 1912 by Victor Hess while studying unexplained ionising radiation observed on Earth [1]. This radiation was thought to be originating from the Earth itself. However, during balloon flights, its intensity was shown to increase rather than decrease with altitude. This marks the beginning of the study of cosmic rays. Even as a better understanding of the phenomenon arose, the old terminology remained. Now, we use "cosmic rays" to refer to charged particles that reach Earth from outer space.

Cosmic rays reach Earth with energies across many orders of magnitude. The most mysterious among them are ultra-high-energy cosmic rays (UHECRs). These extraordinary particles can reach energies beyond 10^{20} eV [2, 3], orders of magnitude higher than even the highest collision energies we can achieve on Earth using particle accelerators [4]. Despite multiple decades of intense research, we still have no clear answers for many questions about their uniquely energetic origins. Deflections due to Galactic and intergalactic magnetic fields make it highly challenging to trace UHECRs back to their sources. In addition, the rate at which UHECR arrive at Earth is particularly low. Not only does the rate of cosmic rays rapidly decrease with increasing energy, the Universe also becomes opaque to them at the highest energies. This limits their expected flux to a single particle per square kilometre per century. We detect UHECRs on Earth by instrumenting large detection areas to measure the so-called extensive air-showers they induce in the atmosphere. Shortly after an UHECR enters the atmosphere, it collides with a nucleus in an air molecule. The energy unleashed in this interaction initiates a massive cascade that can entail billions of particles at its maximum. As of today, the largest detectors for UHECR air-showers are the Pierre Auger Observatory [5] and the Telescope Array [6].

The Giant Radio Array for Neutrino Detection (GRAND) is another upcoming air-shower experiment [7]. The GRAND collaboration plans to construct multiple detectors all over the world with a total area of 200,000 km^2, which is more than half the size of Germany. The main science goal of GRAND is the detection of near-horizontal air-showers induced by Earth-skimming UHE neutrinos. As neutrinos only interact weakly, UHE neutrinos point back directly to their origin, but have an even lower detection rate than UHECRs in turn. Since we know from their energy density that UHE neutrinos and UHECRs are connected [8], they promise unprecedented insight into the sources of UHECRs. The enormous detection areas necessary to detect UHE neutrinos impose sparse antenna density. For the UHECR side, this makes GRAND sensitive to inclined air-showers only.

Among many other experiments, GRAND uses the highly effective radio detection technique to measure with simple radio antennas the radiation emitted by

electrons and positrons of an air-shower in the geomagnetic field. The transparency of the atmosphere to radio waves enables a calorimetric measurement of the electromagnetic energy of an air-shower. Over the course of its development, the majority of the air-shower energy transfers to the electromagnetic component. As such, inclined showers are ideal candidates to study the cosmic-ray energy spectrum since their shower development is guaranteed to finish before they reach the ground. While the radio emission from a vertical air-shower only illuminates a small "footprint" area, the footprint of an inclined air-shower with zenith angle $\geq 65^\circ$ is large enough to be detected by multiple antennas of a sparse array with spacing of the order of a kilometre.

In this work, I adapt a previously developed signal model of the 30–80 MHz radio emission for the Pierre Auger Observatory [9] to the 50–200 MHz frequency band used by GRAND. During this process, I fine-tune the model for two experimental sites to show its general applicability: the site of the Pierre Auger Observatory in Argentina where the GRAND prototype detector GRAND@Auger [10, 11] currently operates, and the site of the GRAND prototype detector GRANDProto300 (GP300) in the Gansu province of China [10, 12]. With Argentina and China serving as extremes of the geomagnetic field strength on Earth, I show the viability of the model for any geomagnetic field configuration. The higher and wider frequency band brings with it differences in the radio emission. The so-called "Cherenkov ring", a high-intensity feature of the radio emission pattern, is more pronounced. The signal also loses coherence due to the shorter wavelengths. In addition, the much stronger magnetic field in China exacerbates this loss of coherence [13]. I address these effects and expand the signal model to accommodate them. In the process, I generalise the model for any frequency band in use at the time of writing. Applying the signal model, I formulate a practical reconstruction of the shower electromagnetic energy.

With my work, I am establishing a basis for the reconstruction and analysis of any GRAND UHECR measurements. I create two CoREAS [14] simulation libraries, simulating the planned final GP300 layout and a possible layout of GRAND10k, a future stage of GRAND covering 10,000 km^2 of detection area. I evaluate the difficulties introduced by sparse antenna arrays, background and transient noise, as well as the reconstruction of all shower parameters, by benchmarking the reconstruction performance at many levels of realism, including fully realistic measurement conditions. I apply the signal model and energy reconstruction to the first measured cosmic-ray event candidates from a partial configuration of GP300. Further, I investigate the detector efficiency and expected number of measured events for both GP300 and GRAND10k.

I organise this thesis as follows. Chapter 2 covers important concepts about cosmic rays, air-shower physics and detection, as well as the radio emission from extensive air-showers. Chapter 3 introduces GRAND and covers its science goals, prototype phases, and challenges. In Chapter 4, I present the principles and methods of the signal model and attached reconstruction algorithm for the electromagnetic energy. In Chapter 5, I show my adaptations to the model for the 50–200 MHz frequency band, and the experiment sites of the two GRAND prototype arrays, GRAND@Auger and GRANDProto300. Subsequently, in Chapter 6, I benchmark the performance of the reconstruction for different antenna layouts, and levels of realism. In Chapter 7, I present the successful reconstruction of multiple cosmic-ray event candidates measured by a partial configuration of GP300. In Chapter 8, I study the detector efficiency, calculate the effective aperture, and estimate the event rate for both GP300 and GRAND10k. I discuss the results of my work in Chapter 9. Finally, I summarise my work and make concluding statements in Chapter 10.

Chapter 2

Theoretical Background

2.1 Cosmic rays

Cosmic rays are generally defined as charged particles that reach Earth from outer space. They mainly consist of charged nuclei ranging from hydrogen to iron. Heavier nuclei are thought to be present in much smaller abundances. Cosmic rays make up a significant part of the Universe's total energy. The cosmic ray energy density of $\sim 1\,\mathrm{eV/cm^3}$ [15] is of the same order of magnitude as the energy density of the cosmic microwave background (CMB) ($0.3\,\mathrm{eV/cm^3}$) [16], the interstellar magnetic field ($2\,\mathrm{eV/cm^3}$) [17], and the local energy density of starlight ($0.4\,\mathrm{eV/cm^3}$) [18].

Generally, the more energy cosmic rays have, the rarer they are. Low energy cosmic rays with high flux play a role in heating up and influencing the composition of the interstellar medium and clouds of gas [19, 20]. They also have an influence on the formation of stars and evolution of galaxies [20]. The rare cosmic rays at the highest energies serve, among others, as messengers from the most energetic sources and processes in the Universe. However, much about the nature of these sources and about the acceleration of ultra-high-energy (UHE) cosmic rays themselves remains unclear [4].

2.1.1 Energy spectrum

Measured energies of cosmic rays range from a few MeV, only detected by Voyager outside the influence of Solar winds [15], up to a few hundreds of EeV, according to indirect detections of large-area surface arrays [2, 3]. This wide energy range indicates that cosmic rays are produced by many different mechanisms. Specifically, the cosmic rays at the highest energies are orders of magnitude more energetic than the collision energies we can achieve with particle accelerators on Earth. Understanding how and where they were accelerated to such extremes is a key question in cosmic-ray research.

Due to their electromagnetic charge, cosmic rays do not travel in straight lines. Galactic and intergalactic magnetic fields apply Lorentz forces and deflect the particles from their initial trajectory. This makes determining the sources of cosmic rays extremely challenging.

The cosmic ray energy spectrum describes the rate at which cosmic rays of all energies arrive on Earth. Figure 2.1 shows the spectrum between 10^9 and 10^{21} eV. Measured data from each included experiment is marked in the plot. The flux—the rate of arriving particles per energy bin, square meter, second and unit of solid angle—is on the y-axis, here called "intensity". It is multiplied with the squared energy of the cosmic rays E. On the one hand, this shows the spectral features more clearly. On the other hand, it also makes the y-axis proportional to the energy density per decade of energy. As such, particles that lie on the same horizontal level share

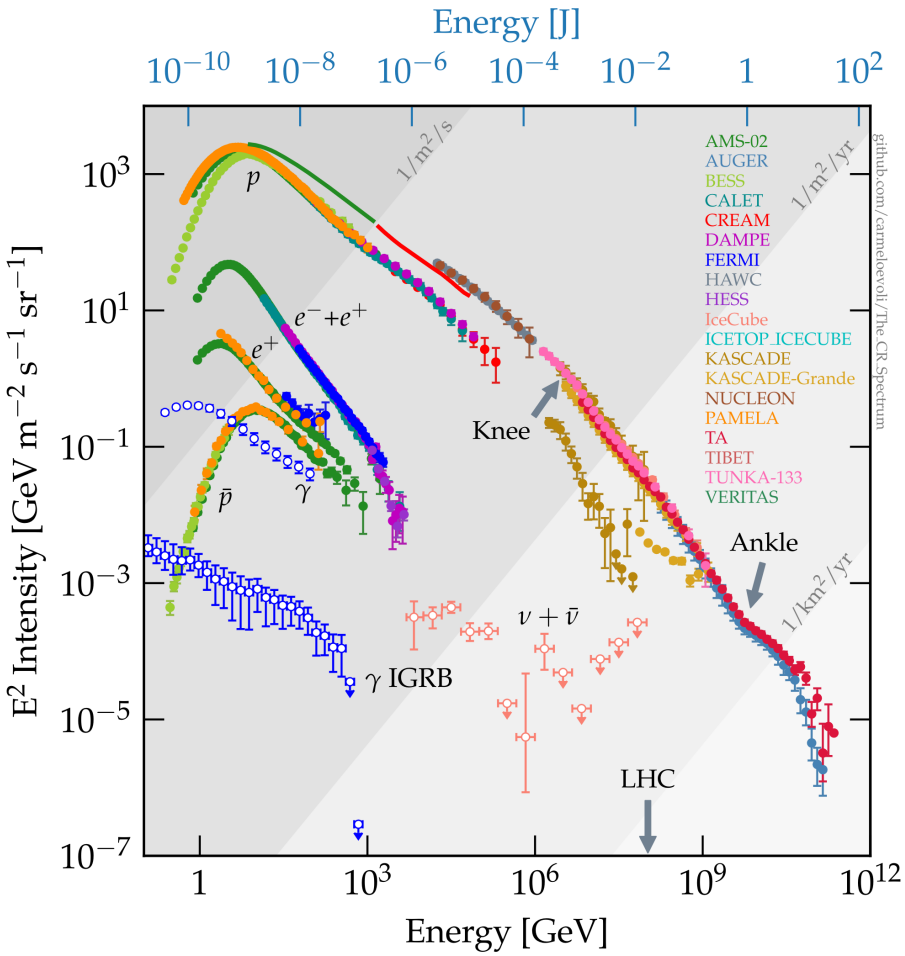

FIGURE 2.1: Energy spectrum of cosmic rays. The flux/intensity on the y-axis is multiplied with the squared cosmic ray energy E^2. This lets particles with the same energy density in the Universe appear at the same horizontal level. The energy equivalent to the maximum centre-of-mass LHC energy is annotated on the x-axis. Diagonally the observable particle flux on Earth's surface is shown with shaded regions. Data from different experiments is labelled by colour. Spectra belonging to specific particles are labelled. More details in the text. Plot adapted from [21]. Data from [22].

the same energy density. In Figure 2.1, this may suggest a common origin between photons, neutrinos, and cosmic rays at the highest energies [8]. The cosmic ray energy spectrum can be divided into multiple parts, separated by its spectral features. The lowest energy feature is the "knee" at $\sim 5 \cdot 10^{15}$ eV. At the knee, the spectrum steepens, analogous to a not fully extended leg. At about 10^{17} eV, we abandon the analogy to human anatomy for the "2nd knee"(not marked in the figure) where the spectrum steepens even further. The 2nd knee is commonly associated with the cut-off of acceleration of iron nuclei in shock fronts of supernova remnants (SNR). The spectrum hardens again at the "ankle" at $\sim 5 \cdot 10^{18}$ eV. Around this energy, cosmic rays stop exhibiting the characteristic anisotropy we expect from sources in the Galaxy. As such, the ankle has been interpreted as the transition from Galactic to extragalactic sources. However, in recent years, a lack of the characteristic anisotropy in measurements of proton primaries above the ankle suggests an earlier transition for light primaries [23].

The highest energy feature is a flux suppression starting at $\sim 5 \cdot 10^{19}$ eV. Commonly, there are two explanations contributing to this phenomenon. For one, we

expect the flux of UHE cosmic rays to be limited by interactions with the cosmic microwave background. Cosmic ray protons interact with CMB photons and lose energy via photo-pion-production. This is called the Greisen-Zatsepin-Kuzmin (GZK) effect. Heavier nuclei undergo photodisintegration, the transformation into another nucleus after interacting with a photon. Naturally, this also affects the cosmic-ray mass composition. The energy loss due to these processes effectively makes the Universe opaque to cosmic rays above the cut-off energy at length scales larger than 50 Mpc [24, 25]. This distance is called the GZK horizon. An additional contribution to the flux cut-off is possibly that cosmic ray accelerators reach their natural energy limit and only produce very few particles at these extraordinary energies.

The most recently discovered feature is the "instep" [26, 27, 28]. It is a hardening of the spectrum between the ankle and flux suppression which starts at $1.3 \cdot 10^{19}$ eV. Finding physical interpretations of the energy spectrum features is one of the main aspects of cosmic-ray research.

2.1.2 The Hillas criterion

A common way to examine possible cosmic ray sources is the so-called Hillas criterion [29]. It was established by Hillas in 1984 to define minimum requirements for an astrophysical object to be able to accelerate cosmic rays up to certain energies. The key concept is confinement. A cosmic ray source can only accelerate charged particles as long as the particle Larmor radius—the radius of its circular motion in a magnetic field—is smaller than the size of the accelerator. In other words, the accelerating object must be of sufficient size to confine the particle long enough to accelerate it. The criterion is a requirement, but it is not a sufficient condition. The Hillas plot is used to illustrate the criterion by comparing source sizes and magnetic field strength.

In Figure 2.2, I show an updated Hillas plot for the example of UHE protons and iron nuclei from reference [30]. The astrophysical objects to the left of the diagonal line do not fulfil the criterion, while objects to the right of it do. Heavy nuclei have a much smaller Larmor radius than protons at the same energy due to their higher charge. Consequently, the Hillas criterion is more lenient for potential sources of UHE iron nuclei as is visible in the figure. Due to this effect, we expect cosmic rays at high energies to transition to a heavier composition. This process is called "Peters Cycle".

2.1.3 Neutrinos

Cosmic rays or, in other words, charged particles, are not the only cosmic messengers we can measure on Earth. Photons and neutrinos reach us as well. They are neutral particles and, consequently, not affected by the magnetic fields that make it so challenging to determine the sources of cosmic rays. From energy density considerations, we know that the same processes that produce cosmic rays at the highest energies also produce gamma-ray photons and neutrinos [8]. In addition, there are also gravitational waves. Combining information from all these different sources is what we call multi-messenger astronomy.

Neutrinos are very difficult to measure because of their low interaction rate. However, the same property ensures the information carried by neutrinos comes directly from where they were created. They can originate directly from a source, or from close to it, and carry the information unchanged all the way to Earth. These neutrinos are called astrophysical neutrinos. The GZK effect is another source of

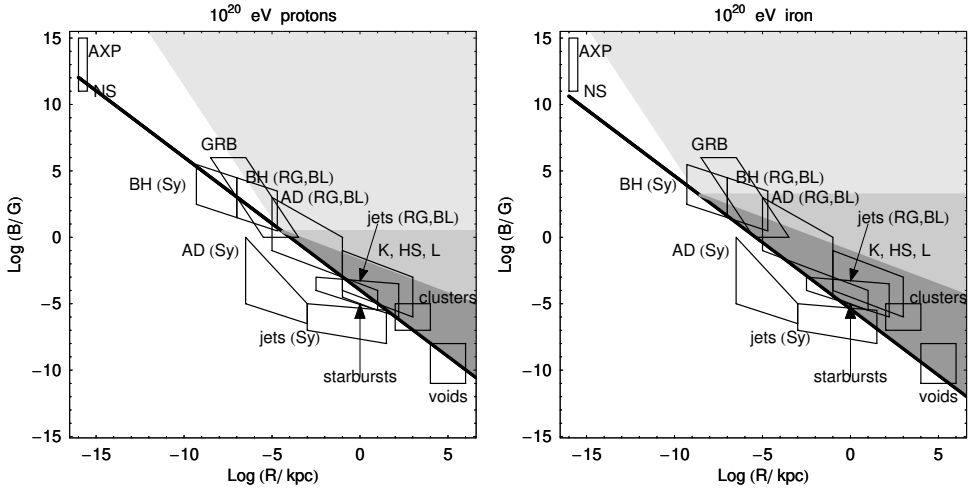

FIGURE 2.2: Updated Hillas plots for protons (left) and iron nuclei (right) with $E = 10^{20}$ eV. Objects to the right of the solid black line fulfil the Hillas criterion. Shaded regions are allowed by different models of radiation and acceleration losses. Lower lines of the labelled regions correspond to the Hillas constraint, upper lines represent radiation-loss constraints. The abbreviations stand for anomalous X-ray pulsars (AXP), neutron stars (NS), supermassive central black holes (BH) of AGNs, central regions of active galaxies (AD), gamma-ray bursts (GRB), galaxy clusters, non-relativistic and relativistic jets, starburst galaxies, intergalactic voids, knots (K), hot spots (HS) and lobes (L) of powerful active galaxies. The galaxy types are low-power Seyfert galaxies (Sy), powerful radio galaxies (RG) and blazars (BL). Plots from [30].

highly energetic neutrinos. Photo-pion-production of UHE cosmic rays interacting with CMB photons produces neutrinos that carry a fraction of the cosmic ray primary energy. These are called cosmogenic neutrinos.

On Earth, we measure neutrinos by monitoring massive detector volumes of water or ice with photo-multiplier tubes (PMTs), i.e., light detectors. If a neutrino interacts inside or close to the detector volume, the charged lepton produced in the interaction will be visible as it passes through the detector. A muon emits Cherenkov light while passing through, producing a light track. An electron triggers an electromagnetic particle cascade. A tau at sufficiently high energy also produces a track, but generally decays immediately. Depending on the decay products, they can trigger a cascade or, in the case of a muon, simply leave another track.

There are multiple experiments designed to detect neutrinos of astrophysical origin. The IceCube experiment at the South Pole uses a cubic kilometre of Antarctic ice, instrumented with digital optical modules on long strings, to detect astrophysical neutrinos between 10^8 and 10^{15} eV [31, 32]. The Cubic Kilometer Neutrino Telescope (KM3NeT) uses the sea water of the Mediterranean Sea in a similar way [33]. For lower neutrino energies between 10^6 and 10^{11} eV, (Super-)Kamiokande in Japan uses a giant water volume, lined with PMTs, to detect any Cherenkov light emitted in the water [34, 35].

Cosmogenic neutrinos are generally too energetic to be measured by these experiments. So far, only KM3NeT has measured a single neutrino event at associated energies [36]. However, the IceCube-Gen2 upgrade plans to extend IceCube's energy range sufficiently by increasing the detector volume and the addition of in-ice radio detectors. The Radio Neutrino Observatory Greenland (RNO-G), currently in the deployment phase, uses radio antennas submerged in the ice sheet on Greenland [37]. It is expected to be sensitive to neutrino-induced in-ice particle showers

above 10^{16} eV.

The Giant Radio Array for Neutrino Detection (GRAND) is another upcoming experiment designed to measure UHE neutrinos. It aims to use giant arrays of ground-based radio antennas to measure air-showers induced by Earth-skimming neutrinos [7]. I discuss GRAND in detail in Chapter 3 since this work is closely connected to it.

2.2 Extensive air-showers

2.2.1 Air-shower physics

When a cosmic ray hits Earth's atmosphere, eventually an air nucleus will be in its path, leading to a collision. The energy carried by the cosmic ray, or "primary particle", is split among the secondary particles produced in the collision. As such, the cosmic ray seeds a cascade of particles since the secondary particles continue to produce more particles in the same fashion. Each particle carries a fraction of the energy of the previous "generation". The production of particles continues until they reach the "critical energy" E_c. This is the point at which energy loss from radiative processes are equal to ionisation losses. From that point on, the particles lose energy primarily to ionisation which leads to the absorption of the cascade in the atmosphere. Over the course of its development, the cascade—which, from here on, I call "extensive air-shower" (EAS), or just air-shower—can contain billions of particles, depending on the initial energy.

The point where the shower reaches the maximum amount of particles is called the shower maximum. The depth of the shower maximum—the amount of matter traversed since the cosmic ray entered the atmosphere—is an important quantity in air-shower physics. It gives information about the type of nucleus and energy of the primary cosmic ray since the penetration depth depends on both. The depth of shower maximum is given in $\mathrm{g/cm^2}$, also called "grammage". It is usually denoted with X_{max}. One can picture X_{max} as a column of air along the shower axis. We use grammage to characterise the shower maximum because it is invariant to whether a cosmic ray enters the atmosphere vertically or at an angle.

We commonly divide the particle content of air-showers into three components. Figure 2.3 displays a simplified diagram showing what makes up each component. The hadronic component contains the hadrons that are produced in the first collision, and all others from further collisions. Most importantly, these are the mesons π^+, π^- and π^0. Other kinds of hadrons, for example Kaons, are produced as well. Many details of the development of the hadronic component are not well-defined since precise knowledge of hadronic interactions is limited to the energy and rapidity range covered by collider experiments. The initial energy of, especially, UHE cosmic rays lies well above that. As such, we describe them by extrapolating from the models at lower energies.

Another part of the shower is the electromagnetic component, made up of electrons, positrons, and photons. It is fed by the hadronic component from the main decay mode of neutral pions,

$$\pi^0 \to \gamma\gamma.$$

The π^0 has a short lifetime of 8.5×10^{-17} s. As such, it decays very quickly after it comes into being without traversing much air and colliding with more nuclei. The photons produced in the decay generate electron-positron pairs through pair-production. These electrons and positrons go on to produce more photons through

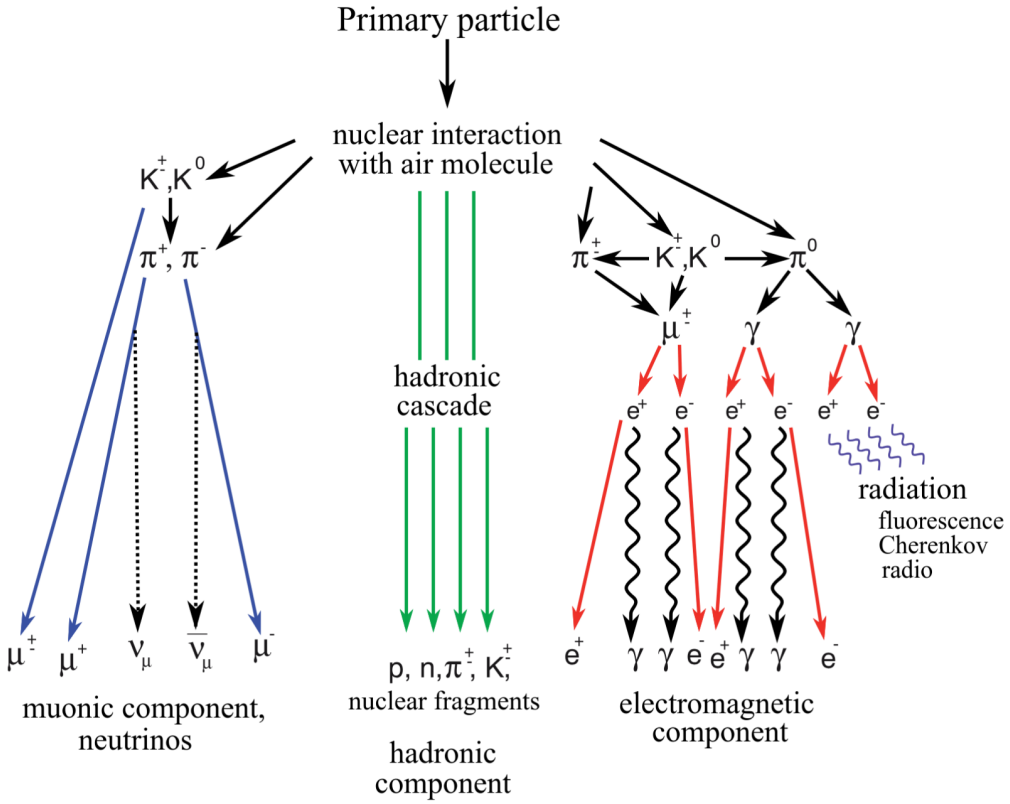

FIGURE 2.3: Simplified schematic of an air-shower and its components. Details in the text. Graphic from [38].

bremsstrahlung. The critical energy for electrons is 87 MeV. Below this threshold, the electrons and positrons primarily ionise atoms in the atmosphere to add more electrons to the cascade. As such, the cascade comes to a halt as the particles are absorbed. The electromagnetic component contains the majority of the energy of the air-shower due to the hadronic component feeding into with every produced π^0.

The third aspect of an air-shower is the muonic component. Besides π^0, the other most common particles in the hadronic cascade are the charged pions, π^+ and π^-. With a branching ratio of over 99.9%, they decay into muons and a neutrino,

$$\pi^+ \rightarrow \mu^+ + \nu_\mu,$$
$$\pi^- \rightarrow \mu^- + \overline{\nu}_\mu,$$

and add to the muonic component. While muons decay into electrons/positrons and neutrinos

$$\mu^+ \rightarrow e^+ + \nu_e + \overline{\nu}_\mu,$$
$$\mu^- \rightarrow e^- + \overline{\nu}_e +, \nu_\mu,$$

their longer lifetime of 2.2×10^{-6} s allows the majority to reach the Earth's surface due to time dilation. A big open question in air-shower physics is the discrepancy between the amount of muons in measurements and simulations of air-showers. Measurements indicate a larger muon content than the simulations predict. This is called the "Muon Puzzle" [39].

We characterise the development of the cascade with the so-called "longitudinal

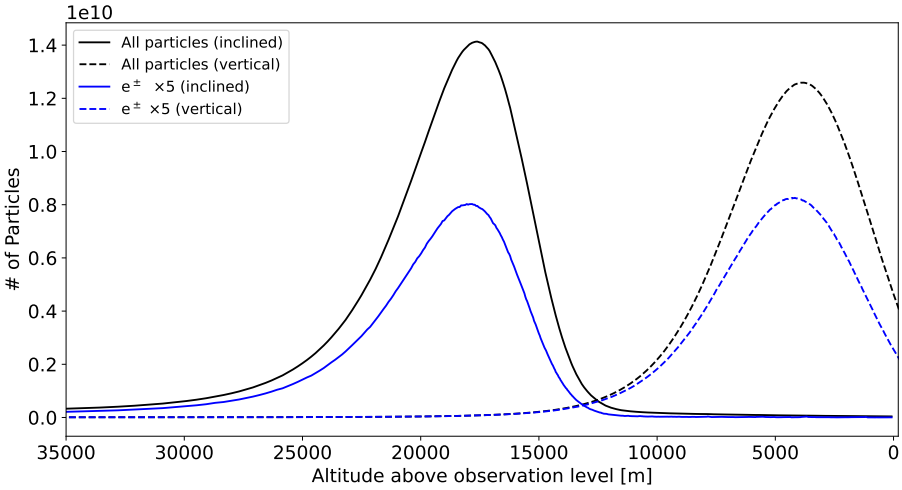

FIGURE 2.4: Comparison of the longitudinal profiles of a vertical (dashed lines) and an inclined (solid lines) air-shower shown against altitude. Both air-showers are simulated with CORSIKA [40] and have proton primaries. The inclined shower is close to horizontal with a 85° zenith angle, and has a primary energy of $2.5 \cdot 10^{18}$ eV. The vertical shower has a 15° zenith angle and 10^{16} eV of primary energy. I multiply the profile of the vertical shower by a factor of 20 to match the horizontal profile. I show all-particle profiles in black, $e^{\pm}$ profiles in blue. The profile of the vertical shower is truncated where it hits the ground plane. The inclined air shower finishes its development more than 10 km above ground.

profile". It shows the number of particles in the cascade, usually as a function of penetration depth into the atmosphere. From the profile, we can determine the shower maximum and also the primary cosmic ray energy since it shows how much energy was released into the atmosphere. Figure 2.4 shows the all-particle longitudinal profile, and the profile of electrons/positrons of a vertical and an inclined air-shower as a function of altitude. I show the profiles here with respect to altitude instead of atmospheric depth to highlight the difference between vertical and inclined air-showers. For the vertical shower, the air-shower development is on-going when it reaches the ground. However, for an inclined shower with a large zenith angle the cascade development has finished at that point, since it travelled along a much longer path through the atmosphere. The air-shower I show in Figure 2.4 finishes its development more than 10 km above the ground. The longitudinal profile is often shown against the atmospheric depth of the shower where the depth of maximum X_{max} is clearly visible as the peak of the curve.

2.2.2 Heitler-Matthews splitting model

To motivate the reconstruction of the electromagnetic shower energy, specifically for inclined air-showers, I introduce the Heitler-Matthews splitting model for air-shower development [1]. Heitler's original model [41] describes the development of electromagnetic particle cascades. The Heitler-Matthews model [42] extends the Heitler model to hadronic cascades. It describes both the hadronic cascade itself, as well as how it feeds into the electromagnetic component. Figure 2.5 shows a schematic representation of the model. In the model, each interaction results in n_{tot}

[1] Much of this subsection follows the corresponding section in reference [4].

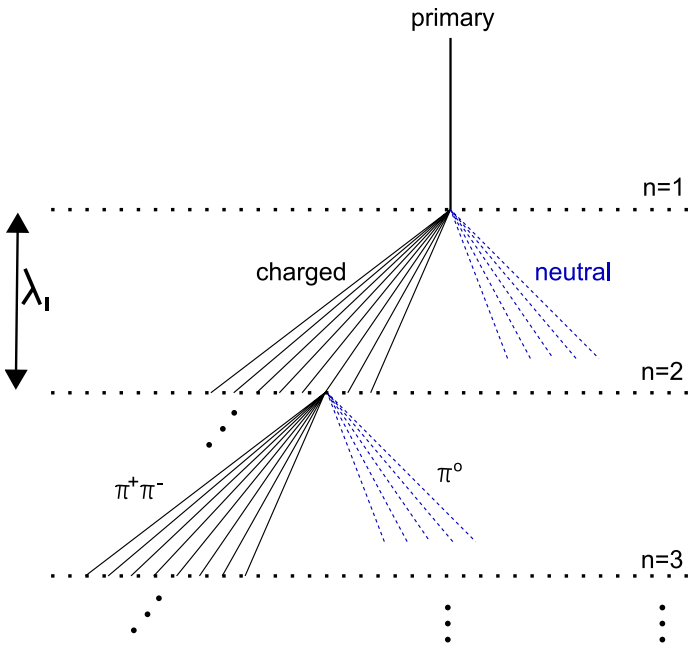

FIGURE 2.5: Heitler-Matthews splitting model. The development of the hadronic component of an air-shower after the primary interaction of a proton or nucleus. Each generation n, defined by the interaction length λ_{int}, the energy splits between neutral (dashed blue lines) and charged particles (solid black lines). The neutral pions decay and feed their energy into the electromagnetic cascade while the charged particles interact after another λ_{int}. Graphic from [43].

new particles. For an interaction with energy E, each interaction product carries the energy E/n_{tot}. Two thirds of the produced particles carry charge, the remaining third is neutral. The figure shows the example of charged and neutral pions since they are the most common hadronic particles in the shower. The neutral particles immediately decay into electromagnetic particles and feed their third of the energy to the electromagnetic component of the cascade. The charged particles travel one mean interaction length λ_{int} before they interact again and repeat the process. Each step is called a generation. After n generations, the respective energy carried by the hadronic and electromagnetic shower component is given by

$$E_{\text{had}} = \left(\frac{2}{3}\right)^n E_0 \qquad \text{and} \qquad E_{\text{em}} = \left[1 - \left(\frac{2}{3}\right)^n\right] E_0. \tag{2.1}$$

Each successive generation, the charged particles receive less and less energy. When they drop below a decay threshold energy E_{dec}, they no longer interact, but decay instead. Each charged hadron decays into a single muon. These features of the simplified model also still reflect the reality of electromagnetic showers. The "decay" threshold corresponds to the critical energy threshold at $E_c = 87$ MeV where ionisation losses begin to dominate over radiation losses. Instead of decaying, the electromagnetic particles are absorbed by the atmosphere.

From Eq. (2.1) it follows, that, after $n = 8$ generations, 95% of the energy of the initial interaction E_0 is transferred to the energy of the electromagnetic component E_{em}. Inclined air-showers, i.e., with zenith angle $\theta > 65°$, are guaranteed to have completed cascade development before they reach the ground. Since the electromagnetic component emits in radio frequencies during the entire development, measuring the radio emission enables a calorimetric measurement of E_{em}. Consequently,

the usefulness of a reconstruction of the energy of the electromagnetic component using the radio emission becomes clear.

Another feature of the model, which holds true for electromagnetic cascades, and also, approximately, for hadronic cascades is the logarithmic dependence of $X_{\max}$,

$$X_{\max} = \lambda_{\text{int}} \frac{\ln(E_0/E_c)}{\ln 2}, \tag{2.2}$$

on the primary energy E_0.

2.2.3 Detection methods

At the low end of the energy spectrum, we measure cosmic rays via direct detection with satellites or balloon experiments. The Alpha-Magnetic Spectrometer (AMS-02) [44] is installed on the International Space Station (ISS). AMS-02 measures cosmic rays with a spectrometer, a silicon tracker, and an electromagnetic calorimeter. Also on the ISS was ISS-CREAM—pronounced "ice cream"—, the spaceborne successor of the Cosmic Ray Energetics and Mass (CREAM) balloon experiments [45]. The cosmic-ray research module Payload for Antimatter Matter Exploration and Light-nuclei Astrophysics (PAMELA) was a research module attached to a satellite which took data for ten years [46]. A different satellite detector is the Fermi Gamma-ray Space Telescope (Fermi-LAT) [47]. However, instead of cosmic rays, Fermi-LAT detects gamma-rays. Among other goals, Fermi-LAT observes active galactic nuclei and supernova remnants to understand their mechanisms of particle acceleration. It scans the sky in search of gamma-ray sources, which also produce cosmic rays. These techniques are valid up to a few hundred TeV. Above that, the cosmic ray flux is too low to collect sufficient amounts of data.

Cosmic rays at the highest energies are exceedingly rare. Approximately one particle per century hits any square kilometre on the Earth's surface. As such, direct detection is impossible, and we have to rely on indirect detection methods. To collect statistically relevant amounts of data, we employ large-scale surface detectors to cover massive areas and increase the rate of high-energy cosmic rays we can detect.

There are multiple detection techniques in use. Water-Cherenkov tanks, equipped with PMTs, can detect Cherenkov light emitted by shower muons and other charged particles passing through the tank. Scintillator panels directly detect charged particles passing through them [48]. They are placed on both the surface and buried underground. The buried scintillators are shielded from the electromagnetic component. Cherenkov tanks and scintillators provide information about the mass composition by discriminating between the muonic and electromagnetic parts of the cascade.

Fluorescence telescopes, during clear and moon-less nights, detect fluorescence light emitted by atmospheric nitrogen molecules excited by air-shower electrons. They are exceptional at inferring the cosmic ray energy and depth of maximum $X_{\max}$ since they directly provide a calorimetric measurement of the longitudinal profile. Their downsides are the expensive instruments, a high energy threshold of $E_{\text{CR}} > 10^{17}$ eV and the poor duty cycle of only 10-15%. In addition, they require precise measurements of the atmospheric conditions for accurate measurements.

Lastly, the electrons and positrons in the air-shower emit radio waves in the MHz regime which we can measure with simple radio antennas. Radio measurements enable direct access to the electromagnetic shower component and enable reconstruction of the shower maximum, arrival direction, and electromagnetic energy. Radio

detection of cosmic ray air-showers is of particular relevance for this work. In Section 2.3, I discuss the radio emission of air-showers in detail.

The two biggest currently operating air-shower detectors are the Pierre Auger Observatory [5] near Malargue, Argentina and the Telescope Array (TA) [6, 3] in Utah, USA. They both employ hybrid detection methods that complement each other for more efficient interpretation of the data.

2.3 Radio emission of cosmic ray air-showers

Radio emission from extensive air-showers was first detected by Jelley et al. [49] in 1965. Research continued into the 1970s, but interest in the technique faded due to, for example, the limits of analogue technology and the promising emerging fluorescence imaging technique. In the early 2000s, the field of cosmic-ray radio detection re-emerged and has steadily grown since. Modern experiments have been able to build on the previous research, and provide valuable measurements alongside other detection techniques. These experiments include CODALEMA [50], the LOFAR Prototype Station (LOPES) experiment [51] and the connected Low-Frequency Array (LOFAR) [52], Tunka-Rex [53], the Auger Engineering Radio Array (AERA) [54, 55] and the AugerPrime Radio Detector (RD) [56, 57].

In this section, I describe the mechanisms and features of cosmic-ray radio emission as well as advantages and problems pertaining its detection. For a complete picture, I refer to the reviews by Huege [58] and Schröder [59].

Since Earth's atmosphere is transparent to radio waves between 10 MHz and a few GHz, the radio emission from extensive air-showers reaches the ground without any loss of signal. The air-shower emits radio waves throughout its entire evolution. As such, its radio emission enables a calorimetric energy measurement. In addition, one can describe the emission analytically using first-principle classical electrodynamics [60]. These properties make it a great tool to infer properties of both the air-shower, and the cosmic-ray primary particle.

The electromagnetic shower component is largely unaffected by the uncertainties of hadronic interaction models that have to be extrapolated to high energies. Particle detectors suffer from systematic uncertainties from these models since they can only measure the particles that reach the ground after the shower evolution [61]. Air-shower radio emission, as it is sourced by the electromagnetic component, is much less affected. Consequently, exclusively the energy of the electromagnetic component can be directly obtained with radio measurements.

In contrast to the 10–15% duty cycle of fluorescence telescopes, radio antennas have a duty cycle close to 100%. Only strong distortions of the electric field conditions, i.e., thunderstorms, prevent accurate measurements. In addition, radio antennas are relatively cheap, which enables the instrumentation of large detection areas for the measurement of UHE cosmic rays.

The main problem radio measurements face is the abundance of transient noise in the relevant frequency bands. Many human-made signals operate in the MHz range, for example television and radio broadcasts. Electrical power lines, generators, and passing aeroplanes are other sources of radio interference, just to name a few. The Milky Way also emits radio waves. However, this Galactic noise is often useful for antenna calibration. The noise problem necessitates the use of remote, radio-quiet areas, and, so far, external triggering from particle detectors. The GRAND collaboration is currently developing an autonomous trigger to be able to economically instrument the necessary area to detect UHE neutrinos (see Chapter 3).

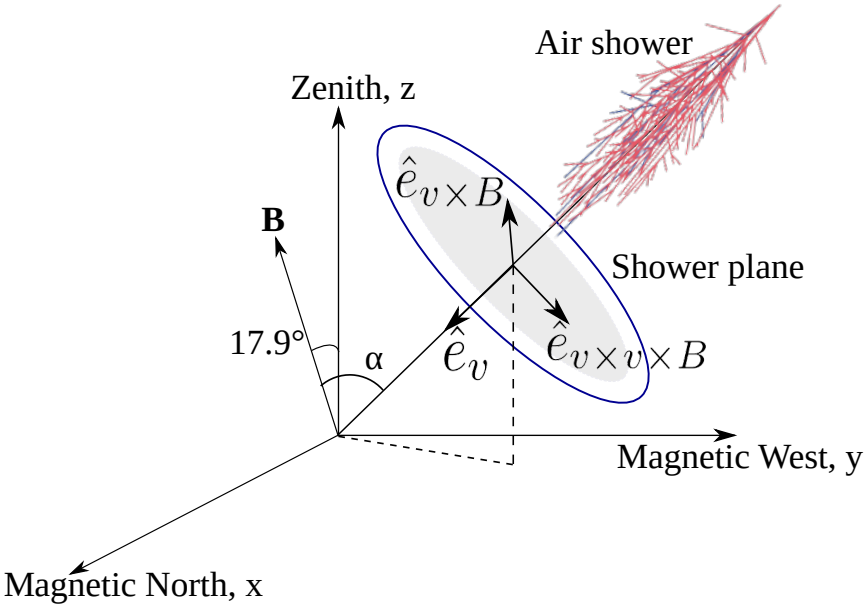

FIGURE 2.6: Illustration of the shower coordinate system. The orientation of the shower plane depends on the shower arrival direction $\hat{e}_v$ and the magnetic field vector **B**. Graphic from [64].

Radio detection is also in use for the detection of particle showers induced by cosmic rays and neutrinos in ice [62, 63, 37] (see Section 2.1.3). In contrast to air, radio waves attenuate in ice. However, the effective range is still multiple kilometres compared to the metre-scale range of optical signals. As such, sparse antenna placement can cover a large detection volume. In the denser medium, the dominant emission component changes and the emission angle increases.

2.3.1 Shower plane coordinate system

To describe the radio emission, it is common to use the coordinate system defined by the shower direction $\vec{v}$ and the geomagnetic field vector $\vec{B}$. The plane perpendicular to $\vec{v}$ is called the shower plane. We choose the basic vectors of this coordinate system

$$\begin{pmatrix} \hat{e}_{\vec{v}\times\vec{B}} \\ \hat{e}_{\vec{v}\times(\vec{v}\times\vec{B})} \\ \hat{e}_v \end{pmatrix} \tag{2.3}$$

as the unit vectors along the $\vec{v}\times\vec{B}$, $\vec{v}\times(\vec{v}\times\vec{B})$, and $\vec{v}$ directions. The $\vec{v}\times\vec{B}$ and $\vec{v}\times(\vec{v}\times\vec{B})$ axes span the shower plane. The $\vec{v}\times\vec{B}$ axis is the direction of the Lorentz force acting on the charged particles of the shower. Figure 2.6 shows an example shower plane with both the magnetic Cartesian and shower plane coordinate systems for illustration. The polarisation of the geomagnetic emission component is always aligned with this direction (see Section 2.3.3). As such, the radio footprint is always oriented the same way in the shower plane, regardless of the direction of arrival or the local geomagnetic field.

2.3.2 Simulation of air-shower radio pulses

Radiation emitted by accelerated charged particles strongly depends on the ratio of charge and particle mass. Consequently, the light electrons and positrons contribute almost all of the radio emission of air-showers. Their emission is described by the Liénard-Wiechert potentials [58]. They are derived from Maxwell's equations and generalise the Coulomb potential for moving charges. Relying on these potentials, there are two formalisms commonly used to calculate the resulting electromagnetic radiation from the acceleration of electrons and positrons in an air-shower. They are called the "endpoint" [65, 66] and "ZHS" [67, 68] formalisms. Notably, implementations of the endpoint formalism fall back on the ZHS formula for emission near the Cherenkov angle where the endpoint description diverges [69, 70]. Both formalisms have been shown to agree with experimental results within 5–10% by the SLAC T-510 experiment [71], and with each other within 1–2% in simulations of the same air-showers [72].

The CoREAS code [14], which was used to simulate the libraries of air-shower events used in this work, uses the endpoint formalism: The path of any single particle of the cascade is segmented into discrete, straight tracks. The emission is calculated for each start- and endpoint. The total radio signal at a given antenna position results from adding up the electric field vector from the start- and endpoints of all particle tracks in the cascade for a given observer position. Consequently, the computational cost of a simulated air-shower increases linearly with the number of simulated antenna positions.

Another factor that increases computational cost is the number of simulated particle tracks. For highly energetic showers, the maximum number of particles can reach 10^{11}. As one can imagine, this quickly escalates to unfeasibly long computing times, specifically for showers with primary energy $E_{\mathrm{CR}} > 10^{17}$ eV. As a numerical solution for this issue, we represent many particles by a single, more heavily weighted particle. This method is called "thinning" [73]. The thinning level $t_f = E_t/E_{\mathrm{CR}}$ is defined by the ratio of the threshold interaction energy E_t, above which the produced particles remain in the simulation, and the primary energy E_{CR}. For interactions below the threshold, only one randomly chosen particle is simulated to represent the discarded ones. Such a particle is then weighted to properly serve as a "replacement", and to obey energy conservation. In addition, the weighted particle has a maximum particle weight of 10^{-15} of the primary energy in eV. Thinning can lead to signal artifacts for antenna positions far away from the shower core—the point where the shower meets the ground—since the replacement particle emits with perfect coherence while an ensemble of lower energy particles does not.

Numerical calculations based on these microscopic pictures of the emission show good accuracy in describing and predicting the data from air-showers measurements [60]. However, they are not a satisfactory explanation on a macroscopic level. Thorough insight into the mechanisms of air-shower radio emission was only achieved through the concurrent development of macroscopic models [74, 75, 76]. I discuss these models in the following section.

2.3.3 Emission mechanisms

The radio emission of cosmic-ray air-showers mainly consists of two components. The geomagnetic component is dominant in air. The geomagnetic field separates the electrons and positrons in the particle cascade. This creates a time-dependent transverse current which emits in radio frequencies. The second component is called

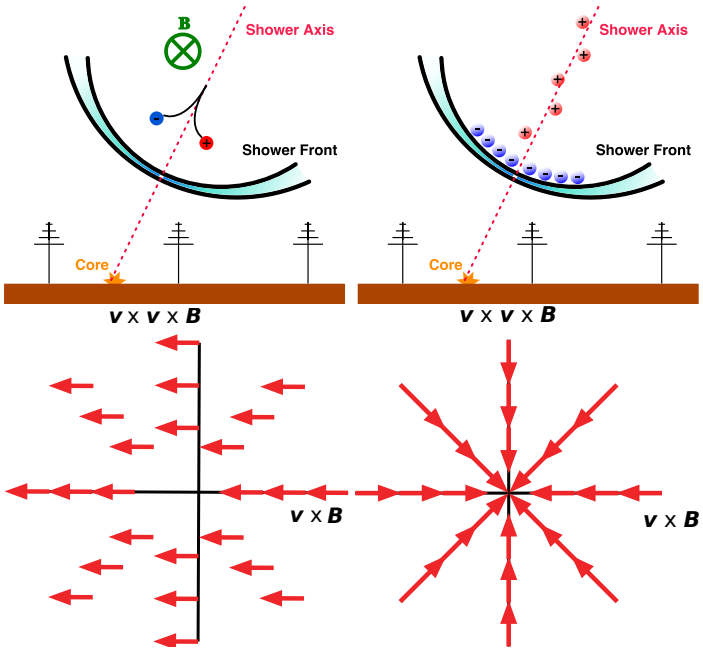

FIGURE 2.7: The two main radio emission mechanisms in cosmic ray air-showers. **Left column:** Geomagnetic emission. **Right column:** Charge excess or Askaryan emission. **Top row:** Schematic view of each mechanism. **Bottom row:** Polarisation patterns of each mechanism. Adapted from [58].

charge excess or Askaryan emission [77]. The shower particles ionise molecules in the atmosphere, and sweep the electrons along with it. This results in a $\sim$ 20% excess of electrons at the shower front. The time-varying current of the negative charge excess electrons at the shower front sources this component.

Figure 2.7 shows the emission mechanisms schematically (top left and right) and displays the polarisation pattern of each component in shower plane coordinates. Individually, the intensity pattern of each component is radially symmetric around the shower axis. The geomagnetic component is polarised along the negative $\vec{v} \times \vec{B}$ direction (cross product of the shower and magnetic field directions; bottom left panel of Fig. 2.7). On the other hand, the charge excess component is polarised radially towards the shower axis (bottom right). The superposition of the emission from both mechanisms leads to an asymmetric radio emission "footprint" with constructive interference along the positive $\vec{v} \times \vec{B}$ direction and destructive interference along the opposite direction.

Figure 2.8 shows, in the panel labelled (c), the 2D interference patterns of simulated air-shower radio pulses for a near-vertical shower (left), and an inclined shower with zenith angle $\theta > 80°$. The two showers I show have different shower energies. However, this does not have a significant impact on the visual shape of the footprint. Mainly, it affects the energy fluence (energy deposited per unit area) of the footprint, displayed in the colour maps. Notably, the asymmetry is different, and also more severe for the vertical shower. As shown in panel (a), the cascade development of the vertical shower is truncated as it hits the ground. The shower

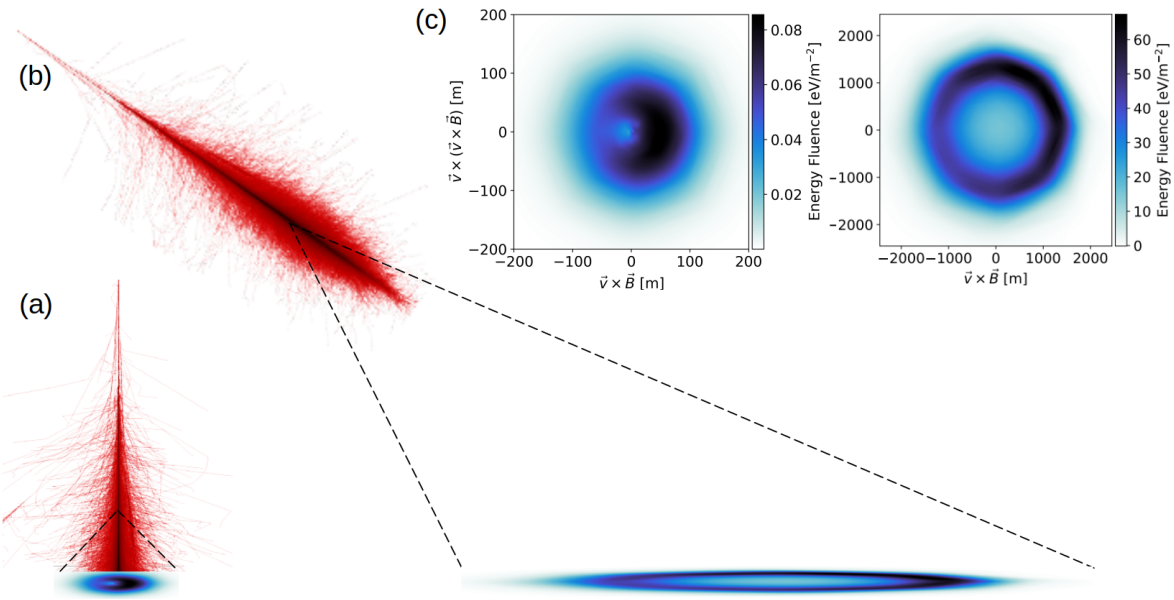

FIGURE 2.8: Illustration of the difference between the radio footprints of vertical and inclined air-showers. **(a)** Truncated development of a vertical air-shower and its small radio footprint. **(b)** Inclined air-shower that completed its cascade development, and the large radio footprint it casts at the ground level (not to scale). **(c)** Plots of the footprints from panels (a) and (b) in the shower plane. On the left, the footprint of a near-vertical shower; on the right, the footprint of the inclined shower. Note the different distance scale on the x- and y-axes. Air-shower visualisation from [78].

does not emit as much radiation as it could if the development had finished. It also does so much closer to the ground. As such, the radio emission is mostly focused closely around the shower core. For inclined showers, the cascade begins higher in the atmosphere in a region of lower air density. Low air density during shower development both benefits the geomagnetic component, since the charges can drift farther before interacting, and detracts from the strength of the charge excess emission, since there are fewer air molecules to ionise. As such, the geomagnetic emission is, relatively, even stronger in inclined showers and dominates the interference pattern. The cascade finishes developing and emits the entire radio signal, forming the characteristic "Cherenkov" ring on its footprint (see Section 2.3.4). The only visible asymmetry is in the intensity of the ring.

2.3.4 The Cherenkov ring

Individually, each emission component forms a radially symmetric pattern. This pattern has a ring-shaped feature which appears much more pronounced for inclined showers (see Figure 2.8). The ring appears because a large fraction of the emission from all parts of the shower development arrives simultaneously at a specific distance from the shower core due to the varying refractive index along the shower axis. I display the time compression schematically in Figure 2.9. We call the ring feature the "Cherenkov ring" because the radius of the ring r_0 can be approximated with a cone with an opening angle equal to the local Cherenkov angle,

$$\delta_0(h_{\max}, n_0) = \arccos\left(\frac{1}{n\left(\rho(h_{\max}), n_0\right)}\right), \tag{2.4}$$

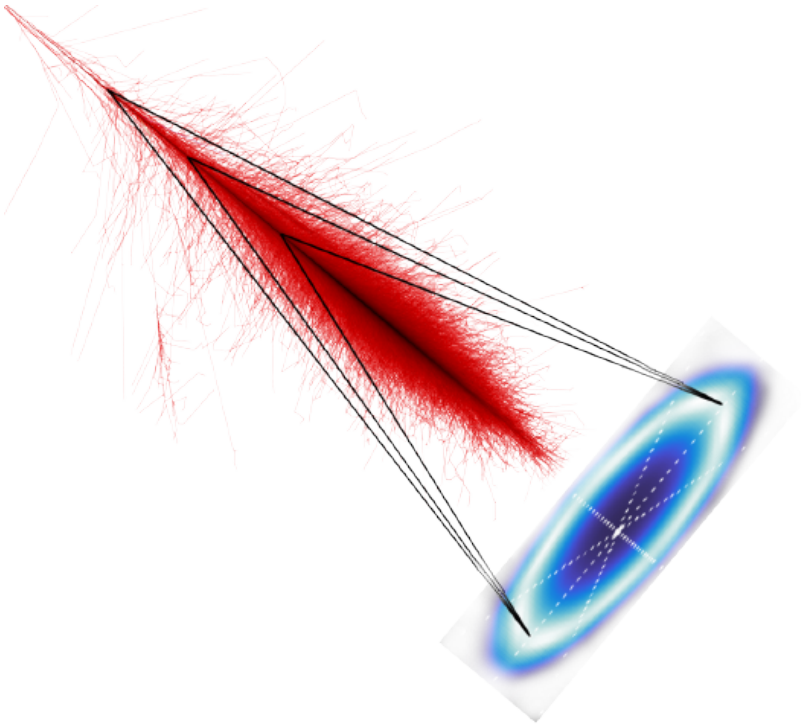

FIGURE 2.9: Sketch of the time compression effect that causes the Cherenkov-like ring pattern in the radio emission footprint. Illustrated by the white ring of high intensity on the blue footprint. The black lines show the path of radio waves emitted at different points in the shower development, with different refractive indices, that arrive on the ground at the same time. Air-shower visualisation from [78].

of a point source moving at the speed of light. $h_{\max}$ is the altitude of the shower maximum above sea level. $n\left(\rho(h_{\max}), n_0\right)$ is the refractive index at that altitude with n_0, the refractive index at sea level. They depend on the local air-density profile $\rho(h)$. For air-shower simulations and to process measurement data, we use models of the density profile of the local atmosphere to supply this information.

From the Cherenkov angle δ_0 follows the "Cherenkov radius",

$$r_0 = \tan\left(\delta_0\right) \cdot d_{\max}\left(\theta, X_{\max}, h_{\text{obs}}\right). \tag{2.5}$$

This is the radius of the Cherenkov cone at ground level. $d_{\max}$ is the distance from the shower core on the ground plane to the shower maximum along the shower axis. As such, it can be interpreted as the height of the Cherenkov cone. We can calculate $d_{\max}$ given the zenith angle θ, the atmospheric depth of the shower maximum $X_{\max}$, the observation altitude h_{obs}—the altitude of the detector above sea level—and, again, the local atmospheric profile.

2.3.5 Loss of coherence

If one views electromagnetic radiation as waves, coherence describes the ability of two waves to interfere with each other. Two waves are coherent if they are, spacially and temporally, emitted sufficiently close to each other. The maximum physical distance between them is called coherence length. They also need to have a constant relative phase which requires them to be close to monochromatic.

In the context of the radio detection of air-showers, the degree of coherence of the emission affects the amplitude of the radio pulses we measure. The radio emission

of a shower with poor coherence has weaker pulses than one where the emission is fully coherent. If not taken into account, this can strongly affect the reconstruction of shower attributes such as the electromagnetic energy.

The emission can become less coherent due to a number of factors. The frequency of the emission affects its coherence because small wavelengths decrease the coherence length. Low air density can also lead to loss of coherence due to the longer mean free path of particles in the shower. This leads to exceeding the coherence length as well. The coherence of the geomagnetic emission is affected by the strength of the geomagnetic field. A stronger field means a stronger Lorentz force on the electrons and positrons, and, consequently, a larger separation between the particles that can exceed the coherence length. I refer to reference [13] for a detailed study on the loss of coherence for different frequencies and magnetic field strengths.

Chapter 3

The Giant Radio Array for Neutrino Detection

The Giant Radio Array for Neutrino Detection (GRAND) is an upcoming radio observatory designed to detect near-horizontal air-showers initiated by UHE cosmic rays, and UHE neutrinos [7]. GRAND has the ambitious goal to detect air-showers from highly energetic particles fully autonomously, i.e. only using radio antennas (see Section 3.1). With sufficient detection area, it expects not only to measure cosmic rays at the energies of the Oh-my-God [2] and Amaterasu particles [3], but, more importantly, UHE neutrinos at energies of 10^{17} eV and beyond (see Section 3.2). From energy density considerations, we know that neutrinos at these energies are connected to cosmic rays with energies beyond the GZK flux suppression [8]. UHE neutrinos might be produced inside astrophysical sources. Since neutrinos point back directly to their source, we expect them to reveal invaluable information about the most energetic sources and processes in the Universe.

GRAND is in a prototype phase, with three prototype arrays currently operating (see Section 3.3). Most notably, the largest prototype, GRANDProto300 (GP300), with a final planned size of 300 antennas, is in deployment in the Gansu province in China. In my work, I use the planned final layout of GP300 and a possible configuration for GRAND10k, a future stage of GRAND with 10,000 antennas, for performance studies of the air-shower electromagnetic energy reconstruction on sparse antenna layouts. Then, I apply the LDF energy reconstruction to some of the first cosmic-ray event candidates measured by GP300. In addition, I calculate the effective aperture of GP300 and GRAND10k and, based on the results, predict the number of events they can expect to detect within a year. I discuss these studies in Chapters 6, 7 and 8, respectively.

I take much of the information in this chapter from the GRAND white paper [7]. I reference any updated or other information as needed.

3.1 The GRAND detection unit

GRAND uses the HorizonAntenna [79]. It has four horizontal arms acting as dipoles. They are aligned with the (geomagnetic) North-South and East-West directions. A fifth, vertical arm is a monopole. The antenna pole and the ground act as its second arm. Each arm is a symmetric kite-shaped steel radiator. The antenna is optimised for the detection of near-horizontal air-showers due to its ability to also measure the electric field polarised in the vertical direction. A GRAND detection unit (DU) consists of an antenna as well as electronics to process, store, and communicate the measurements. Figure 3.1 displays a schematic of a GRAND DU with a HorizonAntenna, and a photo of a deployed DU at the GP300 site in China. Performance tests

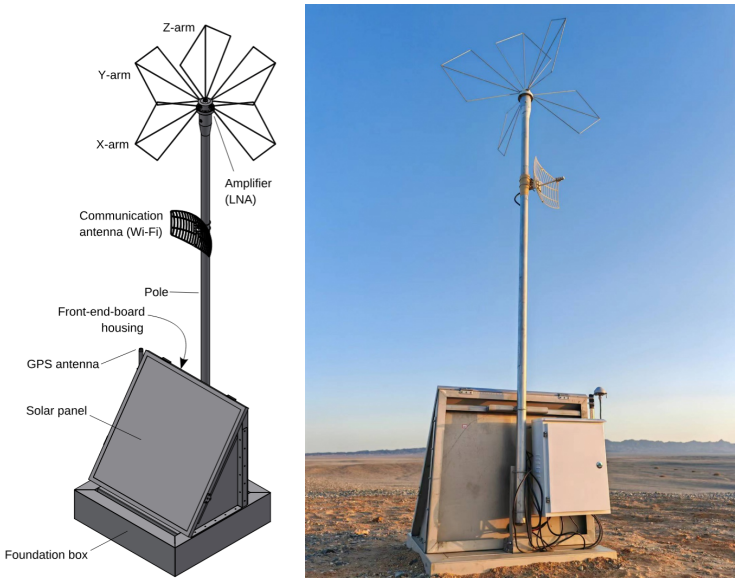

FIGURE 3.1: **Left:** Annotated schematic of a GRAND DU, including the HorizonAntenna used by GRAND. The X- and Y-arms, respectively aligned with the North-South and East-West directions, are dipoles. The vertical Z-arm is a monopole. The pole is 3.5 m tall and the antenna arms span about 1.4 m, corresponding to the wavelength of radio emission at 200 MHz. The foundation box is filled with sand to provide stability. Schematic from [79]. **Right:** A GRAND detection unit deployed at the GP300 site in China. Photo from [10].

of the GRAND DUs at the prototype sites show similar results despite radio backgrounds of different intensity [10]. Further, the GRAND detector simulation is in agreement with measurements from the GP300 DUs [12].

3.2 Detecting neutrinos with radio antennas

There are multiple upcoming experiments designed to measure UHE neutrinos using radio antennas [80, 81, 82]. RNO-G is currently deploying their radio array in the ice sheet of Greenland at $\sim$ 100 m depth. Radio waves in ice has a kilometre-scale attenuation length. As such, a sparse antenna layout can cover a large detection volume. Since the Earth is opaque to UHE neutrinos, the experiment relies on Earth-skimming and near-horizontal arrival directions. RNO-G will be sensitive to UHE neutrinos above 10^{16} eV from slightly below to about 30° above the horizon [37]. The radio array of IceCube-Gen2, the envisioned high-energy upgrade of IceCube, will implement the same technique [83].

GRAND also aims to detect Earth-skimming neutrinos, however, using air-showers. I display the detection principle schematically in Figure 3.2. Neutrinos at low energies have the ability to pass through the whole Earth without interacting [84]. However, the neutrino-nucleon deep inelastic scattering cross-section increases with energy [85]. At 10^{18} eV, the interaction length of neutrinos inside the Earth is only a few hundred kilometres, depending on neutrino direction. Consequently, even neutrinos that just skim the Earth's surface are likely to interact. The charged leptons produced in charged-current interactions could be observed by GRAND if they exited the Earth and initiated an air-shower over the array. GRAND will only be sensitive to tau neutrinos (ν_τ) since the τ decays very quickly and its decay channels into hadrons and electrons lead to air-showers. Before it decays, the τ can travel

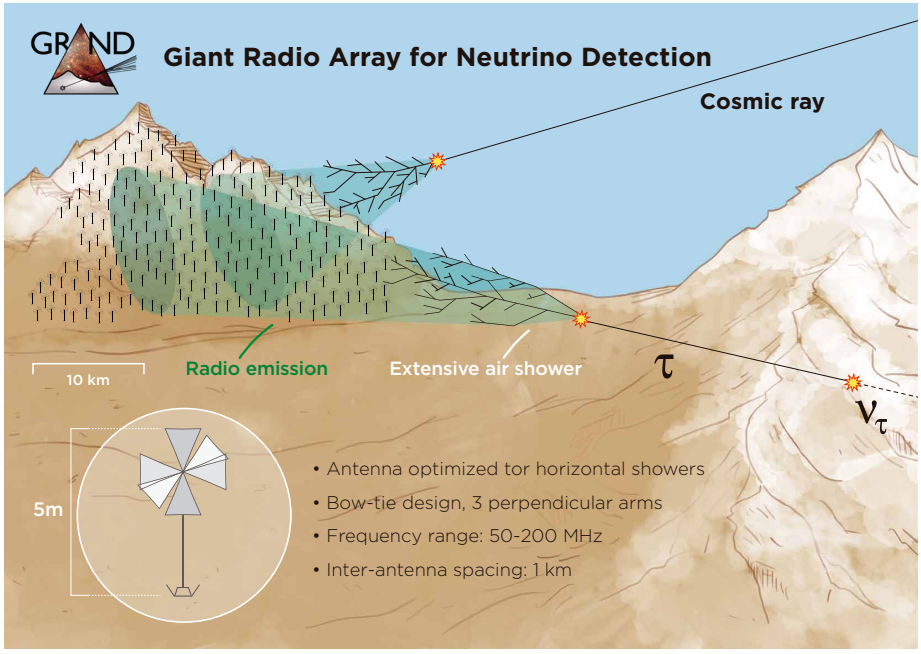

FIGURE 3.2: Illustrated detection principle of GRAND. Pictured is one of the planned sub-arrays with 10,000 antennas covering 10,000 km^2. The array measures inclined air-showers from UHE cosmic rays. Earth-skimming tau neutrinos ν_τ induce air-showers through the decay of the τ produced in the interaction inside the Earth. The HorizonAntenna, designed for GRAND, is shown on the bottom left. Graphic from [7].

between kilometres and tens of kilometres, depending on its energy, and exit the Earth [86]. In air, the τ decay produces a new ν_τ with, on average $\sim$ 30% of the parent τ energy. As such, the ν_τ flux regenerates itself, even if it is shifted to lower energies. Electrons from ν_e interactions generally generate a shower very close to their point of creation, i.e. in the rock. These, by definition, electromagnetic showers are unlikely to be detected by GRAND unless they are induced directly above the array. Muons travel many kilometres in the atmosphere before they decay. As such, GRAND will not be sensitive to ν_μ since the chance to induce a muon-initiated shower over the array after an earth-skimming ν_μ interaction is negligible. In addition, there is a non-negligible contribution from atmosphere-skimming neutrinos that traverse a column depth of matter in air equivalent to 100 m of rock. From this channel, all neutrino flavours could be detected by GRAND.

Due to the low expected flux of UHE neutrinos, GRAND plans to instrument a total detection area of 200,000 km^2 in its final phase, split into sub-arrays with 10,000 antennas each, covering 10,000 km^2. Ideally, the sub-arrays will be located in both hemispheres to ensure coverage of the whole sky. Depending on the neutrino flux at full capacity, GRAND could detect 100 UHE neutrino events over a ten-year detection period [87]. As such, GRAND could open up a new window into the Universe by enabling neutrino astronomy. Figure 3.3 shows an overview of the sensitivity to diffuse neutrino fluxes of multiple current and planned experiments, including GRAND at its full capacity.

3.3 Prototype arrays and deployment phases

GRAND plans to deploy in multiple phases [89]. After the planning phase, GRAND has now moved into a prototype phase. Three prototype arrays have been operating

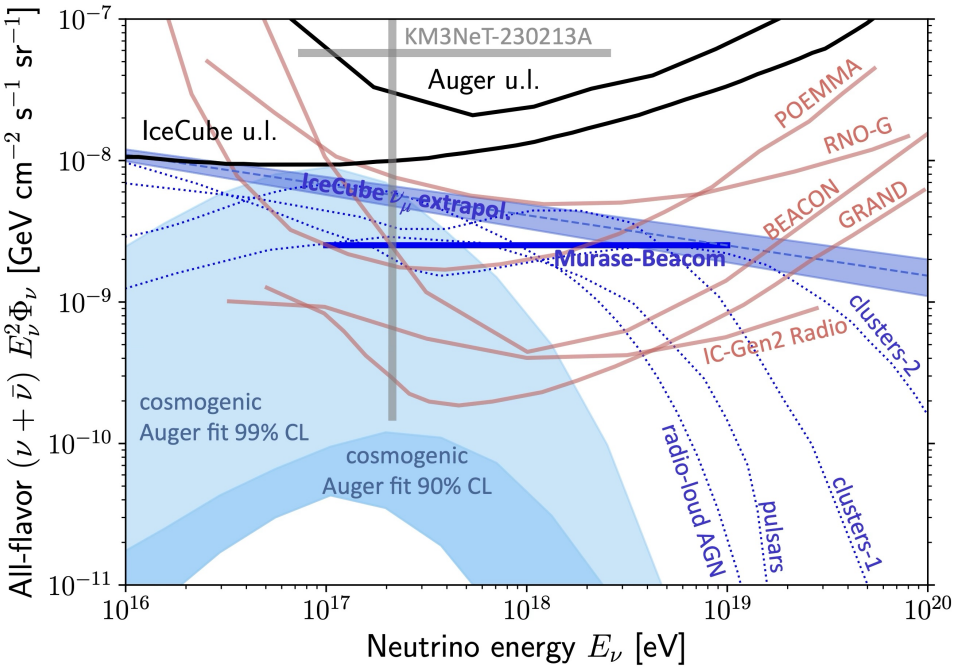

FIGURE 3.3: Predicted diffuse neutrino fluxes from cosmogenic neutrinos (filled light blue regions) and astrophysical neutrinos (dotted blue lines). Pink solid lines denote the 10-year differential sensitivity of GRAND, and multiple other experiments. Black lines show the upper limits for neutrinos detected by IceCube and Auger. Plot from [88].

since 2023:

GRAND@Nançay, with four antennas, serves as a test bench accessible for European scientists in Nançay, France [90].

GRANDProto300 (GP300) is the pathfinder array for the next stages of GRAND [10, 12]. Currently, the deployment of GP300 is still in progress. It is located in a radio-quiet region on a plateau called Xiaodushang in the Gansu province of China, near the city of Dunhuang. The final layout of GP300 is a pure radio array made up of 300 antennas with a detection area of $\sim 200\,\mathrm{km}^2$. Its goals are to provide a proof of principle for the autonomous radio trigger, and to detect UHE cosmic rays. In addition, it serves as a test environment for maintaining the experiment under harsh weather conditions, like heat, rain- and sandstorms, for long periods of time.

The GP300 layout is a sparse array with an antenna separation of 1 km in a triangular pattern and an in-fill with about 90 antennas separated by 577 m. Figure 3.4 shows the full layout of GP300 with the highlighted stations being the already deployed ones. The full array will be sensitive to cosmic rays with energies between $10^{16.5}$ and $10^{18.5}$ eV. It will be able to measure the cosmic ray energy spectrum [91] and probe the transition from Galactic to extragalactic cosmic rays. Reference [91] estimates that GP300 expects to detect $\sim$ 130 cosmic ray events per day above 10^{17} eV and for zenith angles above 65°.

A first, partial configuration of GP300 with 13 antennas was deployed in June 2023. Due to the low number of antennas, it was not large enough to detect cosmic rays reliably. It was instead used for antenna calibration, background measurements

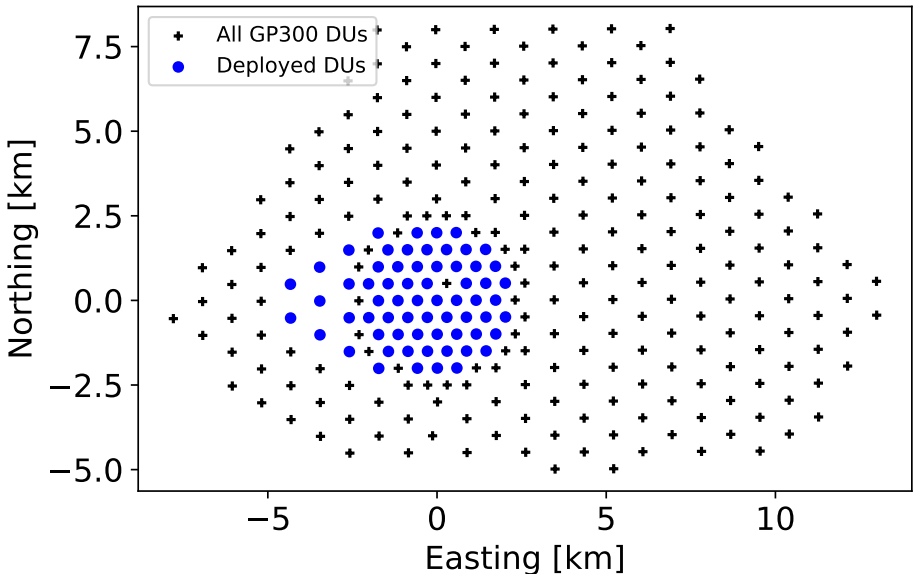

FIGURE 3.4: Full planned layout of GRANDProto300 with 300 antennas, including the in-fill. Black crosses mark the DU positions. The highlighted blue DUs are deployed as of July 2025.

and tests of efficiency. Since December 2024, GP300 has been expanded into an array of 65 antennas in multiple steps. The left panel of Figure 3.5 shows the first and final partial configurations in yellow and red, respectively. The main sources of anthropogenic noise for GP300 are communications from passing aeroplanes, and the transformer of a mine near the experiment [92]. Between December 2024 and March 2025, 41 cosmic ray event candidates have been identified [89, 92].

GP300 is of particular importance for this work. I use the GP300 layout to benchmark the performance of my energy reconstruction algorithm with realistic simulations (see Chapter 6). In Chapter 8, I calculate the effective aperture of GP300 and estimate how many cosmic rays it will be able to detect per day and per year. Furthermore, I apply the signal model and energy reconstruction described in this work to the cosmic-ray event candidates detected by GP300 in Chapter 7.

GRAND@Auger is located at the site of the Pierre Auger Observatory near Malargue, Argentina [10, 11]. In cooperation with the Pierre Auger Collaboration, ten AERA stations were repurposed into GRAND DUs. They have a spacing of 250 m and cover an area of 0.5 km^2. The right panel of Figure 3.5 shows the layout of GRAND@Auger and the positions of the DUs in the Auger coordinate system. The DUs lie within the Auger surface detector 750-m in-fill array, and in the field of view of one of the five fluorescence telescopes [93]. Consequently, GRAND@Auger has the opportunity to validate and cross-check its measurements with the Auger particle detectors, fluorescence telescopes and radio antennas. So far, GRAND@Auger has detected one candidate cosmic-ray event in coincidence with the Pierre Auger Observatory with good agreement between both independent reconstructions [11].

GRAND10k is the next planned deployment stage. It will be a 10,000 km^2 subarray, consisting of 10,000 radio antennas. One 10,000 km^2 array will already have a large enough detection area to probe certain neutrino fluxes [7]. Naturally, the same property also makes it sensitive to UHE cosmic rays. Along with GP300, I study the performance and exposure for a possible layout of GRAND10k in Chapters 6 and 8.

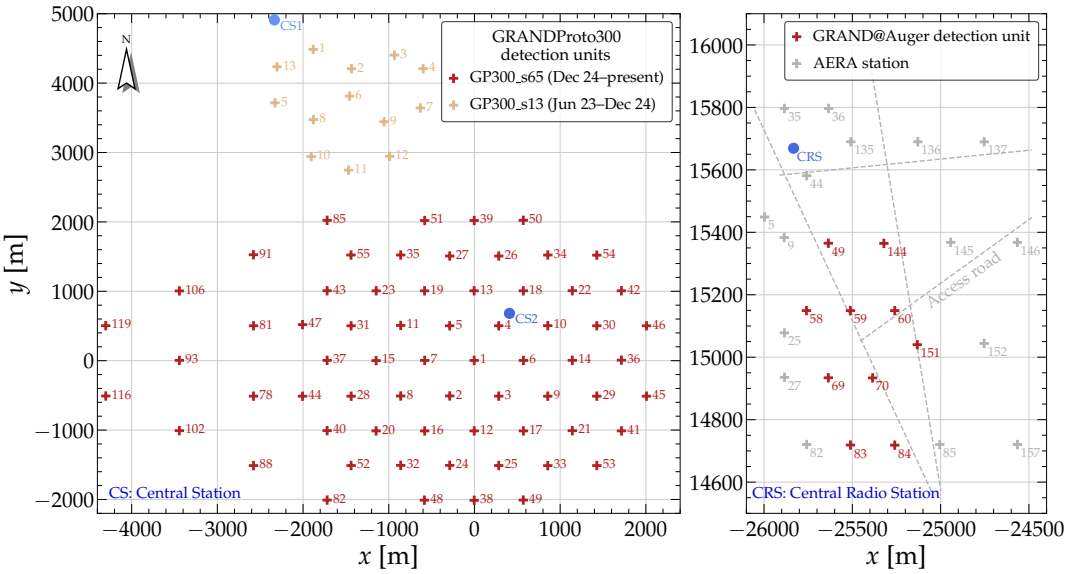

FIGURE 3.5: Deployment status and layouts of GP300 and GRAND@Auger. **Left:** Partial configurations of GP300. 13-antenna stage as yellow crosses and 65-antenna stage as red crosses. The blue points show the positions of the data acquisition units or central stations for each stage. DU positions are given in terms of the position of DU 1. **Right:** Layout of GRAND@Auger with the Pierre Auger Observatory detection area. Positions of the GRAND@Auger DUs as red crosses, AERA stations as gray crosses. Positions in the Auger coordinate system. Plots from [10].

Finally, **GRAND200k** is GRAND at its full planned capacity. It is envisioned to consist of 20 independent sub-arrays of the same size as one GRAND10k array. With 200,000 antennas covering a total of 200,000 km^2 at various global locations, GRAND200k will be sensitive to tiny neutrino fluxes of 10^{-10} GeV cm^{-2} s^{-1} sr^{-1} [80, 82, 89, 94] (see Figure 3.3). The extraordinary number of antennas needed for GRAND200k necessitates an industrial and standardised approach to constructing the antennas and electronics, and to their deployment. GRAND endeavours to maintain a small carbon footprint during this process [95].

3.4 Frequency band and site characteristics

The largest currently operating detector for radio emission from extensive air-showers is the AugerPrime Radio Upgrade (RD) at the Pierre Auger Observatory near Malargüe in Argentina. It lies within the South Atlantic Anomaly where the Earth's magnetic field is at its weakest at 24 μT. This means that the loss of coherence of the radio emission (see Section 2.3.5) barely affects the radiation energy. As reference [13] shows and I show in Section 5.6, it only starts to affect the emission at very low air density, i.e., zenith angles above 80°. This holds true even for the higher 50–200 MHz frequency band.

In contrast, in northern China, where GP300 is being deployed and the first GRAND10k array could be located, the geomagnetic field strength is $\sim$ 56 μT, close to the maximum value on the whole planet. Figure 3.6 shows the Earth magnetic field as of 2020. I highlight the locations of GRAND@Auger and GP300 on the map from Finlay et al. [96]. The strong magnetic field leads to much more drastic loss of coherence with decreasing air-density at the shower maximum. It also starts affecting the emission at lower zenith angles of down to 70°. Compensating for the

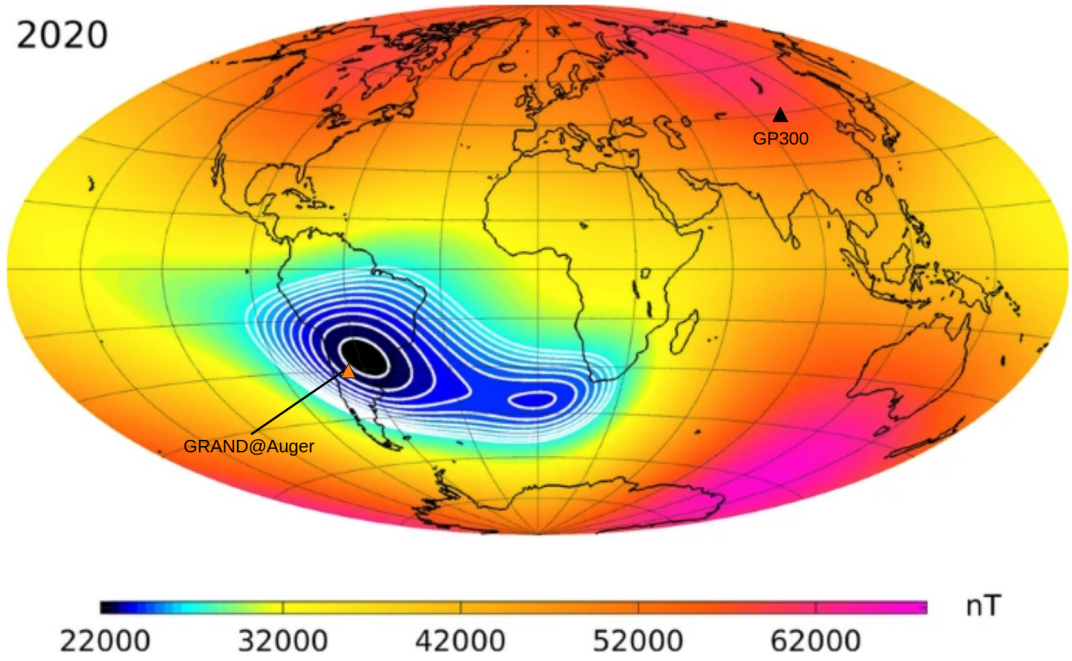

FIGURE 3.6: Field strength of the geomagnetic field on the Earth's surface as of 2020. The South Atlantic Anomaly is shown in blue colours of the logarithmic colour map. The locations of GRAND@Auger and GP300 are marked with red and black triangles, respectively. Graphic adapted from [96].

coherence loss is one of the key problems I tackle when adapting the signal model for the site in China (see Section 5.6).

3.5 The radio self-trigger

The ability to reliably identify radio signals produced by air-showers with only the use of radio antennas is a key feature of GRAND. Without autonomous radio detection, it would be too costly to instrument a detection area as large as GRAND intends to. However, the rate of noise pulses is much higher than the rate of pulses from air-showers. As such, the signal identification has to be pure and reliable in real time—as an "online" trigger—for the amount of data to be manageable.

The development of the trigger algorithm is still on-going. It will consist of a first-level (FLT) and second-level trigger (SLT). The FLT acts on the level of single DUs and employs pulse template matching to identify radio pulses possibly induced by air-showers. In the next step, the SLT uses the DUs that pass the FLT to make the final trigger decision using multi-DU criteria. These criteria include signal amplitude, polarisation of the electric field, and agreement between multiple methods to determine the arrival direction. The overall goal is to the reduce the expected data rate from multiple kHz to the order of 1 Hz. The trigger is being developed as part of the NUTRIG project [97], which this work is also belongs to.

Chapter 4

Signal Model of the Radio Emission

My work on the signal model and energy reconstruction for the radio emission of inclined air-showers in the 50–200 MHz frequency band builds on the previous iteration of the model by Schlüter and Huege [9]. In this chapter, I describe and explain the general principles and methods which both models use, and the subsequent reconstruction of the electromagnetic shower energy. In addition, I state the assumptions I make about the radio signal.

First, asymmetry effects introduced by the shower geometry are dealt with. In the next step, the charge excess fraction a_{ce} of the emission is parametrised using the polarisation properties of the geomagnetic and charge excess component. With this parametrisation, the geomagnetic energy fluence f_{geo} is determined solely from the energy fluence polarised in the $\vec{v} \times \vec{B}$ direction. A lateral distribution function (LDF) $f_{\mathrm{LDF}}(r)$ for the distribution of f_{geo} is formulated. The geomagnetic radiation energy $E_{\mathrm{geo}} = \int f_{\mathrm{LDF}}(r)\,\mathrm{d}r$ is corrected for variations due to air-density and the geomagnetic angle α. Finally, the corrected radiation energy S_{geo} is correlated with the electromagnetic shower energy E_{em}.

In Chapter 5, I describe the simulation libraries I used to tune the signal model parameters and dive into the changes I make to adapt the model to the 50–200 MHz frequency band, and for other experimental sites.

4.1 Assumptions about the radio signal

Realistically, the radio signal is emitted over the whole development of the particle cascade, in the time between the creation of each particle pair and their next interaction, as well as due to acceleration in the interaction. Multiple studies have been conducted on this subject [98, 99, 100, 101], which do not reach a clear consensus. In this work, I adopt the approximation that the shower maximum emits all of the emitted radiation in point-like emission. This allows for the correction to first order of asymmetries introduced by early-late effects [102].

In addition, it has been shown that the emission from the geomagnetic and charge excess components arrives at an antenna with a slight time delay [103]. This results in a small component of circular polarisation. Naturally, this component scales with the fraction of the sub-dominant charge excess component in the air-shower radio pulses. Reference [9] evaluates the relevance of the circular polarisation component for inclined showers in the 30–80 MHz frequency band. They find a small charge excess fraction and a time delay $\Delta t < 1\,\mathrm{ns}$. Consequently, they assume, for simplicity, that both emission components arrive simultaneously and in phase. As I discuss in Section 5.2, the relative strength of the charge excess component further decreases

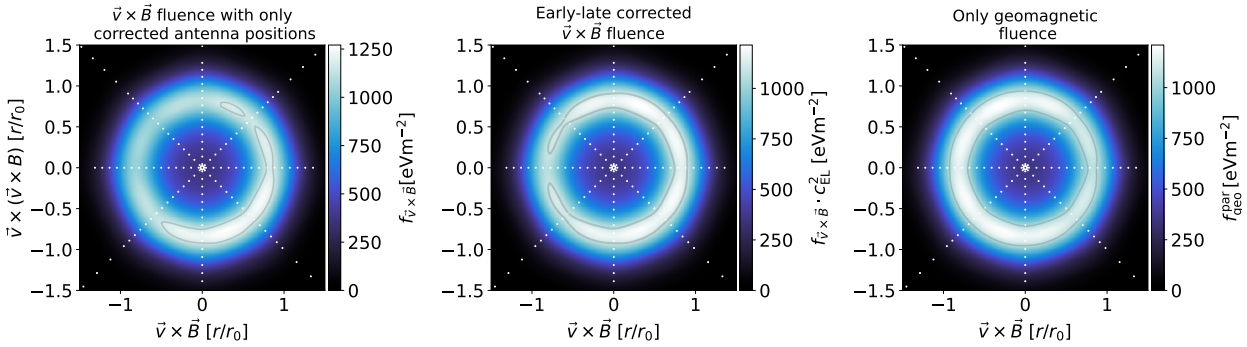

FIGURE 4.1: Radio emission pattern or radio footprint in shower plane coordinates in the 50–200 MHz frequency band. Antennas (white points) are simulated on the ground plane in a pattern that appears as a star when viewed along the shower axis. The distances on the $\vec{v}\times\vec{B}$ and $\vec{v}\times(\vec{v}\times\vec{B})$ axes are given in terms of the Cherenkov radius. The energy fluence distribution, displayed as a colour map, is an interpolation between fluence values on the four arms of the star-shaped antenna pattern. The part of the distribution with $> 90\%$ of the maximum is highlighted with a grey outline. **Left:** Raw $\vec{v}\times\vec{B}$ fluence and early-late corrected antenna positions. **Middle:** $\vec{v}\times\vec{B}$ fluence with early-late correction applied to antenna positions and energy fluence. **Right:** Energy fluence only from the geomagnetic emission, calculated for every antenna with the parametrisation of the charge excess fraction (see Eq. (4.7)).

for the 50–200 MHz frequency band. Accordingly, the assumption is valid for this work as well.

4.2 Steps of the signal model

4.2.1 Early-late correction

As I discuss in Section 2.3, the ground pattern of the radio emission is asymmetrical due to interference of the two emission mechanisms. In the case of an inclined air-shower, the geometry of the shower itself leads to additional asymmetries in the radio emission pattern. Figure 4.1, in its left panel, shows an example of the overall asymmetry of the radio footprint in the shower plane in the 50–200 MHz frequency band. I only show the energy fluence in the $\vec{v}\times\vec{B}$ polarisation since it represents the vast majority of the radiated energy. I explain the remaining panels of the figure in this, and the following section.

Antenna stations on the ground plane with the same angular distance to the shower axis can have different physical distances to the emission source. Since the signal strength decreases with distance to the source, antennas that are further away receive a weaker signal than closer antennas. This causes an additional asymmetry of the emission where the signal strength increases towards the shower arrival direction. This problem is solved by calculating so-called early-late correction factors [102],

$$c_{\mathrm{el}} = \frac{d_{\max} + \vec{r}\cdot\vec{e}_v}{d_{\max}}. \tag{4.1}$$

These factors are calculated for each station using the distance from the shower core to the shower maximum $d_{\max}$ along the shower axis, and the station position $\vec{r}$.

Figure 4.2 shows the early-late correction and its steps in a schematic illustration. The correction factors are applied to the station axis distances r_{raw} to ensure equal

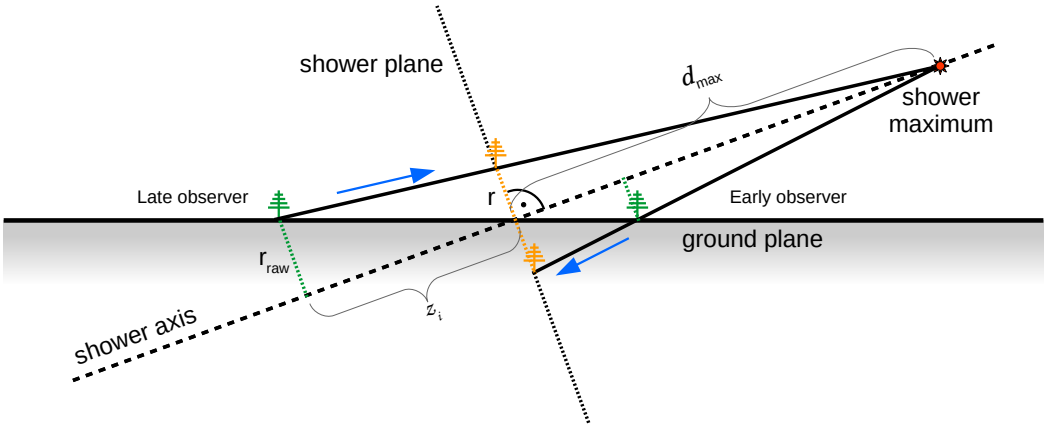

FIGURE 4.2: Illustration of the early-late correction. The early and late antennas or observers in green have the same angular distance, but different physical distance to the shower axis. As such, they do not receive the same signal. They are projected into the shower plane in orange. There, they have the same physical distance r to the shower axis and receive the same signal strength. This is done by applying early-late correction factors c_{el} to the distance to the shower axis r_{raw} and, in quadrature, to the measured energy fluence f_{raw}. Diagram from [9].

angular distance for a given axis distance r in the shower plane. They are also applied to the energy fluence f_{raw} at each station in quadrature to nullify the energy fluence asymmetry from the shower geometry.

$$r = \frac{r_{\text{raw}}}{c_{\text{el}}}, \tag{4.2}$$

$$f = f_{\text{raw}} \cdot c_{\text{el}}^2. \tag{4.3}$$

These steps are equivalent to projecting all antennas into the shower plane (see Section 2.3.1) along the line-of-sight between antenna and shower maximum. Notably, the asymmetry introduced by the early-late effects does not have a fixed orientation, but rather depends on the arrival direction.

The middle panel of Figure 4.1 shows the footprint of an inclined shower after the early-late correction is applied. The remaining asymmetry along the $\vec{v} \times \vec{B}$ axis is solely due to the interference of the emission mechanisms. The right panel of Figure 4.1 shows only the energy fluence from the geomagnetic emission component.

4.2.2 Parametrisation of the charge excess fraction

With the early-late asymmetries eliminated, the next step towards isolating the geomagnetic energy fluence is understanding and parametrising the charge-excess component of the emission. In most cases, it is possible to determine both the geomagnetic energy fluence $f_{\text{geo}}^{\text{pos}}$ and charge-excess fluence $f_{\text{ce}}^{\text{pos}}$ separately from the energy fluence in the $\vec{v} \times \vec{B}$ and $\vec{v} \times (\vec{v} \times \vec{B})$ polarisation directions, $f_{\vec{v}\times\vec{B}}$ and $f_{\vec{v}\times(\vec{v}\times\vec{B})}$. The polarisation direction of each emission component is known for any point relative to the shower axis, as shown in Figure 2.7. Under the assumption that the pulses from both emission components arrive at the same time (see Section 4.1), one uses simple projections, using the angle ϕ between the position of the station and the $\vec{v} \times \vec{B}$ axis,

to calculate $f_{\text{geo}}^{\text{pos}}$ and $f_{\text{ce}}^{\text{pos}}$ analytically:

$$f_{\text{geo}}^{\text{pos}} = \left(\sqrt{f_{\vec{v}\times\vec{B}}} - \frac{\cos\phi}{|\sin\alpha|} \cdot \sqrt{f_{\vec{v}\times(\vec{v}\times\vec{B})}} \right)^2, \tag{4.4}$$

$$f_{\text{ce}}^{\text{pos}} = \frac{1}{\sin^2\phi} \cdot f_{\vec{v}\times(\vec{v}\times\vec{B})}. \tag{4.5}$$

I denote these energy fluences with the superscript "pos" because they are calculated using the antenna positions. This method relies heavily on an accurate measurement of $f_{\vec{v}\times(\vec{v}\times\vec{B})}$ which is weak for inclined air-showers. In the presence of noise, it is not reliable enough to determine the charge excess fluence with sufficient accuracy. In addition, the projections do not work for antennas near the $\vec{v}\times\vec{B}$ axis of the shower plane where the polarisation directions of both components are parallel and cannot be separated.

To ensure the calculation of the geomagnetic fluence is possible with accuracy for any antenna position, the model employs a parametrisation of the charge excess fraction,

$$a_{\text{ce}} \equiv \sin^2(\alpha) \cdot \frac{f_{\text{ce}}^{\text{pos}}}{f_{\text{geo}}^{\text{pos}}}, \tag{4.6}$$

of the radio emission based on the analytically calculated fluences from the polarisation method. Here, α is the geomagnetic angle between the shower axis and the magnetic field. This angle determines the scaling of the geomagnetic emission with the magnetic field. By rearranging and inserting Eqs. (4.4) and (4.5) into Eq. (4.6), the expression for the parametrised geomagnetic energy fluence is given by

$$f_{\text{geo}}^{\text{par}} = \frac{f_{\vec{v}\times\vec{B}}}{\left(1 + \frac{\cos\phi}{|\sin\alpha|} \cdot \sqrt{a_{\text{ce}}}\right)^2}. \tag{4.7}$$

This method only depends on measurements in the $\vec{v}\times\vec{B}$ polarisation direction, which contains the majority of the emission, and on the value of $d_{\max}$.

There are two factors that affect a_{ce}: the distance to the shower maximum $d_{\max}$, which is strongly determined by the zenith angle θ, and the lateral distance from the shower core. For larger $d_{\max}$, i.e., more strongly inclined showers, the density at the shower maximum $\rho_{\max}$ decreases. This leads to a longer mean free path length of the particles in the electromagnetic cascade and, subsequently, to stronger geomagnetic emission. In addition, the charge-excess emission dominates in dense media [104]. It follows that lower air-density causes charge-excess radiation with less intensity. Both effects lead to a decrease in the contribution of the charge-excess component to the overall emission, i.e., the charge-excess fraction decreases as well. Furthermore, increasing lateral distance to the shower axis leads to an increase in the charge-excess fraction [105].

The parametrisation of a_{ce},

$$a_{\text{ce}} = \underbrace{\left[0.348 - \frac{d_{\max}}{851\,\text{km}}\right] \cdot \frac{r_{\text{axis}}}{d_{\max}} \cdot \exp\left(\frac{r_{\text{axis}}}{622\,\text{m}}\right)}_{\text{lateral term}} \cdot \underbrace{\left[\left(\frac{\rho_{\max}}{0.428\,\text{kg m}^{-3}}\right)^{3.32} - 0.0057\right]}_{\text{density term}}, \tag{4.8}$$

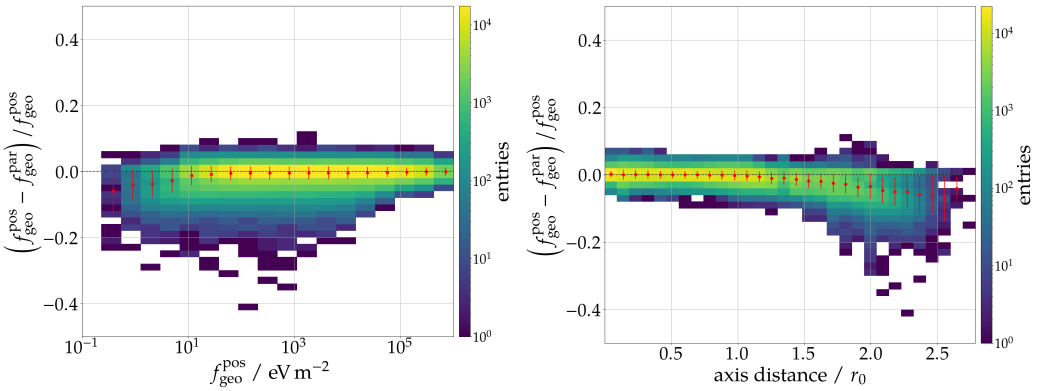

FIGURE 4.3: Evaluation of the calculation of the geomagnetic energy fluence $f_{\text{geo}}^{\text{par}}$ using the parametrised charge-excess fraction for the low-frequency model by Schlüter and Huege [9]. Idealised air-shower simulations for the Pierre Auger Observatory were used for the evaluation. Amount of entries per bin is represented with colour. Red points with error bars show the mean and standard deviation of each column. **Left:** Deviation against true energy fluence. **Right:** Deviation against axis distance in units of Cherenkov radii r_0. Plot from [9].

as published by Schlüter and Huege [9], reflects these factors in two terms. Equation (4.8) shows the explicit form for the Radio Detector of the Pierre Auger Observatory. The first term uses an exponential to describe the lateral distribution while accounting for the shower geometry by including the off-axis angle, defined by the axis distance r_{axis} divided by d_{max}. The density term describes the dependence of a_{ce} on ρ_{max}, which can be determined with d_{max}. In Figure 4.3, the performance of the low frequency model a_{ce} parametrisation for the Pierre Auger Observatory is shown by evaluating the geomagnetic energy fluence calculation. The fluence $f_{\text{geo}}^{\text{par}}$, determined using Eqs. (4.8) and (4.7), shows remarkable agreement with the analytically calculated fluence $f_{\text{geo}}^{\text{pos}}$ for fluence values $> 10\,\text{eV/m}^2$ and axis distances $< 1.5\,r_0$. The simulations used for the evaluation are idealised, i.e., they have dense antenna layouts, tailored to the expected radio footprint, and do not feature background noise.

Finally coming back to Figure 4.1, the right panel shows the emission footprint of the geomagnetic energy fluence $f_{\text{geo}}^{\text{par}}$ obtained with Eq. (4.7) by applying the updated parametrisation for the 50–200 MHz model (see Section 5.2). The emission pattern now shows the radial symmetry expected from a single isolated emission component. $f_{\text{geo}}^{\text{par}}$ is calculated with the early-late corrected $f_{\vec{v}\times\vec{B}}$. As such, it is early-late corrected by construction.

4.2.3 Lateral distribution function of the geomagnetic energy fluence

On its own, f_{geo} forms a rotationally symmetric radio footprint in the shower plane, as shown in the right panel of Fig. 4.1. Under the assumption that one can sample the entire footprint, the geomagnetic radiation energy E_{geo} is easily calculated with a two-dimensional integral over the energy fluence deposited in the ground in the detection area. In practice, however, we measure inclined air-showers with sparse antenna arrays with spacing on the order of a kilometre. In this case, the measurements do not provide enough information to reconstruct the energy with a simple integral. The approach of the signal model instead relies on the symmetry of the geomagnetic footprint to display the geomagnetic energy fluence as a one-dimensional

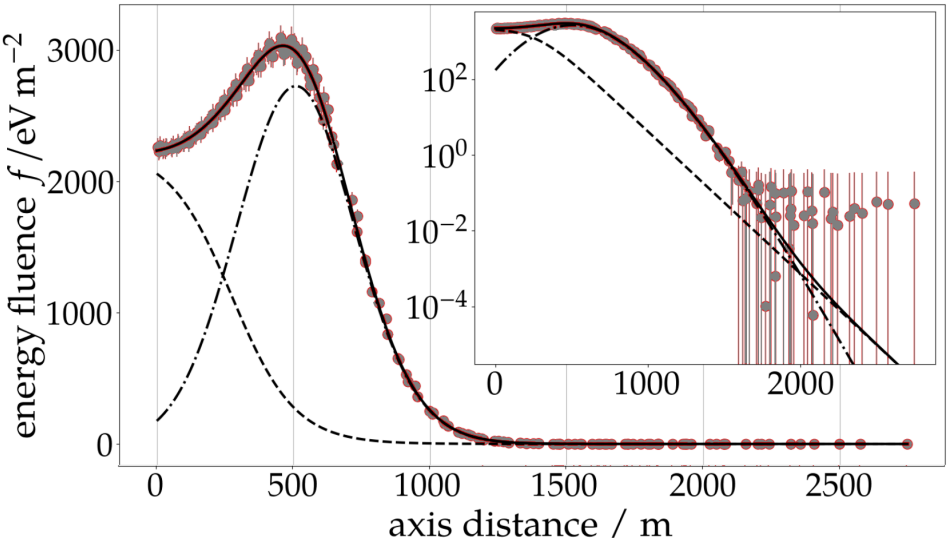

FIGURE 4.4: An example LDF fit from the low-frequency model for an idealised air-shower simulation for the Pierre Auger Observatory. The simulated geomagnetic energy fluence is shown as grey points with error bars. The LDF fit, and its Gaussian and sigmoid components, are shown in black as solid, dot-dashed, and dashed lines, respectively. The inset shows the same data on a logarithmic scale. Plot adapted from [9].

lateral distribution. A function is fitted to this distribution which I call the geomagnetic fluence lateral distribution function or, much shorter, the "LDF" from now on.

The functional form of the LDF as defined by Schlüter and Huege [9] is

$$\begin{aligned} f_{\mathrm{LDF}}(r) &= \frac{E_{\mathrm{geo}}}{A_0} \cdot f_{\mathrm{shape}}(r, r_0, \sigma, p, a_{\mathrm{rel}}, s, r_{02}) \\ &= \frac{E_{\mathrm{geo}}}{A_0} \left[\exp\left(-\left(\frac{r - r_0}{\sigma} \right)^{p(r)} \right) + \frac{a_{\mathrm{rel}}}{1 + \exp\left(s \cdot \left(\frac{r}{r_0} - r_{02} \right) \right)} \right] . \end{aligned} \tag{4.9}$$

They settle on the function for the geomagnetic fluence f_{LDF} by iterating on previous models and studying idealised CORSIKA/CoREAS air-shower simulations with star-shaped antenna layouts. The shape of the LDF f_{shape} is characterised by a Gaussian and a sigmoid term. It has six shape parameters: the Gaussian peak position r_0, the Gaussian width σ, the Gaussian exponent $p(r)$, the amplitude a_{rel} of the sigmoid relative to the Gaussian, the sigmoid slope s, and the sigmoid length scale r_{02}. An additional fit parameter is the position of the symmetry centre of the radio-emission footprint ("radio core") which influences the value of r for every antenna. The radio core position is allowed to vary to accommodate its shift from the particle core of the shower due to refractive displacement [106]. Figure 4.4 shows an example of an LDF fit from the low-frequency model for an idealised simulation of an air-shower for the site of the Pierre Auger Observatory.

The LDF explicitly correlates the shape of the signal to the geomagnetic radiation energy E_{geo}. The normalisation factor,

$$A_0 = 2\pi \int_0^{5r_0} f_{\mathrm{shape}}(r) \cdot r \, \mathrm{d}r, \tag{4.10}$$

for the radiation energy enables this. A_0 is the radial integral over the emission footprint defined by the shape terms of the LDF. Effectively, it is the normalised

footprint area. From here, it is easy to see that the integral of f_{LDF} over the lateral axis distance r,

$$\begin{aligned} 2\pi \int_0^{5r_0} f_{\mathrm{LDF}}(r) \cdot r \, \mathrm{d}r &= \frac{E_{\mathrm{geo}}}{A_0} \cdot 2\pi \int_0^{5r_0} f_{\mathrm{shape}}(r) \cdot r \, \mathrm{d}r \\ &= \frac{E_{\mathrm{geo}}}{A_0} \cdot A_0 = E_{\mathrm{geo}}, \end{aligned} \tag{4.11}$$

corresponds to E_{geo}. The maximum integration distance is $5\,r_0$, sufficiently far away from the radio core to include all of the significant signal strength. By including the integral over f_{shape} in the LDF, the fit to the geomagnetic fluence directly yields the geomagnetic radiation energy E_{geo} as one of the fit parameters.

However, the LDF has too many free parameters to work well for measurements of air-showers with a sparse antenna array. In many cases, especially for small zenith angles and low cosmic-ray primary energies, only a small number of antennas receives the radio signal with sufficient signal strength and signal-to-noise ratio. To solve this problem, all LDF shape parameters were parametrised in terms of the distance to the shower maximum d_{max}. This reduces the number of degrees of freedom to only four: E_{geo}, d_{max} and the two radio core coordinates. As such, the LDF fit only requires five antennas to characterise the emission accurately.

4.3 Reconstruction of the electromagnetic shower energy

The geomagnetic radiation energy E_{geo}, reconstructed with the LDF fit, has a second-order dependence on both the geomagnetic angle of the shower α and the air-density at the shower maximum ρ_{max}. In order to arrive at an energy independent of these factors, one calculates the corrected geomagnetic radiation energy S_{geo}

$$S_{\mathrm{geo}} = \frac{E_{\mathrm{geo}}}{\sin^2(\alpha)} \cdot \frac{1}{(1 - p_0 + p_0 \cdot \exp(p_1 \cdot [\rho_{\mathrm{max}} - \langle\rho\rangle]))^2}, \tag{4.12}$$

following the method from Glaser et al. [98]. $\langle\rho\rangle$ is the average air density at the shower maximum of an air-shower with zenith angle $\theta = 75^\circ$ and an average $X_{\mathrm{max}} = 750\,\mathrm{g/cm^2}$. Naturally, this value depends on the density profile of the local atmosphere. With S_{geo}, one finds the electromagnetic shower energy E_{em} with a power law

$$E_{\mathrm{em}} = 10^{19}\,\mathrm{eV} \left(\frac{S_{\mathrm{geo}}}{S_{19}} \right)^{1/\gamma} \tag{4.13}$$

with the index $\frac{1}{\gamma}$. S_{19} is a reference energy, representing the geomagnetic radiation energy of an air shower with cosmic-ray primary energy of $10^{19}\,\mathrm{eV}$ and air-density of $\rho_{\mathrm{max}} = \langle\rho\rangle$ at its shower maximum.

Chapter 5

Model Adaptation and Generalisation

In this chapter, I present my work on adapting the signal model and energy reconstruction to the 50–200 MHz frequency band, and to an additional site with a much stronger magnetic field. Initially, I carry out the adaptation for the site of the Pierre Auger Observatory in Argentina where the GRAND prototype array GRAND@Auger is located. For this, the only change with respect to the previous iteration of the model [9] is the frequency band. For the Auger site, I use the Auger (October) atmosphere model as it is implemented in CORSIKA [40] and in the `radiotools` module [107]. Further, I adapt the model to the site of the main prototype array of GRAND, GP300, in the Gansu province of China. This site has a different observation altitude, atmosphere model and, most importantly, geomagnetic field vector. For the GP300 site, I use an atmospheric model for this region in China, labelled "Dunhuang" in `radiotools`. The Dunhuang atmospheric profile was modelled by Zhang [108]. I implemented it in `radiotools` myself. As I discuss in Section 3.4, the geomagnetic field strengths at the two sites are close to the global extremes with Argentina and China at the low and high end, respectively. Consequently, by adapting the model to both sites, I demonstrate its viability for any site regardless of the configuration of the geomagnetic field.

In the following sections, I discuss the adaptations I make, and introduce new model parameters for both experimental sites side-by-side. For visual clarity, I use green and red in monochromatic plots, as well as the `matplotlib` [109] colour maps *viridis* and *plasma* for GRAND@Auger/Argentina and GP300/China, respectively.

5.1 Simulation libraries

I use two cosmic ray air-shower simulation libraries to adapt the signal model for the two sites. The air-shower simulations are generated with CORSIKA [40]. The corresponding radio emission is simulated using the CoREAS [14] module of CORSIKA. Any shower libraries I created myself use CORSIKA version 7.7550 and CoREAS version 1.4. I use the hadronic interaction model SIBYLL-2.3d [110] with UrQMD [111, 112] for low-energy hadronic interactions. I set the thinning threshold to $t_f = 10^{-6}$ with optimised particle weight limitation.

In order to optimally tune the model parameters, I use an idealised antenna layout for each simulation. The 240 antennas are all located at the height of the previously defined observation altitude for the given site. Viewed in the shower coordinate system, the antennas are centred around the true shower core along four arms, forming an eight-pronged star-shaped pattern. Two of the arms arms are aligned

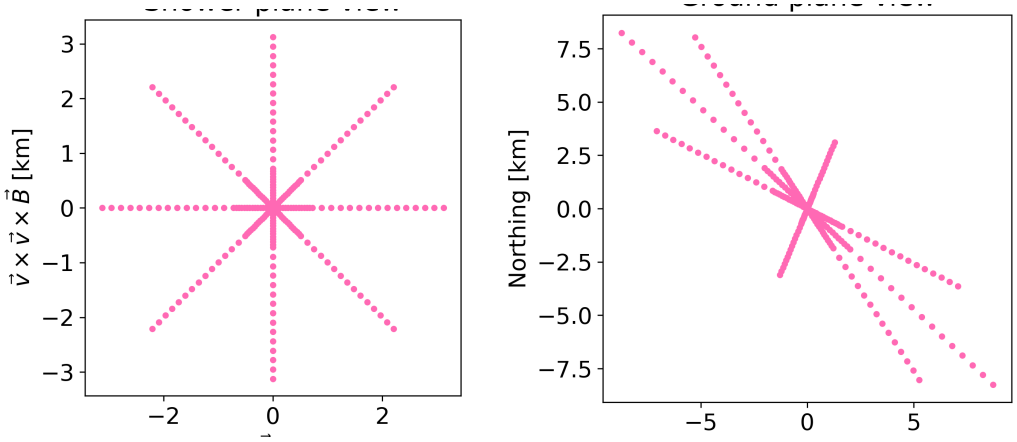

FIGURE 5.1: Star-shaped antenna layouts for an idealised CoREAS simulation with zenith angle $\theta = 75°$ and azimuth angle $\phi = 225°$ (arriving from the bottom right of right panel). The pink points represent the 240 simulated antennas. All antennas are set at the pre-defined observation altitude. **Left:** Eight-pronged star-shaped layout in the shower plane system. Densely covered area near the origin closely corresponds to area inside the Cherenkov ring. **Right:** Projected layout viewed in ground plane coordinates. The projected star-shape approximates the shape of the radio footprint on the ground.

with the $\vec{v} \times \vec{B}$ and $\vec{v} \times (\vec{v} \times \vec{B})$ axes, respectively. The antennas are densely clustered near the shower core and inside the Cherenkov ring. Outside the ring, the antennas of each arm are farther apart and extend up to five Cherenkov radii from the shower core. From vertically above, the pattern looks stretched out instead, approximating the shape of the radio footprint on the ground plane. In Figure 5.1, I present an example star-shaped layout in shower plane coordinates (left panel) and ground plane North-West-Vertical (NWU) coordinates (right). The idealised pattern for each air-shower simulation in both libraries is generated according to the shower geometry.

For Argentina, I use the "RdStar" library that is also used for the previous iteration of the model by Schlüter and Huege [9] for the AugerPrime Radio Upgrade. It uses the QGSJetII-04 [113], UrQMD interaction models, and a thinning level of $t_f = 5 \cdot 10^{-6}$. The CoREAS simulation output yields the electric field for the full frequency range of the emission. Consequently, I am able to filter it to a different frequency band without having to create a new library. I display the shower parameters of the library in the left panel of Table 5.1. Every combination of primary particle, energy and shower geometry is simulated three times which results in different values of $X_{\max}$. This is meant to take shower-to-shower fluctuations into account. The local magnetic field at the site of the Pierre Auger Observatory (PAO) is used for the simulations. It has a field strength of $|\vec{B}_{\text{PAO}}| = 24\mu\text{T}$ and an in inclination of $\sim -35°$. In the context of air-showers, this corresponds to a zenith angle of 55°. In total, the RdStar library contains 4309 simulated events.

For the GRAND site in China, I generate a new simulation library. I call it "GRAND star-shape" library from now on. I display its shower parameters in the right panel of Table 5.1. I use the same composition of primaries and binned energy distribution as the RdStar library. For the shower geometry, I choose continuous distributions. This also takes shower-to-shower fluctuations into account. In addition, the continuous distributions cover the parameter space more fully, especially for the large differences between showers just $\sim 1°$ apart in zenith angle for zenith angles

TABLE 5.1: Shower parameters for the star-shape simulation libraries I used to characterise the emission in Argentina and China. Energy is binned log-linearly with $\log(0.2/\mathrm{eV})$ spacing for both libraries. **Left:** Parameters of the RdStar library for Argentina. **Right:** Parameters of the GRAND star-shape library for China. Zenith and azimuth angles are distributed continuously and uniformly within the given ranges.

RdStar	**Value(s)**	**GRAND Star-shape**	**Value(s)**
# of events	4309	# of events	3677
Antennas/event	240	Antennas/event	240
Obs. altitude	1400 m a.s.l.	Obs. altitude	1142 m a.s.l.
Prim. energy	$\log([18.4, 20.2]/\mathrm{eV})$	Prim. energy	$\log([18.4, 20]/\mathrm{eV})$
Prim. particle	50% p & 50% Fe	Prim. particle	50% p & 50% Fe
Zenith angle	$[65, 85]^\circ$ (2.5° bins)	Zenith angle	$[65, 85]^\circ$ (cont.)
Azimuth angle	$[0, 360]^\circ$ (45° bins)	Azimuth angle	$[0, 360]^\circ$ (cont.)
Atmosph. model	Auger (October)	Atmosph. model	Dunhuang
Hadr. model	QGSJetII-04	Hadr. model	SIBYLL-2.3d
Thinning level	$5 \cdot 10^{-6}$	Thinning level	10^{-6}

$> 80^\circ$. The magnetic field strength at the location of GP300 is $|\vec{B}_{\mathrm{GP300}}| = 56\mu\mathrm{T}$. The magnetic field inclination is $\sim 60^\circ$ since it takes positive values in the northern hemisphere. This corresponds to a zenith angle of 30°. The GRAND star-shape library contains 3677 simulated events in total.

In the following sections, I also refer to the two simulation libraries as simulations for the GRAND@Auger and GP300 sites, respectively.

5.2 Refit of the charge excess parametrisation

For the 30–80 MHz frequency band, used in the previous iteration of the signal model, the charge excess fraction a_{ce} takes values up to $a_{\mathrm{ce}} = 0.15$ for the RdStar simulation library (compare Fig. 6 in reference [9]). Here, I analytically calculate a_{ce} for the RdStar and GRAND star-shape libraries in the 50–200 MHz frequency band. I consider antennas for the calculation if they are unaffected by thinning (see Section 2.3.2), and are far enough away from the $\vec{v} \times \vec{B}$ axis in the shower plane. I determine which antennas are affected by thinning artifacts by taking into account their frequency spectra. While the spectrum is expected to slope downward due to lower signal coherence at higher frequencies, thinning artifacts cause a noisy plateau. Where the plateau starts to affect the 50–200 MHz frequency band, I discard the corresponding antennas. This happens at large axis distances where the overall emission becomes so weak, that thinning artifacts become relevant. For either library, about 40% of antennas are affected by thinning. This thinning criterion is described in more detail in reference [9]. For the angular distance of antennas to the $\vec{v} \times \vec{B}$ axis, I use the criterion $\phi > 5^\circ$, where ϕ is the angle between the $\vec{v} \times \vec{B}$ axis and the position vector of the antenna in the shower plane.

In Figure 5.2, I display the results for all viable antennas in the top panels. For the Pierre Auger Observatory site and the higher frequency band, I find that a_{ce} only reaches values up to $a_{\mathrm{ce}} = 0.06$ (top left panel). There is little research on why the fraction decreases simply due to the change of frequency band. A study of the frequency spectrum of the geomagnetic and charge excess emission components shows decreasing signal amplitudes with rising frequency up to 125 MHz [114]. Further,

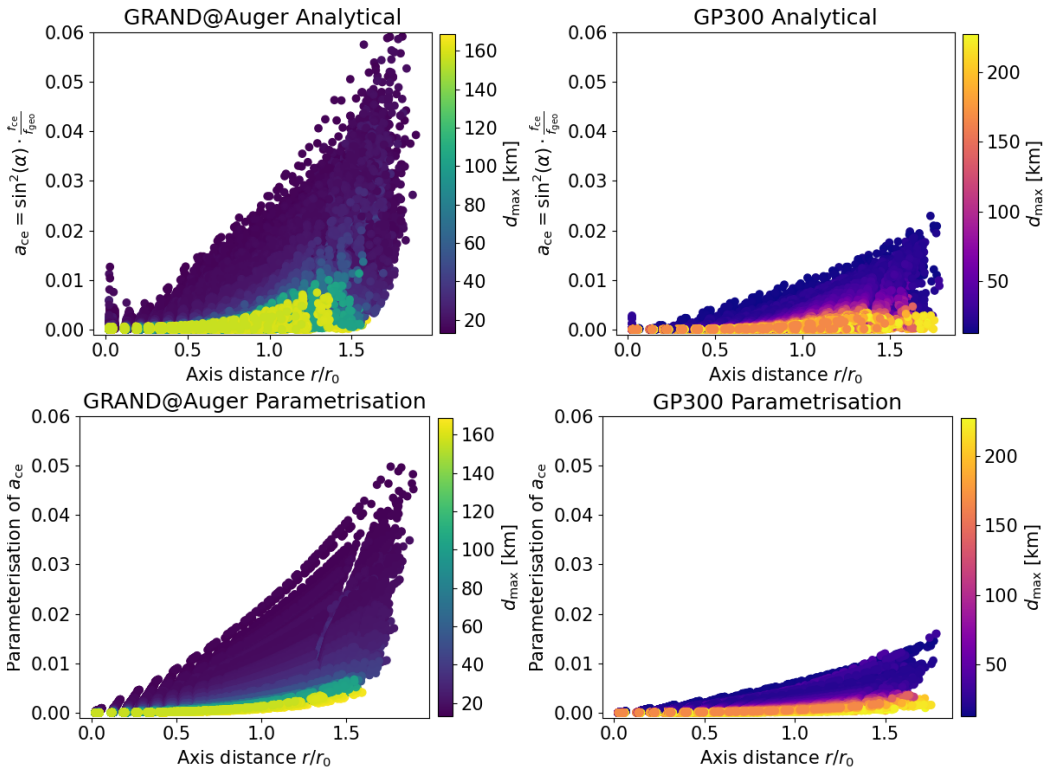

FIGURE 5.2: Radio emission charge excess fraction a_{ce} as a function of axis distance in units of Cherenkov radii r_0. The colour maps show the distance to shower maximum d_{max}. **Left column:** GRAND@Auger site. **Right column:** GP300 site. **Top row:** Calculated analytically from antenna position and emission polarisation. I exclude antennas close to the $\vec{v} \times \vec{B}$ axis, and those affected by thinning (see Sec. 2.3.2). **Bottom row:** Parametrisations of a_{ce} fitted to the points in the top panels. All antennas unaffected by thinning are included.

the radio emission loses signal coherence with increasing frequency [13]. A possible explanation is that the charge excess component is more strongly affected by this effect, leading to a lower fraction at higher frequencies. a_{ce} is even smaller at the site of GP300, only reaching values up to $a_{ce} = 0.02$ (top right panel). This is due to the higher magnetic field strength. The magnetic field at the GP300 site is almost three times stronger than at GRAND@Auger. The strength of the geomagnetic field has an indirect impact on a_{ce} since it directly impacts the strength of the geomagnetic emission. As such, this is in line with expectations.

The colour mapping in Figure 5.2 shows the distance to shower maximum d_{max} as a proxy for the zenith angle. Showers with large values of d_{max}, i.e., the most inclined showers, show the smallest values of a_{ce}. This reflects the dependence of the strength of the charge-excess emission on the air-density at the shower maximum. The more inclined a shower, the lower the air-density at the shower maximum, and, consequently, the lower is its charge-excess fraction. In addition, a_{ce} generally increases with the axis distance. I already discussed both effects in Section 4.2.2 as motivation for the parametrisation of a_{ce}.

As a next step, I parametrise a_{ce} for both sites. For this purpose, I perform fits of the function in Eq. (4.8) to the analytically calculated charge excess fraction I show in the top panels of Figure 5.2. The different geomagnetic field strength leads to significant differences between charge excess fraction parametrisations for

the GRAND@Auger $a_{\mathrm{ce}}^{\mathrm{ARG}}$ and GP300 $a_{\mathrm{ce}}^{\mathrm{CHN}}$ sites, respectively,

$$a_{\mathrm{ce}}^{\mathrm{ARG}} = \left[0.30 - \frac{d_{\max}}{729\,\mathrm{km}}\right] \cdot \frac{r_{\mathrm{axis}}}{d_{\max}} \cdot \exp\left(\frac{r_{\mathrm{axis}}}{682\,\mathrm{m}}\right) \cdot \left[\left(\frac{\rho_{\max}}{0.42\,\mathrm{kg\,m^{-3}}}\right)^{2.98} + 0.18\right], \quad (5.1)$$

$$a_{\mathrm{ce}}^{\mathrm{CHN}} = \left[0.23 - \frac{d_{\max}}{1106\,\mathrm{km}}\right] \cdot \frac{r_{\mathrm{axis}}}{d_{\max}} \cdot \exp\left(\frac{r_{\mathrm{axis}}}{614\,\mathrm{m}}\right) \cdot \left[\left(\frac{\rho_{\max}}{0.67\,\mathrm{kg\,m^{-3}}}\right)^{1.43} + 0.17\right]. \quad (5.2)$$

Using these parametrisations, I calculate a_{ce} for any antenna not affected by thinning. I show the resulting values of a_{ce} for both sites in the bottom panels of Figure 5.2. It does not reproduce a feature of the true distribution at minimal axis distances where some antennas have charge excess fractions up to 0.015. In addition, the parametrised fraction for GRAND@Auger shows small gaps in its distribution not present in the true distribution. However, since these features are small, the effect is not noticeable going forward.

In the next step, I use Eq. (4.7) to calculate the geomagnetic energy fluence $f_{\mathrm{geo}}^{\mathrm{par}}$ with the parametrisation of a_{ce}. In Figure 5.3, I evaluate $f_{\mathrm{geo}}^{\mathrm{par}}$. I compare $f_{\mathrm{geo}}^{\mathrm{par}}$ with the analytically calculated fluence $f_{\mathrm{geo}}^{\mathrm{pos}}$ from which I parametrised a_{ce} (see Eqs. (4.4) and (4.5)). I display two pairs of two-dimensional histograms, one pair for each site. On the left, I display the relative deviation between $f_{\mathrm{geo}}^{\mathrm{par}}$ and $f_{\mathrm{geo}}^{\mathrm{pos}}$ against the absolute values of $f_{\mathrm{geo}}^{\mathrm{pos}}$. On the right, I plot it against the axis distance in units of Cherenkov radii r_0. Analytical and parametrised geomagnetic fluence overall agree well with each other for both sites for true energy fluence values $> 10\,\mathrm{eV/m^2}$, and axis distances $< r_0$. For Argentina, the fluence agrees within 2%. For China, the fluence agrees within $< 1\%$. For lower fluence values and larger axis distances, a small negative bias of the order of 1% appears. In a practical context, however, antennas with such low energy fluence are often dominated by noise. Within the Cherenkov radius, the parametrised fluence is remarkably accurate. The fluence calculation for the GP300 site performs slightly better due to the generally lower charge excess fraction.

5.3 Functional form of the LDF

Next, I revise the functional form of the geomagnetic fluence lateral distribution function (LDF) for the 50–200 MHz frequency band. In comparison to the 30–80 MHz band, the total intensity of the radio emission increases since the higher band is wider. The additional intensity is mainly concentrated on the Cherenkov ring. As a result, the amplitude on the ring is larger compared to its inside than in the previous iteration of the model. To account for this, I introduce a new shape parameter p_{inner} to the LDF. I include p_{inner} in the expression of $p(r)$

$$p(r) = \begin{cases} p_{\mathrm{inner}} & r < r_0 \\ 2 \cdot (r_0/r)^{b/1000} & r \geq r_0. \end{cases} \quad (5.3)$$

It allows the slope of the "Gaussian" to become steeper for $r < r_0$. For $r \geq r_0$, the functional form of $p(r)$ remains as described by Schlüter and Huege [9]: The parameter b is determined in the fit and allows $p(r)$ to increase from 2 to describe the tail of the LDF more accurately.

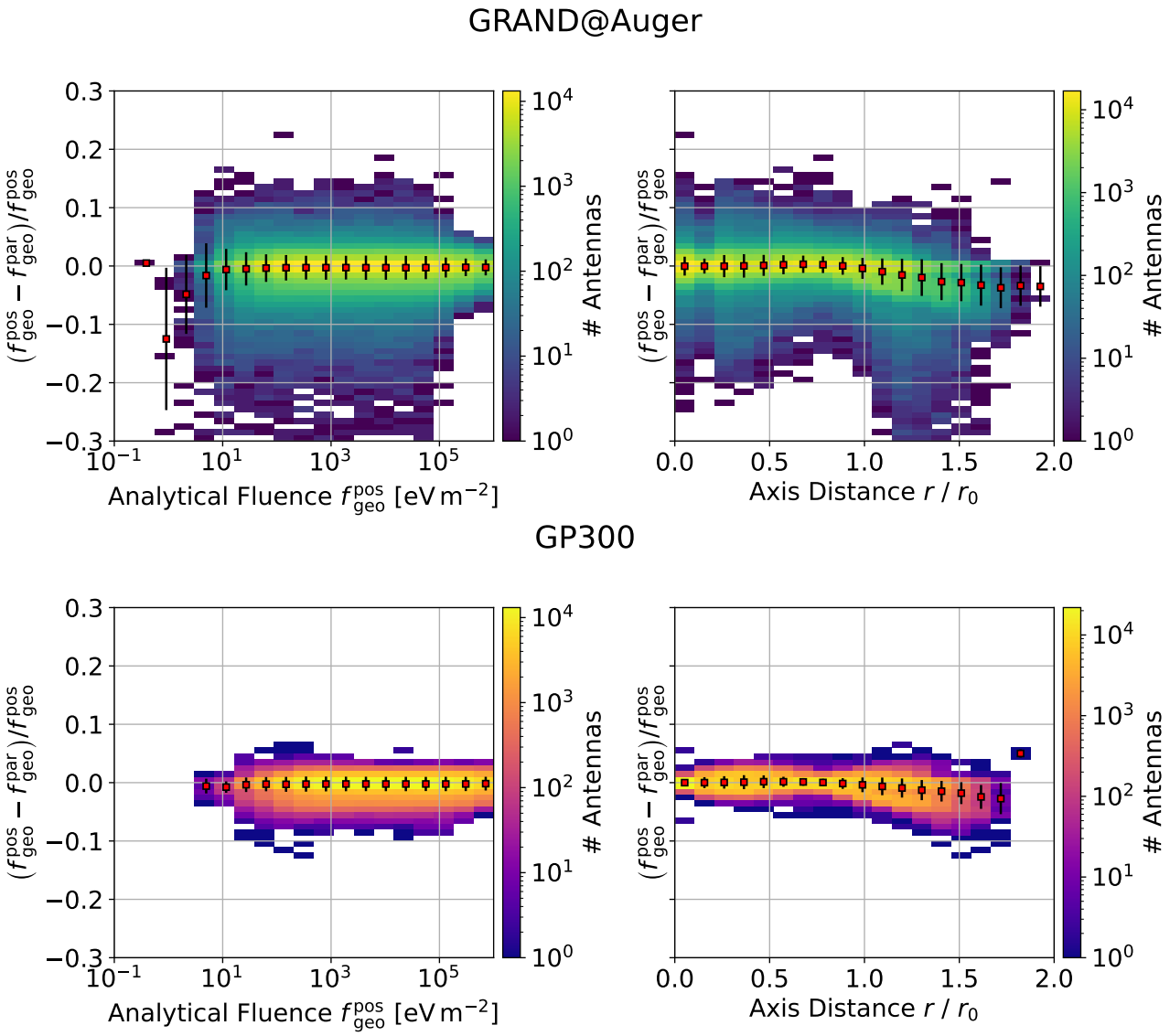

FIGURE 5.3: Evaluation of the parametrised geomagnetic energy fluence f_{geo}^{par}. The colour scale shows the amount of antennas represented by each bin. On the y-axes, I draw the relative deviation of f_{geo}^{par} from the analytically calculated f_{geo}^{pos}. The red points display the means of each column, their error bars the standard deviations. Extreme outliers > 0.3 are cut. **Top row:** GRAND@Auger (158 outliers). **Bottom row:** GP300 (0 outliers). **Left:** Relative deviation as a function of f_{geo}^{pos}. **Right:** Relative deviation as a function of the axis distance, normalised by the radius of the Cherenkov ring r_0.

The updated LDF

$$f_{\mathrm{LDF}} = \begin{cases} \frac{E_{\mathrm{geo}}}{A_0}\left[\exp\left(-\left(\frac{|r-r_0|}{\sigma}\right)^{p_{\mathrm{inner}}}\right) + \frac{a_{\mathrm{rel}}}{1+\exp\left(s\cdot\left(\frac{r}{r_0}-r_{02}\right)\right)}\right] & \text{for } r < r_0, \\ \frac{E_{\mathrm{geo}}}{A_0}\left[\exp\left(-\left(\frac{r-r_0}{\sigma}\right)^{p(r)}\right) + \frac{a_{\mathrm{rel}}}{1+\exp\left(s\cdot\left(\frac{r}{r_0}-r_{02}\right)\right)}\right] & \text{for } r \geq r_0. \end{cases} \tag{5.4}$$

has seven free shape parameters in addition to E_{geo} and the radio core position (see Section 4.2.3 for details of the roles of the shape parameters). In addition to modifying the LDF equation, I make an optimisation to the fit of the radio core position. The radio core is off-set from the particle shower core for inclined showers due to refractive displacement [106]. I find that a free fit of the radio core struggles to reliably converge on the symmetry centre for the higher frequency band. I constrain the fit by fixing the possible core positions to a line defined by the projection of the shower axis onto the ground plane. This prevents shifts to the side that have no physical basis.

Figure 5.4 shows LDF fits for both sites to example simulations from the RdStar and GRAND star-shape libraries, respectively. The two simulated events both have primary energy $E_{\mathrm{CR}} = 10^{18.8}\,\mathrm{eV}$ and zenith angle $\theta = 75°$, as well as the closest possible match in geomagnetic angle. The area under each curve represents the geomagnetic radiation energy E_{geo}. The difference in amplitude and, thus, E_{geo} between the simulations for the two sites stems from the differing magnetic field strength. For both fits, all LDF shape parameters are free fit parameters.

5.4 LDF fit procedure

Practically, I carry out the geomagnetic fluence LDF fit by minimising the following function for a given air-shower:

$$\chi^2 = \sum_{i=0}^{N} \left(\frac{f_{\vec{v}\times\vec{B},i} - f^{\mathrm{pred}}_{\vec{v}\times\vec{B},i}(\vec{x}_i, E_{\mathrm{geo}}, d_{\mathrm{max}})}{\sigma_{f_{\vec{v}\times\vec{B},i}}} \right)^2 . \tag{5.5}$$

Here, N is the total number of antennas in the event. $f_{\vec{v}\times\vec{B},i}$ and $\sigma_{f_{\vec{v}\times\vec{B},i}}$ are, respectively, the value and uncertainty of the energy fluence for the i-th antenna along the $\vec{v}\times\vec{B}$ polarisation direction from the data (be it simulation or measurement). I use the $\vec{v}\times\vec{B}$ fluence for the minimisation because, in the case of a measurement, I can obtain its error $\sigma_{f_{\vec{v}\times\vec{B}}}$ directly. This saves the step of propagating the error through the steps of the signal model. Instead, I apply the steps of the signal model inversely to the geomagnetic energy fluence predicted by the LDF model. This results in the last missing quantity in Eq. (5.5), $f^{\mathrm{pred}}_{\vec{v}\times\vec{B},i}$, which is the $\vec{v}\times\vec{B}$ fluence predicted by the LDF model. I use the `lmfit` [115] python module for the minimisation. In order to display the fit results, I apply the signal model normally to $f_{\vec{v}\times\vec{B},i}$, $\sigma_{f_{\vec{v}\times\vec{B},i}}$, and $f^{\mathrm{pred}}_{\vec{v}\times\vec{B},i}$ after the minimisation to find the geomagnetic fluence. Figure 5.4 from the previous section shows examples of this. The minimisation procedure, in the end, yields E_{geo}, d_{max}, and the core position as well as their respective uncertainties.

For the uncertainty model while characterising the LDF model with simulations

$$\sigma_{f_{\vec{v}\times\vec{B},i}} = 0.03\, f_{\vec{v}\times\vec{B},i} + 10^{-4} f^{\mathrm{max}}_{\vec{v}\times\vec{B}}, \tag{5.6}$$

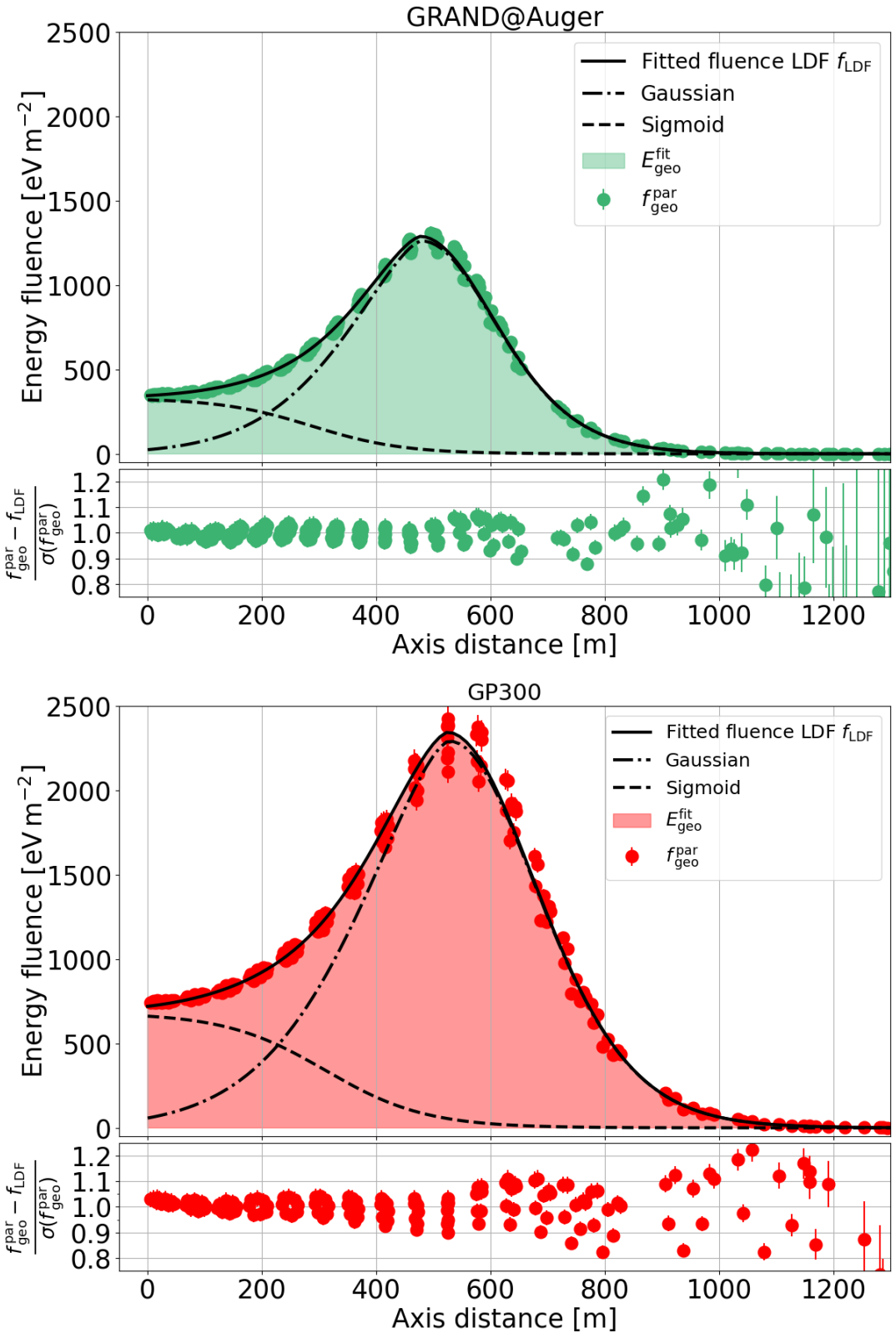

FIGURE 5.4: Fits of the updated LDF $f_{\mathrm{LDF}}(r)$ to the geomagnetic fluence $f^{\mathrm{par}}_{\mathrm{geo}}$ of two example simulations from the RdStar and GRAND star-shape libraries. The events have identical total energy and zenith angle, and a close match in geomagnetic angle. I show the parametrised geomagnetic energy fluence $f^{\mathrm{par}}_{\mathrm{geo}}$ at each antenna as green or red points. The fitted LDF is the solid black line. The dot-dashed and dashed lines represent the Gaussian and sigmoid components of the LDF, respectively. The coloured areas under the curves represent the geomagnetic radiation energy E_{geo}. **Top:** RdStar event for the site in Argentina. **Bottom:** GRAND star-shape event for the site in China.

I use 3% of the fluence $f_{\vec{v}\times\vec{B},i}$ of each antenna. This results in a χ^2/n.d.f.-distribution with a mean around 2. In addition, I add a small fraction of the maximum fluence of the event $f^{\max}_{\vec{v}\times\vec{B}}$. For the LDF fit, I do not discard the antennas affected by thinning. However, they form a noisy plateau in the tail of the lateral distribution due to the thinning artifacts. This is visible in Figure 5.4 in the residuals of the points in the distributions tails, and also, for the low-frequency model, in the logarithmic inset of Figure 4.4. I find that the added fraction of the maximum fluence assigns, relatively, large uncertainties to these antennas to prevent the thinning noise from introducing any biases to the fit.

Both the minimisation procedure and the uncertainty model I describe in this subsection closely follow the methods from Schlüter and Huege [9].

5.5 Parametrisation of the LDF shape parameters with $d_{\mathbf{max}}$

In this section, I parametrise the shape parameters of the geomagnetic energy fluence LDF as a function of the distance to the shower maximum $d_{\max}$ to decrease the number of free parameters. This makes the LDF fit viable for measurements with few antennas, and enables the energy reconstruction for these events.

5.5.1 LDF input parameters

In addition to the shape parameters and the other fit parameters—E_{geo}, $d_{\max}$, and the radio core position—the LDF fit has a number of input parameters that depend on the specific air-shower. Since the LDF fit operates in the shower plane coordinate system, the shower arrival direction as well as its angle to the local geomagnetic field vector are necessary. The fit also requires start values for the shower core position, the geomagnetic radiation energy E_{geo} and $d_{\max}$. Consequently, the calculation of a start value for $d_{\max}$ requires the depth of shower maximum $X_{\max}$, the local atmospheric profile, and the observation altitude. Since I am parametrising the LDF shape parameters using idealised simulations, I use "true" information for this purpose. I use the primary energy, shower geometry, geomagnetic field vector, atmosphere model, and observation altitude from the simulation input. From the simulation output, I take $X_{\max}$ and calculate from it the true $d_{\max}$. Normally, $d_{\max}$ is a free parameter in the fit. However, in order to characterise the shape parameters, I fix it to its true value. I roughly estimate a start value for E_{geo} using the cosmic-ray primary energy and the geomagnetic angle. In addition, I calculate the refractive displacement of the radio symmetry centre from the simulation shower core using the method given in reference [106] to use as a start value for the radio core.

For the parametrisation process, I do not consider air-showers with a geomagnetic angle $\alpha < 20°$. A small geomagnetic angle leads to weak geomagnetic emission. I find such air-showers to often have a poor LDF fit which could introduce biases to the shape parameters. For the RdStar library, I remove 240 such events. No events in the GRAND star-shape library are affected since the local geomagnetic field is more vertical. Consequently, all air-showers have sufficiently large geomagnetic angles.

5.5.2 Physical meaning of shape parameters r_0 and σ

Before fixing the shape parameters, I investigate r_0 and σ as physical quantities. r_0 describes the Gaussian peak position and closely corresponds to the Cherenkov

radius. In the low-frequency model [9], r_0 is fixed directly to the radius of the Cherenkov cone,

$$r_0^{\text{pred}} = \tan\left(\delta_0^{\text{pred}}(n(h_{\max}))\right) \cdot d_{\max}, \tag{5.7}$$

where the emission hits the ground (see Eq. (2.5)). δ_0^{pred} is the Cherenkov cone opening angle. It is determined with Eq. (2.4) using the refractive index $n(h_{\max})$ at the altitude $h_{\max}$ of the shower maximum above sea level, which depends on the atmospheric model. $d_{\max}$ corresponds to the height of the cone, along the shower axis. For this calculation, it is assumed that the emission originates from a single point-like source at the shower maximum $X_{\max}$ (see Section 4.1). For the low-frequency model, the fitted Gaussian peak position r_0^{fit} shows remarkable agreement with the predicted Cherenkov radius for high zenith angles. However, it corresponds to an axis distance slightly larger than that of the fluence maximum due to the relative significance of the sigmoid component. Any deviations from the fixed r_0 in the low-frequency model are sufficiently compensated for by the other LDF fit parameters.

In contrast, for the high-frequency model, r_0^{fit} closely matches the maximum of the fluence distribution of the radio emission in the higher frequency model. This happens since the fluence maximum is more dominant relative to the inside of the ring. The sigmoid, by design, is only significant inside the Cherenkov ring, i.e., before the fluence distribution reaches its maximum. As such, the Gaussian represents almost all of the emission at the peak. The LDF fits in Figure 5.4 exemplify this.

I evaluate how closely the fluence maximum at r_0^{fit} matches the Cherenkov radius r_0^{pred} estimated with Eq. (2.5). I calculate $\delta_0(r_0^{\text{fit}})$ by arranging Eq. (5.7) for δ_0 and inserting r_0^{fit}. Figure 5.5 displays both angles against $d_{\max}$, respectively, for the GRAND@Auger and GP300 sites in the top panels. I find a significant $d_{\max}$ dependent deviation between the opening angle of the Cherenkov cone $\delta_0(n(h_{\max}))$ and $\delta_0(r_0^{\text{fit}})$. In the lower panel, I show the ratio between the angles. A ratio < 1 indicates a value of r_0^{fit} that is smaller than the radius of the Cherenkov cone. The deviation shows a clear behaviour with respect to $d_{\max}$. For the GRAND@Auger site, the deviation is close to constant at $\delta_0^{\text{fit}}/\delta_0^{\text{pred}} \approx 0.9$. For the GP300 site, the deviation is more significant at small values of $d_{\max}$, and decreases for large $d_{\max}$. The former corresponds to small zenith angles, the latter to large zenith angles. For both sites, no strong dependence on the primary cosmic-ray energy is apparent.

I account for the deviations by parametrising δ_0 for both sites with $d_{\max}$

$$\delta_0 = \delta_0^{\text{pred}} \cdot \left(d_1 + d_2 \cdot d_{\max} + \frac{d_3}{d_{\max}^2}\right). \tag{5.8}$$

I determine the parameters d_1, d_2 and d_3 by fitting Eq. (5.8) to the deviation of δ_0^{fit} from δ_0^{pred} (listed in Eqs. (5.15) and (5.21)). Since the opening angle of the Cherenkov cone is of the order of one degree, I use Eq. (5.7) and the small-angle approximation to apply the parametrisation to r_0 directly.

σ is another shape parameter with a physical meaning. It corresponds to the standard deviation or width of the Gaussian component and can also be interpreted as the thickness of the high intensity Cherenkov ring. Generally, σ increases, similarly to the overall size of the radio footprint, with the distance to the emission source at the shower maximum. I parametrise its value with the function,

$$\sigma = \left(s_1 \cdot \left(\frac{d_{\max} - 5\,\text{km}}{\text{m}}\right)^{s_2} + s_3\right) \text{m}, \tag{5.9}$$

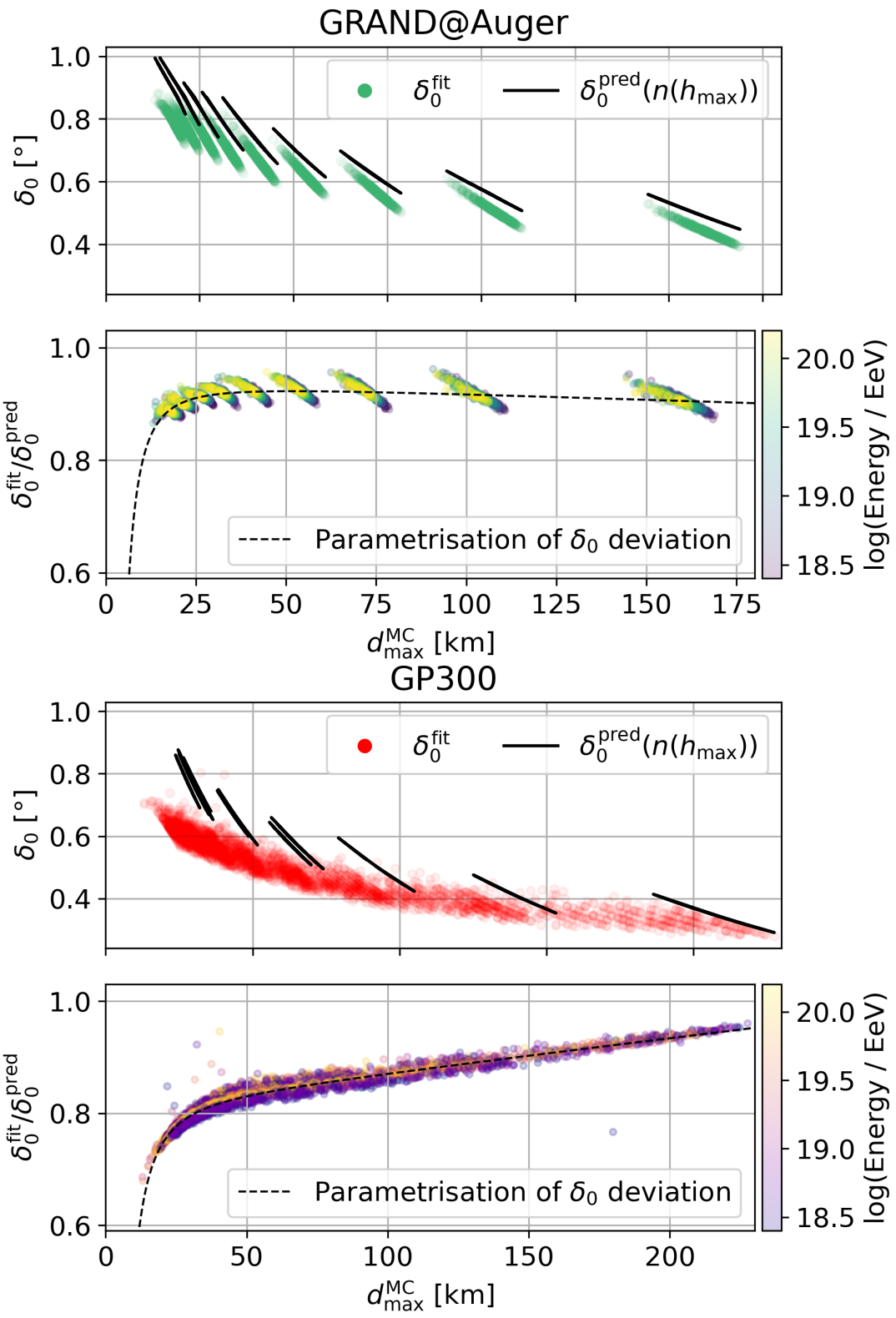

FIGURE 5.5: **Top row:** Comparison of the predicted opening angle of the Cherenkov cone $\delta_0^{pred}(n(h_{max}))$ (black lines), and the values of $\delta_0(r_0^{fit})$ with r_0^{fit} when freely fitted in the LDF fit (green/orange points). $n(h_{max})$ is the refractive index of the atmosphere at the altitude h_{max} of the shower maximum above sea level. **Bottom row:** Deviation of δ_0^{fit} from δ_0^{pred} as coloured points, colour mapped by cosmic-ray primary energy. The parametrisations for r_0 in Eqs. (5.15) and (5.21) are the best fit values of the dashed black lines to the data points. **Left:** RdStar simulations using Auger (October) atmosphere. **Right:** GRAND star-shape using Dunhuang atmosphere.

that I adopt unchanged from the low-frequency model. The normalisation $d_{\max} - 5\,\mathrm{km}$ is used to stabilise the fitted parameters s_1, s_2, and s_3 against statistical fluctuations. I provide the explicit values of the parametrisations of r_0 and σ in Eqs. (5.15) and (5.21) in the following subsection as part of the iterative parametrisation of all LDF shape parameters with $d_{\max}$.

5.5.3 Iterative parametrisation of the shape parameters

Initially, I fit the LDF to all events in each library with no parameters fixed. Then, in an iterative process, I pick an LDF shape parameter, and investigate its behaviour as a function of $d_{\max}$. I fit a parametrisation, that describes this behaviour, to the shape parameter. In the next iteration of the fit, I fix this shape parameter to its $d_{\max}$ parametrisation, and pick another shape parameter to parametrise. I repeat these steps until the LDF only depends on E_{geo}, $d_{\max}$, and the two core coordinates. Differently from the other shape parameters, I fix the parameter s, describing the slope of the sigmoid component, to a constant $s = 6$. This happens as a first step for both sites to ensure that the sigmoid component is only significant inside the Cherenkov radius. The process and the order in which I fix the parameters is identical for both sites. I label the parametrisations of each shape parameter with the abbreviations ARG (Argentina) and CHN (China) for the two sites.

As I discussed in the previous subsection, the parameters r_0 and σ have physical meaning. As such, their values stay stable in every iteration of the fit. For the remaining shape parameters, r_{02}, a_{rel}, p_{inner}, and b, I find a growing dependence on the primary energy in later iterations of the fit if not fixed to their parametrisation early on. r_0 and σ do not show significant dependence on the energy. For these reasons, I choose to parametrise σ and r_0 in the second-to-last and last iterations, respectively. I fit the shape parameters r_{02}, p_{inner}, a_{rel}, and b with a fit function of the same form as the factor multiplied to δ_0^{pred} in Eq. (5.8). I give the parametrisation functions for r_0 and σ in the previous subsection.

Fig. 5.6 and 5.7 display the behaviour of the shape parameters as functions of $d_{\max}$, their parametrisations, and the order in which I fix them for GRAND@Auger and GP300, respectively. Except for p_{inner} at low values of $d_{\max}$, the parameters for both site behave in the same manner. I choose not to show the error bars of the individual points in favour of highlighting the energy dependence with the colour maps. The larger range of $d_{\max}$ values for the GRAND star-shape library is a result of the lower observation altitude. For both sites, I find good descriptions of the LDF shape parameter behaviour using the $d_{\max}$ parametrisations. The parameter a_{rel}, determining the relative amplitude of the sigmoid component, and the Gaussian slope parameters b and p_{inner} show vertical spread. The spread corresponds to a dependence of the shape parameters on the cosmic-ray primary energy. The observed spread of the order of 100 of b does not have a large impact on the LDF shape since b only serves to slightly decrease the Gaussian exponent from $p(r) = 2$ for $r > r_0$. The vertical spread for a_{rel} and p_{inner} is more significant since their values directly impact the LDF shape. As such, I parametrise b last before the parameters with physical meaning. The remaining three shape parameters show less significant dependence on the energy, and, as such, less vertical spread. However, I find that attempts to reduce the spread, and to optimise the parametrisations by describing the energy dependence lead to worse reconstruction performance.

Equations (5.10)-(5.15) show the best fit values for the parametrisations of each shape parameter for the site of GRAND@Auger in Argentina:

$$r_{02}^{\mathrm{ARG}} = 0.598 + \frac{d_{\mathrm{max}}}{771.9\,\mathrm{km}} - \frac{98.65\,\mathrm{km}^2}{d_{\mathrm{max}}^2}, \tag{5.10}$$

$$p_{\mathrm{inner}}^{\mathrm{ARG}} = 1.464 - \frac{d_{\mathrm{max}}}{18{,}982\,\mathrm{km}} + \frac{32.94\,\mathrm{km}^2}{d_{\mathrm{max}}^2}, \tag{5.11}$$

$$a_{\mathrm{rel}}^{\mathrm{ARG}} = 0.233 + \frac{d_{\mathrm{max}}}{4848\,\mathrm{km}} - \frac{3.79\,\mathrm{km}^2}{d_{\mathrm{max}}^2}, \tag{5.12}$$

$$b^{\mathrm{ARG}} = 282.2 - \frac{d_{\mathrm{max}}}{2.73\,\mathrm{km}} - \frac{6457\,\mathrm{km}^2}{d_{\mathrm{max}}^2}, \tag{5.13}$$

$$\sigma^{\mathrm{ARG}} = \left(0.027 \cdot \left(\frac{d_{\mathrm{max}} - 5\,\mathrm{km}}{\mathrm{m}}\right)^{0.805} + 61.97\right)\mathrm{m}, \tag{5.14}$$

$$r_0^{\mathrm{ARG}} = r_0^{\mathrm{pred}} \cdot \left(0.941 - \frac{d_{\mathrm{max}}}{4536\,\mathrm{km}} - \frac{15.96\,\mathrm{km}^2}{d_{\mathrm{max}}^2}\right). \tag{5.15}$$

Eqs. (5.16)-(5.21) show the best fit values for the parametrisations of each shape parameter for the GP300 site in China:

$$r_{02}^{\mathrm{CHN}} = 0.560 + \frac{d_{\mathrm{max}}}{957.7\,\mathrm{km}} - \frac{143.9\,\mathrm{km}^2}{d_{\mathrm{max}}^2}, \tag{5.16}$$

$$p_{\mathrm{inner}}^{\mathrm{CHN}} = 1.520 + \frac{d_{\mathrm{max}}}{2614\,\mathrm{km}} - \frac{42.64\,\mathrm{km}^2}{d_{\mathrm{max}}^2}, \tag{5.17}$$

$$a_{\mathrm{rel}}^{\mathrm{CHN}} = 0.266 + \frac{d_{\mathrm{max}}}{1740\,\mathrm{km}} - \frac{19.28\,\mathrm{km}^2}{d_{\mathrm{max}}^2}, \tag{5.18}$$

$$b^{\mathrm{CHN}} = 246.5 - \frac{d_{\mathrm{max}}}{4.48\,\mathrm{km}} - \frac{9299\,\mathrm{km}^2}{d_{\mathrm{max}}^2}, \tag{5.19}$$

$$\sigma^{\mathrm{CHN}} = \left(0.039 \cdot \left(\frac{d_{\mathrm{max}} - 5\,\mathrm{km}}{\mathrm{m}}\right)^{0.760} + 61.00\right)\mathrm{m}., \tag{5.20}$$

$$r_0^{\mathrm{CHN}} = r_0^{\mathrm{pred}} \cdot \left(0.812 + \frac{d_{\mathrm{max}}}{1613\,\mathrm{km}} - \frac{31.82\,\mathrm{km}^2}{d_{\mathrm{max}}^2}\right). \tag{5.21}$$

I parametrise the shape parameters with d_{max} to stabilise the behaviour of the LDF fit in the presence of few data points, i.e., antennas with a viable signal. If an event has many data points, for example a strongly inclined shower with a large footprint, leaving one or more shape parameters free can lead to an improved accuracy of the LDF fit. One can apply this on an event-by-event basis for the reconstruction of individual events. However, this would likely lead to different systematic uncertainties between the events. For the application of the reconstruction to a large number of events with a wide range of shower parameters, for example the simulation libraries I analyse in this work, the fully parametrised LDF is preferable.

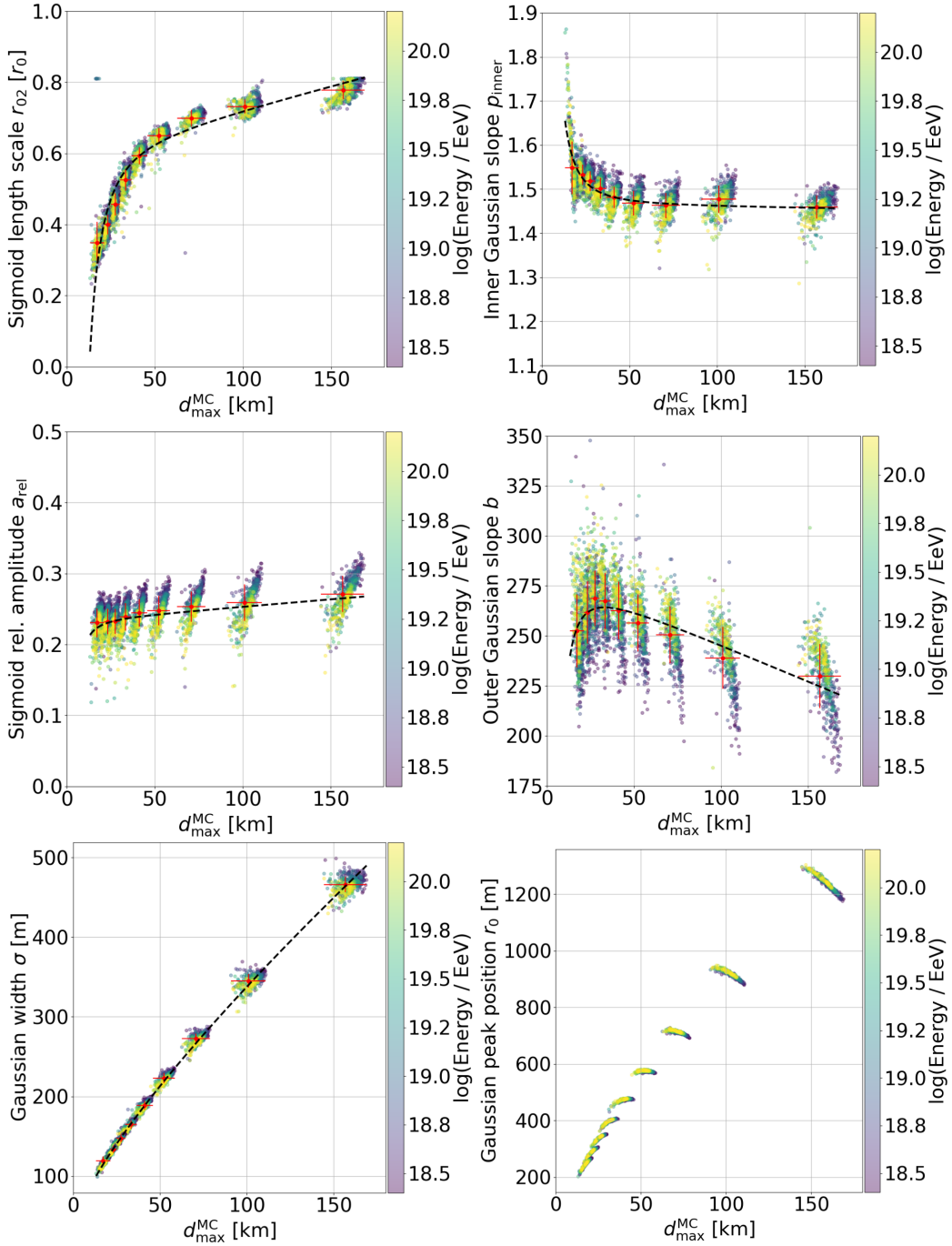

FIGURE 5.6: Behaviour of LDF shape parameters with d_{max} for the GRAND@Auger site. The points indicate the values of the parameters determined by the LDF fit to the events. The events are binned linearly in zenith angle which leads to the increasing spacing between the point clusters with d_{max}. The red squares, and horizontal and vertical error bars represent, respectively, the mean, the bin width and the standard deviation of the points. The colour map shows the cosmic-ray primary energy of each event. The black dashed lines show the best fits of the d_{max} parametrisations to the fitted parameter values. Eqs. (5.10)-(5.15) show their functional forms and best fit values. Each panel shows the parameter in the iteration of the fit before I fixed them to its parametrisation. I indicate the order I fix the parameters by the order of the plots from left to right and top to bottom. I show the parametrisation of r_0 in Figure 5.5.

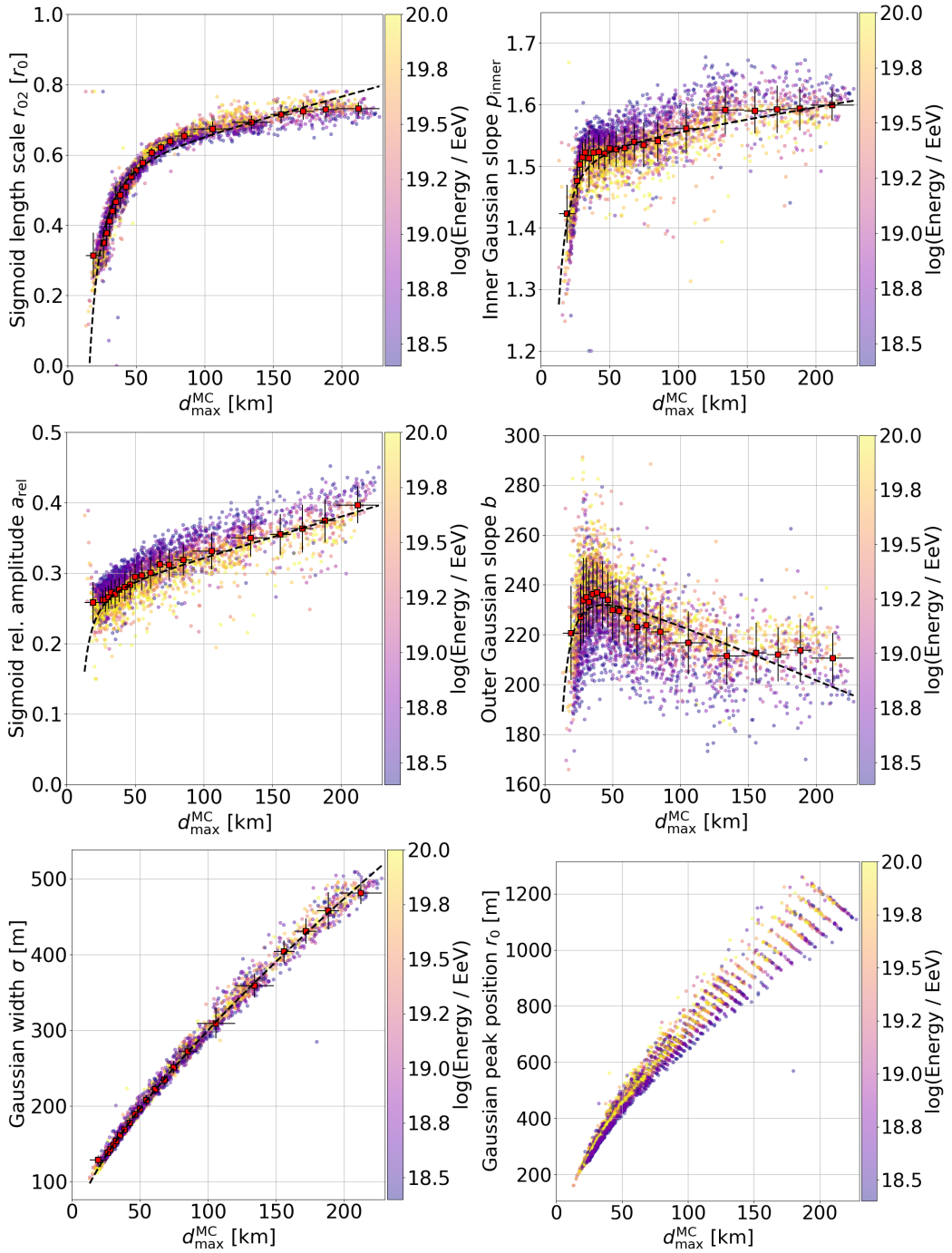

FIGURE 5.7: Behaviour of LDF shape parameters with $d_{\max}$ for the GP300 site. The points indicate the values of the parameters determined by the LDF fit to the events. The red squares, and horizontal and vertical error bars represent, respectively, the mean, the bin width and the standard deviation of the points within the bin. The colour map shows the cosmic-ray primary energy of each event. The black dashed lines show the best fits of the $d_{\max}$ parametrisations to the fitted parameter values. Eqs. (5.16)-(5.21) show their functional forms and best fit values. Each panel shows the parameter in the iteration of the fit before I fixed it to its parametrisation. I indicate the order I fix the parameters by the order of the plots from left to right and top to bottom. I show the parametrisation of r_0 in Figure 5.5.

5.6 Density correction and electromagnetic shower energy

For the 50–200 MHz frequency band, I expect a loss of coherence of the radio emission (see Section 2.3.5) which leads to some of the emitted power not being measured. The site of GP300 in China also features a stronger magnetic field than at GRAND@Auger. This contributes to the coherence loss, especially at the highest zenith angles, and influences the polarisation signatures of the emission as well [13].

In the model, this plays into the correction I apply to the radiation energy E_{geo} to calculate the corrected radiation energy S_{geo}. The loss of coherence causes E_{geo} to fall off at low air-density at the shower maximum ρ_{max}. A stronger magnetic field leads to a strongly varying dependence of this fall-off on the geomagnetic angle α. To take these effects into account, I modify the density correction in Eq. (4.12) with three new parameters c_α, p_2 and p_3. This yields the normalisation,

$$S_{\text{geo}} = \frac{E_{\text{geo}}}{\sin^{c_\alpha}(\alpha)} \cdot \frac{1}{y^2}, \tag{5.22}$$

for E_{geo} with the density correction term,

$$y = 1 - p_0 + p_0 \cdot \exp\left(p_1 \cdot [\rho_{\text{max}} - \langle\rho\rangle]\right) - \frac{p_2}{\rho_{\text{max}}} + p_3. \tag{5.23}$$

The parameters p_2 and p_3 account for the fall-off of E_{geo} at low air densities. The exponent c_α describes the deviation from the natural scaling of the radiation energy with $\sin^2\alpha$ due to continuous interactions with air molecules. A stronger deviation is expected for air-showers developing under the influence of a stronger magnetic field [98]. It effectively normalises this fall-off for all showers since E_{geo} falls off more steeply for geomagnetic angles closer to 90°.

From here, to be able to reconstruct the electromagnetic energy of a measured air-shower at a given experimental site, I solve Eq. (4.13),

$$E_{\text{em}} = 10^{19}\,\text{eV} \left(\frac{S_{\text{geo}}}{S_{19}}\right)^{1/\gamma},$$

with the updated density correction from Eq. (5.22). To find the parameter values for the density correction as well as the reference energy S_{19} and power law index γ for each experimental site, I perform a joint fit. To this end, I combine the two equations, insert the true electromagnetic energy $E_{\text{em}}^{\text{MC}}$, and rearrange for the predicted $E_{\text{geo}}^{\text{pred}}$:

$$E_{\text{geo}}^{\text{pred}} = S_{19} \left(\frac{E_{\text{em}}^{\text{MC}}}{10^{19}\,\text{eV}}\right)^{\gamma} \cdot \sin^{c_\alpha}(\alpha) \cdot y^2. \tag{5.24}$$

I use the *iminuit* [116] module to minimise

$$\sum \chi^2 \quad \text{with} \quad \chi = \frac{E_{\text{geo}}^{\text{fit}} - E_{\text{geo}}^{\text{pred}}}{\sigma(E_{\text{geo}}^{\text{fit}})}, \tag{5.25}$$

for all LDF fits. Table 5.2 shows the resulting values for the parameters S_{19}, γ, c_α, p_0, p_1, p_2 and p_3 I find with this fit for both experimental sites. The uncertainty $\sigma(E_{\text{geo}})$ on E_{geo} results from the LDF fit. I calculate the final uncertainty on the electromagnetic shower energy by propagating $\sigma(E_{\text{geo}})$ with Gaussian error propagation.

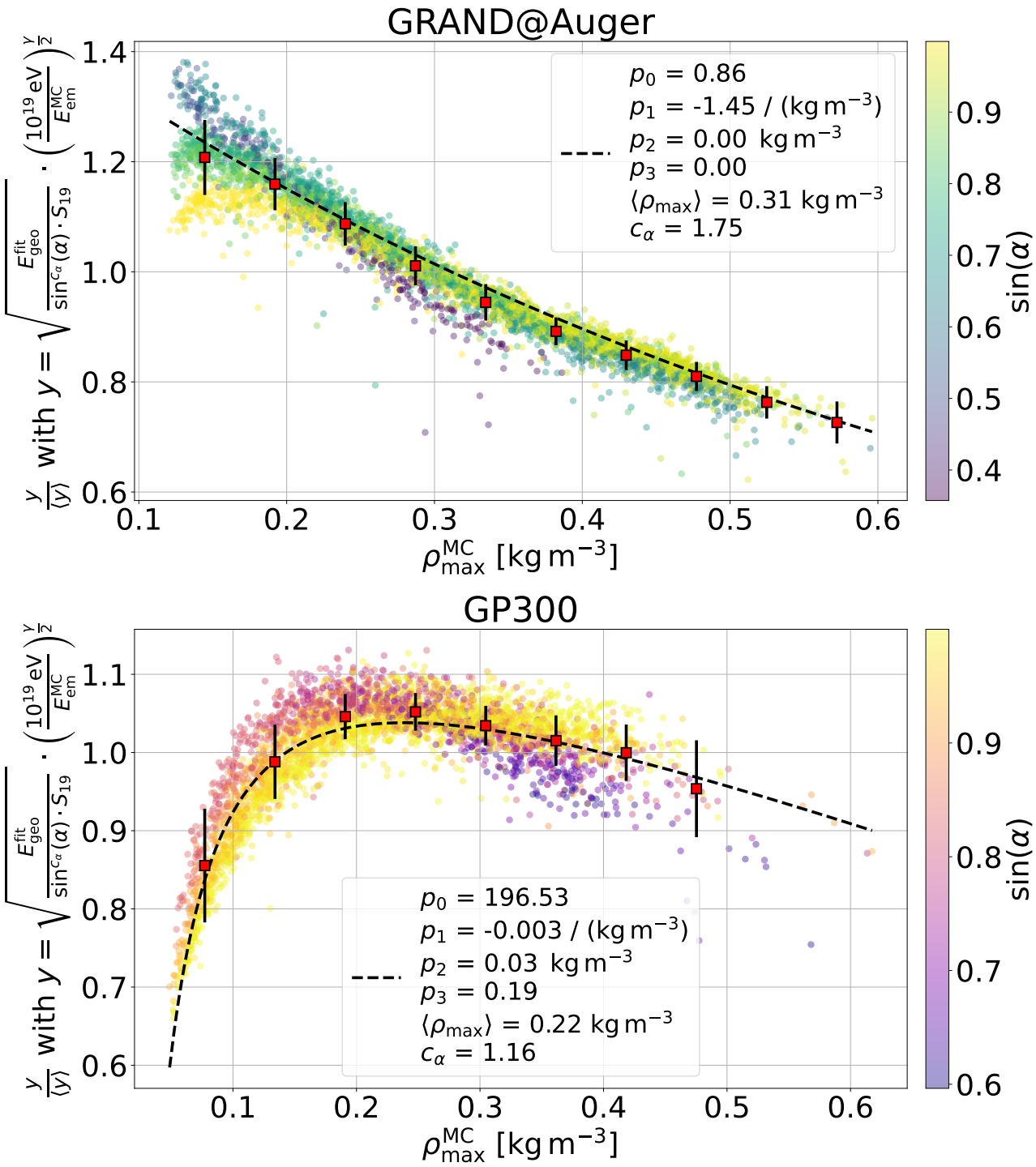

FIGURE 5.8: Behaviour of the fitted density correction for the calculation of S_{geo} as a function of the density at shower maximum ρ_{max}^{MC}. The colour maps show the dependence on the geomagnetic angle α. The black dashed lines represent the best fit of the density correction function. Notably, it is not directly fitted to the data points, but rather in the combined fit. The red points and black error bars show the means and standard deviations of the data, respectively. **Top:** GRAND@Auger. **Bottom:** GP300.

TABLE 5.2: Average air density $\langle\rho\rangle$ and values for parameters S_{19} (in GeV), γ, p_0, p_1 (in $\mathrm{kg}^{-1}\mathrm{m}^3$), p_2 (in $\mathrm{kg\,m}^{-3}$), p_3, and c_α for both GRAND@Auger (G@A) and GP300.

Site	$\langle\rho\rangle$	S_{19}	γ	p_0	p_1	p_2	p_3	c_α
G@A	0.31	5.61	1.993	0.86	-1.45	0.00	0.00	1.75
GP300	0.22	14.64	1.996	196.53	-0.003	0.03	0.19	1.16

To display the behaviour of the density correction, I arrange Eqs. (5.22) and (4.13) for y,

$$y = \sqrt{\frac{E_{\mathrm{geo}}}{\sin^{c_\alpha}(\alpha)\cdot S_{19}}}\cdot\left(\frac{10^{19}\,\mathrm{eV}}{E_{\mathrm{em}}^{\mathrm{MC}}}\right)^{\gamma/2}, \tag{5.26}$$

Figure 5.8 shows the density correction resulting from the minimisations for the 50–200 MHz frequency band for the site of GRAND@Auger (top), and the GP300 site (bottom). Displayed on each vertical axis is $y/\langle y\rangle$ for each shower: I normalise the density correction by its own mean over all showers to compensate for shower-to-shower fluctuations. For GRAND@Auger, I observe slight effects of coherence loss for large values of $\sin(\alpha)$ at low ρ_{max} (i.e., for high zenith angles). While there is a slight fall-off from the darker to the lighter points, I find no change with respect the low-frequency model ($p_2 = 0$, $p_3 = 0$, $c_\alpha = 2$) is necessary to describe the average behaviour. This is due to the weak local geomagnetic field, and the resulting minimal loss of coherence of the radio emission. Non-vanishing values for the parameters p_2 and p_3 do not have positive impact. Their function is to describe the fall-off of the density correction due to loss of coherence at low air-density. This phenomenon is barely present in Argentina. Initially, I did not use the new parameters for Argentina. However, a revision near the end of the project revealed that a slight variation of c_α leads to an improved energy resolution and a vanishing bias by decreasing the dependence of the density correction on the geomagnetic angle. This is the version of the density correction I present in Figure 5.8 and Table 5.2.

The loss of coherence is much more significant for the stronger magnetic field at the GP300 site. Starting approximately at $\rho_{\mathrm{max}} = 0.2\,\mathrm{kg/m}^{-3}$, the density correction strongly falls off, indicating loss of coherence. For the GP300 site, the new parameters describe the coherence loss fall-off well. The dependence on the geomagnetic angle is strongly mitigated by c_α. As such, I am able to describe the corrected radiation energy S_{geo} well, despite of the significant fall-off in the received signal by the antennas.

In a previous version of the density correction from Glaser et al. [98], a factor explicitly including the geomagnetic field strength is used. Upon exploring the use of a similar factor instead of modifying the exponent of $\sin(\alpha)$, I found the reconstruction performance worsens.

5.7 Significance of the clover-leaf emission pattern

In the process of this work, I briefly investigated the presence of a novel emission pattern in the $\vec{v}\times(\vec{v}\times\vec{B})$ component of the radio emission [13]. The pattern appears at high frequencies for highly inclined showers and takes a clover-leaf shape in the shower plane. For the 50–200 MHz frequency band, the pattern emerges starting at zenith angles $\sim 75^\circ$ for Argentina. For the stronger magnetic field in China, the pattern is visible from $\sim 70^\circ$ onwards. The pattern is the result of geo-synchrotron radiation emitted by the shower electrons and positrons in the geomagnetic field.

Naturally, the strength of the geo-synchrotron emission increases with the strength of the magnetic field. Additionally, it increases with decreasing air density at the shower maximum due to the longer mean free path length of particles. However, even for the most inclined showers in the strong magnetic field at the GP300 site, the intensity of this novel emission component is orders of magnitude lower than that of the charge-excess component, which itself only makes up $< 1\%$ of the emission for these showers. As such, the presence of the clover-leaf pattern is negligible for the effective description of the geomagnetic emission with the signal model.

Chapter 6

Energy Reconstruction Performance

In this chapter, I progressively show more realistic benchmarks of the LDF reconstruction method to reflect the development of my work on this project. I introduce the additional simulation libraries I create for this purpose in Section 6.1. I discuss the quality cuts I apply to the reconstructed events before considering them for the performance studies in Section 6.2. In Section 6.3, I show the intrinsic performance, i.e., the performance on the RdStar and GRAND star-shape simulation libraries, that I also used to tune the model parameters. In Section 6.4, a sparse antenna layout serves as the first step towards realism. Here, I still use "true" information—information either from the simulation input or output—for the reconstruction. This includes the arrival direction (zenith and azimuth angles), the particle shower core, and the depth of shower maximum X_{max}. In Section 6.5, I add artificial noise to the electric-field traces from CoREAS as the next step. In Section. 6.6, while using the same traces, I reconstruct all shower parameters necessary for reconstruction only from the input that would be available from real measurements. Here, I use an average value for X_{max}, estimate a core position using the antenna positions, and reconstruct the arrival direction from pulse timing information. Finally, in Section 6.7, I simulate fully realistic measurement conditions by applying the GRAND detector simulation. I add real noise, measured by GP300, to the traces at the Analogue-to-Digital Converter (ADC) level and, from there, reconstruct the electric-field traces, the energy fluence and, finally, the electromagnetic energy. Any information on data processing and LDF input parameters relevant for a specific analysis, I discuss in the corresponding section.

Additionally, in Section 6.8, I investigate whether the energy reconstruction shows any bias with respect to the cosmic-ray primary particle that induced the air-shower.

6.1 Simulation libraries

I create two new simulation libraries to test and benchmark my reconstruction method on. Once more, I use CORSIKA and CoREAS (see Section 2.3.2) to simulate the air-showers. The libraries simulate two different detector arrays with realistic, sparse layouts. Figure 6.1 displays the layouts of the two arrays. The left panels shows the final planned layout of GRANDProto300, the right panel a possible configuration of a GRAND10k array. For the star-shape libraries, I generated the idealised star-shaped layout for each shower geometry individually. In contrast, for these simulations of sparse arrays, I randomly pick the shower core for any event within a pre-defined area on the array. I show the area containing the possible core positions for each layout with dashed outlines in the corresponding panel. For GP300,

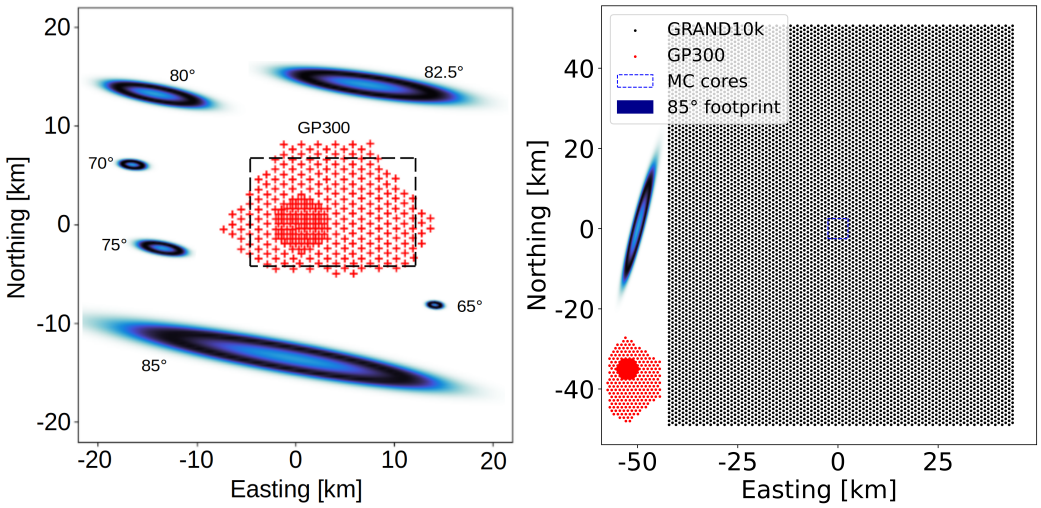

FIGURE 6.1: Sparse antenna layouts for which I generate two simulation libraries. Red crosses and black points indicate detections unit (DU) positions in both panels. The areas marked by dashed lines show the possible range of randomly generated shower core positions for any air-shower. The GRANDProto300 array has an in-fill consisting of 90 antennas. Terrain elevation is not shown. **Left:** Planned layout of GRANDProto300 array on the Xiaodushang plateau near Dunhuang, China with radio footprints of showers with zenith angles between 65 and 85° as a scale comparison. **Right:** Possible layout of a GRAND10k array with GP300 (red) and the footprint of an 85° air-shower (blue contour) for scale.

∼90% of the randomly generated shower cores are contained in the array area. For GRAND10k, 100% of simulated showers have a contained core.

To keep the computational cost of each simulation reasonable, I do not simulate the antenna positions of the entire array for every air-shower. This is especially significant for simulations of GRAND10k. Using the observation altitude, pre-determined arrival direction, local atmospheric profile, and an average $X_{\max}^{\text{avg}} = 750\,\text{g/cm}^2$, I estimate the Cherenkov radius r_0 in the shower plane with Eq. (2.5). I take a circular area with radius $r_{\text{sim}} = 5\,r_0$ in the shower plane, and project it to the ground plane. This matches the range of axis distances covered by the star-shape layouts for the idealised simulations. I simulate the electric field only for the antennas within this area. In the presence of noise, I discard most antennas further than two Cherenkov radii away from the radio core using quality criteria.

Strongly inclined showers with large footprints are likely to have boundary issues for GP300. This means that parts of the footprint, or even the shower core itself, might not fall in an area instrumented with antennas. For GRAND10k, I choose a small shower core area relative to the total size of the array. This effectively eliminates boundary issues entirely since the radio footprint is completely contained in the array for any shower geometry. The reason is that, in reality, due to the large size of the array, only a small fraction of detected showers will have boundary issues. In Figure 6.1, I illustrate this with the, comparatively, small radio footprint of an 85° shower next to the GRAND10k array.

I present the shower parameters with which I generated the air-shower simulations for both libraries in Table 6.1. For GRAND10k, I simulate 5891 events. The GP300 library contains 14,934 simulated events in total. I limit the study on reconstruction performance in this chapter to only showers with zenith angle up to 85°. I find the LDF fit to perform unreliably for showers with larger zenith angles. This

TABLE 6.1: Shower parameters of simulated events in the GP300 and GRAND10k simulation libraries. Boundaries of the area where the shower core can randomly fall, as well as zenith angle ranges are given separately for the two experiments. All other parameters are identical for both libraries.

Parameter	**Value(s)**
Shower core (GP300)	([-5.2, 11.3], [-4.4, 6.5]) km
Shower core (10k)	([-2.5, 2.5], [-2.5, 2.5]) km
Zenith angle (GP300)	$[65, 88]^\circ$
Zenith angle (10k)	$[65, 85]^\circ$
Azimuth angle	$[0, 360]^\circ$
Primary energy	$[10^{17}, 10^{20}]$ eV
Primary particle	50% p & 50% Fe
Observation altitude	1265.54 m
Atmospheric model	Dunhuang
Hadronic model	SIBYLL-2.3d
Thinning level	10^{-6}

leaves 12,995 events in the GP300 library for the performance study. I use the "Dunhuang" atmosphere both for the generation of the simulation libraries as well as for the signal model I apply to the simulated events.

The output from simulations using CORSIKA and CoREAS is, among other things, the electric-field vectors as a function of time at each antenna position. CoREAS determines the vectors for a configurable time window with a binning of 0.5 ns around the radio pulse of the simulated air-shower. For the simulations I created for this work, this time window is $t_{\text{sim}} = 1.2^{-}$s. This is what we commonly call the "time traces" of the electric field or "electric field traces". Other significant outputs of the simulation include the longitudinal profile of the air-shower, and the time at which the radio signal arrived at each antenna position.

Depending on the level of realism, I process the output of the CoREAS simulations in my simulation libraries in different ways. At minimum, this means determining the depth of maximum from the CORSIKA longitudinal profile and filtering the broadband electric-field traces from CoREAS to the desired frequency band. For the highest level of realism, replicating measurement conditions, I propagate the electric-field traces through the GRAND detector simulation to generate Analog-to-Digital Converter (ADC) traces and add measured noise in the same format. Then, I reconstruct all necessary parameters from the resulting ADC traces, the antenna positions, and the timing information.

Using the ADC traces introduces the concept of saturation effects during analogue-to-digital conversion. A measurement is saturated if the received signal is so strong that the maximum number of ADC counts per time sample is reached. In principle, the signal at that point in time can exceed this threshold, however, the measured ADC trace cannot reflect that. In the case of the GP300 DUs, a measurement saturates if the ADC count per time sample reaches $n_{\text{max}}^{\text{ADC}} = 8192$. Naturally, such measurements do not reflect the signal strength reality. In my work, I flag saturated ADC traces and I do not consider the affected antennas for the LDF fit. However, I still process the affected antennas to include them when plotting an event. From here on, I call the antennas affected by saturated ADC traces "saturated detection units" or "saturated antennas".

In the following sections, I detail the quality cuts, processing steps, and input

TABLE 6.2: Quality cuts for the reconstruction performance studies on GP300 simulations. On the left are short-hands for the quality cuts I describe in Section 6.2. Percentages are always relative to the total number of events. The bold column headers label the analysis the cuts apply to. From left to right, they stand for the analyses without noise (Section 6.4), with added artificial noise (Section 6.5), no true parameters (Section 6.6), and under realistic measurement conditions (Section 6.7). Variations in the total number of events between the columns result from failed arrival direction reconstructions due to $n_{\text{ant}} < 3$.

GP300	**No noise**	**Artif. noise**	**Rec. Params.**	**Real. conditions**
Total	**12,995**	**12,995**	**12,986**	**12,804**
MC X_{max}	12,995 (100%)	12,995 (100%)	12,986 (100%)	12,804 (100%)
$\sigma_{\text{dir}} < 0.5°$	—	—	12,982 (99.9%)	12,657 (98.9%)
$n_{\text{ant}} \geq 5$	12,948 (99.6%)	10,385 (79.9%)	10,385 (80.0%)	9270 (72.4%)
LDF success	12,948 (99.6%)	10,385 (79.9%)	10,385 (80.0%)	9270 (72.4%)
Valid errors	12,948 (99.6%)	10,385 (79.9%)	10,214 (78.7%)	9191 (71.8%)
$n_{r<r_0} > 0$	11,340 (87.3%)	9496 (73.1%)	9359 (72.1%)	7048 (55.1%)
$\sigma_{d_{\text{max}}}$	11,336 (87.2%)	8806 (67.7%)	7549 (58.1%)	6215 (48.5%)
$\sigma_{E_{\text{geo}}}$	11,331 (87.2%)	8782 (67.6%)	7347 (56.6%)	6100 (47.6%)

parameters for each analysis, as well as the results of each performance study. Figure 6.2 shows all possible "paths" of data processing in a single diagram.

6.2 LDF fit quality cuts

I apply a number of signal quality criteria to the individual antennas of simulated events based on their ADC and electric-field traces, as well as the pulse timing before passing them to the LDF fit. Since these criteria vary based on how I process the simulations in each step, I discuss them in the corresponding section. I apply additional quality cuts to the fitted events before considering them for the studies of reconstruction performance. In this section, I discuss the quality cuts in the order I apply them in. I display the results of the quality cuts on both simulation libraries, and all relevant versions of the performance study in Tables 6.2 and 6.3.

The atmospheric depth of the primary interaction of the air-shower is determined randomly in CORSIKA. Consequently, showers that develop extraordinarily early and in extremely low-air density are possible. Such showers have a very shallow X_{max} and do not reflect the average air-shower behaviour at ground level. I exclude all showers with $X^{\text{MC}}_{\text{max}} < 200\,\text{g/cm}^2$ from the analysis to retain consistency. However, this happens rarely. Only a single one of the idealised simulations for GRAND@Auger is affected. I list the cut in the tables for completeness.

For the versions of the analysis where I reconstruct the arrival direction, I apply a quality cut on the uncertainty of the reconstructed direction σ_{dir}. As I discuss in Section 6.5, this is an uncertainty on the plane wave front used to reconstruct the arrival direction, and not on the arrival direction itself. I discard any events with $\sigma_{\text{dir}} > 0.5°$.

I consider the antenna multiplicity in the next step. As I discussed in Chapters 4 and 5, the LDF fit requires at least five signal antennas for the function to be stable and to reliably reconstruct the electromagnetic energy. Here, I filter out all events that, after the signal quality criteria I apply to the antennas, have fewer than five signal antennas. This affects events with low zenith angles since they have a small footprint and might not illuminate enough antennas. Low energy events with a lot

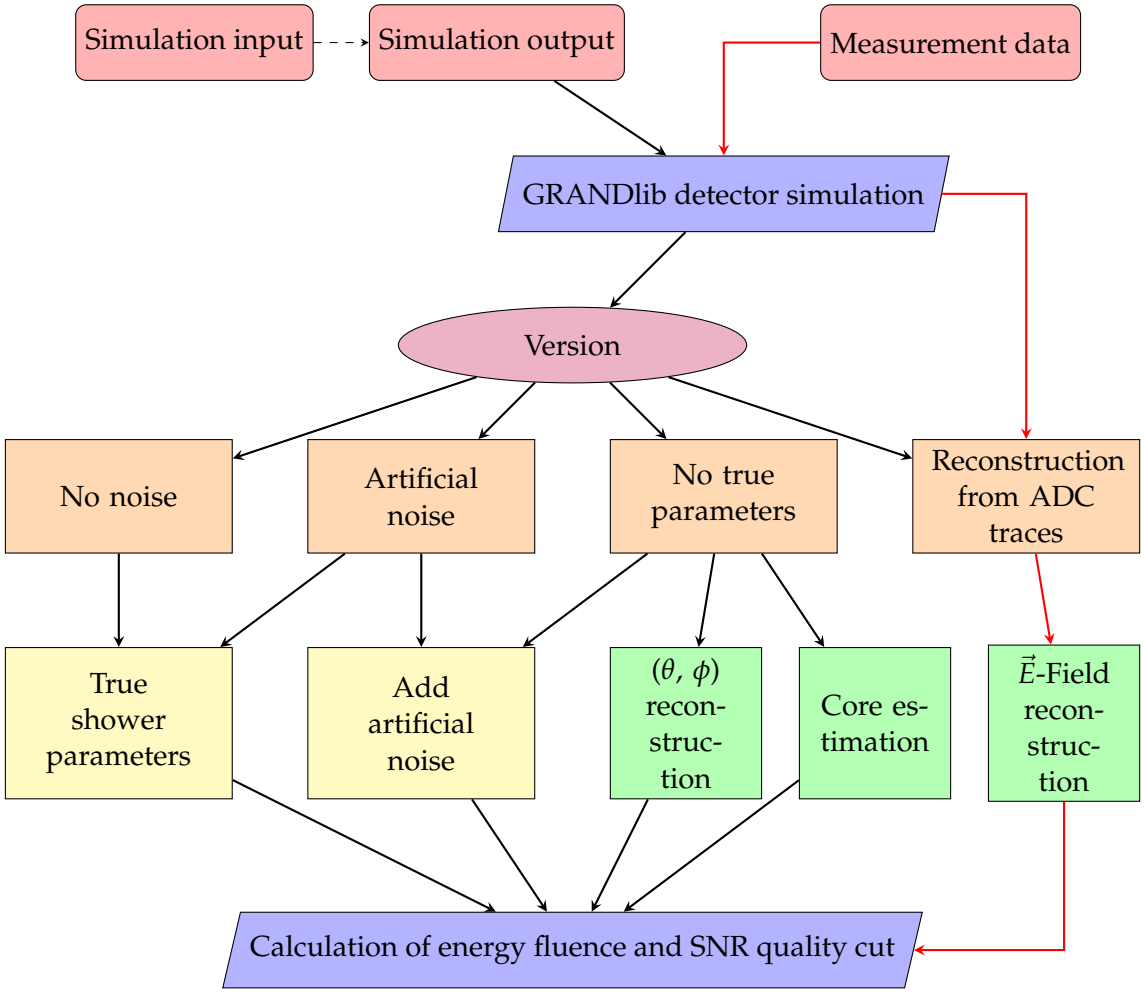

FIGURE 6.2: Data processing diagram for both simulation and measurement data. Black arrows annotate processing of air-shower simulation data. Red arrows represent the path viable for real measurements. The red row on top refers to the two different kinds of input data for the LDF fit. The next row represents the data processing with GRANDlib, including the bandpass filter, unified trace timing, addition of artificial noise, and the detector simulation. The orange boxes, from left to right, correspond to the four analyses in Sections 6.4, 6.5, 6.6, and 6.7. In the row above, I make the decision on which data to draw for the analysis. Naturally, measurements automatically proceed to the realistic version. Yellow boxes give context for the processes performed by GRANDlib for each analysis. Green boxes show reconstruction processes. In the last line, I use the processed data to calculate the energy fluence. Afterwards, I pass all shower parameters to the LDF fit. From then on, I handle any input identically.

TABLE 6.3: Quality cuts for the reconstruction performance studies on GRAND10k simulations. On the left are short-hands for the quality cuts I describe in Section 6.2. Percentages are always relative to the total number of events. The bold column headers label the analysis the cuts apply to. From left to right, they stand for the analyses without noise (Section 6.4), with added artificial noise (Section 6.5), no true parameters (Section 6.6), and under realistic measurement conditions (Section 6.7). Variations in the total number of events between the columns result from failed arrival direction reconstructions due to $n_{\text{ant}} < 3$.

GRAND10k	**No noise**	**Artif. noise**	**Rec. Params.**	**Real. conditions**
Total	**5991**	**5991**	**5991**	**5861**
MC X_{max}	5991 (100%)	5991 (100%)	5991 (100%)	5861 (100%)
$\sigma_{\text{dir}} < 0.5°$	—	—	5991 (100%)	5818 (99.3%)
$n_{\text{ant}} \geq 5$	5991 (100%)	4826 (80.6%)	4826 (80.6%)	4349 (74.2%)
LDF success	5991 (100%)	4826 (80.6%)	4826 (80.6%)	4349 (74.2%)
Valid errors	5991 (100%)	4826 (80.6%)	4821 (80.5%)	4320 (73.7%)
$n_{r<r_0} > 0$	5271 (88.0%)	4355 (72.7%)	4348 (72.6%)	3276 (55.9%)
$\sigma_{d_{\text{max}}}$	5271 (88.0%)	4047 (67.6%)	3954 (66.0%)	2941 (50.2%)
$\sigma_{E_{\text{geo}}}$	5271 (88.0%)	4031 (67.3%)	3909 (65.3%)	2875 (49.1%)

of stations rejected due to noise are also affected. High energy events at low zenith angles with few antennas and too many antennas flagged for saturated traces are also removed. Effectively, this cut leaves all events that I pass to the LDF fit.

Subsequently, I eliminate all events for which the LDF fit fails to converge. First, I discard any events for which the LDF fit does not converge. Secondly, I also discard the events that do converge, but do not return errors for at least one of the fit parameters. Naturally, this quality cut shows for which fraction of the events the LDF fit converges and removes any unlikely outliers from results.

For all fitted events, I require there to be at least one signal antenna located at distance $r < r_0$ from the radio symmetry centre. r_0 is the LDF shape parameter corresponding to the radius of the Cherenkov ring. Without an antenna inside the ring to constrain the amplitude of the LDF peak, the fit struggles to reconstruct the electromagnetic energy correctly. As a result, I remove most events that have a radio footprint not contained in the array. This cut also filters out high-energy events for which all antennas inside the Cherenkov ring, i.e. the region where the emission has high intensity, are affected by saturation effects.

I apply two more criteria on the quality of the LDF fit results. This concerns the two main fit parameters, the geomagnetic radiation energy E_{geo}, and the distance to shower maximum d_{max}. I discard any events with relative errors either < 0.001 or > 0.3 for either of the parameters. Mainly, this deals with outliers due to bad fits. In addition, I remove any fits with unreasonably small errors.

These quality cuts I also apply to the star-shape simulations for intrinsic reconstruction analysis. However, due to their idealised nature, no events are affected.

Saturated measurements

Saturation effects during analogue-to-digital conversion only affect the analysis under realistic measurement conditions. I attempted two methods to handle the events that include saturated DUs. On the one hand, the approach to discard all events with any saturated DUs works well, but removes a large number of events. On the other hand, the quality cut regarding at least one antenna within the Cherenkov radius discards most events with saturated DUs that reconstruct badly. I do not consider the

saturated DUs in the LDF fit in any version. For the analysis I show in Section 6.1, I choose the second option. This leads to higher statistics overall, but slightly worsens the reconstruction performance at the highest energies.

6.3 Intrinsic reconstruction performance

As a first evaluation, I investigate how the energy reconstruction performs intrinsically. For this analysis of the reconstruction performance and every other iteration I show in this chapter, I fix all shape parameters of the LDF to their $d_{\max}$ parametrisation. I apply the reconstruction to the idealised star-shape simulation libraries (see Section 5.1) which I use to characterise both the signal model and the LDF parametrisation in Chapter 5. For these simulation libraries, I calculate the energy fluence directly from the simulated electric-field traces. For these purposes, I use a functionality of the HDF5 converter provided with CORSIKA. Since the traces are initially simulated for a broad frequency band, I apply an idealised rectangle bandpass filter for the 50–200 MHz frequency band. I use the zenith and azimuth angle as well as the local geomagnetic field vector to rotate the traces from NWU coordinates to the shower plane coordinate system. Then, I take the Hilbert envelope of all three components of the trace. The maximum of the quadratic sum of all three envelope components and its timing indicate the amplitude and time of the radio pulse. I define, symmetrically around the pulse time, a signal window lasting from t_1 to t_2 with a length of 100 ns. Given this window for the electric field trace $\vec{E}$ of an antenna, the energy fluence f from the radio emission at the position of the antenna follows from

$$f = \epsilon_0 c \cdot \int_{t_1}^{t_2} |\vec{E}|^2 \, \mathrm{d}t. \tag{6.1}$$

Here, ϵ_0 is the vacuum permittivity and c the speed of light. The time sampling interval between data points is 2 ns across all analyses. I calculate the energy fluence I use for the characterisation of the signal model identically as I do for this analysis. In both cases, I assign uncertainties to the energy fluence of each antenna according to Eq. (5.6).

All other shower parameters I use in this analysis are directly from the simulation in- or output. I use the true shower geometry to construct the shower plane coordinate system. I take the true shower core, including its predicted refractive displacement, as the radio core start value for the LDF fit. As long as I use the true azimuth and core, I limit the core fit along the shower direction to prevent shifts to the side. Along that axis, I let it vary by up to 1500 m. The true $X_{\max}$ serves to calculate the start value of $d_{\max}$ which is now a free parameter. I also use $X_{\max}$ and $d_{\max}$ to calculate the true density at the shower maximum $\rho_{\max}$. This true value I later use in the density correction as well. The start value for the geomagnetic radiation energy E_{geo} I estimate roughly with the true primary energy.

Figure 6.3 shows the intrinsic performance for the RdStar and GRAND star-shape libraries, respectively. For the RdStar library, I discarded the 240 events with geomagnetic angle $\alpha < 20^\circ$, leaving 4069 events. The reconstruction shows excellent agreement with the true energy for both libraries. For both libraries and across all energies, the resolution is stable around 3% with negligible biases. With respect to the zenith angle, the resolution decreases to 5% for the largest angles. The bias fluctuates, but still remains around $\pm 1\%$. This indicates that the accuracy of the model starts to degrade at the highest zenith angles. I investigated using the fitted $d_{\max}^{\mathrm{fit}}$ to

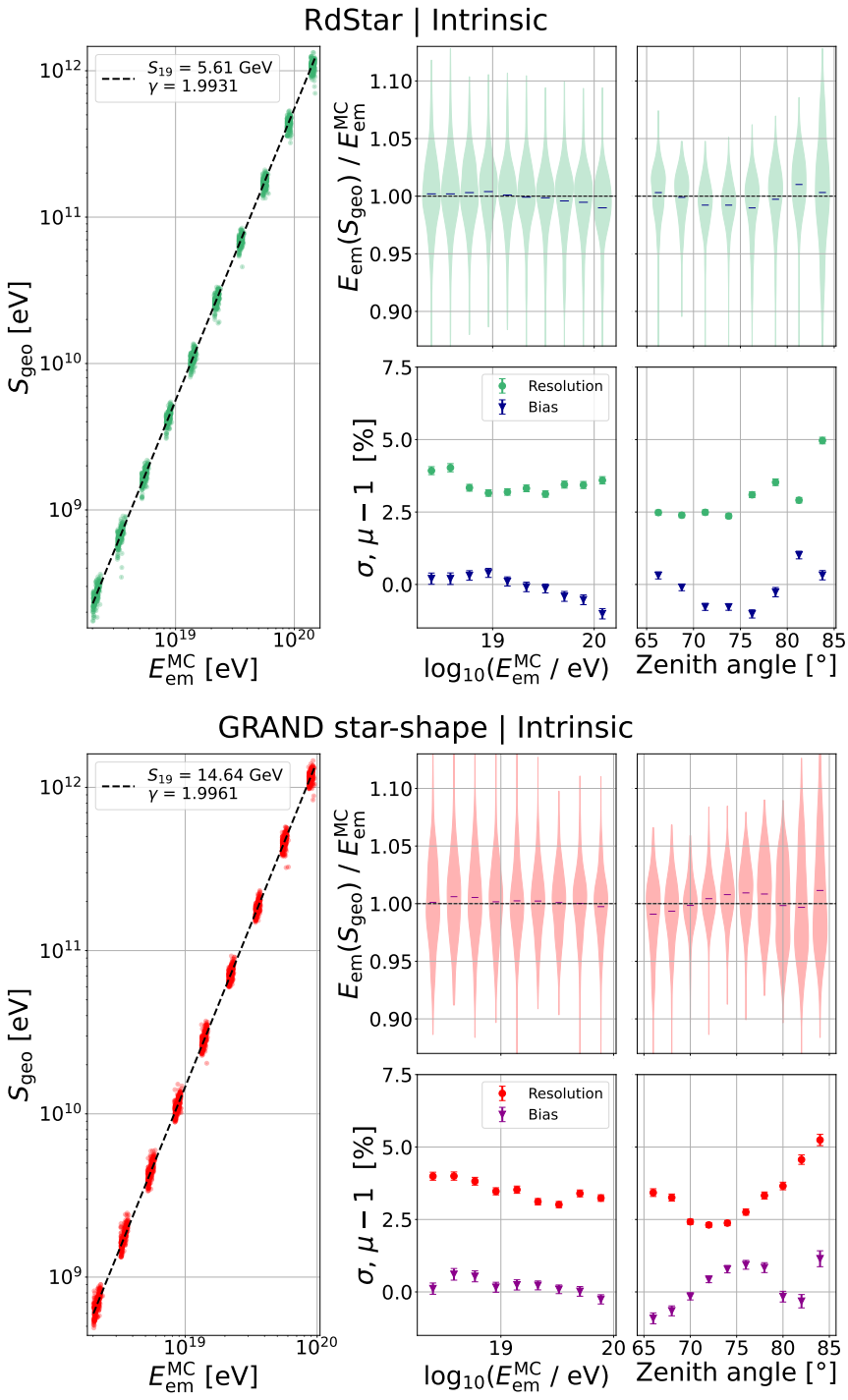

FIGURE 6.3: Intrinsic reconstruction performance of the electromagnetic shower energy $E_{\rm em}$ with the LDF fit method on idealised star-shape simulations from the RdStar and GRAND star-shape libraries. **Left plots:** Correlation between reconstructed corrected radiation energy $S_{\rm geo}$ and the true electromagnetic energy $E_{\rm em}^{\rm MC}$. I draw the $S_{\rm geo}$ points with their error bars. The dotted black line is the power-law correlation I fitted in Chapter 5. **Right plots:** The top row displays the deviation of the reconstructed $E_{\rm em}(S_{\rm geo})$ from the true $E_{\rm em}^{\rm MC}$ as violin plots. The bottom row shows the resolution and bias of the reconstruction with error bars. The left column shows these quantities as functions of $E_{\rm em}^{\rm MC}$ in log-scale, and the right column as functions of the zenith angle θ. **Top:** 4069 RdStar events in green. **Bottom:** 3667 GRAND star-shape events in red.

update $\rho_{\max}$ for the calculation of S_{geo}. However, using the true value lead to a better reconstruction performance which I show in the figure.

6.4 Sparse antenna grid without noise

For this first step towards realism, the only differences with respect to the study of the intrinsic performance are the antenna layout and the observation altitude. I use the GP300 and GRAND10k simulation libraries I created for the specific array layouts, and described in Section 6.1. For visual clarity, I consistently show results for GP300 in blue, and results for GRAND10k in violet from this point on.

Instead of the 240 antennas, which compose a star-shaped layout, the simulated antenna positions are those of the sparse layouts of GP300 and GRAND10k (see Figure 6.1). From this analysis onwards, I process the simulation output from CORSIKA and CoREAS with the GRANDlib software [79] by the GRAND collaboration instead of the HDF5 converter provided with CORSIKA 7. For all results I present in this thesis, I have used the "dev" branch of the GRANDlib github repository[1]. For the analysis I describe in this section, GRANDlib only applies the idealised rectangle bandpass filter. As in the previous, section, I calculate the energy fluence directly from the electric-field traces, filtered to the 50–200 MHz band. There is no noise present in the traces. As such, I again assign errors to the energy fluence according to Eq. (5.6). Shower parameters are from the simulation in- and output. I handle the input parameters identically to the previous section.

The simulation output from CORSIKA includes the value of $X_{\max}$. This value is known to be unreliable for air-showers with zenith angles larger than 80° [9]. The HDF5 converter provided with CORSIKA corrects this error by recalculating $X_{\max}$ from the longitudinal profile. GRANDlib, however, relies on the value from the CORSIKA simulation output. As such, the analyses I describe in this section and in Section 6.5 are affected by this inaccuracy since they use GRANDlib and true shower information. I discuss the impact of this effect on the reconstructions in Section 9.3. However, since I do not use true shower information in Sections 6.6 and 6.7, these analyses are not affected. The intrinsic reconstruction performance is not affected either since it uses the HDF5 converter

Figures 6.4 and 6.5 each show a specifically chosen example of the LDF fit for the GP300 and GRAND10k library, respectively. I show these specific events for each analysis in this chapter. Additionally, I use them as a case study for optimising the LDF fit by considering the number of shape parameters fixed to their $d_{\max}$ parametrisations. However, note that, for a wider analysis with many events, one should commit to a single configuration of the LDF fit for the sake of consistency.

Figure 6.4 shows an example LDF fit to a simulated GP300 event. I choose the example event based on the type of cosmic rays GP300 is designed to detect. The simulated cosmic-ray air-shower has primary energy $E_{\text{CR}} \approx 10^{18}\,\text{eV} = 1\,\text{EeV}$, and zenith angle $\theta^{\text{MC}} \approx 70°$. This lies in the energy range GP300 expects to probe. The zenith angle corresponds to the most common zenith angles of the measured event candidates by GP300 (see Section 7.3). Here, I consider all 26 simulated antennas (called detection units or DUs in the figure) in the LDF fit, even in the far tail of the lateral distribution. The uncertainty model assigns large errors to the DUs far away from the shower axis. Due to the considerable number of data points, I left r_0, which controls the position of the peak, as a free fit parameter. Any additional shape

[1] https://github.com/grand-mother/grand/tree/dev
CommitID: 51d2bd03c3d3d25734c744a8ad2b53a8a82a5846 from August 7, 2025.

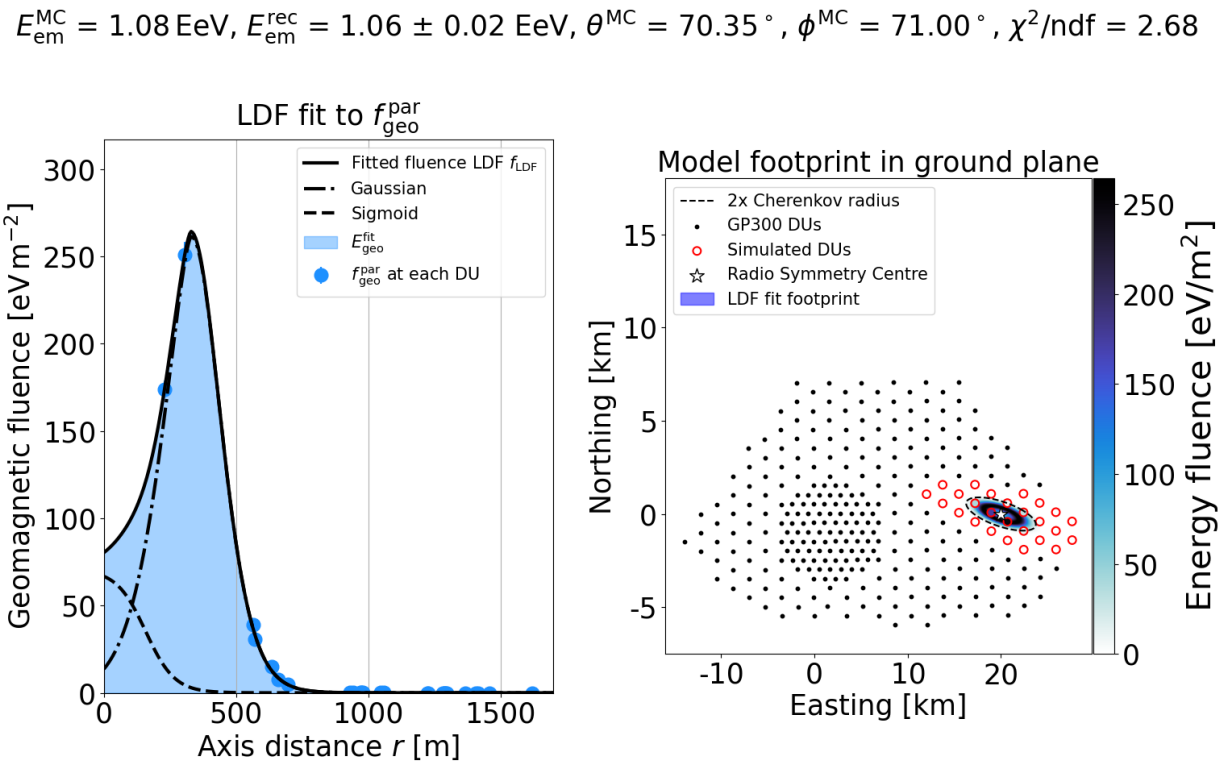

FIGURE 6.4: LDF fit result of the chosen GP300 simulation without noise. The event has 26 simulated DUs in total. Above the panels, I display the true electromagnetic shower energy E_{em}^{MC}, the reconstructed value E_{em}^{rec}, the true zenith θ^{MC} and azimuth ϕ^{MC} angles, and the goodness of fit. I display the best fit with r_0 as a free fit parameter. **Left:** LDF fit (black solid line) to f_{geo}^{par} (blue points). **Right:** Top-down view of the GP300 array (black points) with the simulated DUs for this event highlighted as larger coloured points with red borders. The colour map shows the LDF fit footprint and the fluence corresponding the DUs. The matching colours indicate agreement, as shown in the left panel.

parameters as free fit parameters lead to a worse fit. This marginally improved the energy reconstruction in this case by allowing the peak to freely adapt to the DU positions.

Figure 6.5 shows a simulated event for GRAND10k. Here, I choose the example event to show the capabilities of the large detection area of the array. I choose an event with a high primary energy $E_{CR} > 10^{19}$ eV and $\theta^{MC} \approx 85°$. Due to its large detection area, GRAND10k will commonly measure such energetic events with a fully contained radio footprint. The northern and southern array edges are visible in the right panel. Even the full area of all 752 simulated DU positions, up to five Cherenkov radii from the true shower core, is still fully contained in the array area. This choice also highlights the reconstruction for large zenith angles with many signal antennas. For this example, the LDF fit with all shape parameters fixed did not match the peak of the data points well. I found that r_0 as a free fit parameter fixed this issue. Additionally, σ (width of Gaussian) and b (outer Gaussian slope) as additional free parameters have lead to further improvement of the fit. This version, with three shape parameters as free fit parameters, is reflected in the figure.

Figure 6.6 displays the overall energy reconstruction performance for this analysis. Differently from the idealised simulations, the quality cuts I discuss in Section 6.2 apply from now on. I show the quality cuts I applied to the two simulation

$E_{em}^{MC} = 64.10\,\text{EeV}, E_{em}^{rec} = 65.80 \pm 0.14\,\text{EeV}, \theta^{MC} = 84.59^\circ, \phi^{MC} = 21.06^\circ, \chi^2/\text{ndf} = 2.09$

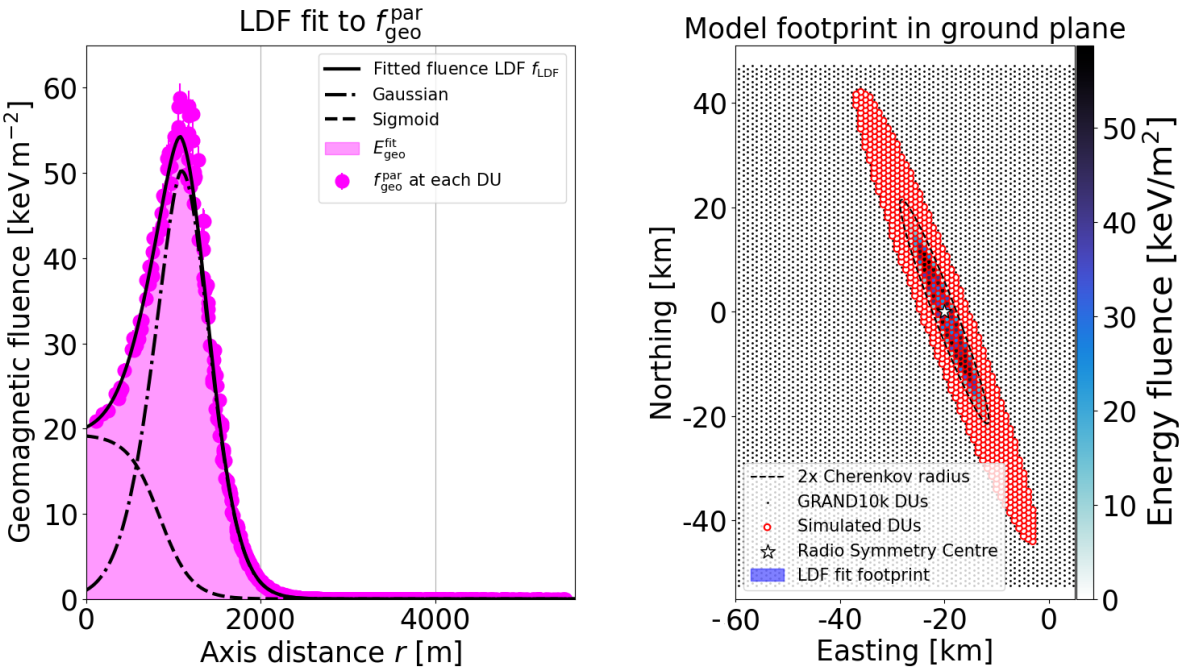

FIGURE 6.5: LDF fit result of the chosen GRAND10k simulation without noise. In total, I simulate 752 DUs for this event. Same structure as Figure 6.4. I display the best fit with r_0, σ, and b as free fit parameters. **Left:** LDF fit (black solid line) to f_{geo}^{par} (pink points). **Right:** Top-down view of the GRAND10k array (black points) with the simulated DUs for this event highlighted as larger coloured points with red borders. In this case, the footprint is only visible by the DU colours

libraries for all analyses in this chapter in Table 6.2 and 6.3, respectively. Upon using the reference energy $S_{19} = 14.64\,\text{GeV}$ which I determined in Chapter 5 for the energy reconstruction, I find a negative bias of $\sim -4\%$. This bias could partly stem from the change in observation altitude between the idealised and array simulations. However, the difference is only $\sim 100\,\text{m}$ and, as such, is unlikely to lead to a noticeable difference. A more plausible explanation is a difference in the processing of the simulated electric field traces between the CORSIKA HDF5 converter and the GRANDlib software, resulting in a systematic shift of the calculated energy fluence values. However, since I use GRANDlib from this point on, I remove the bias by adjusting the reference energy S_{19}. I find the adjusted reference energy $S_{19} = 13.49\,\text{GeV}$ by repeating the joint fit of Eqs. (4.13) and (5.22) with only S_{19} as a free parameter. For this purpose, I use the GRAND10k simulation library since the radio footprint of every simulated showers is contained within the array area.

The reconstruction shows worse energy resolution for events at low energies. The cause for this is likely the low energy fluence values at antennas of low energy events. I determine the parametrisation of the charge-excess fraction only with simulations with primary energies down to $10^{18.4}\,\text{eV}$. The energies in the simulation libraries for GP300 and GRAND10k range between 10^{17} and $10^{20}\,\text{eV}$. As I discuss in Section 5.2, the calculation of the geomagnetic energy fluence using the charge excess parametrisation shows a small negative bias for fluence values $< 10\,\text{eV/m}^2$, or large axis distances. While there is no statistically relevant data for even lower fluence values, I do not expect this bias to improve. As such, the low fluence values

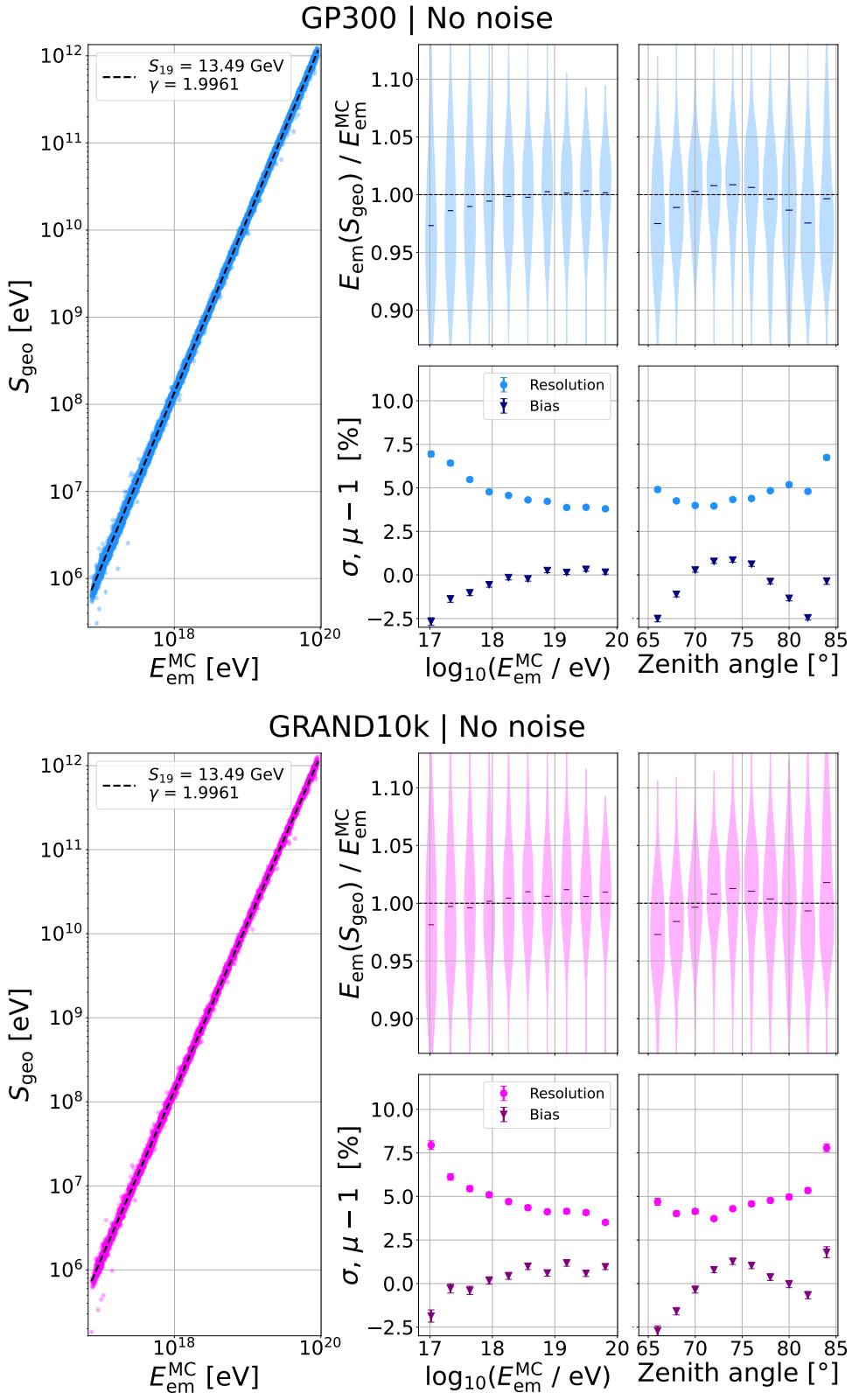

FIGURE 6.6: Reconstruction performance of the electromagnetic shower energy E_{em} without noise for GP300 and GRAND10k simulation libraries (see Figure 6.1). I determine the new value for the reference energy $S_{19} = 13.49\,\text{GeV}$ with the GRAND10k library. See caption of Figure 6.3 for a detailed description of the panels.

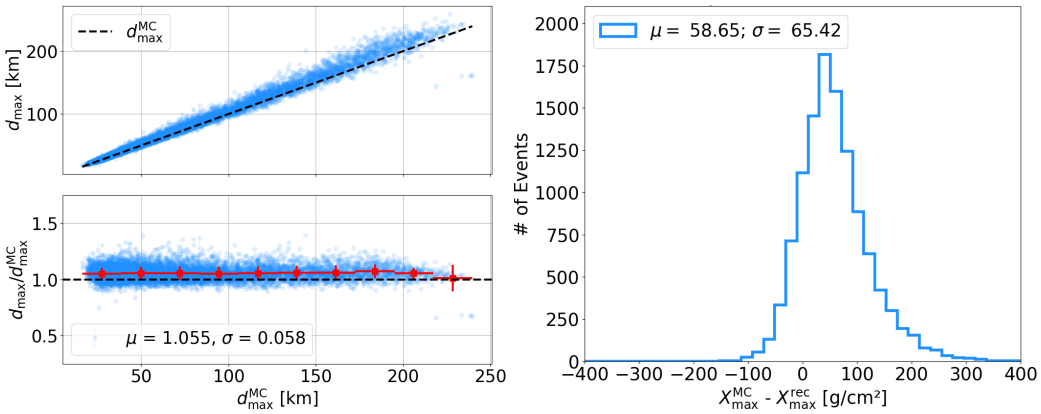

FIGURE 6.7: Evaluation of distance to shower maximum d_{max} determined in the LDF fit, and the corresponding X_{max}^{rec} for the analysis without noise. **Upper left:** Fitted d_{max} shown against true value with the true d_{max}^{MC} also displayed as the black dashed line. **Lower left:** Relative deviation of the fitted d_{max} from the true value. Red points, vertical, and horizontal error bars show the mean, standard deviations, and bin widths of the binned data, respectively. The mean of the blue points μ corresponds to the bias, and the standard deviations σ to the resolution. **Right:** Distribution of deviation of the corresponding X_{max}^{rec} from the true X_{max}^{MC}.

of low energy events are likely affected by this bias. However, such small fluence values are not likely to be relevant under realistic conditions since antennas with such low signal amplitude are often dominated by background noise. The energy resolution gradually improves to $\sim$ 3% with rising energy, matching the intrinsic resolution. For high zenith angles, I observe a slight degradation of the energy resolution, analogously to the intrinsic analysis. In this iteration of the analysis, there is little difference between the two array layouts.

In addition to the reconstructed energy, I also evaluate the distance to the shower maximum d_{max} determined with the LDF fit. The fact that I determine d_{max} also suggests the possibility of the reconstruction of X_{max}. Figure 6.7 shows in its left panel the accuracy of the fitted d_{max} with respect to the true value d_{max}^{MC}, as well as the deviation of the corresponding reconstructed X_{max}^{rec} from the true X_{max}^{MC}. I calculate X_{max}^{rec} from the fitted d_{max} with `radiotools` using the true zenith angle, observation altitude, and atmospheric profile. For either quantity, there is no significant difference between the two libraries. As such, I show only the results for the GP300 library here due to its higher number of events. For simulations without noise, the LDF fit determines d_{max} with a resolution of 5.8%. It has a positive bias of 5.5%. For GRAND10k, the resolution is 5.7% with a 6% bias. A possible cause for the d_{max} bias is the difference in observation altitude between the GRAND star-shape, and the GP300 and GRAND10k simulation libraries. The signal model parametrisations for the charge-excess fraction and the LDF shape parameters explicitly depend on d_{max}. Differences in observation altitude, naturally, translate to different values of d_{max}. The magnitude of the difference depends on the zenith angle. However, since the difference in observation altitude is small at $\sim$ 100 m, I expect this effect to only minor. As such, there might be other explanations for this bias. The corresponding X_{max} reconstruction has a resolution of 65.42 g/cm^2 with a large 58.65 g/cm^2 bias. This happens since small relative variations in d_{max} lead to large absolute changes in X_{max}. Consequently, even without the presence of noise, the X_{max} reconstruction is not accurate enough to be of practical use.

6.5 Sparse antenna grid with artificial noise

In this iteration of the analysis, I add artificial noise to the electric field traces of the simulations of GP300 and GRAND10k. For this purpose, I use an additional functionality of the GRANDlib software. To simulate the constant radio noise from the Galaxy, I use artificial Gaussian noise. I randomly draw values from a normal distribution of values in $\mu\mathrm{Vm}^{-1}$ around zero with a standard deviation of 64 $\mu\mathrm{Vm}^{-1}$. I then add one of these drawn values to every entry of the electric-field traces. This approximately matches the noise level measured by GP300 DUs [12]. In addition, I smear the electric-field pulse amplitude by 7.5% and add a time jitter of 5 ns to simulate measurement uncertainties for the detectors. This process involves unifying the timing of the radio pulse for all traces and placing it at $t_{\mathrm{pulse}} = 800\,\mathrm{ns}$. It also sets the length of the trace to 2 μs which matches the trace length for GP300 measurements.

Now, with noise present in the electric field traces, I define a noise window from t_3 until t_4 that lasts from the beginning of the trace until shortly before the beginning of the signal window. I place the noise window before the signal window, instead of, for example, at the end of the trace, to exclude the possibility of including any remnants of the radio pulse. Accordingly, I modify Eq. (6.1) to take the background noise into a account,

$$f = \epsilon_0 c \cdot \left(\int_{t_1}^{t_2} |\vec{E}|^2 \, \mathrm{d}t - \frac{t_2 - t_1}{t_4 - t_3} \int_{t_3}^{t_4} |\vec{E}|^2 \, \mathrm{d}t \right). \tag{6.2}$$

The first term calculates the fluence in the signal window, as previously. The second term represents the fluence in the noise window. I normalise it by the length of the signal window and subtract it from the total fluence of the signal window. Under the assumption that the background noise stays consistent throughout the whole trace, this removes the background contribution from the total fluence within the signal window. Further, I introduce a quality cut on the signal-to-noise ratio (SNR),

$$\mathrm{SNR} = \frac{\hat{A}_{\mathrm{max}}}{V_{\mathrm{RMS}}}, \tag{6.3}$$

to eliminate antennas that receive an insufficiently strong signal. The maximum signal amplitude $\hat{A}_{\mathrm{max}}$ is the maximum of the Hilbert envelope of the total trace (see Section 6.3). V_{RMS} is the root-mean-square for the noise window of the same Hilbert transform, representing the average noise level. I disregard all antennas with SNR < 5 since this is also serves as the amplitude threshold for a triggered DU for GP300. This is equivalent to a 5-sigma confidence level. As such, it is a fairly high threshold, but suitable considering the pure radio nature of GRAND.

In addition, I estimate the uncertainty on the energy fluence based on the noise in the trace and the detector uncertainty. I use the same uncertainty model as employed in the Offline software [117] of the Pierre Auger Observatory. I define the total uncertainty,

$$\sigma_{\mathrm{tot}}(f) = \sqrt{\sigma^2_{\mathrm{noise}} + \sigma^2_{\mathrm{detector}} + f^2_{\mathrm{noise}}}, \tag{6.4}$$

on the energy fluence f as the sum of three contributions. I determine f in Eq. (6.1) with a subtraction of a noise fluence, calculated for a pure noise window, from the signal fluence, calculated for the signal window. Naturally, the background noise is

also present in the signal window. As such, I estimate the uncertainty

$$\sigma^2_{\text{noise}} = 4|f|\epsilon_0 c\Delta t \cdot V^2_{\text{RMS}} + 2\,(t_4 - t_3)\,(\epsilon_0 c)^2\,\Delta t \cdot V^4_{\text{RMS}} \tag{6.5}$$

resulting from this method using V_{RMS}, the length of the time window (using the same notation as in Eq. (6.1)) and the time step Δt. This equation was derived by Glaser [118]. It assumes the trace to be the superposition of the signal pulse and white noise. Additionally, it assumes the noise amplitude in each time sample to be Gaussian distributed with a vanishing mean and a standard deviation $\sigma^2 = V_{\text{RMS}}$. The second term of Eq. (6.4) represents the uncertainty introduced by a (so far hypothetical) detector. I choose an uncertainty on the detector sensitivity for measurements of the electric field $\vec{E}$ of $\sigma_{\vec{E}} = 0.075$. The motivation for this is the 7.5% amplitude smearing I applied to the simulated electric field traces. As such, the detector error yields

$$\sigma^2_{\text{detector}} = \left(2f \cdot \sigma_{\vec{E}}\right)^2. \tag{6.6}$$

The factor of 2 follows from the quadratic relation between the energy fluence and electric-field amplitude, $f \sim \hat{A}^2$.

Lastly, I also add the energy fluence calculated from the noise window f_{noise}

$$f_{\text{noise}} = \epsilon_0 c \cdot \frac{t_2 - t_1}{t_4 - t_3} \int_{t_3}^{t_4} |\vec{E}|^2 \,\mathrm{d}t \tag{6.7}$$

to the uncertainty, normalised by the length of the signal window. Here, t_1 and t_2 are the boundaries of the signal window, and t_3 and t_4 the boundaries of the noise window. While the impact of noise on the uncertainty is already addressed in the first term of Eq. (6.4), I motivate this addition by, specifically, too small uncertainties for antennas with a weak signal far away from the shower axis. This can lead to thinning artifacts influencing the LDF fit. Another reason is to avoid such low signal antennas having too strong an influence on the LDF fit. I achieve the same goal for simulations without noise with Eq. (5.6) by adding a percentage of the maximum fluence to the error. Overall, for the values I choose here, the detector uncertainty in the second term dominates the energy fluence uncertainty.

To observe purely the effects of the addition of noise and more realistic errors, I still use true information for the input of the LDF fit. This, I discussed in Section 6.3. Due to the SNR criterion on the traces, I do not consider antennas for the LDF fit with pulses not sufficiently strong in comparison with the background noise. In Figure 6.8, I show the effect of this on the example LDF fits for GP300 and GRAND10k. Antennas in the tail of the LDF are now flagged by the SNR cut. Only antennas up to about twice the Cherenkov radius remain relevant for the LDF fit. The lower panels of each plot show the fit residuals and, naturally, only the antennas considered in the fit. The GP300 event now has much fewer data points since 19 out of the 26 antennas do not have sufficient SNR. Consequently, I now fix all shape parameters to their parametrisations, including r_0, which was a free parameter in the previous section. The LDF fit for GP300 results in a too small χ^2. This happens due to the 7.5% amplitude smearing. The large uncertainties ensure that, for any outcome of the amplitude smearing, the LDF fit still describes the event well. In this case, the close fit of the LDF to the fluence points with large uncertainties leads to a too small χ^2. As a result of this, the fit underestimates the electromagnetic energy.

For the GRAND10k event, the amplitude smearing is apparent in the vertical

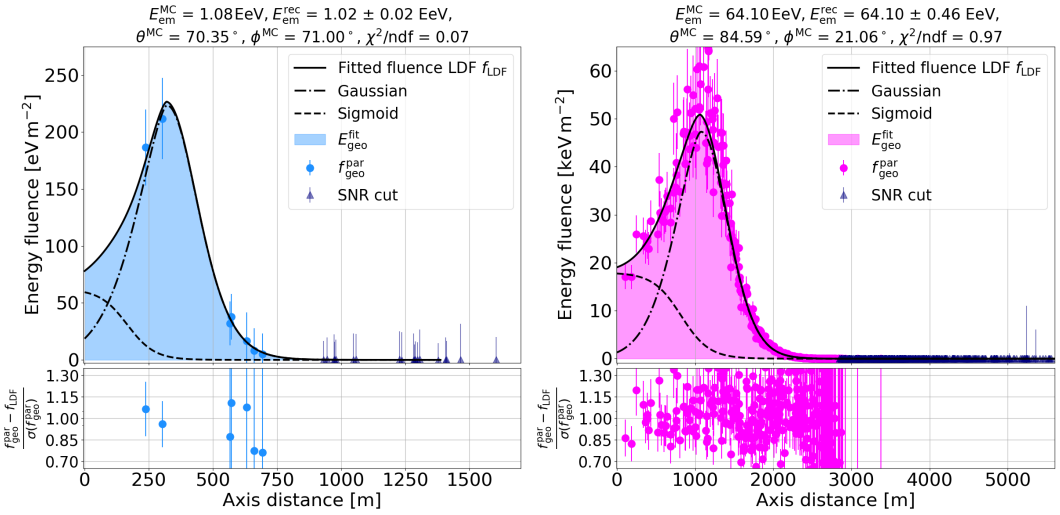

FIGURE 6.8: LDF fits of the same events I show in Figures 6.4 and 6.5, here with artificial noise added. Above each LDF are the shower parameters. The lower panels show the residuals of the LDF fit, only including the antennas considered for the fit. The triangular data points in each plot show the antennas flagged by the SNR quality criterion. **Left:** GP300 event in blue. 7/26 antenna remain viable for the fit. All shape parameters are now fixed to their d_{max} parametrisation. **Right:** GRAND10k event in pink. 327/752 antennas remain viable for the fit. r_0, σ, and b are free fit parameters. Note the keV m^{-2} scale on the y-axis due to the higher energy of the event.

spread of the lateral distribution. However, due to the adequately estimated uncertainties, the LDF fit reconstructs the energy correctly. Here, I left the shape parameters r_0, σ, and b free for the best fit. The SNR cut eliminates 425 antennas in the tail of the LDF.

Figure 6.9 shows the reconstruction performance for this analysis. The antennas I discarded due the SNR cut, naturally, affect the antenna multiplicity quality cut. Many events did not qualify for the performance study due to possessing too few antennas with appreciable signal (see Tables 6.2 and 6.3). The presence of noise leads to a further overall worsening of the energy resolution to 5% while the bias is of the order of 1%. The reconstruction reaches peak performance at the highest energies where the presence of noise has the smallest impact on the reconstruction. For low-energy events, the resolution worsens further to 10% for GP300 and 13% for GRAND10k with substantial positive biases. At these energies, the background noise approaches the amplitude level of the air-shower signals which leads to many events with low antenna multiplicity. Naturally, the lower antenna multiplicity affect the energy resolution for these events. GRAND10k is more strongly affected since the simulated layout does not feature an in-fill. This leads to even lower antenna multiplicities at the lowest energies, and less likelihood for the high-intensity region of the footprint to hit enough antennas. Across the zenith angle range, the resolution is mostly stable at 5%. It slightly worsens for low zenith angles since these, after the SNR cut, often only have the minimum amount of antennas required for the LDF fit. Again, I observe a degradation of the reconstruction performance for the highest zenith angles.

In Figure 6.10, I show the pull distribution of the geomagnetic fluence to the LDF fit across all fitted events in each library. In essence, this means evaluating the compatibility of the energy fluence data points with the fitted LDF by taking into account the uncertainties assigned to the data. I compare the pull distributions for

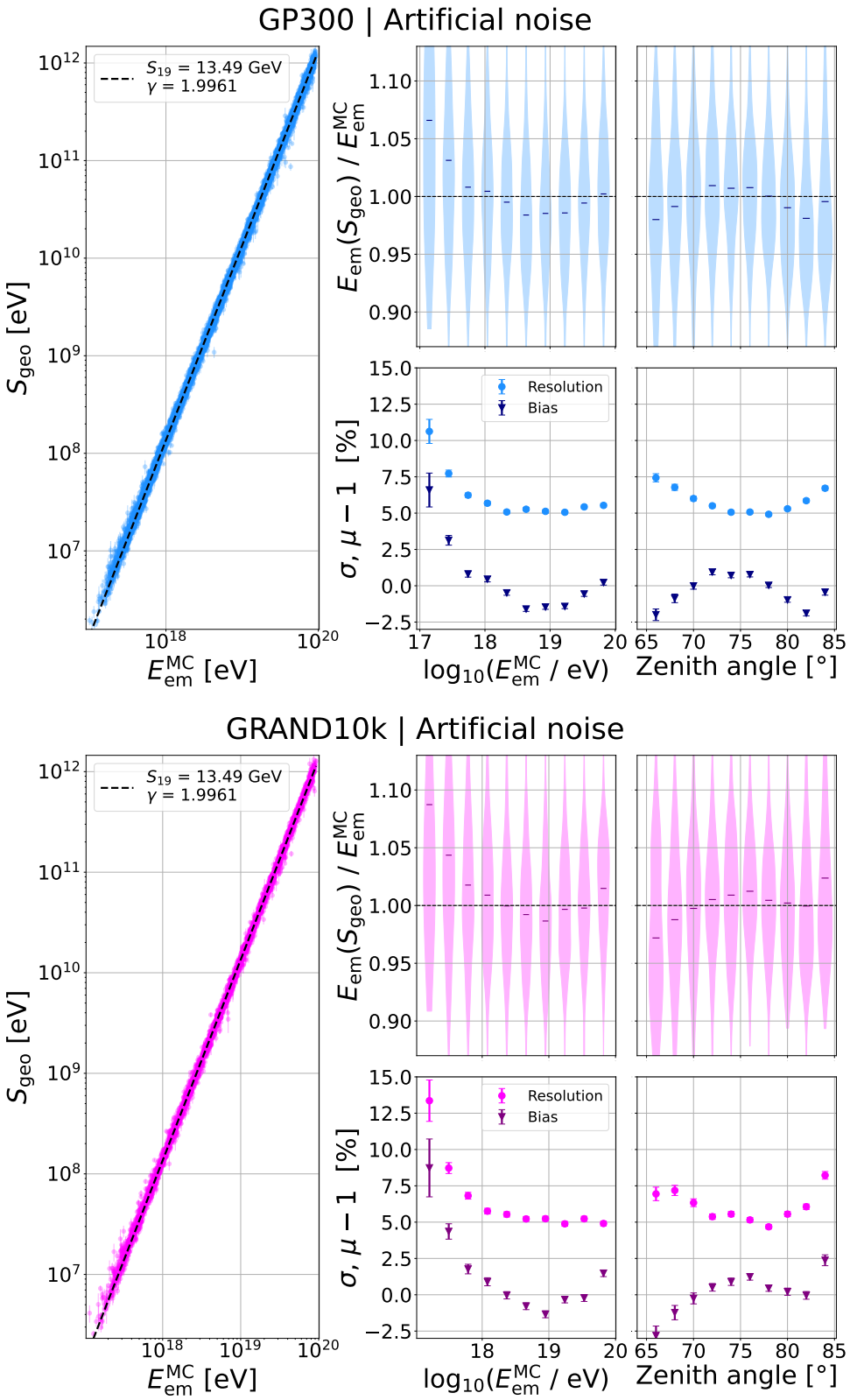

FIGURE 6.9: Reconstruction performance of the electromagnetic shower energy E_{em} with artificial noise for GP300 and GRAND10k simulation libraries (see Figure 6.1). See caption of Figure 6.3 for a detailed description of the panels.

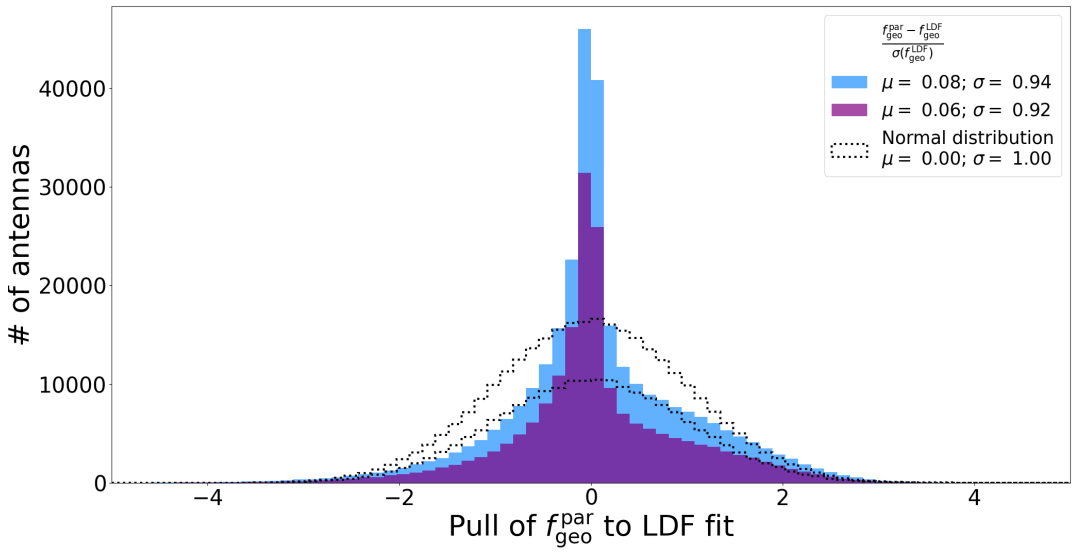

FIGURE 6.10: Pull distributions of the energy fluence data points of each antenna to the LDF fit. I show GP300 in light blue, and GRAND10k in purple. Dotted lines show normal distributions as comparisons with the corresponding amount of data for each simulation set.

GP300 and GRAND10k, respectively, to normal distributions (dotted histograms) with the same amount of samples. These represent the ideal pull distributions. The distribution for GP300 is blue. For GRAND10k, the distribution is purple. While both distributions have means close to zero, and standard deviations close to one, they are not Gaussian-distributed. This indicates too large energy fluence uncertainties. However, a reduction of the detector uncertainty, which dominates the fluence error, does not lead to better pull distributions compared to what I show here.

Furthermore, I evaluate the accuracy of the energy fluence calculation from the electric-field traces in the presence of background noise. Figure 6.11 shows the relative deviation of $\vec{v} \times \vec{B}$ fluence $f_{\vec{v}\times\vec{B}}^{rec}$, calculated with Eq. (6.2), from the true fluence $f_{\vec{v}\times\vec{B}}^{MC}$. I calculate the true fluence from the CoREAS output using Eq. (6.1) after applying the idealised rectangle bandpass filter. I show the relative deviation with respect to primary energy, the true fluence, zenith angle, and azimuth angle. For this study, I only used the GP300 simulation library since it provides higher statistics. The study is agnostic to the array layout. The data I show are only signal antennas of events which pass the SNR cut. I cut outliers beyond the range shown in the figure. However, they represent $< 1\%$ of the total amount of antennas in the study. The red squares, showing the calculation biases, agree with zero within 4% or better for most of the parameter space. The resolution is $\sim 15\%$. A positive bias of up to 30% appears for low primary energies approaching 10^{17} eV. For fluence values of and below the order of $1\,\mathrm{eV/m^2}$ there is an up 50% bias. At lower fluence values, the bias continues to increase, however, the number of antennas is not statistically relevant. For these parts of the parameter space, the resolution worsens as well. This likely contributes to the worsening energy resolution for low-energy cosmic rays.

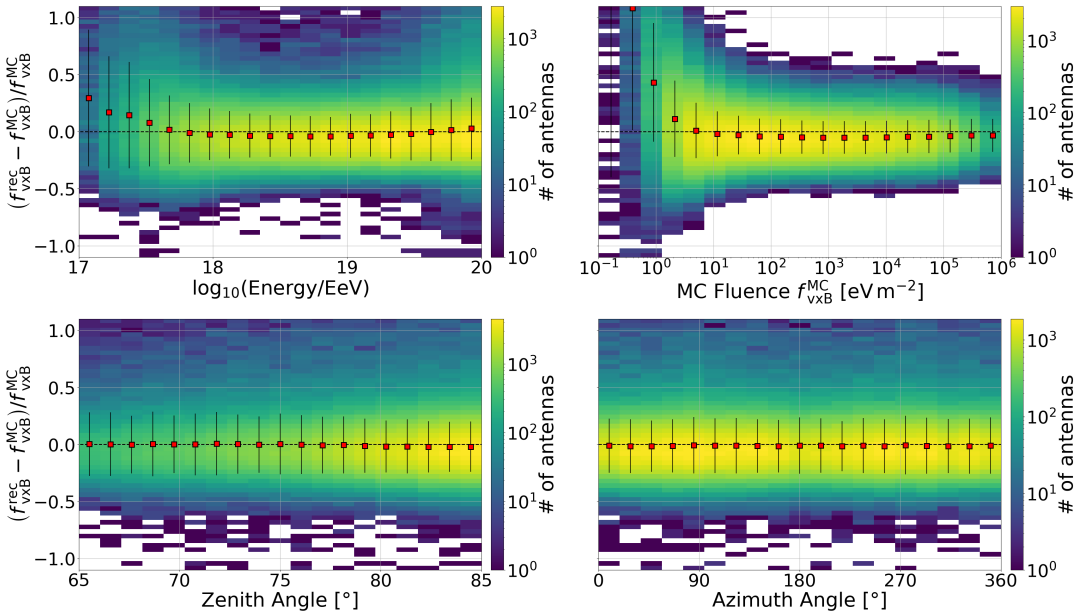

FIGURE 6.11: Evaluation of the calculation of the energy fluence in the presence of background noise. I calculate the relative deviation of the calculated fluence $f^{\mathrm{rec}}_{v\times B}$ from the energy fluence $f^{\mathrm{MC}}_{v\times B}$ directly from CoREAS. I show the deviation as two-dimensional histograms with a colour map. The red squares and black error bars show the mean and standard deviation of each column. I cut 2666 ($< 1\%$) outliers beyond the shown range. I display the deviation with respect to four different quantities: **Top left:** Cosmic-ray primary energy. **Top right:** $f^{\mathrm{MC}}_{v\times B}$. **Bottom left:** Zenith angle. **Bottom right:** Azimuth angle.

6.6 Sparse antenna grid with artificial noise and no "true" information

As a significant step towards a realistic performance study, I now only use timing data and antenna positions as available in the case of an actual measurement to calculate the shower parameters for this analysis. For this purpose, I estimate the starting value for the fit of the radio core by taking the barycentre ,

$$\vec{x}^{\,\mathrm{est}}_{\mathrm{core}} = \frac{1}{n_{\mathrm{ant}}} \sum_i \vec{x}^{\,i}_{\mathrm{ant}}, \tag{6.8}$$

of all n_{ant} simulated antenna positions $\vec{x}^{\,i}_{\mathrm{ant}}$. I reconstruct the arrival direction of the simulated air-shower using the plane-wave-front (PWF) reconstruction by Ferrière et al. [119]. For inclined air-showers, a plane wave is a good approximation for the radio emission since the emission originates from sufficiently far away. For the pulse arrival time at each antenna, I assume an uncertainty of $\sigma_t = 5\,\mathrm{ns}$ to account for GPS jitter, as was imprinted on the simulations. In practice, there is an additional timing uncertainty of the signal peak in the presence of noise. However, it is dependent on SNR and, as such, the high SNR threshold I use makes it negligibly small. The PWF reconstruction takes as input the antenna positions and the pulse arrival times of the radio pulse at each antenna with uncertainties to calculate the arrival direction of the plane wave. Then, it returns the zenith and azimuth angles with uncertainties for the air-shower coming from that direction. However, the reconstruction does not calculate the uncertainty on the arrival direction, but rather on the shape of the wave front. As such, I do not use the PWF uncertainty to calculate any uncertainties

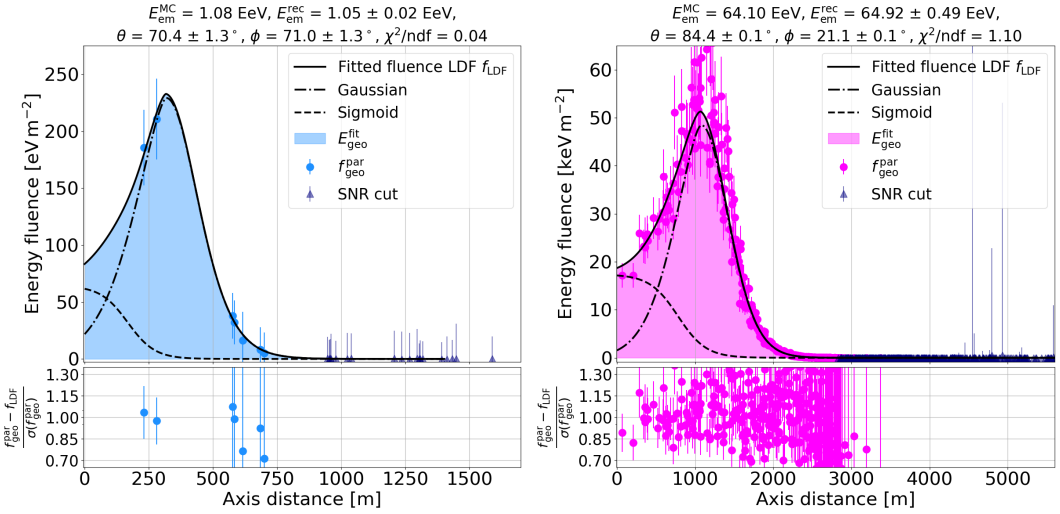

FIGURE 6.12: LDF fits of the same events I show in Figures 6.4 and 6.5, here with artificial noise added and no true parameters used. Above each LDF, I show the reconstructed shower parameters. The lower panels show the residuals of the LDF fit, only including the antennas considered for the fit. The triangular data points in each plot show the antennas flagged by the SNR quality criterion. **Left:** GP300 event in blue. 7/26 antenna remain viable for the fit. All shape parameters are fixed to their d_{max} parametrisation. **Right:** GRAND10k event in pink. 327/752 remain viable for the fit. r_0, σ, and b are free fit parameters. Note the keV m^{-2} scale on the y-axis due to the higher energy of the event.

on the energy fluence, or reconstructed electromagnetic energy. Instead, I apply a quality cut on the reconstructed events based on the PWF uncertainty, as I discussed in Section 6.2. To yield a result for the arrival direction, the PWF reconstruction requires at least three antennas.

The electric-field traces I use remain the same as in the previous step. While nothing inherently changes for the fluence calculation in comparison to the previous section, the reconstructed arrival direction can have an impact on the calculated energy fluence if it differs too much from the true value. This happens because the zenith and azimuth angle define the transformation matrix which I use to transform the electric-field vectors from NWU to shower plane coordinates.

Regarding the remaining shower parameters, I only pass on the site-specific parameters (antenna positions, geomagnetic field vector, observation altitude and atmospheric model) to the LDF reconstruction. For shower-specific parameters, I use average values, $X_{max}^{avg} = 750\,\mathrm{g/cm^2}$ and $E_{CR} = 5 \cdot 10^{18}\,\mathrm{eV}$, to calculate start values for the fit parameters d_{max} and E_{geo}. I also use X_{max}^{avg} to calculate the density at shower maximum ρ_{max}^{avg}. I use ρ_{max}^{avg} in the signal model to calculate the geomagnetic energy fluence, and later in the energy reconstruction for the density correction. Without access to the true shower core, I no longer use the prediction of its shift due to refractive displacement as a start value for the core fit. Instead, I take the barycentre of the antenna positions as the new start value and widen the core fit boundaries to 6500 m in any direction. The wider boundaries can lead to the fit not converging on the correct radio symmetry centre. However, such bad fits typically show either large errors on d_{max} or do not have a station within the fitted Cherenkov radius. Consequently, they are filtered out regardless by the corresponding quality cuts.

Figure 6.12 shows the GP300 and GRAND10k example LDF fits for this analysis level. There are few changes in comparison to the fits I show to the previous section.

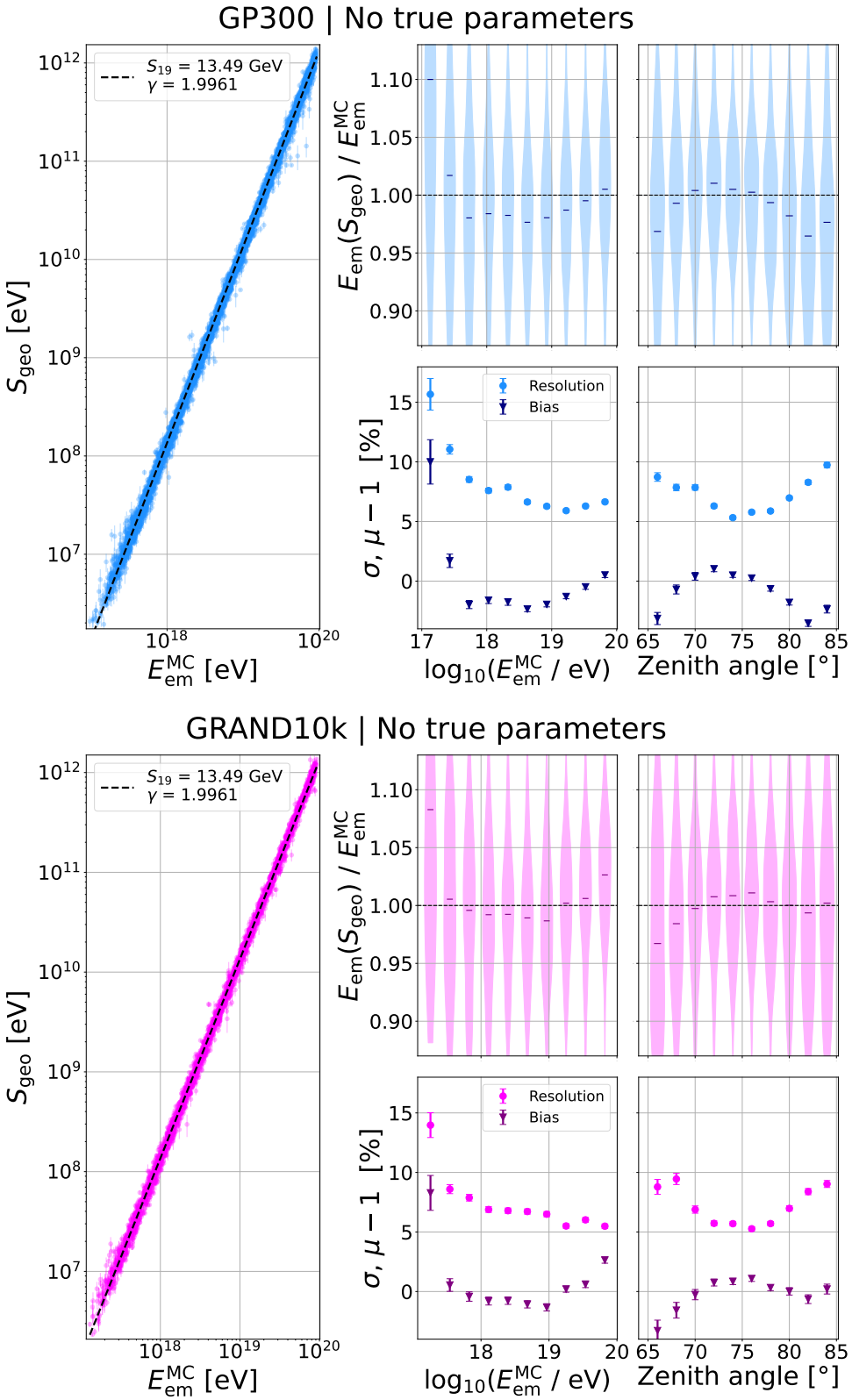

FIGURE 6.13: Reconstruction performance of the electromagnetic shower energy E_{em} with artificial noise and no true shower parameters for GP300 and GRAND10k simulation libraries (see Figure 6.1). See caption of Figure 6.3 for a detailed description of the panels.

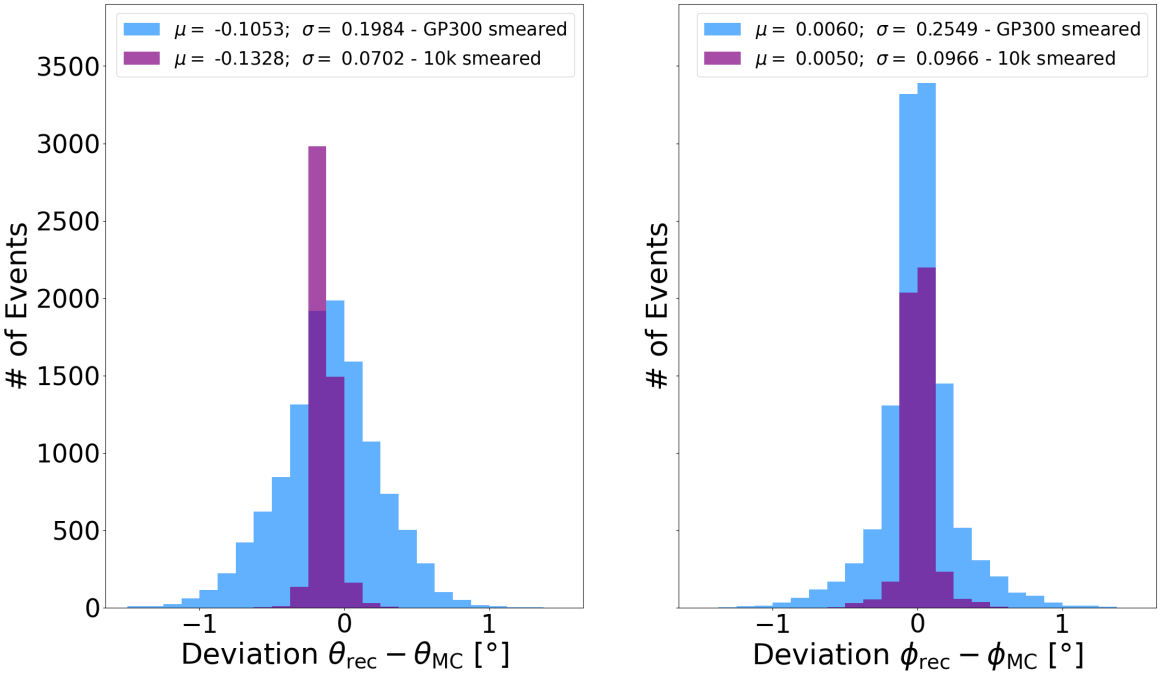

FIGURE 6.14: Evaluation of the arrival direction reconstruction for the analysis with artificial noise and no true parameters. I use the PWF reconstruction by Ferrière et al. [119]. I consider all simulated antennas for the reconstruction. I show histograms of the deviation from the true arrival direction. I display the mean and standard deviation of each distribution in the corresponding legend. **Left:** Zenith angle. **Right:** Azimuth angle.

The number of shape parameters fixed to their parametrisation as well as the number of viable antennas for the fit remain the same for both events. However, I now reconstruct the arrival direction. The parameter listings above each LDF plot show the reconstructed values of the zenith and azimuth angles. The PWF reconstruction determines the zenith and azimuth angles for both examples within 0.1° of the true values (see Figure 6.8).

Figure 6.13 shows the overall energy reconstruction performance. The features of the "spectra" of energy resolution remain identical to the previous section. However, the absence of true information for the arrival direction and fit start values shows clearly in another slight worsening of the energy resolution across the board. In addition, a number of events now show bad fit quality or large errors. For this analysis, I discarded them in the corresponding quality cut (see Tables 6.2 and 6.3). In this regard, GRAND10k shows a larger fraction of well-fitted events. This happens because the array layout guarantees the containment of any simulated radio footprint in the detector area. In comparison to the previous analysis, I observe no significant change in the worsening of the energy resolution at the largest zenith angles. This indicates that the unreliable X_{max} from CORSIKA does not have a significant impact since, here, I use an average value for X_{max} instead.

I once again investigated updating the density at maximum ρ_{max} for the density correction using the fitted value for d_{max}. However, the result was a significantly worse energy reconstruction performance. This indicates a growing bias in the fitted values of d_{max}. I evaluate d_{max} again under measurement conditions in the following section. I opted to use ρ_{max}^{avg} for the calculation of S_{geo} for a more accurate energy reconstruction. This is what I show in Figure 6.13.

I evaluate the accuracy of the arrival direction reconstruction using the PWF

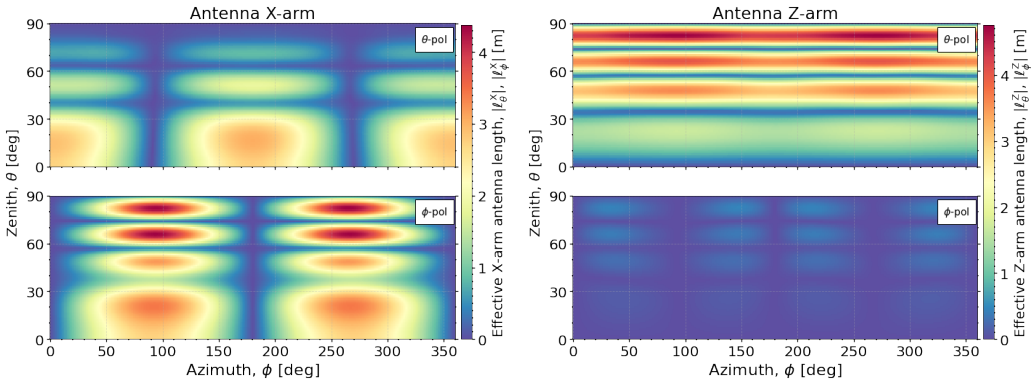

FIGURE 6.15: Simulated gain pattern of the GRAND HorizonAntenna. The response is shown at 150 MHz, in the local spherical coordinate system of an antenna in the θ (top), and ϕ (bottom) polarizations. **Left:** Pattern of horizontal antenna X-arm. The Y-arm pattern is similar, but shifted by 90° in azimuth since the arms are orthogonal. **Right:** Pattern of vertical antenna Z-arm. Plots from [79].

method. Notably, I use all simulated antennas in the PWF reconstruction, before applying the SNR cut. Figure 6.14 shows histograms of the deviation of the reconstructed zenith angle θ_{rec} and azimuth angle ϕ_{rec} from the true arrival direction in degrees. I consider the same events as for the reconstruction performance for this study. The GP300 reconstruction is excellent with angular resolution $< 0.2°$ for the zenith angle. The azimuth angles are similarly well-reconstructed with a bias consistent with zero and 0.25° angular resolution. GRAND10k generally shows even better angular resolution ($< 0.1°$) for both angles than GP300 due to the much larger array area. Both arrays show a $\sim -0.1°$ negative bias in the zenith angle reconstruction.

6.7 Realistic measurement conditions

In this final step, I reconstruct all necessary information for the energy reconstruction from the only data that are available in the case of a measurement. Naturally, this also enables the application of the reconstruction to real measurements (see Chapter 7). I use the antenna positions and the arrival time of the radio pulse at each antenna from the simulation output. I assume an uncertainty of 5 ns for the pulse timing, representing GPS jitter.

In Figure 6.15, I show the antenna response, or antenna-gain pattern of the GRAND HorizonAntenna [79]. The antenna gain is maximal when a component of the electric field oscillates parallel to the antenna arm. Shown here are the θ and ϕ polarisations of the local spherical coordinate system of the antenna $(\vec{r}, \theta, \phi)$ where $\vec{r}$ points towards the emission source. The polarisation along $\vec{r}$ is not shown since it is negligible for air-showers. The left panel shows the gain of the horizontal arms. The electric field oscillates parallel to the X-arm (Y-arm) for azimuth angles of 90 (0) or 270° (180°). This makes the antenna gain overall independent of the azimuth angle. The gain of the vertical arm in the right panel lies almost entirely in the θ polarisation. The striped pattern is due to the destructive interference of the radio signal with itself after reflecting off the ground. While the gain is invariant to the azimuth angle, both horizontal and vertical arms show particularly low gain for zenith angles around 75°.

I apply the GRAND detector simulation with the GRANDlib software [79] to the electric-field traces from the CoREAS output to obtain the corresponding ADC

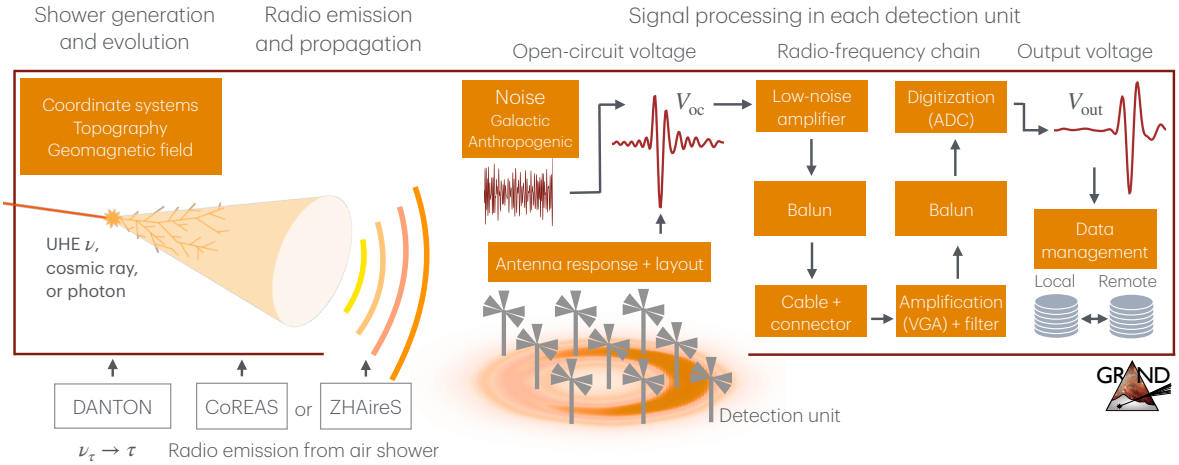

FIGURE 6.16: Illustration of GRANDlib functionalities, including the detector simulation on the right side. Graphic from [79].

traces. Figure 6.16 shows an illustration of the GRANDlib features, which includes the detector simulation steps. The detector simulation first converts the simulated electric field to an open-circuit voltage by applying the gain pattern of the GRAND HorizonAntenna. The combined voltage trace is then processed with the radio-frequency (RF) chain. The RF chain produces the output voltage and ADC traces by simulating the effects of a low-noise amplifier, balancing units (Balun), a cable with connector, a variable-gain amplifier (VGA), a filter, and ADC chip. At this point, the measured noise from GP300 is added to the ADC traces in the same format [89]. The noise was measured on February 4, 2025 within three hours with periodic triggers every 190 s. After these steps, the ADC traces correspond as closely as possible to data from measured events.

To reconstruct the electric field from the ADC traces, I use the method developed by Zhang et al. [120, 121]. Note that this method has a known bias for signal with low SNR for the case of using the HorizonAntenna. This is documented in Figure 16 of reference [120]. I modify the method slightly to include the reconstruction of the arrival direction, the estimation of the Cartesian position of the shower maximum, and the antenna barycentre for the estimated core. The arrival direction and position of $X_{\max}$ are necessary to calculate the direction and distance to the emission source from each antenna. For each trace component, the average ADC noise level $\hat{\alpha}_{\text{noise}}$ is computed by taking the standard deviation of a noise window at the beginning of the trace. As a first quality cut, the maximum ADC value $\hat{\alpha}_{\max}$ of any trace component is compared with the noise level. This is typically the peak of the radio pulse unless there is a strong transient pulse, or the radio pulse is so weak as to not exceed the noise level. Only antennas with at least one trace component with $\hat{\alpha}_{\max} > 5 \cdot \hat{\alpha}_{\text{noise}}$ are considered signal antennas. I flag the remaining antennas as below threshold, however, I still apply the reconstruction to them to have complete information. Subsequently, I only use signal antennas to reconstruct the arrival direction and to determine the antenna barycentre. During this process, I also flag any antennas with saturated ADC traces. In addition, I use an average value for the depth of maximum for $X_{\max}^{\text{avg}} = 750\,\text{g/cm}^2$ to estimate the Cartesian position by calculating its physical distance from the ground along the shower axis. For this, I use the `radiotools` [107] module. The position of the shower maximum is needed to accurately look up the gain of each arm of the antenna for the detector simulation.

Before the electric field is reconstructed, there is another quality cut applied to the

antennas regarding the timing of the pulse. After the ADC traces of an antenna are converted to voltage, the maximum of the Hilbert envelope $\hat{V}_{\text{max}}$ of each component is taken and compared to its average noise level $\hat{V}_{\text{noise}}$. For each component with $\hat{V}_{\text{max}} > 5 \cdot \hat{V}_{\text{noise}}$, the time of the peak τ_{peak} is noted. If multiple components show a peak with sufficient amplitude to pass the previous cut, the peak timing has to coincide within 100 ns. Only the antennas passing this cut remain signal antennas. Later, I only pass these antennas, i.e., antennas that pass both signal quality cuts, to the SNR quality criterion where I decide whether they are viable for the LDF fit.

The reconstruction for a single antenna takes the three components of the voltage trace. They correspond to the three antenna arms which are aligned with the axes of the NWU coordinate system. Another input parameter is the local noise-amplitude spectrum in the frequency domain. I obtain this by combining 1000 of the measured noise traces [89], taking their Fast-Fourier Transform (FFT) and calculating the mean of the absolute value of the amplitude for each trace component and frequency sample. Additional input parameters are the antenna gain of each arm for the direction of the emission source, and the output frequency band of 50–200 MHz. The reconstruction returns two electric-field trace components $\hat{e}_{\theta_{\text{ant}}}$ and $\hat{e}_{\phi_{\text{ant}}}$. θ_{ant} and ϕ_{ant} are the angles defining the direction of the emission source in a spherical coordinate system with the position of the antenna as its origin. I rotate the trace back to NWU coordinates using the standard transformation from a spherical coordinate system defined by $(\vec{r}, \theta_{\text{ant}}, \phi_{\text{ant}})$ to NWU coordinates by assuming the third trace component $\vec{r}$—polarised along the line-of-sight towards the emission source—is vanishing. This is a valid assumption since only a negligible fraction of the radio emission is polarised in the direction of the shower axis [58]. For a complete description of the electric-field reconstruction, I refer to Zhang et al. [120].

I pass the reconstructed electric field traces, along with the arrival direction and antenna barycentre, determined only from signal antennas, to the fluence calculation. I calculate the fluence as described in Section 6.3 with errors as described in Section 6.5. Finally, I pass the energy fluence, arrival direction, and barycentre to the LDF reconstruction.

The quality cut on ADC pulse amplitude in the electric-field reconstruction method from Zhang et al. [120] effectively replaces the SNR criterion on the electric-field traces. As such, almost all antennas that pass through the electric-field reconstruction without being flagged, also pass the SNR cut. I apply this version of the analysis with only small changes to real GP300 measurements of cosmic-ray event candidates in Chapter 7.

As a next step, I investigate the significance of the bias present in the electric-field reconstruction. For this purpose, I evaluate the energy fluence determined with the reconstructed electric-field traces $f^{\text{rec}}_{\vec{v}\times\vec{B}}$ against the fluence calculated directly from the CoREAS output $f^{\text{MC}}_{\vec{v}\times\vec{B}}$. Figure 6.17 shows the relative deviation between them against the cosmic-ray primary energy, the true fluence, and the zenith and azimuth angles. I only use the GP300 simulation library for this study since the electric-field reconstruction and fluence calculation are not sensitive to the layout of the array. Naturally, I only consider signal antennas for this comparison. I previously established that the fluence calculation has excellent accuracy for fluences larger than of the order of $1\,\text{eV}/\text{m}^2$ (see Figure 6.11). As such, the effect of the electric-field reconstruction bias on the fluence for the HorizonAntenna can be observed here directly. The reconstructed energy fluence generally shows good agreement with the true fluence for in primary energies $> 10^{19}$ eV and true energy fluence values $> 100\,\text{eV}/\text{m}^2$. It is especially accurate for antennas with high energy fluence values in the top right

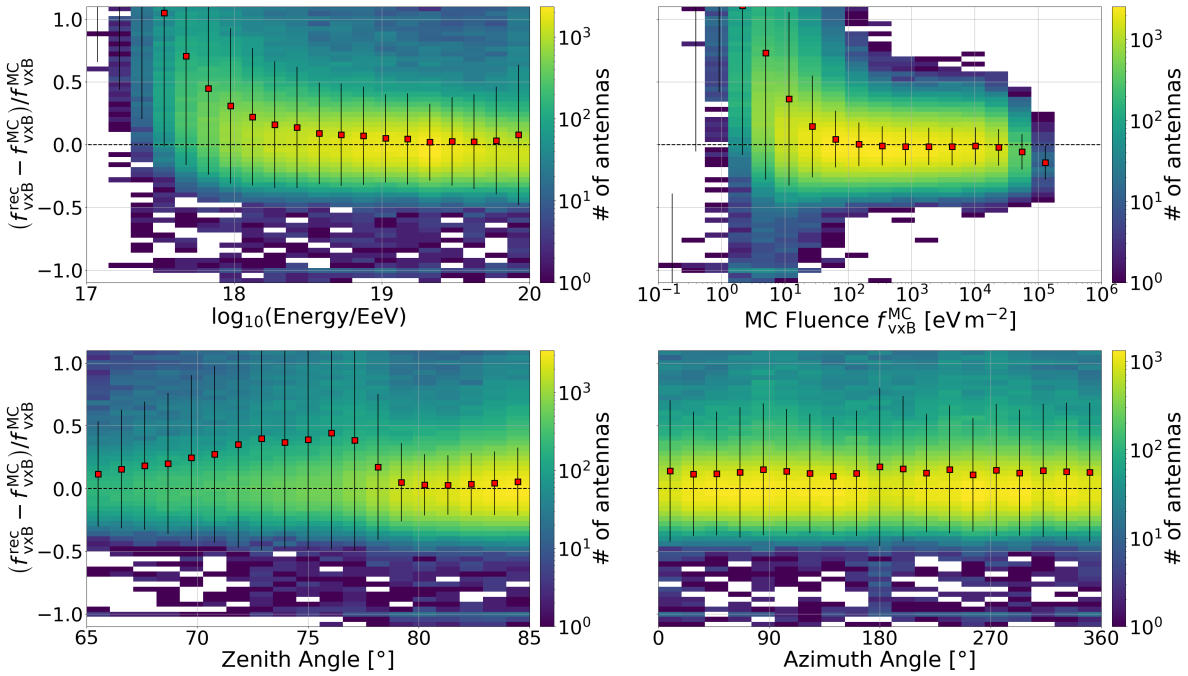

FIGURE 6.17: Evaluation of the $\vec{E}$-field reconstruction by calculating the relative deviation of the reconstructed fluence $f^{rec}_{v\times B}$ from the true energy fluence $f^{MC}_{v\times B}$ from CoREAS. I show the deviation as two-dimensional histograms with a colour map. The colour shows the amount of entries in each bin. The red squares and black error bars show the mean and standard deviation of each column. I cut 13,287 ($\sim$ 5%) outliers beyond the shown range. I display the deviation with respect to four different quantities: **Top left:** Cosmic-ray primary energy. **Top right:** $f^{MC}_{v\times B}$. **Bottom left:** Zenith angle. **Bottom right:** Azimuth angle.

panel with a resolution of 15% and no significant bias, matching the previous evaluation of the energy fluence. The much wider spread of the deviation for the other panels happens because any event has antennas with low energy fluence. For lower energies and fluence values, however, the resolution worsens drastically to up to 100%. In addition, an increasing bias of up to 100% appears for the same antennas for bins with statistically relevant amounts of antennas. When looking at the deviation as a function of zenith angle, the bias most strongly affects events with zenith angles between 70 and 80°. Low zenith angle events are affected as well due to their low antenna multiplicity which still always entail antennas with low energy fluence. High zenith angle events only show a 2% positive bias with an average fluence resolution of 20%. The stronger bias lies in the same zenith angle range as the antenna-gain "blind-spot" of the HorizonAntenna around 75°. This indicates that the antenna-gain pattern is a factor in the reconstruction bias, especially since Zhang et al. [120] found a less significant bias for a dipole antenna. The reconstruction bias appears across the entire azimuth angle range as a $\sim$12% positive bias, but does show not any sensitivity to specific azimuth angles. About 5% of values lie outside the shown range. However, I included them in the resolution and bias calculations.

Figure 6.18 shows the LDF fits for the two example events under realistic measurement conditions. For the GP300 event in the left panel, the 19 antennas previously discarded by the SNR cut, I discard now due to the ADC noise criterion in the electric-field reconstruction. In addition, I flag one additional antenna for bad pulse timing. This means that a noise pulse high enough to pass the ADC noise

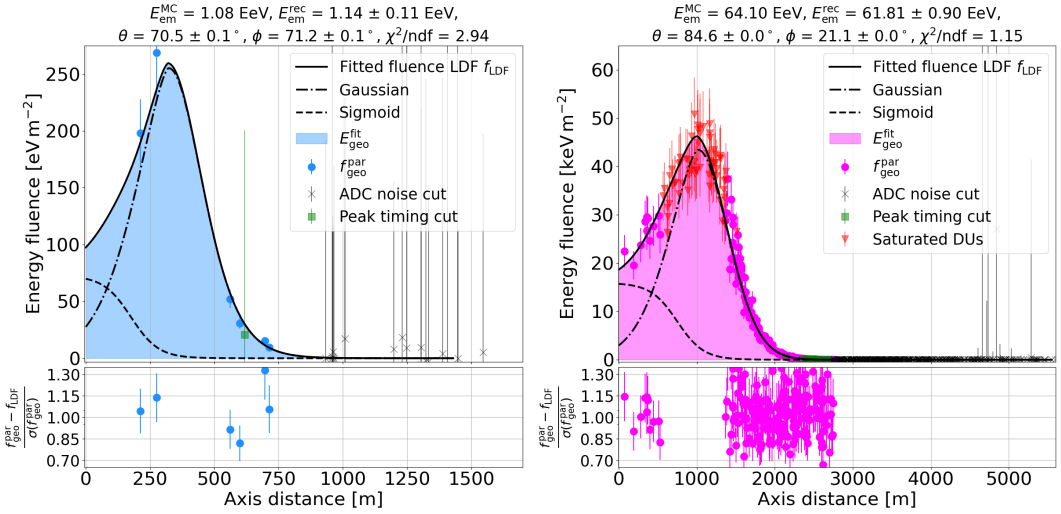

FIGURE 6.18: LDF fits of the same events I show in Figures 6.4 and 6.5, here performed under realistic measurement conditions. Above each LDF, I show the reconstructed shower parameters. The lower panels show the residuals of the LDF fit, only including the antennas considered for the fit. The black crosses and green squares show the antennas flagged by the ADC noise criterion and peak timing criteria in the $\vec{E}$-field reconstruction. Red triangles show antennas with saturated ADC traces. **Left:** GP300 event in blue. 6/26 signal antennas with 1 flagged by the peak timing cut and 19 by the ADC noise cut. All shape parameters are fixed to their d_{max} parametrisation. **Right:** GRAND10k event in pink. 209/752 signal antennas with 65 saturated, 20 flagged by the peak timing cut and 458 by the ADC noise cut. r_0, σ, and b are free fit parameters. Note the keV m^{-2} scale on the y-axis due to the higher energy of the event.

criterion is present in its trace further than 100 ns from the signal. However, due to its disparate timing from the timing of the air-shower pulse, the antenna is flagged and not considered for the LDF fit. The reconstruction of the zenith and azimuth angles is slightly less accurate than in the previous iteration since I only use the six signal antennas for the PWF reconstruction. In the last section, I reconstructed the arrival direction before I applied the SNR cut. As such, I used all simulated antennas in the PWF reconstruction. This is acceptable for simulations. However, under measurement conditions, it is important to only use signal antennas. Otherwise, a noise signal could contaminate the reconstruction. The energy remains well-reconstructed. I fix all shape parameters to their d_{max} parametrisations for the best fit result. The fluence values for the four signal antennas in the tail of the distribution are likely affected the electric-field reconstruction bias. However, since the antennas at the distribution peak are unaffected due to their higher SNR, the energy is still reconstructed accurately within the uncertainty.

For the GRAND10k event in the right panel, I discard 458 antennas in the tail with the ADC noise cut and 20 more antennas due to the peak timing cut. Importantly, I flag 65 antennas close to the peak energy fluence as saturated. This leads to an underestimation of the electromagnetic energy of $\sim$ 4% due to the peak of the distribution not being available to the fit. However, the arrival direction reconstruction remains excellent since there are 209 signal antennas available that span a large area. I display the best LDF fit result with the shape parameters r_0, σ, and b as free fit parameters. The event does not feature many antennas with energy fluence $< 100\,\mathrm{eV/m^2}$. As such, the reconstruction is unlikely to be affected by the bias from the electric-field reconstruction.

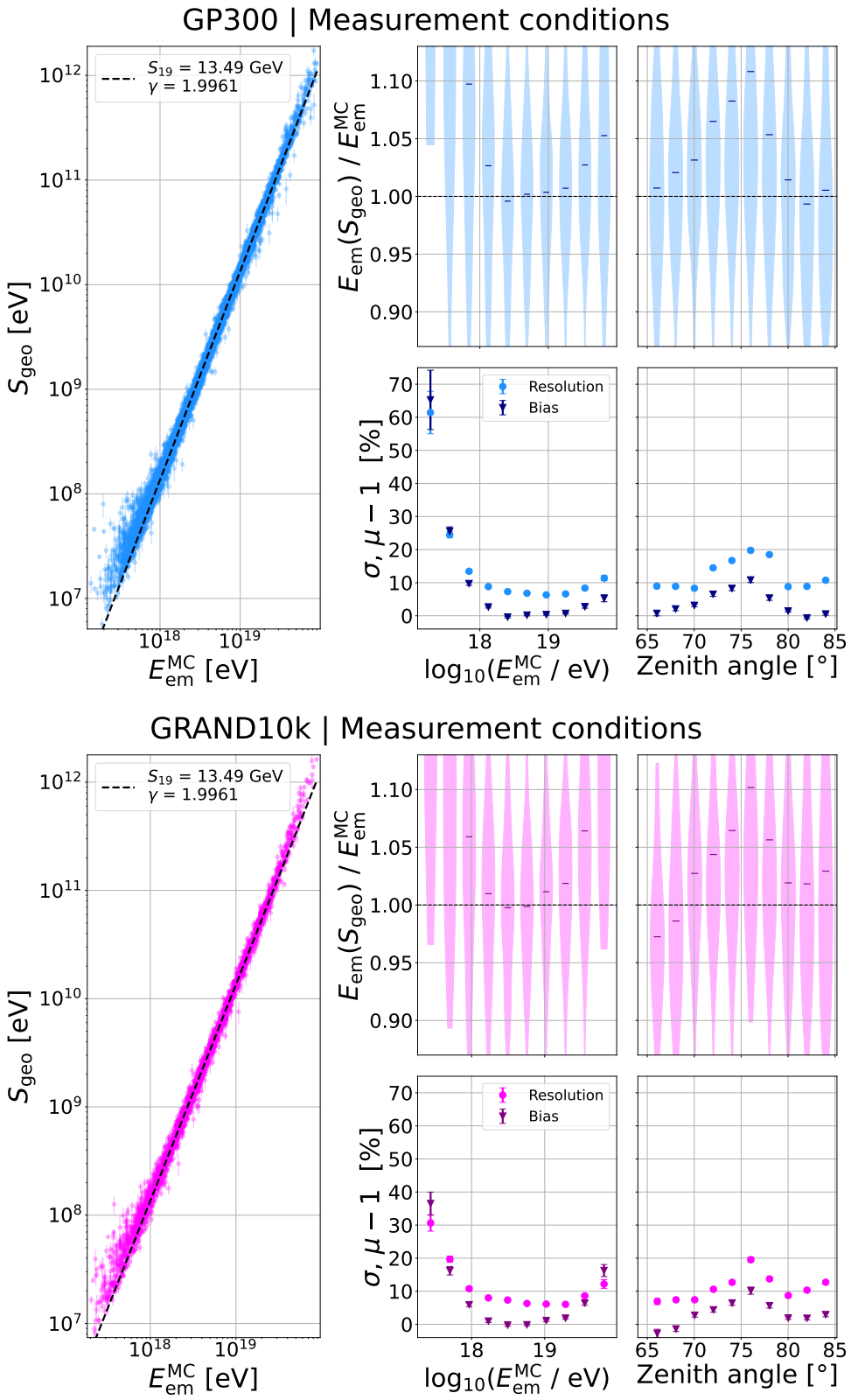

FIGURE 6.19: Reconstruction performance of the electromagnetic shower energy E_{em} under realistic measurement conditions for the GP300 and GRAND10k simulation libraries (see Figure 6.1). See caption of Figure 6.3 for a detailed description of the panels.

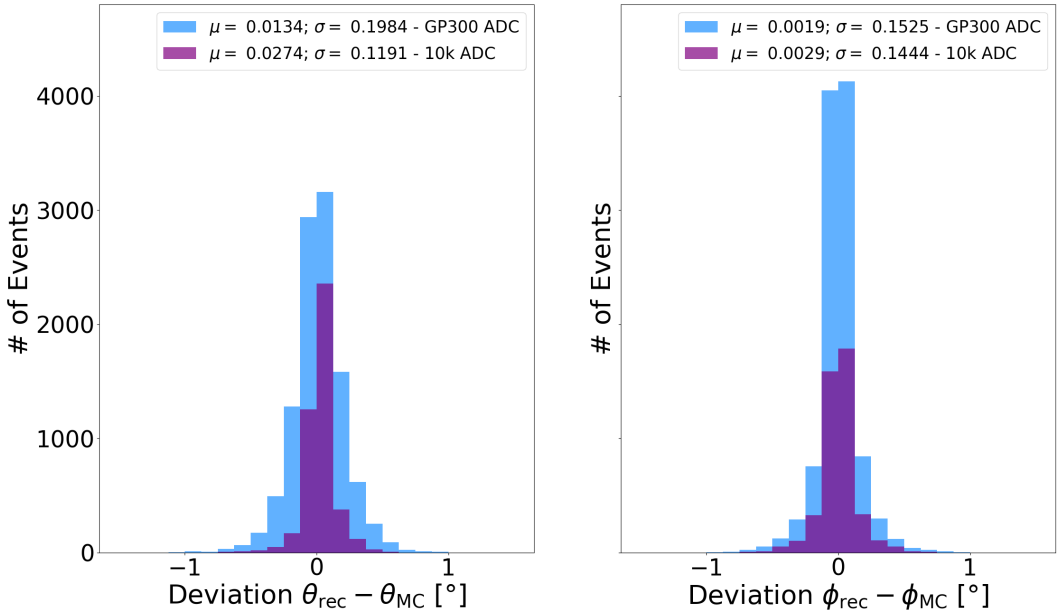

FIGURE 6.20: Evaluation of the arrival direction reconstruction for the analysis under realistic measurement conditions. I use the PWF reconstruction by Ferrière et al. [119]. I only consider signal antennas for the reconstruction. I show histograms of the deviation from the true arrival direction. I display the mean and standard deviation of each distribution in the corresponding legend. **Left:** Zenith angle θ. **Right:** Azimuth angle ϕ.

Figure 6.19 shows the overall reconstruction performance of the LDF fit under realistic measurement conditions. For GP300 in the top plot, the reconstruction remains excellent with a mean resolution of $\sim$ 7% and a vanishing bias above electromagnetic energies of 10^{18} eV. At the highest energies, the performance worsens slightly due to events affected by saturated traces. However, I include these events in the analysis since the impact is not large, and, more importantly, to have better statistics at high energies. For energies $< 10^{18}$ eV, the resolution worsens drastically due to two factors: First, at low energies, there are fewer events since I discard many events with too few antennas after the quality criteria applied to the traces. Secondly, the bias present in the electric-field reconstruction comes into play for the antennas of low-energy events, and leads to both a strong degradation in resolution, and an equally strong bias for the energy reconstruction. Regarding zenith angles, one observes the effects of the reconstruction bias in the same zenith angle range as in Figure 6.17. Between 70 and 80° the energy resolution worsens to up to 20% with an up to 10% positive bias. The connection between zenith angle, corresponding to size and energy spread of the radio footprint, explains why the most inclined showers are often unaffected by antenna saturation. The large area of the footprint, over which the radiation energy spreads out, leads to lower signal amplitudes for the antennas. Generally, the resolution for energies $> 10^{18}$ eV is 10% or better.

GRAND10k also shows a resolution of 7% and a vanishing bias above electromagnetic energies of 10^{18} eV. The lower number of events in the GRAND10k library causes the more drastic degradation in performance at the highest energies due to the events with saturated traces. At low energies, GRAND10k is not as strongly affected by the electric-field reconstruction bias as GP300. This happens since the layout I choose for GRAND10k does not have an in-fill. As such, it is less sensitive to low-energy showers. Only low-energy showers with small zenith angles show up

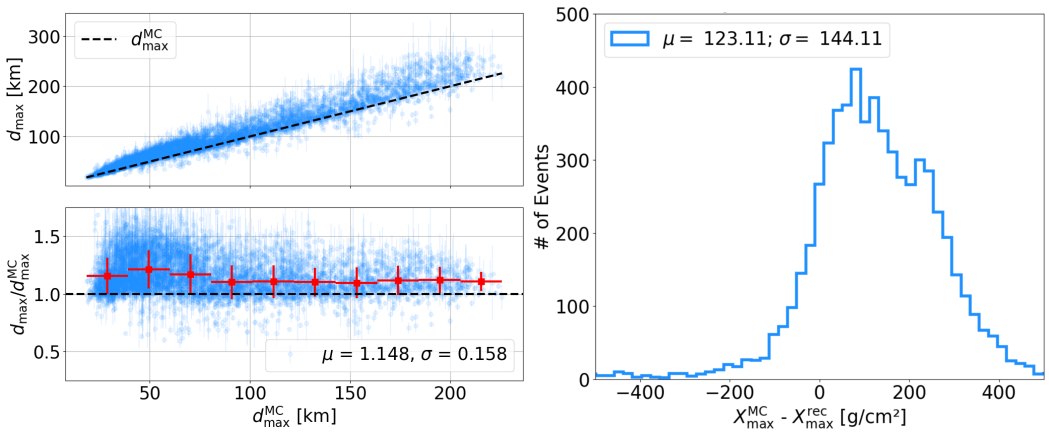

FIGURE 6.21: Evaluation of distance to shower maximum d_{max} determined in the LDF fit and corresponding X_{max}^{rec} under realistic measurement conditions. **Upper left:** Fitted d_{max} shown against true value with the true d_{max}^{MC} also displayed as the black dashed line. **Lower left:** Relative deviation of the fitted d_{max} from the true value. Red points, vertical, and horizontal error bars show the mean, standard deviations, and bin widths of the binned data, respectively. The mean of the blue points μ corresponds to the bias, and standard deviation σ to the resolution. **Right:** Distribution of deviation of the corresponding X_{max}^{rec} from the true X_{max}^{MC}. I cut 47 outliers outside the shown region.

here, if they have the sufficient amount of signal antennas. For these cases, the signal is stronger at each antenna and they are less likely to be affected by the bias. The reconstruction performance with respect to the zenith angles reflects this as well. There is a only a significant dip in the resolution and bias for showers with zenith angles between 73 and 78°, further strengthening the case of the influence of the antenna-gain pattern. For both array layouts, I observe again slightly worse energy resolution for the largest zenith angles.

Figure 6.20 shows the performance of the arrival direction reconstruction for the analysis shown in this section. For GP300, I reconstruct the zenith angles with an angular resolution of $< 0.2°$, and a minimal bias of $\sim 0.01°$. GRAND10k shows a slightly larger bias of $\sim 0.03°$ and an angular resolution of $0.1°$. The azimuth angles reconstruct with an angular resolution of $0.15°$ and vanishing biases for both arrays. In comparison to the previous section (see Figure 6.14), the reconstruction improved. Notably, the zenith angle bias significantly decreased. The reason for this is likely that I only used signal antennas for the reconstruction in this section.

In Figure 6.21, I examine once again the accuracy of the fitted d_{max} with respect to the true value d_{max}^{MC}, as well as the corresponding X_{max}^{rec} reconstruction. Again, I only show the results for the GP300 library in the figure since the results from GRAND10k are not significantly different. The accuracy worsens in comparison to the previous study on the fitted d_{max} for the analysis without added noise (see Figure 6.7). The resolution decreases to 15.8% with a 14.8% bias for GP300. Similarly, the d_{max} fit for GRAND10k has a resolution of 15.8% with a 15.7% bias. The X_{max} reconstruction suffers accordingly. The bias increases to $144\,g/cm^2$, and the resolution worsens to $123\,g/cm^2$.

In Figure 6.22, I also revisit the pull distributions of the energy fluence. I show the pull distributions for the fit under measurement conditions for both simulation libraries. Both distributions are approximately Gaussian-distributed. The distributions, respectively, are shifted from zero by $\mu_{GP300} = 0.32$ and $\mu_{10k} = 0.48$. This shows the presence of the positive bias from the electric-field reconstruction. This shift is mitigated if I discard the low energy events, but never fully eliminated since

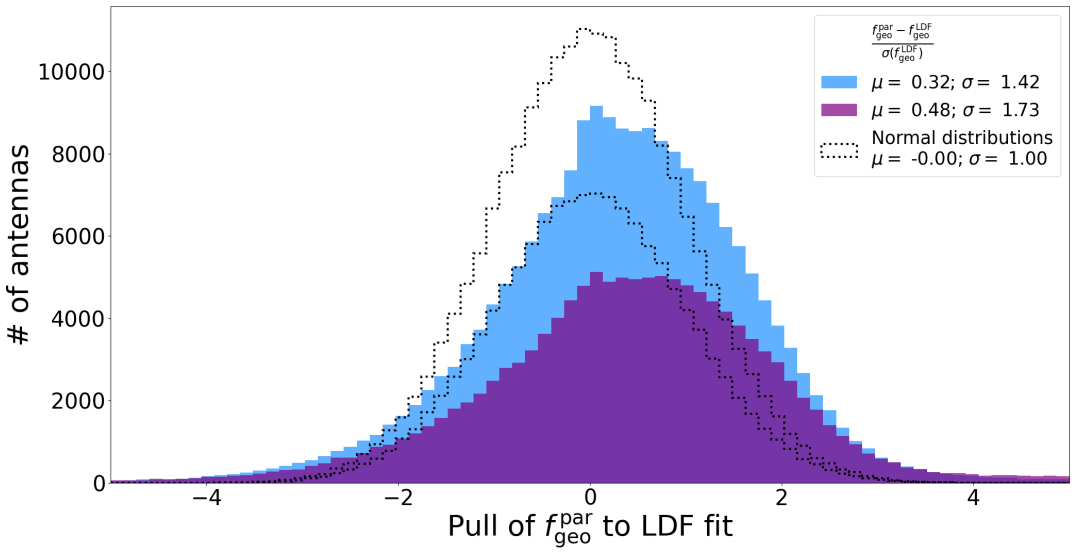

FIGURE 6.22: Pull distribution of the energy fluence data point of each antenna of the LDF fit. I show GP300 in light blue, and GRAND10k in purple. Dotted lines show normal distributions as comparisons with the corresponding amount of data for each simulation set.

almost all events have antennas with low energy fluence values. Both distributions also show standard deviations > 1. This indicates that the uncertainties assigned to the energy fluence are too small. These uncertainties are difficult to optimise across the wide parameter space of the shower parameters and the resulting range of possible energy fluence values. As I discuss in Section 6.6, the detector uncertainty dominates the energy fluence error. For this analysis, I use a detector uncertainty of 7.5% for consistency with the artificial noise analyses. Typical values for this uncertainty range from 5 to 10%. It should not be raised arbitrarily to obtain a more ideal pull distribution.

6.8 Comparison of proton and iron cosmic-ray primaries

The low-frequency model for the Pierre Auger Observatory finds no bias on the reconstructed electromagnetic energy with respect to the cosmic-ray primary particle [9]. In this section, I investigate the existence of such a bias in the model I describe in this work. Both the idealised RdStar and GRAND star-shape libraries, as well as the GP300 and GRAND10k simulation libraries have a 50/50 mixed composition of proton and iron nuclei primaries. While this is, naturally, not a realistic composition, it shows the two extremes of the common cosmic-ray primaries. In order to investigate a bias depending on the primary particle, I conduct the energy reconstruction separately on the proton and iron fraction of each library. At low primary energies, it is possible that only "upward-fluctuating" proton showers have sufficient antenna multiplicity for the LDF fit. Protons generally have a deeper X_{max} and, as such, smaller radio footprints. To avoid this, I exclude events with primary energy $< 10^{18.4}$ eV for this study. In Figure 6.23, I display the accuracy of the energy reconstruction with artificial noise, identical to Section 6.5, for the two halves of the GP300 library. Note that I use true shower parameters for the input of the LDF fit. In addition, to the energy threshold, I consider for this analysis only events passing

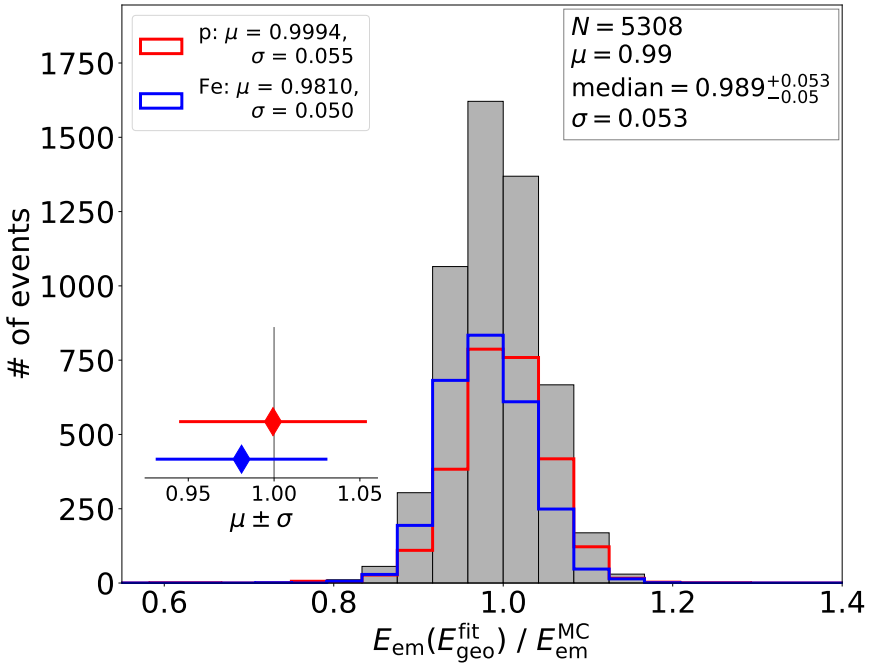

FIGURE 6.23: Relative deviation between the reconstructed electromagnetic energy $E_{\mathrm{em}}(E^{\mathrm{fit}}_{\mathrm{geo}})$ and the true energy $E^{\mathrm{MC}}_{\mathrm{em}}$ for proton and iron primaries for the analysis with artificial noise (see Section 6.5). The grey, filled histogram shows the entire data set, while red and blue histograms show proton and iron primaries, respectively. The inset shows the respective means as diamonds, and the standard deviations with error bars. On the top right, I display the total number of events, and the mean, median, and standard deviation of the entire data set. In this context, the mean μ represents the reconstruction bias, and the standard deviation σ the energy resolution.

the quality cuts (see Tables 6.2 and 6.3). For proton and iron primaries among the remaining 5308 events, I find reconstruction biases of consistent with zero and $\sim -2\%$, respectively. Both have an energy resolution of $\sim 5\%$. The overall distribution has a -1% bias and a 5.3% energy resolution.

I show the results of this study for each of the analyses I discuss in the previous sections in Table 6.4. For the analysis under realistic measurement conditions, I additionally discard events with primary energy $> 10^{19.5}$ eV to avoid introducing a bias due to saturated measurements. For the two intrinsic analyses, there is no bias between the primaries. The difference between the primaries remains $< 2\%$ up to and including the analysis with artificial noise, which I show in Figure 6.23. However, the analyses with no true shower parameters and under measurement conditions, respectively, show 3% and 5% differences. The main distinguishing feature for cosmic-ray primaries in air-showers is X_{max}. Protons generally penetrate deeper into the atmosphere than iron nuclei before interacting. As such, the bias introduced in the later analyses is likely caused by the average value for $X^{\mathrm{avg}}_{\mathrm{max}} = 750\,\mathrm{g/cm^2}$ I use to determine the air-density at maximum ρ_{max} for the energy reconstruction. The additional difference in the analysis under measurement conditions could also be due to the electric-field reconstruction bias.

TABLE 6.4: Means and standard deviations of the distributions of the relative deviation between the reconstructed electromagnetic energy $E_{\mathrm{em}}(E^{\mathrm{fit}}_{\mathrm{geo}})$ and the true energy $E^{\mathrm{MC}}_{\mathrm{em}}$ for proton and iron primaries. The last two lines show the analysis under measurement conditions from Section 6.7 without the events affected by saturated measurements. The left-most column indicates the analysis the values correspond to. The right-most column shows the total number of event in the analysis.

	Proton		**Iron**		
Analysis	μ	σ	μ	σ	N
RdStar (intr.)	0.9986	0.039	0.9995	0.031	4069
GRAND (intr.)	1.0095	0.037	0.9947	0.032	3676
GP300 (no noise)	1.0108	0.042	0.9923	0.0436	5384
10k (no noise)	1.0160	0.043	1.0014	0.036	2425
GP300 (art. noise)	0.9994	0.055	0.9810	0.050	5308
10k (art. noise)	1.0047	0.054	0.9906	0.049	2393
GP300 (no true)	1.0069	0.063	0.9726	0.061	4644
10k (no true)	1.0189	0.062	0.9847	0.058	2335
GP300 (realistic)	1.0267	0.063	0.9813	0.061	3172
10k (realistic)	1.0320	0.062	0.9847	0.060	1443

Chapter 7

Reconstruction of Event Candidates from GRANDProto300

A partial configuration of the GRAND prototype array GRANDProto300 (GP300) has been taking data since November 2024. In the time period between December 2024 and March 2025, the GRAND collaboration has identified 41 cosmic-ray air-shower event candidates. In this chapter, I apply the signal model and energy reconstruction, which I tuned and benchmarked in the preceding chapters, to these event candidates. As I did in Chapter 3, in the direct GRAND context, I refer to antennas as detection units (DUs).

7.1 Selection of cosmic-ray event candidates

I briefly discuss the selection of the event candidates among all data measured by GP300. For a complete description, I refer to reference [92].

GP300 has been measuring with a setup of 46 DUs in the time periods December 7, 2024 to February 4, 2025, February 14 to 19, and March 4 to 12. It is important to note that the detector is still in the deployment phase. As such, instabilities in the measurement setup and its monitoring are expected. In the left panel of Figure 7.2, I show the array layout of the 46 deployed DUs. In Figure 7.1, I show the data taking periods. As such, these time periods were chosen for the cosmic ray search. During this time, 533,466 coincident events—pulses that triggered at least 5 DUs within 10 μs—were recorded. DUs trigger if a transient signal at 5-sigma above background noise is detected. From these coincident events, 41 cosmic-ray event candidates were identified, homogeneously distributed over the three data taking periods.

We apply a spacial and temporal clustering cut to the data. For this purpose, we label as clusters multiple events occurring within an angular distance of 5°, and within a 5 s time window. This is an appropriate method to search for cosmic-ray events since a radio pulse from an air-shower only lasts $\leq$ 100 ns. Consequently, it cannot trigger more than one coincidence event. This cut eliminates 79% of the data as clusters of coincidence events caused by anthropogenic, transient noise sources, like air-craft communication or a nearby transformer. The arrival direction is reconstructed using the PWF reconstruction by Ferrière et al. [119].

Another cut is applied on the polarisation direction of the radio pulses. The polarisation signature of the air-shower radio emission is orthogonal to the local geomagnetic field vector due to the Lorentz force giving rise to the geomagnetic emission. We take the scalar product of the normalised voltage $\vec{e}_V$ and geomagnetic field vectors $\vec{e}_B$. Low values indicate orthogonality of the emission polarisation and the magnetic field. Passing events must fulfil $\vec{e}_V \cdot \vec{e}_B < 0.25$. This method is based on work by Chiche et al. [122].

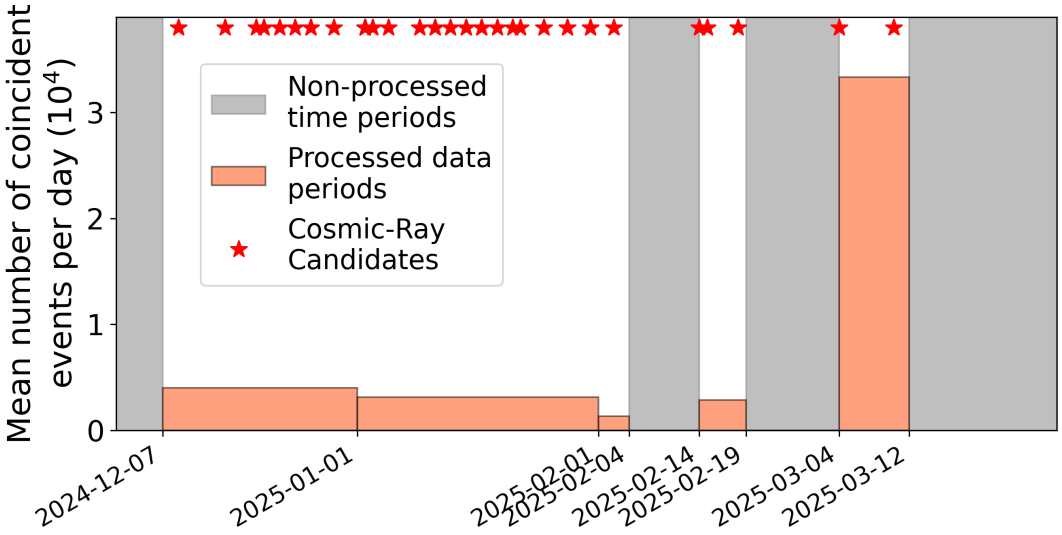

FIGURE 7.1: Data taking periods of the stable 46 DU GP300 configuration. Periods where data was processed are shown in orange with their level of average number of coincident events per day on the y-axis. Grey areas show the time periods during which data was not processed. Cosmic ray candidates are shown as red stars. Trigger settings were changed in March, resulting in a higher rate of coincidence events. Plot from [92].

We apply cuts on the zenith angle angle range ($\theta \in [60°, 88°]$), and PWF reconstruction error ($\sigma_{\mathrm{PWF}} < 0.5°$). All DUs in an event are required to have signal-to-noise ratio $\mathrm{SNR}_Y \geq 5$ in their Y-axis trace (West-east component). Due to the orientation of the geomagnetic field, this selection criterion focuses on the strongest signals from air-showers. In addition, limits on root-mean-square (RMS) values at specific frequencies for the X and Y channels are designed to eliminate residual noise events from the nearby transformer. The limits are defined by the three conditions: [$\mathrm{RMS}_{X,Y}$(50–80 MHz) < 2 mV], and [RMS_X(160–225 MHz) < 1 mV], and [RMS_Y(160–225 MHz) < 3 mV]. Lastly, manual cuts are performed to eliminate events with disconnected footprints, bad traces, and timing that could stem from multiple sources.

7.2 Processing of measurement data

I discussed the method to process simulation data to emulate realistic measurement conditions in Section 6.7. After the measurements are converted to the GRANDlib data format, I apply the electric-field reconstruction to the measured ADC traces in the same way as to simulations processed with the detector simulation. For the cosmic-ray event candidates, I use an uncertainty on the pulse arrival time of $\sigma_t = 15\,\mathrm{ns}$, increased from 5 ns for simulations, to match the observed timing uncertainty during calibration. For the detector uncertainty, I keep using $\sigma_{\mathrm{detector}} = 7.5\%$ as a middle ground between 5% and 10%, which I consider to yield too small and too large uncertainties on the energy fluence, respectively. For the signal model, I use the same "Dunhuang" model of the local atmospheric profile as for the GP300 and GRAND10k simulations in Chapter 6.

While the process to determine the energy fluence remains the same for the most part, a few additional hurdles appear along the way. First, I define the observation altitude h_{obs} which I use to calculate many shower parameters. I use the average altitude of the deployed DUs $\langle h_{\mathrm{ant}} \rangle = 1242\,\mathrm{m}$. This observation altitude differs by

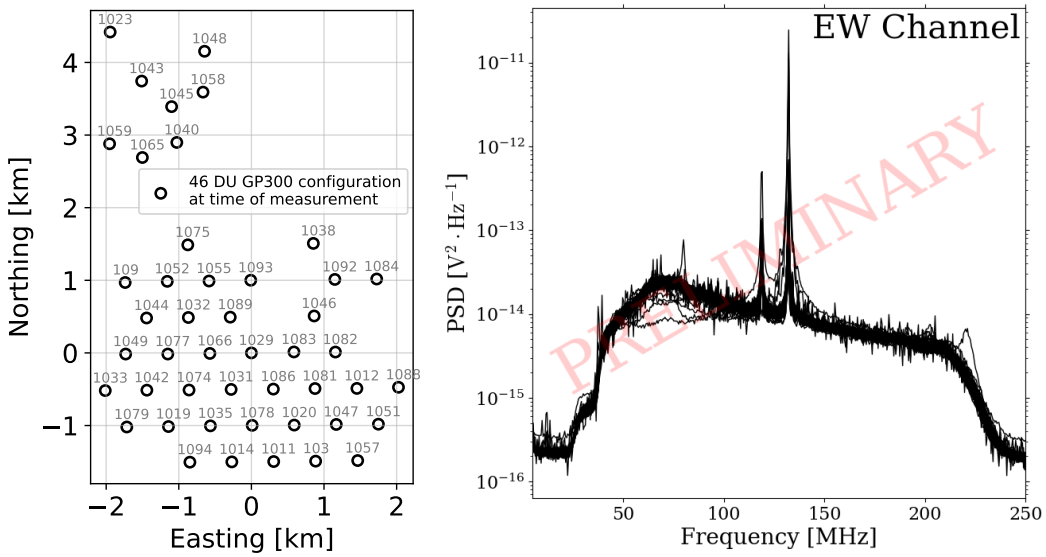

FIGURE 7.2: **Left:** Partial configuration of GP300 with 46 DUs that were deployed during the measurement time periods. Axes are aligned with magnetic East (x-axis) and North (y-axis) directions, respectively. **Right:** Power spectrum density curves measured on June 22, 2025 of the West-East arms of all 65 deployed GP300 DUs over the whole day. The frequencies affected by aeronautic communications, 119, 133, and 137 MHz show large amplitude spikes. Plot from [89].

$\sim$ 100 and $\sim$ 25 m from the altitudes I use for the GRAND star-shape and GP300 simulation libraries, respectively. As such, it could introduce inaccuracies in the energy reconstruction. However, this is likely only a minor effect. Regardless, for a more exact energy reconstruction, a new simulation set for GP300 would be beneficial, reflecting the exact DU positions and average observation altitude.

In addition, GP300 uses notch filters to block out certain frequencies. The frequencies 119 , 133 , and 137 MHz are strongly contaminated by anthropogenic radio noise from aeronautic communication channels. The right panel of Figure 7.2 shows power spectrum density curves of the currently deployed DUs where the noisy frequencies are clearly visible. We use these filters in order to make trigger decisions without being affected by the noise [12]. Due to bandwidth considerations, only the data for the x and y trace components of the measurements were saved without active notch filters. Consequently, the z trace I use for the energy reconstruction is filtered, slightly reducing the received power. To compensate for this, and to treat all trace components identically, I apply digital filters for the three affected frequencies to the x and y trace components. I accomplish this by setting the corresponding frequency bins to zero in the frequency domain. Additionally, the unfiltered z trace component has a timing offset of -80 ns. I correct for the offset in the pulse timing quality criterion, and during the calculation of the energy fluence from the reconstructed traces by shifting the signal window for the affected trace component accordingly.

Then, identically to the Section 6.7, I pass the reconstructed energy fluence for each DU, together with all necessary shower parameters to the LDF fit.

TABLE 7.1: Reconstructed shower parameters and goodness of fit of the LDF fit reconstruction for six event candidates measured by GP300. Parentheses behind parameter values show the corresponding uncertainty for the last digits. Time of measurement is given in local time at the site of the experiment.

CR candidate no. & date	E_{em} [EeV]	θ^{rec} [°]	ϕ^{rec} [°]	$d^{\mathrm{fit}}_{\mathrm{max}}$ [km]	χ^2/n.d.f
CRC00 (09.12.24, 05:47)	0.55(3)	78.6(6)	137.6(2)	75(16)	0.35
CRC04 (20.12.24, 04:39)	1.07(14)	79.3(5)	34.5(2)	119(40)	2.99
CRC10 (02.01.25, 00:37)	0.87(1)	70.4(8)	45.5(5)	26(1)	0.03
CRC11 (02.01.25, 01:32)	0.67(11)	72.4(4)	25.8(5)	60(44)	2.24
CRC18 (11.01.25, 22:05)	0.36(0)	70.9(5)	51.2(4)	29(2)	0.01
CRC31 (03.02.25, 12:54)	0.47(5)	69.8(5)	43.7(5)	45(20)	3.49

7.3 Reconstruction of six selected GP300 cosmic-ray candidates

By applying the LDF fit to all 41 candidates, I find 31 candidates with a converging LDF fit. The ten rejected candidates have too few DUs for the LDF fit after I apply the signal quality criteria to their traces. 17 event candidates remain after another quality cut on unreasonably large uncertainties on either arrival direction ($\sigma_{\mathrm{dir}} > 1°$), the fitted d_{max}, or the reconstructed electromagnetic energy (both relative errors >100%). I choose the six candidates I show here manually out of these 17. I motivate the selection with a preference of a high amount of triggered vs. non-triggered antennas on the footprint, and the agreement of the LDF fit with the geomagnetic fluence calculated from the event DUs with the signal model. As such, I consider them the event candidates with the highest confidence level to be real cosmic-ray events.

In Table 7.1, I show the candidate IDs, time of measurement, reconstructed shower parameters, and goodness of LDF fit for each candidate. The candidate IDs refer to a GRAND internal list of the 41 candidates, simply ordered by time of measurement.

Figure 7.3 shows the arrival directions of the six event candidates. It also shows the direction of the local geomagnetic field vector. Five of the candidates are in a cluster close to 45° in azimuth angle. This is partly due to the combination of this azimuth angle and a zenith angle of $\sim 70°$ leading to a geomagnetic angle close to 90°. Such a geomagnetic angle is naturally preferred since it leads to stronger geomagnetic emission. The clustering only appears on the western part of the sky due to the location of the mine transformer to the East of the array. As such, preference was given to the western part of the sky during the manual cuts of the cosmic-ray search [92]. In addition, this specific arrival direction is also preferred by the layout of the array. For air-showers coming from the North-West, i.e., the upper left in Figure 7.2, left panel, the array has a longer baseline.

In Figures 7.4–7.9, I display the results of the signal model and LDF fit energy reconstruction for each of the six event candidates In the top left panel of each figure, I display the LDF fit to the measured fluence. The top right panel shows how well the measured pulse arrival time at each DU agrees with the propagation of the reconstructed plane wave front for the arrival direction. The bottom panels show the radio footprint predicted by the LDF model on the array in ground and shower plane coordinates. The black-and-white dots show the deployed DUs at the time of measurement. For the ground plane, I also draw an ellipse representing the area inside twice the Cherenkov radius. This the range within which one can reasonably expect DUs to trigger. In the shower plane, I draw the actual Cherenkov radius to distinguish whether antennas lie in- or outside of it.

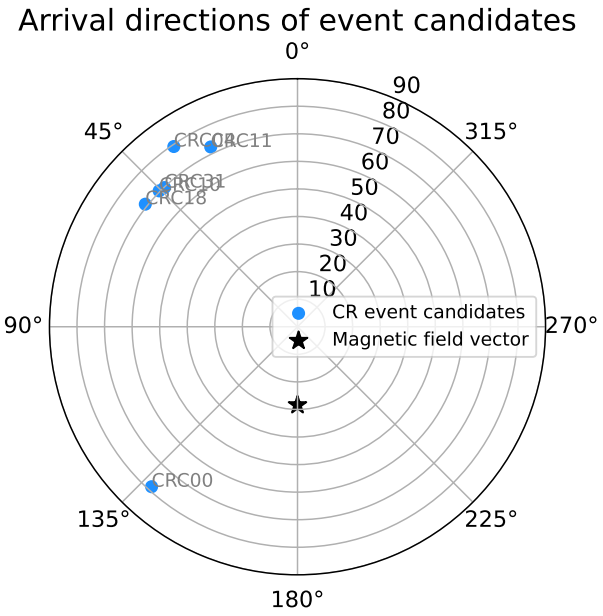

FIGURE 7.3: Polar plot of the arrival directions of the six cosmic-ray event candidates I show in Figures 7.4–7.9. Zero degrees corresponds to North, 90° to West. I show the arrival directions as blue points, each labelled with the corresponding candidate ID. The black star represents the direction of the local geomagnetic field vector.

Critically, detailed information about whether the deployed DUs were active at the time of measurement is not available. Unfortunately, this prevents conclusive discussion on the reasons why DUs on the high intensity parts of a footprint were triggered or not. For active DUs, the measured trigger efficiency is $\sim$ 75% [89]. This means that, in the case of an air-shower, approximately 75% of active DUs that would have been expected to see a signal will register the event. Naturally, none of the event candidates have DUs flagged for noisy ADC traces or low SNR since the same thresholds are used as trigger criteria.

Cosmic-ray candidates CRC00 (Fig. 7.4) and CRC04 (Fig. 7.5) have the largest antenna multiplicities and zenith angles among the six candidates. The large zenith angles lead to a larger radio footprint area than for the other candidates. Large parts of both footprints lie outside the array area. Both candidates have more than 5 deployed DUs within their footprint area which did not trigger. For CRC00, the fluence values do not follow the LDF fit line closely, but are compatible with it due to large uncertainties. With the exception of the DU closest to the shower core, all timing residuals are < 10 ns. For CRC04, two of its eight DUs are flagged by the peak timing cut. It has both the most non-triggered DUs and largest timing residuals out of the six candidates. As such, I consider CRC04 to have the lowest confidence level out of the six.

Candidates CRC10 (Fig. 7.6), CRC11 (Fig. 7.7), CRC18 (Fig. 7.8), and CRC31 (Fig. 7.9) all have zenith angles close to 70°. Consequently, their antenna multiplicities and footprints are smaller. For all of them, the LDF model fits closely to the measured energy fluence. With few exceptions, the timing residuals agree with the PWF reconstruction within the 15 ns uncertainties. For candidates CRC10 and CRC11, one can interpret the timing residuals as an arc of a circle with its lowest point at the shower core. Such an arc shows the realistic propagation of the radio emission as a spherical wavefront, slightly deviating from the plane wave approximation for smaller distances to the emission source. However, with only a small

amount of data points for each event and the inconsistent presence of the arc in the event candidates with lower zenith angles, I cannot confidently observe the presence of such an arc.

Notably, candidates CRC00, CRC10, and CRC18 all show too small values of χ^2/n.d.f.. By examining the LDF fits, it is apparent that this is caused by too large fluence uncertainties for these events. For the remaining candidates, the uncertainties seem adequately estimated. This is another indicator that there is room for improvement for the energy fluence uncertainty model.

I consider CRC31 to have the highest confidence level out of the six candidates. It has a stable LDF fit and reasonable uncertainties on the reconstructed energy and $d_{\max}$. All triggered DUs qualify as signal DUs. Since this candidate was chosen to be presented at ICRC25 [89], I specifically investigated the non-triggered DUs 1066 and 1032 on its Cherenkov ring. I found that DU1066 was inactive at the time of measurement. In addition, DU1032 showed a disproportionate amount of noise during the measurement time periods. As such, I consider there to be no active DUs on its footprint which did not trigger. However, I consider it to be only marginally better than candidates CRC00, CRC10, CRC11, and CRC18.

In Figure 7.10, I also show the measured voltage traces for candidate CRC31. I display the trace measured by each of the six triggered DUs in its own panel, ordered from earliest to latest pulse arrival time. The total measured trace is 2 μs long [92]. As I discuss in Section 7.2, the z component of the trace has a -80 ns offset. I show the offset in the plots with two grey bars. The signal pulse of the air-shower is clearly visible on all x and y channels at 520 ns after the start of each shortened trace. This is the time to which GRANDlib sets the measured pulse arrival time. Due to the nature of the HorizonAntenna DU (see Section 3.1), the z component is measured with only one real antenna arm. In addition, the vertical component typically receives a weaker signal than the horizontal x and y channels due to its orientation. This results in generally low-amplitude pulses in the z channel. This is consistent with the measurements. Notably, the response of the z channel does not quite reflect reality, as documented in reference [79] with the simulated antenna response to Galactic noise. Only DUs 1077 and 1031 have signal pulses in the z channel which stand out above the background noise. DUs 1074 and 1031 stand out with weaker pulse relative to the level of background noise. This is in line with expectations since they have large axis distances and, as such, receive a less intense signal.

All candidates, with the exception of CRC10, show values of the energy fluence which are likely affected by the electric field reconstruction bias. The parametrised geomagnetic fluence I show in the LDF plots is proportional to the $\vec{v} \times \vec{B}$ energy fluence (see Eq. (4.7)). The energy fluence at these DUs is likely overestimated. As such, the reconstructed electromagnetic energy of the candidates might be overestimated as well. However, it is not possible to quantify the impact precisely with such a small sample size. A reconstruction of the energy with a higher level of confidence necessitates an unbiased electric-field reconstruction. In addition, the positive bias I found for the fitted values of $d_{\max}$ (see Fig. 6.21) suggests that the $d_{\max}$ values for the event candidates are overestimated as well.

Within the GRAND collaboration, two other methods for the reconstruction of the electromagnetic energy of cosmic-ray air-showers have been developed. The angular distribution function (ADF) method by Guelfand et al. [123, 124] reconstructs the energy directly from the measured voltage traces. Another method by Ferrière and Benoit-Lévy [125] uses graph neural networks (GNN) for the reconstruction. For all six event candidates I show in this chapter, the reconstructed electromagnetic

energies from the method described in this work and the ADF reconstruction agree within a few percent. The GNN reconstruction agrees on the same level for candidates CRC00, CRC04, and CRC10, but yields higher energies for CRC11, CRC18, and CRC31.

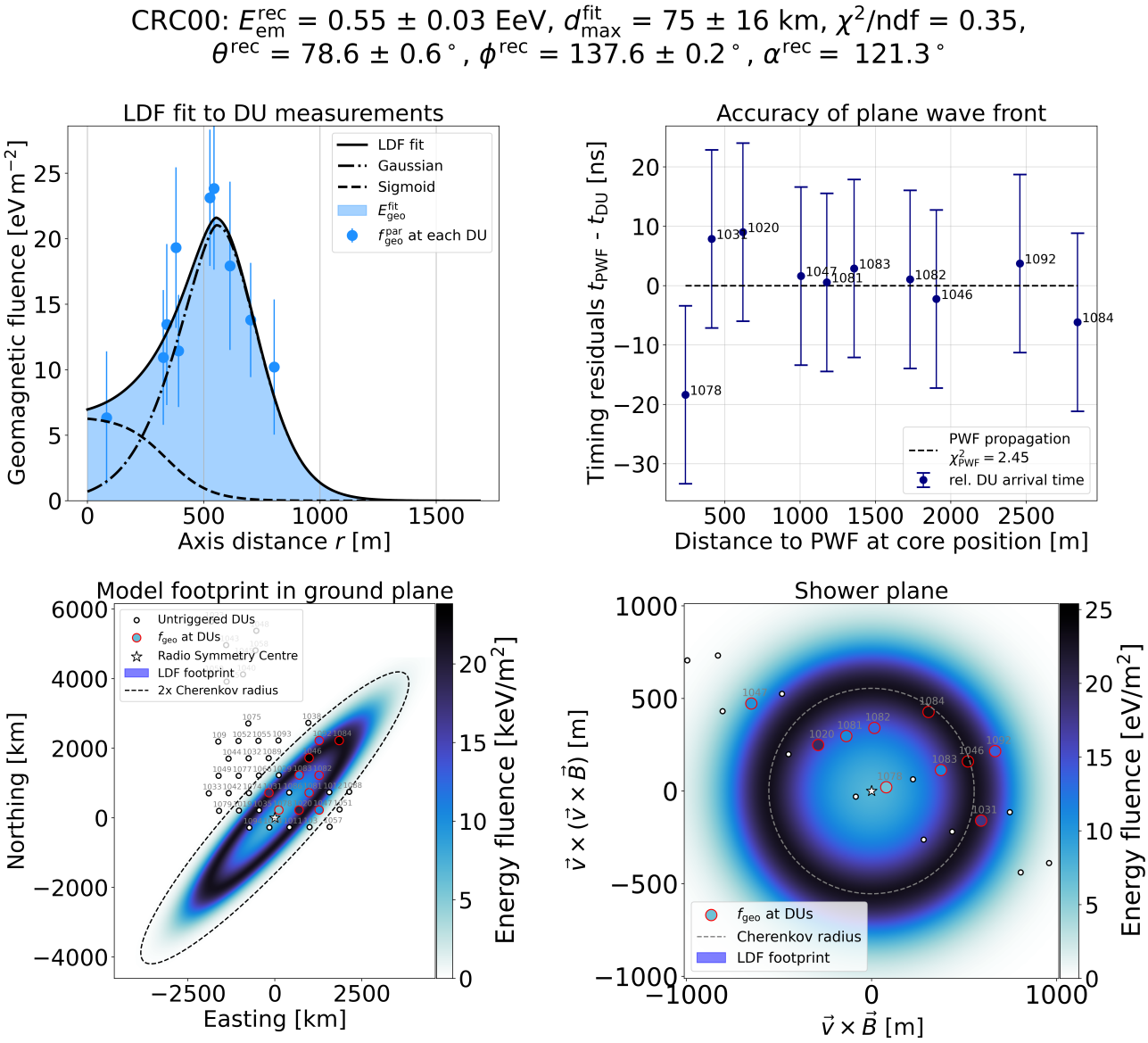

FIGURE 7.4: Signal model and LDF fit energy reconstruction applied to cosmic-ray event candidate CRC00 measured by a partial configuration of GP300. Reconstructed air-shower parameters in figure title and in Table 7.1. **Top left:** LDF fit (black solid line) to the geomagnetic energy fluence (blue points) calculated from the voltage traces measured by each DU against the radial axis distance r from the fitted radio symmetry centre. The dot-dashed and dashed lines, respectively, show the Gaussian and sigmoid components of the LDF. The coloured area under the LDF curve represents the geomagnetic radiation energy E_{geo}. **Top right:** Time difference between the plane wave front, propagating at the speed of light and the measured arrival time at each DU. The data are shown with respect to the distance to the plane wave front, intersecting with the ground at the radio symmetry centre. **Bottom left:** Top-down view of GP300 configuration at time of measurement. DUs that measured a signal and were not eliminated by quality cuts are shown as coloured points with red borders. Black-and-white dots show the positions of DUs which did not trigger during the event. The white star shows the fitted radio symmetry centre position. I display the fluence footprint from the LDF fit as a blue contour on the array. A DU with the same colour as the background indicates agreement with the model. I label each DUs with its ID. **Bottom right:** Same information as bottom left in shower plane coordinates.

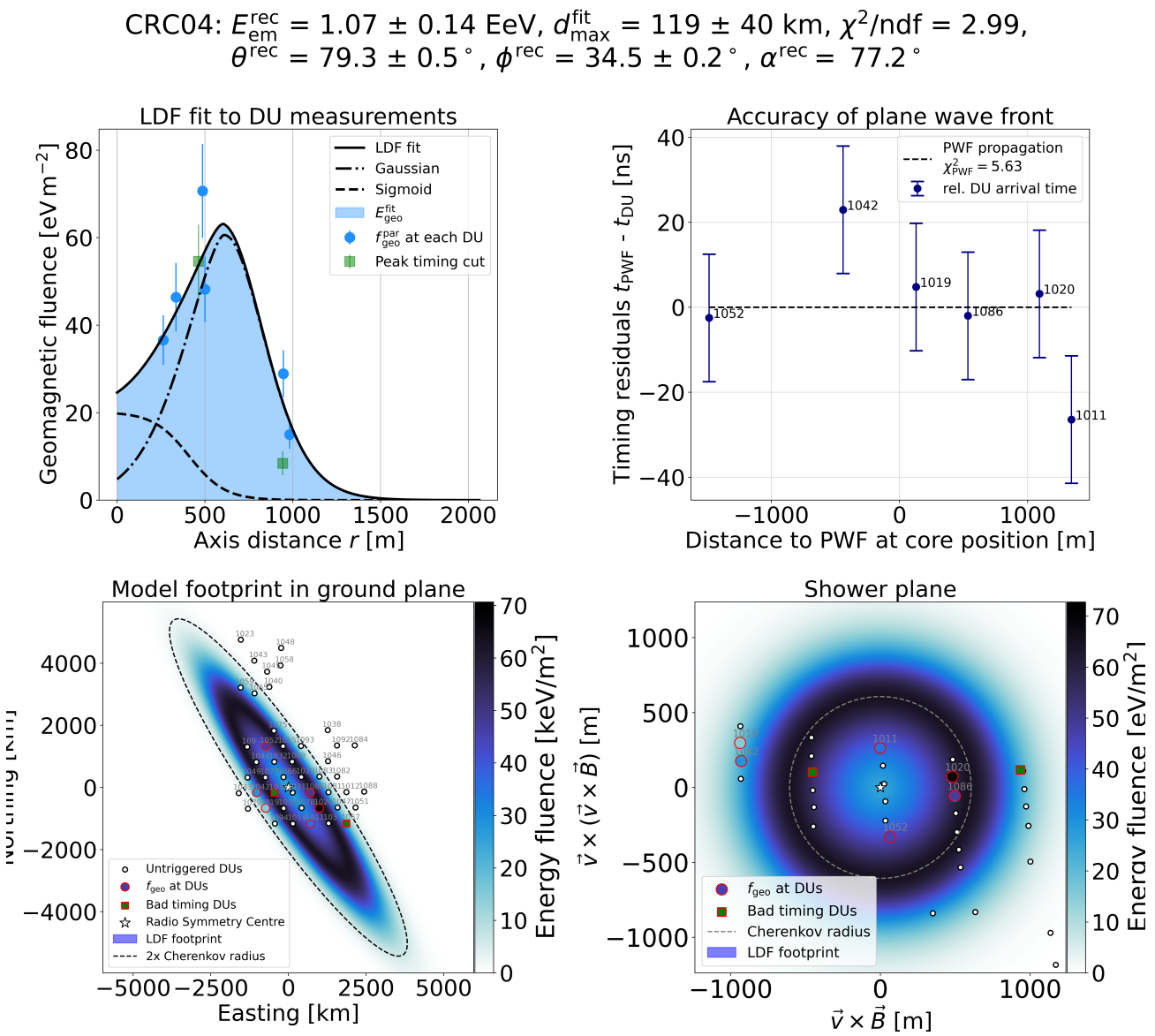

FIGURE 7.5: Signal model and LDF fit energy reconstruction applied to cosmic-ray event candidate CRC04 measured by a partial configuration of GP300. Reconstructed air-shower parameters in figure title and in Table 7.1. See caption of Figure 7.4 for a detailed description of the panels. Green squares show DUs eliminated by the peak timing criterion in both bottom panels.

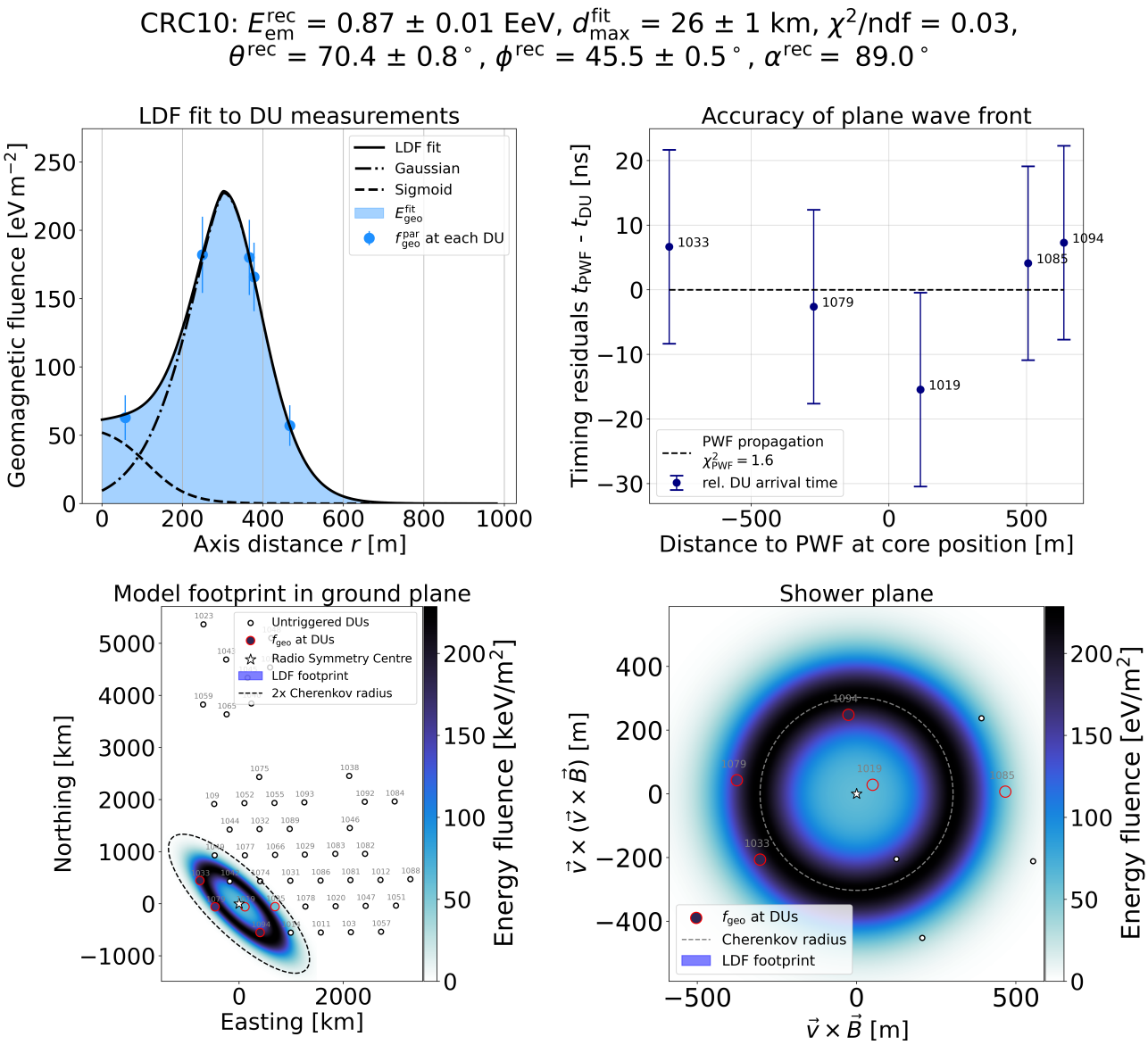

FIGURE 7.6: Signal model and LDF fit energy reconstruction applied to cosmic-ray event candidate CRC10 measured by a partial configuration of GP300. Reconstructed air-shower parameters in figure title and in Table 7.1. See caption of Figure 7.4 for a detailed description of the panels.

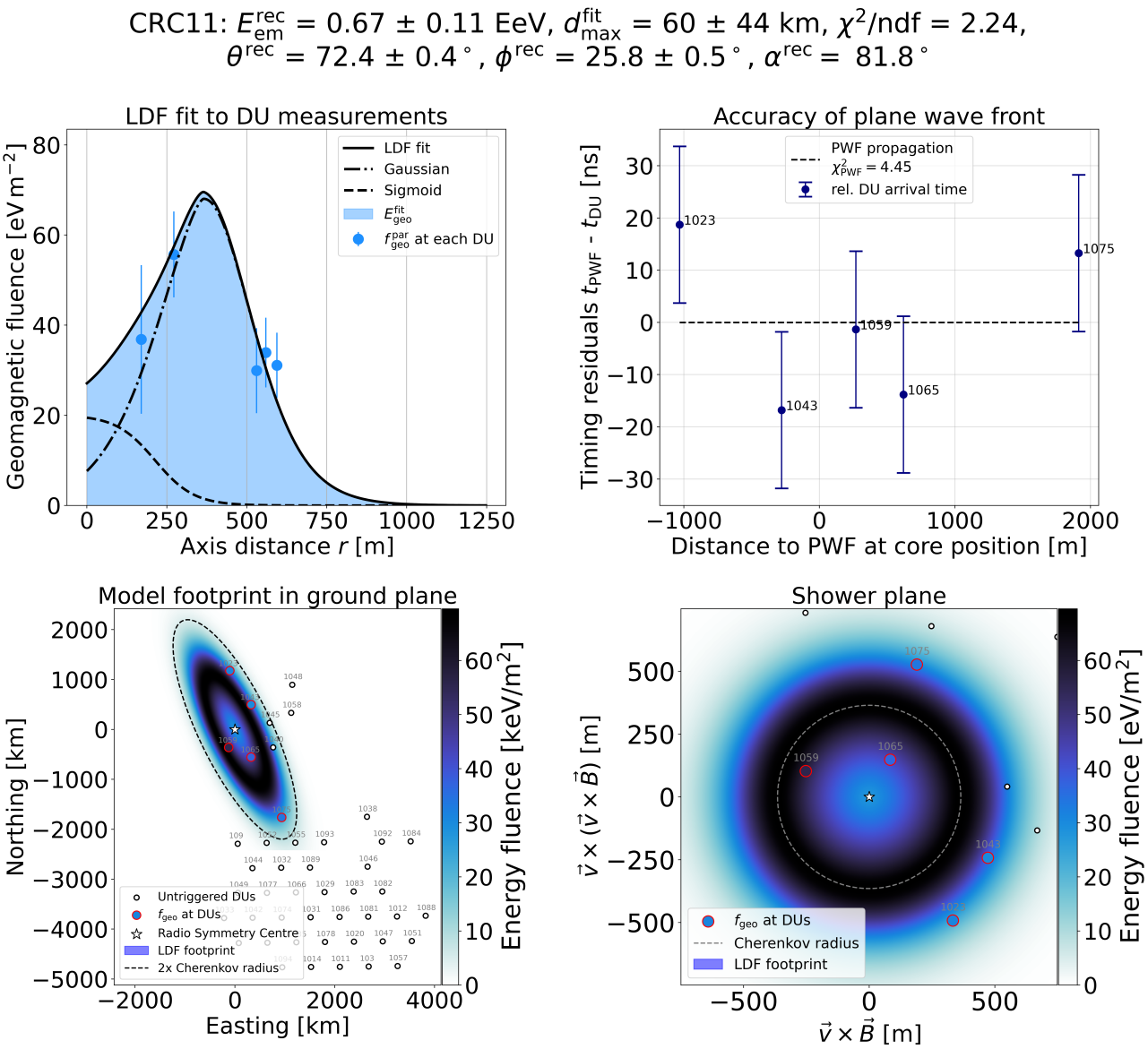

FIGURE 7.7: Signal model and LDF fit energy reconstruction applied to cosmic-ray event candidate CRC11 measured by a partial configuration of GP300. Reconstructed air-shower parameters in figure title and in Table 7.1. See caption of Figure 7.4 for a detailed description of the panels.

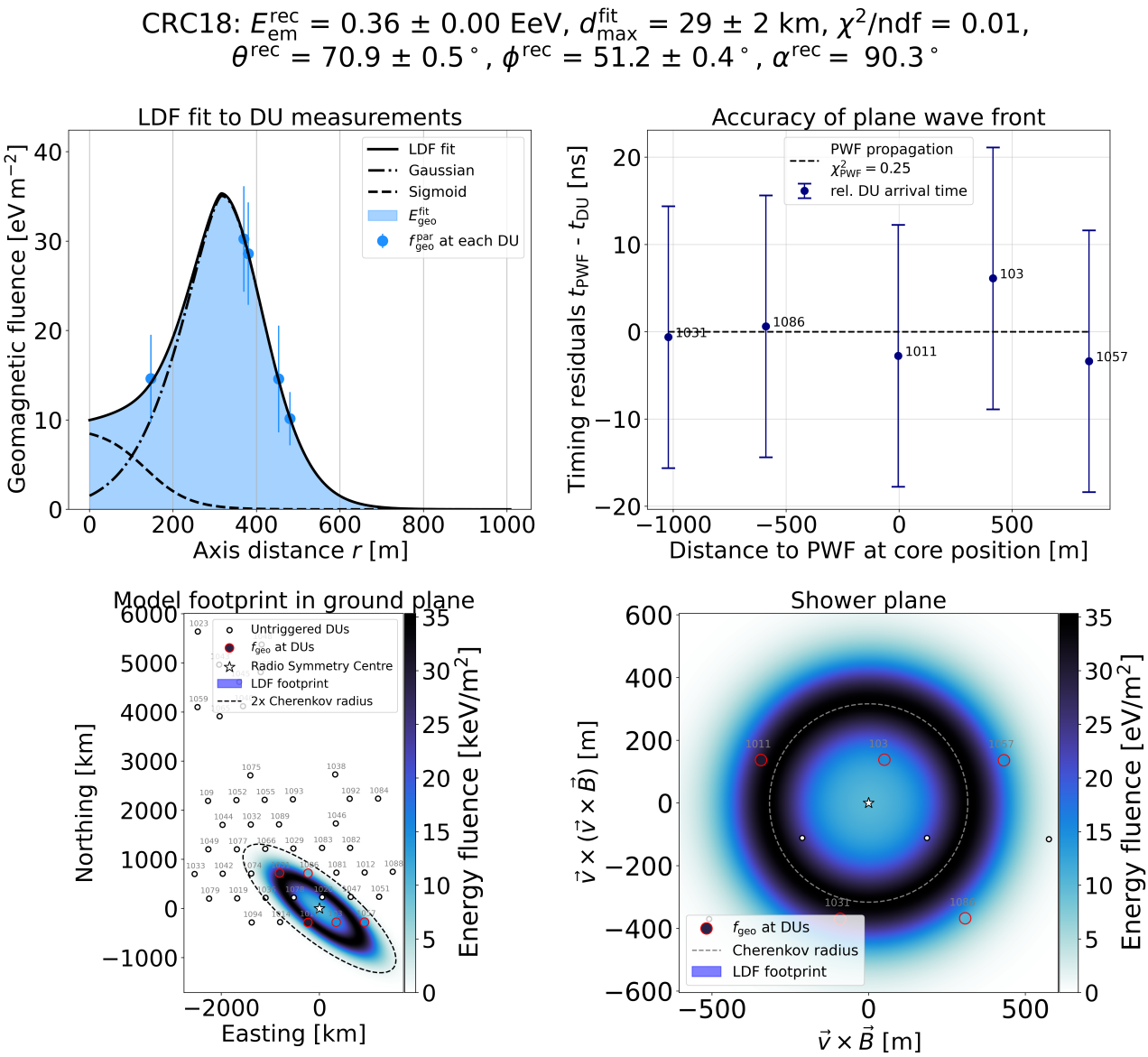

FIGURE 7.8: Signal model and LDF fit energy reconstruction applied to cosmic-ray event candidate CRC18 measured by a partial configuration of GP300. Reconstructed air-shower parameters in figure title and in Table 7.1. See caption of Figure 7.4 for a detailed description of the panels.

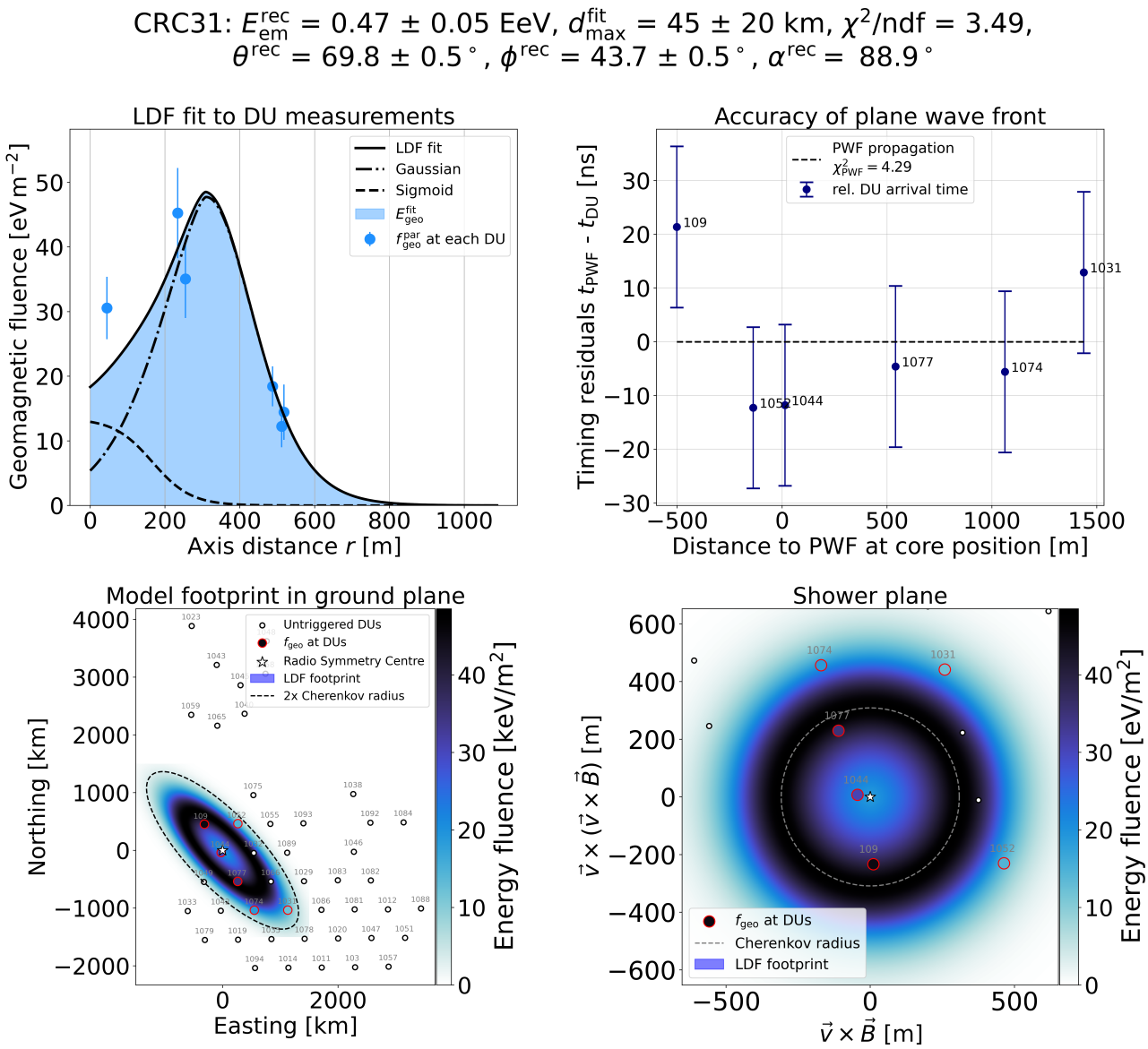

FIGURE 7.9: Signal model and LDF fit energy reconstruction applied to cosmic-ray event candidate CRC31 measured by a partial configuration of GP300. Reconstructed air-shower parameters in figure title and in Table 7.1. See caption of Figure 7.4 for a detailed description of the panels.

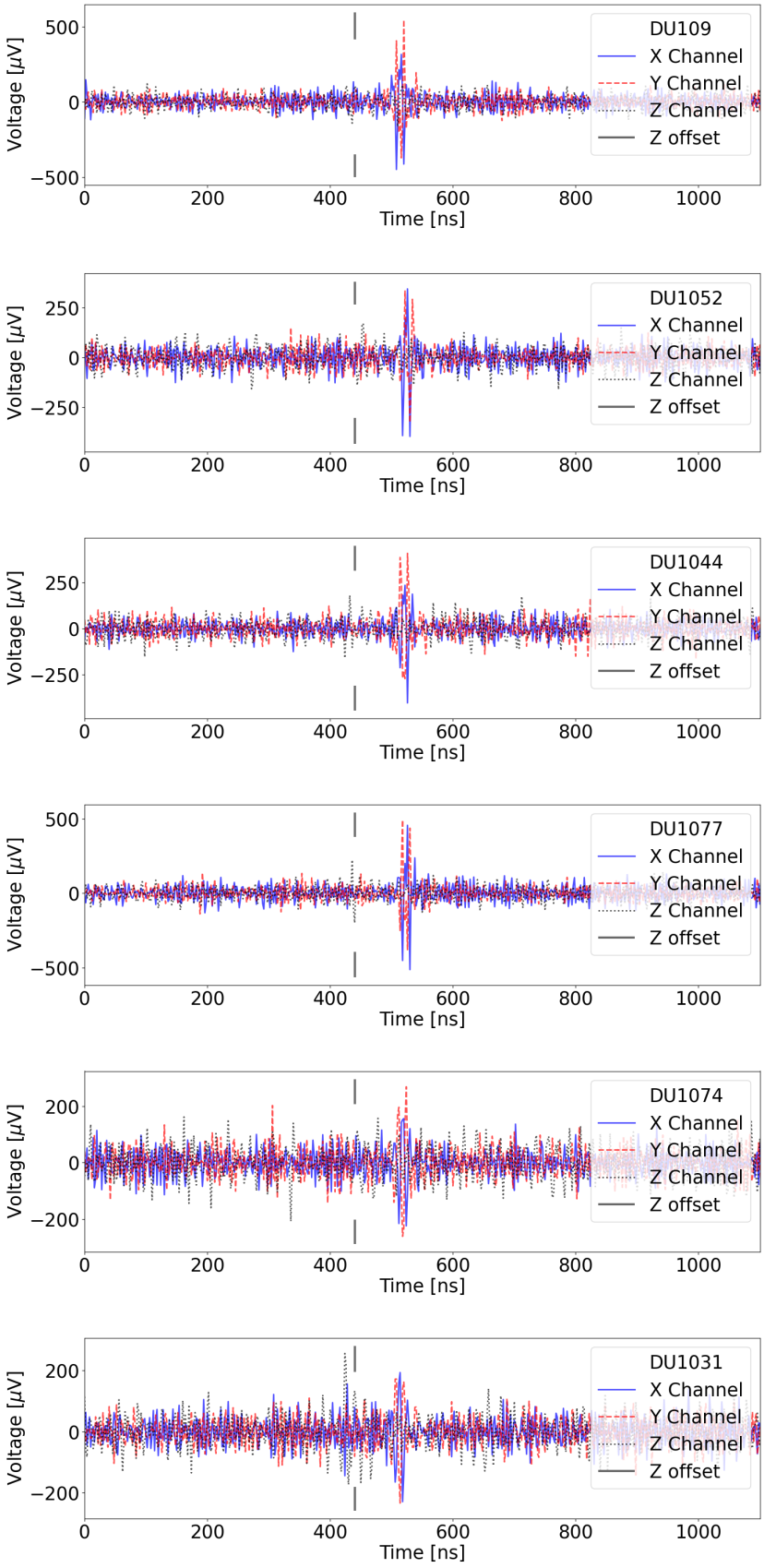

FIGURE 7.10: Measured voltage traces of GP300 cosmic-ray event candidate CRC31. I give the ID of the measuring DU in each plot legend. The grey vertical lines indicate the pulse timing of the unfiltered Z trace with its timing offset.

Chapter 8

Study of GP300 and GRAND10k Detection Performance

Building on my work on the signal model and energy reconstruction, their performance on simulations, and their application to measured cosmic-ray event candidates, I present in this chapter a simulation study on detector performance. The detectors in questions are the GRAND prototype array GRANDProto300 (GP300) and a possible configuration of GRAND10k, the next stage of GRAND. For details on GRAND, see Chapter 3. I use the same simulation libraries as for the reconstruction performance study (see Section 6.1). For this study, I again exclude all simulated GP300 events with zenith angles $> 85^\circ$ for the sake of consistency with my reconstruction performance study.

I calculate the detection efficiency based on the same criteria for signal viability, antenna multiplicity, and LDF fit success I also used for the analysis under measurement conditions in Section 6.7. This includes all effects of the hardware chain, measured background noise, electric-field reconstruction, and LDF fit reconstruction. As such, for GP300 specifically, this is a fully realistic performance study. I divide the simulated events into bins of both zenith angle and primary energy to resolve details of the efficiency. Subsequently, I calculate the effective aperture of the detector for each zenith angle and energy bin. I determine the exposure for a given time period of measurements with the detector by multiplying the total aperture with the time period. Finally, I estimate the number of events the detector expects to measure during the exposure time by integrating the cosmic-ray energy spectrum over the relevant energy range and multiplying with the exposure.

8.1 Detector efficiency

I define the detection efficiency,

$$\epsilon = \frac{N_{\text{detected}}}{N_{\text{total}}}, \tag{8.1}$$

as the ratio of the number of "detected" events N_{detected} to the total number of simulated events N_{total}. An event counts towards the "detected" fraction if it fulfils the two following criteria: On the one hand, an event has to have at least five signal antennas. The signal an antenna receives has to pass the quality cuts on ADC and voltage amplitude in the electric-field reconstruction (see Section 6.7). Further, I require the reconstructed electric-field trace to have a signal-to-noise ratio SNR > 5 (see Section 6.5). I choose a high SNR threshold due to the radio-only nature of the simulated detectors. Signals with a lower SNR will be difficult to distinguish from thermal noise fluctuations in practice. If the signal at an antenna passes these steps,

TABLE 8.1: Total detection efficiency of GP300 and GRAND10k for all cosmic-ray events in the two simulation libraries I described in Section 6.1. n_{ant} stands for the antenna multiplicity. "LDF fit" refers to whether an event has a converging LDF reconstruction.

GP300	**N**	**%**
Total	12,804	100%
$n_{\text{ant}} \geq 5$	9278	72.5%
LDF fit	9198	71.8%

GRAND10k	**N**	**%**
Total	5891	100%
$n_{\text{ant}} \geq 5$	4352	74.3%
LDF fit	4321	73.7%

I consider the antenna viable. These are the same criteria I use for antennas to be included in the LDF fit. As the second condition, I require each event to have a converging LDF fit with reasonable errors. Since this study focuses simply on detection, I also count antennas with saturated ADC traces towards the antenna multiplicity. However, I still do not consider them in the LDF fit. Naturally, events, that only reach the required antenna multiplicity by including saturated DUs, cannot have a converging LDF fit.

Table 8.1 shows the total amount of simulated events, and the percentage of events passing the detection criteria for each detector. A slightly larger fraction of events pass the detection criteria for GRAND10k. Notably, almost all events passing the antenna multiplicity criterion also have a converging LDF reconstruction. To analyse the detection efficiency of the two detectors in more detail, I bin the simulated events in cosmic-ray primary energy and zenith angle. Due to the identical parameter space concerning cosmic-ray primary energy and arrival direction of the simulation libraries for the two detectors, the binning in energy and zenith angle is the same as well. I divide the zenith angle range from 65 to 85° into ten equidistant bins with a width of 2°. For the energy, I choose either six or twelve equidistant, logarithmic bins to properly reflect the three orders of magnitude spanned by the energy range of 10^{17} to 10^{20} eV. For each experiment, every bin has approximately the same number of events since the zenith angles and primary energies of the simulations are uniformly distributed along the binned axes.

When analysing the detection efficiency across these wide parameter spaces, I consider how the radio footprint of an air-shower changes with respect to the zenith angle and primary energy. Trivially, a higher primary energy leads to a higher intensity radio footprint for a constant zenith angle. The primary energy has no significant impact on the size of the footprint features, like the Cherenkov radius, but higher intensity causes antennas further from the radio core to receive a sufficiently strong signal. The zenith angle influences the footprint intensity as well. A larger zenith angle leads to a longer distance d_{max} between the shower maximum and the detector. Since I assume point-like emission from the shower maximum (see Section 4.1), it follows that the radio emission loses intensity with $1/d_{\text{max}}^2$. Further, the size of the radio footprint on the ground plane strongly depends on the zenith angle as the illuminated area grows with the distance from the source and the inclination of the shower. As such, showers with large zenith angles generally have a higher antenna multiplicity. In addition, the depth of maximum X_{max} has an influence since it directly impacts d_{max}. However, especially at zenith angles above 75°, changes in zenith angle have a more dominant effect on d_{max}.

Figure 8.1 displays the efficiency binned in zenith angle and energy. The shown efficiency includes whether the LDF fit converges. Here, the energy range is divided into six bins with two bins together spanning an order of magnitude. The behaviour of the radio emission I describe above clearly appears in the efficiency curves. The

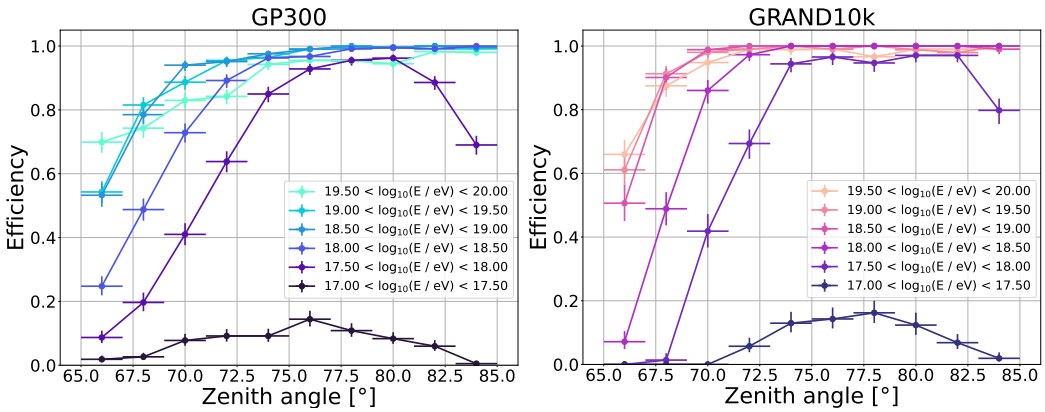

FIGURE 8.1: Detection efficiency as a function of shower zenith angle. The detection criteria are described in the text. The efficiency is binned in 2° zenith angle bins (x-axis) and logarithmic bins in cosmic-ray primary energy (colour mapping). For the vertical error bars, I use binomial statistics to determine the statistical uncertainty at a 1-sigma confidence level. The horizontal bars indicate the 2° zenith angle bin width. **Left:** GP300. **Right:** GRAND10k.

left panel shows the efficiency for GP300. For the lowest energy bin, background noise and low antenna multiplicity leads to most simulated events not counting as detected across all zenith angles. In the next higher energy bin, the efficiency rises with the zenith angle until the loss of intensity from the distance to the emission source dominates and leads to a decrease for the highest zenith angle bins. For the remaining energy bins, the efficiency rises with increasing zenith angle until reaching full efficiency around 77° for the four highest energy bins. For the highest energy bin, the efficiency is slightly lower due to saturated measurements.

For GRAND10k in the right panel, the behaviour with respect to energy is similar. For the lowest energies, the middling zenith angles reach slightly higher efficiency than for GP300. In addition, the next higher energy bin only loses efficiency for the highest zenith angles. Both effects are due to the large size of GRAND10k. It guarantees the containment of the footprint within the array area. Many of of the events I simulate for GP300 have footprints that partly lie outside of the array area. Analogously to GP300, saturated measurements affect GRAND10k, but are mitigated by the large array area as well. For low zenith angles, GRAND10k is less efficient due to the lack of an in-fill. However, the efficiency grows more steeply with zenith angle than it does for GP300 and reaches maximum efficiency for the four highest energy bins at 72°.

Analogously to Section 6.8, I investigate the existence of a bias in detection efficiency depending on the cosmic-ray primary particle. Figure 8.2 shows the efficiency curves for protons and iron nuclei in four energy bins. The wider energy binning leads to a higher efficiency for the lowest energy bin in each panel. For both detectors, the detection efficiency is higher for protons for the lowest energy bin. For the remaining three energy bins, the efficiency is slightly higher for iron. This is in line with expectations since showers initiated by iron nuclei have a shallower X_{max}, and, as such, their footprints spread out over a larger area. The resulting lower energy fluence at each antenna leads to more undetected events. For higher energies, the same effects lead to a larger radio footprint which benefits its likelihood of having sufficient antenna multiplicity. However, these differences are small. The 1-sigma confidence intervals, indicated by the vertical error bars, overlap for the majority of data points.

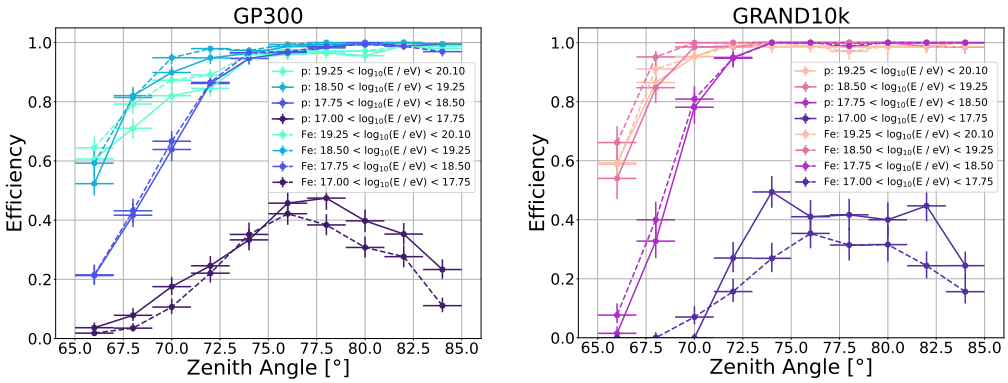

FIGURE 8.2: Detector efficiency as a function of shower zenith angle, shown separately for the proton and iron nuclei primaries of each simulation library. Solid lines show the efficiency for protons, dashed lines for iron. The efficiency is binned in 2° zenith angle bins (x-axis) and logarithmic bins in cosmic ray primary energy (colour mapping). For the vertical error bars, I use binomial statistics to determine the statistical uncertainty at a 1-sigma confidence level. The horizontal bars indicate the 2° zenith angle bin width. **Left:** GP300. **Right:** GRAND10k.

8.2 Aperture

The aperture of a radio array for the detection of air-showers is, analogously to the aperture of a camera or an ordinary telescope, the "opening" through which the instrument can receive a signal. For a radio array, the "opening" is the effective area of the array for air-showers arriving at a certain zenith angle multiplied with the solid angle, i.e., the region of the sky, such air-showers can come from. As such, the aperture $\mathcal{A}$ for a zenith angle range $\Delta\theta = [\theta_1, \theta_2]$ follows from

$$\mathcal{A}(\Delta\theta) = A \cdot \pi \cdot \left[\cos^2(\theta_1) - \cos^2(\theta_2)\right]. \tag{8.2}$$

This equation is derived in references [126, 127] as part of a larger derivation. The zenith angle term reduces the aperture for large zenith angles since the effective area of the array—the area of the array when projected into the shower plane—decreases for more inclined showers. In other words, these showers are less likely to "hit" the array directly, i.e., the aperture I calculate here is for "contained events" that have a radio core within, or very close to, the area of the array. In the case of GRAND, the signal can arrive from any direction on the sky, and even from slightly below the horizon for air-showers initiated by Earth-skimming neutrinos. Due to the wide antenna spacing of 1 km^2, both detectors are significantly less sensitive at zenith angles $< 65°$. The radio footprint for these angles becomes much smaller and is unlikely to illuminate enough antennas. As such, I use 65° as the lower zenith angle boundary, and 85° as the upper boundary. Applying this range, Eq. (8.2) yields a maximum (geometrical) aperture of $\mathcal{A}_{\text{max}}^{\text{GP300}} = 107\,\text{km}^2\,\text{sr}$ for GP300. For GRAND10k, I reduce its total area of 10,000 km^2 by a 5 km edge all around the array to 8050 km^2. I motivate this with the small 5×5 km area in the middle of the array where the simulated shower cores can fall (see right panel of Figure 6.1). The edge, of the same width as the core area, addresses that no simulated shower can have a core on this edge and, consequently, have its footprint not contained in the array area. This results in a more conservative maximum (geometrical) aperture of $\mathcal{A}_{\text{max}}^{\text{10k}} = 4325\,\text{km}^2\,\text{sr}$.

For the effective aperture, I simply multiply the maximum aperture, now also binned in zenith angle and primary energy, by the binned efficiency I determine in

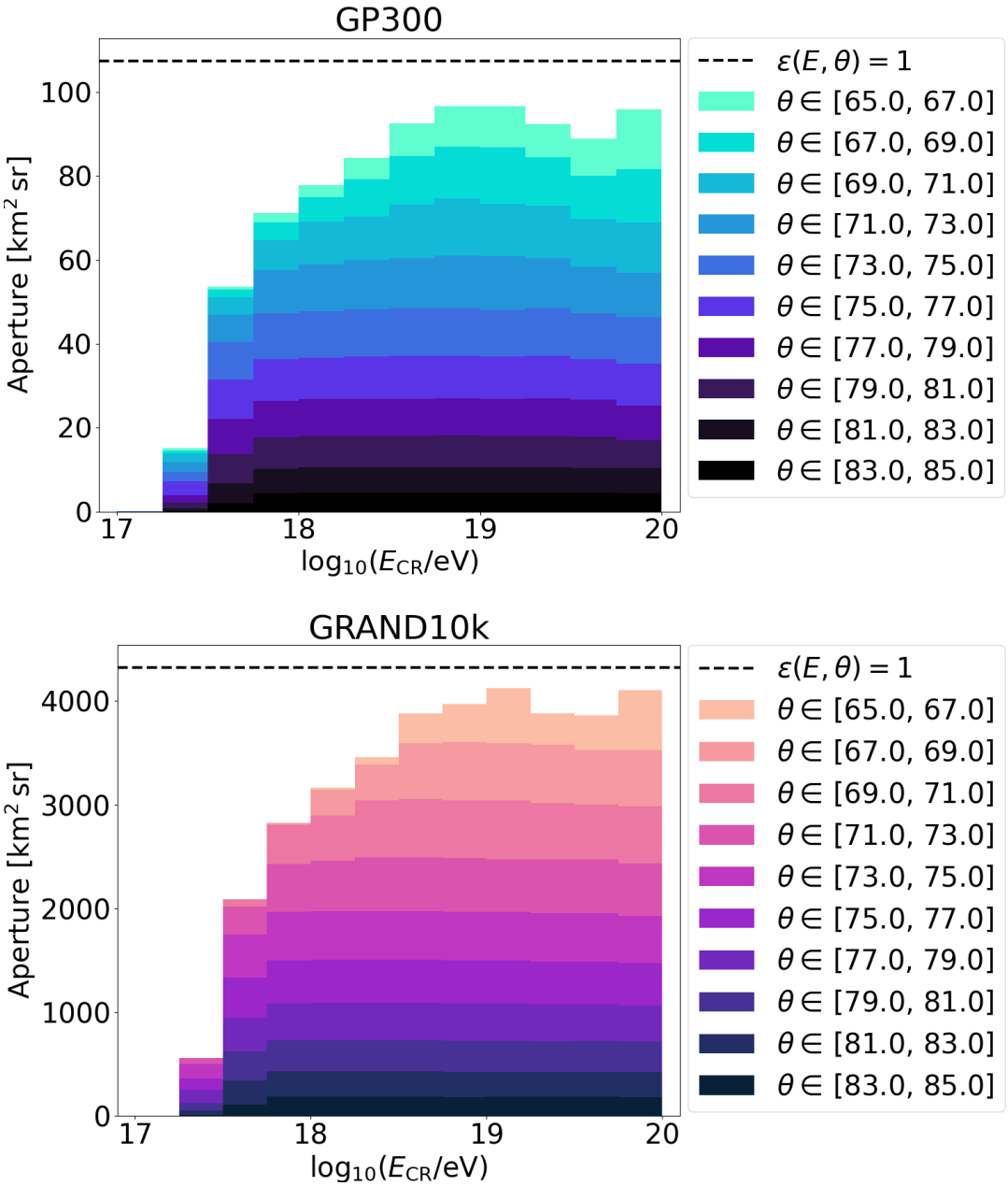

FIGURE 8.3: Stacked histograms showing the effective aperture of the detectors for each energy bin. The black dashed line at the top shows the maximum aperture for zenith angles between 65 and 85° for the respective total detector area. Note the different y-axis scales. Zenith angle bins are expressed in the colour maps. I calculate the aperture with Eq. (8.3). **Top:** GP300 with an area of 200 km^2. **Bottom:** GRAND10k with an area of 10,000 km^2., reduced to 8050 km^2 by the 5 km edge.

the previous section. For any zenith angle bin $\Delta\theta$, energy bin ΔE, and their detection (and reconstruction) efficiency ϵ, the effective aperture reads:

$$\mathcal{A}_{\text{eff}}(\Delta\theta, \Delta E) = A \cdot \pi \cdot \left[\cos^2(\theta_1) - \cos^2(\theta_2)\right] \cdot \epsilon(\Delta\theta, \Delta E). \tag{8.3}$$

Figure 8.3 shows the binned effective apertures of the detectors as stacked histograms. I show the maximum (geometrical) aperture as a dashed line in each panel. Naturally, the maximum aperture of GP300 is much smaller than that of GRAND10k due to the difference in detection area. Here, I use twelve energy bins. The equidistant zenith angle bins lead to decreasing maximum aperture per bin for increasing zenith angles. This is visible in the figure by the shrinking vertical size of the horizontal contours towards darker colours. Smooth horizontal contours indicate full efficiency for the corresponding zenith angle bin. Accordingly, the figure shows that GRAND10k is fully efficient for a larger fraction of its parameter space than GP300. For primary energies $E_{\text{CR}} < 10^{18.5}$ eV, the effective aperture of GRAND10k decreases more steeply than that of GP300. Neither array reaches its ideal aperture for any of the energy bins. The reason for this is a high detection threshold, enforced by the noise level and the quality criteria on the pulse amplitude, timing, and SNR for showers with faint signals.

8.3 Expected number of events

Based on the effective aperture, I estimate the number of events each detector will detect and be able to reconstruct within an exposure time τ_{exp}. The exposure $\mathcal{E}$ of an array with effective aperture $\mathcal{A}_{\text{eff}}$ follows from,

$$\mathcal{E} = \tau_{\text{exp}} \cdot \sum_{\Delta\theta} \left(\sum_{\Delta E} \mathcal{A}_{\text{eff}}(\Delta\theta, \Delta E) \right), \tag{8.4}$$

where I sum over all aperture bins in energy and zenith angle from the previous section. I calculate the number of events N detected above a threshold energy E_{thr},

$$N(E > E_{\text{thr}}) = \mathcal{E} \int_{E_{\text{thr}}}^{10^{20}\,\text{eV}} \mathcal{J}\, \mathrm{d}E, \tag{8.5}$$

by multiplying $\mathcal{E}$ by the flux of cosmic rays. I obtain the flux by integrating over the cosmic-ray energy spectrum $\mathcal{J}$ from E_{thr} to 10^{20} eV, the upper boundary of the energy range I use in this work. I use the energy spectrum as it is characterised in reference [128].

Figure 8.4 shows the cumulative event numbers above E_{thr} within an observation time of one year for both detectors. In both panels, the upper points in light colours represent the numbers for the full effective aperture I calculate in the previous section. The lower points in dark colours show the event numbers if only aperture bins with efficiency $> 97\%$ are included. Only such bins can be used to infer the statistical behaviour of the measured events. I determine the upper and lower limits of each point by varying the efficiency to the edges of its confidence intervals and repeating the calculation. Following from the aperture calculation, GRAND10k has a much larger exposure than GP300. As such, GRAND10k expects to detect event numbers orders of magnitude higher at every level of energy. Neither detector has any energy bins with fully efficient aperture for $E_{\text{thr}} < 10^{17.75}$ eV. Using their full effective aperture, GP300 and GRAND10k, respectively, expect to detect about $35{,}200^{+7900}_{-4300}$ and

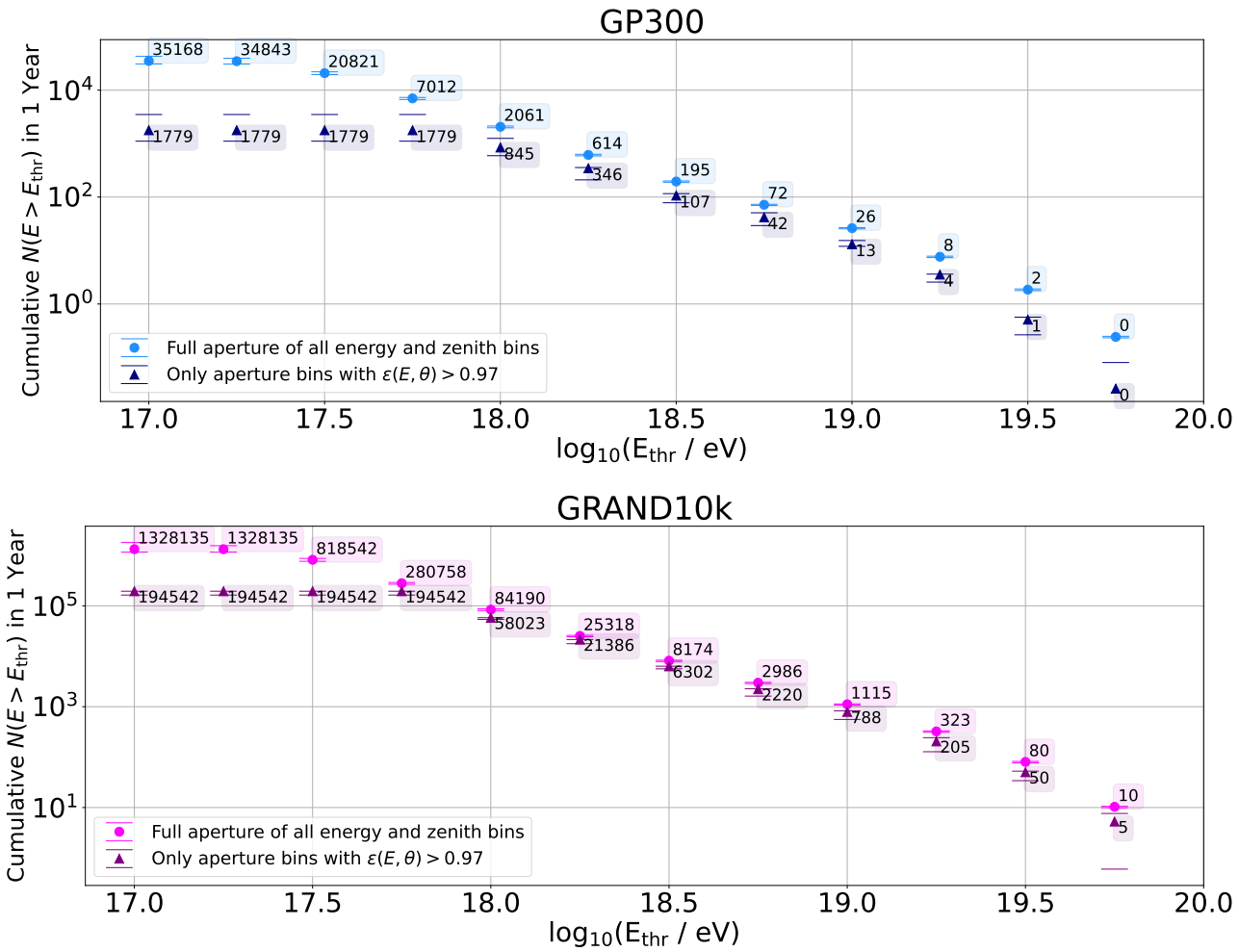

FIGURE 8.4: Number of detected and reconstructed cosmic-ray events with primary energy above a threshold energy E_{thr} expected within one year of exposure for the respective detector. I calculate each number by integrating the energy spectrum above E_{thr} and then multiplying by the one-year exposure from Eq. (8.4). I round each number to the closest integer. I use the energy spectrum as characterised by reference [128]. The points show the number of events using the full effective aperture indicated by the stacked histograms in Figure 8.3. The triangles indicate the number of events for only the bins which have at least 97% detection efficiency. I calculate the upper and lower limits by varying the efficiency to the edges of its confidence intervals. **Top:** GP300. **Bottom:** GRAND10k.

$1{,}330{,}000^{+470{,}000}_{-170{,}000}$ cosmic-ray events above $E_{\text{thr}} = 10^{17}\,\text{eV}$ within one year of exposure. However, for this energy threshold, the detection efficiency strongly depends on exact knowledge of the hardware response, as well as the level of background noise. The expected event numbers are doubly affected since the multiplied flux of cosmic rays is at its highest at the lower energy boundary. As such, a more "stable" comparison is a threshold energy of $E_{\text{thr}} = 10^{18}\,\text{eV}$. For this threshold, GP300 and GRAND10k expect to detect $\sim$2000 and $\sim$84,000 events per year, respectively. In addition, the event numbers for the full aperture and $> 97\%$ effective aperture begin to correspond more closely to each other for both detectors.

For completeness, I also calculate the event numbers when considering the full area of GRAND10k. In this case, GRAND10k expects to detect about $1{,}650{,}000^{+590{,}000}_{-210{,}000}$ cosmic-ray events above $E_{\text{thr}} = 10^{17}$ eV, and about $\sim$105,000 cosmic-ray events above $E_{\text{thr}} = 10^{18}\,\text{eV}$ within one year of exposure.

Chapter 9

Discussion

In this chapter, I discuss the results of my work. I put the different aspects of my work in context with each other. I point out and discuss open questions, as well as possible improvements concerning the analyses I presented in the previous chapters. I also discuss possible future applications of my work.

9.1 Signal model and energy reconstruction

I determine the uncertainties on the reconstructed electromagnetic energy E_{em} from the uncertainties assigned to the fit parameter E_{geo} during the LDF fit. I propagate it with Gaussian error propagation. Similarly to previous iterations of the model [129, 9], these uncertainties generally seem underestimated. There are two factors which likely contribute to this. The signal model and energy reconstruction go through three layers of parametrisation: the determination of the geomagnetic fluence with the charge-excess fraction, the description of the LDF shape parameters with d_{max}, and, finally, the correction of the geomagnetic radiation energy and its correlation with E_{em}. Only from the third step onwards do I propagate any uncertainties forward. As such, I neglect any systematic or statistical uncertainties affecting the previous two steps. On the other hand, the uncertainties on the energy fluence appear too small while tuning the model. In the presence of noise, I add an additional noise term to the energy fluence uncertainty to mitigate this. However, the pull distributions for both the analysis with artificial noise and under realistic measurement conditions still suggest that a revision of the uncertainty models is necessary. The pull distributions also indicate that, currently, the goodness-of-fit of the LDF fit is not a fully reliable indicator for whether a measurement is a real cosmic-ray event.

9.2 Universality of the signal model

Both for the RdStar library, representing the GRAND@Auger site, and the GRAND star-shape library, representing the site of GP300, I observe excellent intrinsic reconstruction performances with a resolution of $\sim$3% and a vanishing bias. This is on-par with the intrinsic resolution achieved by the low-frequency model for the Pierre Auger observatory [9]. A slight degradation is apparent only for the largest zenith angles. This indicates a loss of accuracy of the LDF model for the most inclined showers. As such, I successfully and accurately apply the signal model and energy reconstruction to both sites. The two sites correspond to near-extreme values of the geomagnetic field strength. This implies the viability of the model for any configuration of the geomagnetic field, given the chosen site is radio-quiet.

It is important to note that intrinsic study only includes energies down to 10^{18} eV. This could impact the performance in the reconstruction studies with realistic layouts in the energy range between 10^{17} and 10^{18} eV. This might explain the worse performance at low cosmic-ray energies for the study without artificial or measured noise. However, for the subsequent studies, I expect the noise to have a larger impact on the performance.

The changes I make to the LDF functional form and the density correction term are extensions of the previous iteration of the signal model. As such, the model is viable for the whole 30-200 MHz frequency band. I expect the use of any sub-band within this frequency range to require retuning of the model parameters, but no further modification of the model itself. I also expect the signal model to be viable for even higher frequencies in the same way. However, I expect an upper boundary where the loss of signal coherence becomes too severe to accurately compensate for.

9.3 Reconstruction performance studies under increasingly realistic conditions

The subsequent iterations of the reconstruction performance study each bring the analysis a step closer to realistic measurement conditions. In addition, they show the reconstruction performance also for primary energies $E_{\mathrm{CR}} < 10^{18}$ eV which is the lower energy boundary for the star-shape simulations. Each iteration reveals the impact of the element of realism added. Using sparse antenna layout leads to a slight decrease in energy resolution, only reaching the same resolution as the intrinsic analysis at high energies. The addition of artificial noise to the simulated electric field traces leads to a substantially lower energy resolution for events with electromagnetic energy $< 10^{18}$ eV. I show the calculation of energy fluence to be accurate in the presence of noise for fluence values $> 1\mathrm{eV/m^2}$. For smaller values of the energy fluence, a positive bias appears. In the next step, I cease to use the true values of the shower parameters provided by the simulation output. Instead, I either reconstruct them, if applicable, or use average values. This leads to another general decrease in energy resolution to $\sim 7\%$, and exacerbates the loss of resolution at low energies and high zenith angles. Both analyses using artificial noise show potential for improvement in the energy fluence uncertainty model, and the antennas used for the reconstruction of the shower arrival direction. However, in the context of this work, they were primarily stepping stones on the way to a more realistic analysis. As such, I did not spend the time and effort necessary to fully optimise them.

In the final iteration, simulating realistic measurement conditions, I reconstruct the electric field from ADC traces, including real noise measured by GP300. I use the electric-field reconstruction method by Zhang et al. [120]. A quality criterion on the signal amplitude in the ADC traces in the electric-field reconstruction effectively replaces the antenna SNR criterion I apply to the electric traces in previous iterations. This suggests that the amplitude threshold used in the electric-field reconstruction is too conservative. The electric-field reconstruction has a significant positive bias for antennas receiving a weak signal, likely intensified by the antenna-gain pattern of the GRAND HorizonAntenna. This, even further than any other effects I discuss, exacerbates the bias and the loss of energy resolution for low energy events. The bias most strongly affects events with zenith angles between 70 and 80°. In addition, the effects of saturated measurements lead to a decrease in reconstruction performance at the highest energies. However, due to its small size, GP300 is unlikely to measure

a significant number of events at the energies where saturated measurements are relevant. As the detection of UHE cosmic rays is one of the goals of GRAND10k, these saturation effects need to be addressed by proper dimensioning of amplification and dynamic range in the experimental setup. For the parameter space unaffected by either of these adverse effects, the LDF fit under measurement conditions achieves an excellent average energy resolution of 7% for both arrays. The biases are consistent with zero.

I consider it a mark of excellence that the energy reconstruction, overall, performs equally well for GP300 and GRAND10k across the entire energy and zenith angle range. It achieves this performance despite the substantial differences in detection area and the resulting likelihood for GP300 to not fully contain the radio footprint. In another remarkable feat, close to 100% of events with sufficient antenna multiplicity ≥ 5, the main criterium to be passed to the LDF fit, also have a converging LDF fit.

Across all analyses, the reconstruction performance degrades slightly at the highest zenith angles. I exclude the influence of an inaccurate true X_{max} value as the cause since it does not affect analyses where I use no true shower information. A possible explanation is that the LDF model loses validity for the most inclined showers. This could potentially be improved by simply leaving one or more LDF shape parameters free since such inclined showers typically have many signal stations. In a more extreme scenario, it could necessitate further modification of the model. On the other hand, the accuracy of air-shower simulations so close to horizontality has so far not been validated conclusively with experimental data [130]. The effects of the radio emission of air-showers with zenith angles $> 85^{\circ}$ propagating close to the ground, as well as reflection on the ground or dense pockets of air are currently not fully understood or implemented in simulations. However, as these effects are not included in the simulations, they cannot be the reason for the performance degradation. Before the validity of any signal model can be considered for such showers, these effects need to be understood better.

For both analyses without true shower parameters, I show the reconstruction of the zenith and azimuth angle to be accurate within fractions of a degree. The biases of all presented distributions are close to zero.

The values of d_{max}, determined in the LDF fits for GP300 and GRAND10k, show a bias, possibly due to the difference in observation altitude between the sparse array simulations and the star-shape simulations with which I tune the model parameters. However, since the difference in altitude is small, other factors might cause the bias instead. Under realistic measurement conditions, I observe a resolution of the fitted d_{max} of $\sim$ 16%. The bias increases to $\sim$ 16% as well. The determination of d_{max} suggests a possible X_{max} reconstruction. However, small relative variations in d_{max} lead to large absolute variations in X_{max}. The resolution for the X_{max} reconstruction by calculating it from the fitted d_{max} is $> 100\,\mathrm{g/cm^2}$ and strongly biased. As such, the LDF fit model is not applicable as an X_{max} reconstruction. Better reconstruction results upon using either the true air-density at X_{max}, or an average value rather than the value calculated with d_{max} determined from the LDF fit further support this. This is also consistent with the findings of Schlüter and Huege [9] for the low-frequency model.

I investigate the pull distribution of all LDF fits under measurement conditions that pass the quality cuts for the reconstruction performance study. I find the distribution to have a positive bias due to the electric-field reconstruction bias. In addition, it indicates that the estimated fluence uncertainties are too small. In future applications, an unbiased electric-field reconstruction method, and a revision of the

energy fluence uncertainty model, such as presented by Martinelli et al. [131] and Ravn et al. [132], can address these issues.

I do not evaluate the fit of the radio symmetry centre because I have no information about the true position. The simulation output provides the true core position of the particle shower, however, the radio symmetry diverges centre from it due to refractive displacement. The shift from the particle core increases with the zenith angle. One of the few measures available for the accuracy of the radio core is the symmetry of the radio footprint with respect to the fitted core. For simulations without noise, a badly fitted core becomes obvious by a vertical spread of fluence values in the lateral distribution. However, this indicator loses significance in the presence of noise, or when pulse-amplitude smearing is applied since they both introduce vertical spread themselves. Another indicator for a badly fitted core are the error values of the two other free fit parameters of the LDF, $d_{\max}$ and E_{geo}. Core fits deviating from the symmetry centre often lead to large errors on these parameters due to the lack of symmetry. Accordingly, I take measures to discard any fits with badly fitted radio cores from the reconstruction performance studies.

I investigated the impact of the primary particle, initiating the air-shower, on the energy reconstruction. For the intrinsic analysis, the difference between the energy reconstruction distributions of proton and iron nuclei is $< 1\%$. For analyses using true shower information, the difference remains $< 2\%$. However, the analyses with no true shower parameters, and under realistic measurement conditions show differences of 3–5% between primaries. I strongly suspect that this is caused by the average $X_{\max}^{\text{avg}} = 750\,\text{g/cm}^2$ to calculate $\rho_{\max}$ I used for the energy reconstruction. Consequently, I consider the LDF and its energy reconstruction, inherently, to not be significantly biased with respect to the primary particle. I expect future optimisations of the method to eliminate the bias introduced under more realistic conditions. For example, a more accurate $d_{\max}$ fit could make the corresponding $\rho_{\max}$ viable for use in the energy reconstruction. The detector efficiency does not show a significant dependence on the primary particle.

9.4 Case studies of single LDF fits

I used one example event each from the GP300 and GRAND10k libraries as case studies for the progression of the LDF fit from close to ideal, up to measurement conditions. In addition, I explore the optimisation of the LDF fit for these single events by leaving one or more LDF shape parameters as free fit parameters instead of fixing them to their $d_{\max}$ parametrisation. For GP300, I found the best fit with all shape parameters fixed due to the small number of signal antennas. The exception is the analysis without noise since significantly more signal antennas were available. For the GRAND10k event with many more signal antennas, I found improved fit quality upon leaving up to three shape parameters as free parameters. In addition, this event is affected by antenna ADC traces under measurement conditions. However, since it still has many antennas remaining inside the Cherenkov radius, the reconstructed energy is only slightly underestimated. Both events show how I discard antennas with the different signal quality criteria in each iteration of the analysis. The fit quality and, thus, energy reconstruction of single events can be improved in this way. This approach could be applied to more accurately reconstruct the energy of rare extreme energy ($> 10^{20}\,\text{eV}$) cosmic ray events, like the "Oh-my-god" or "Amaterasu" particles. According to the results of my detection efficiency study, GRAND10k expects to detect multiple events at similar energy per year. However,

this approach would likely introduce varying systematic uncertainties for different events.

9.5 Reconstruction of GP300 cosmic-ray event candidates

I applied the energy reconstruction to real cosmic-ray event candidates measured by GP300. While GRAND@Auger is currently operating and taking measurements as well, there are no event candidates available with sufficient antenna multiplicity for the LDF reconstruction. I use a high 5-sigma SNR threshold for the viability of signal antennas, matching the antenna trigger threshold of GP300. In comparison, the radio detector of the Pierre Auger Observatory uses a $\sqrt{10}$-sigma threshold [133]. This is possible due to access to particle detectors as an external trigger. For the radio-only nature of GRAND, a higher threshold guarantees the presence of a non-background signal. More importantly, for the large detection areas GRAND plans to instrument in the future, it is especially vital to use high-threshold and high-purity trigger criteria to limit the rate of data to a manageable amount. The current criteria used for the selection of cosmic-ray event candidates from the GP300 measurements use signal amplitude thresholds equal to the thresholds in the electric-field reconstruction. As such, for the measured event candidates, I do not observe any DUs flagged by the pulse amplitude or SNR criteria. This is another indicator that these thresholds are potentially too conservative.

I presented the LDF fit reconstructions for six cosmic-ray event candidates. I consider all six candidates to have a high-confidence level as real cosmic-ray events due to the strict selection criteria during the cosmic-ray search, as well as the good performance of each LDF fit to the measured data. Due to the excellent reconstruction of the arrival directions for simulations, I am also confident in the reconstructed directions for the event candidates. The larger uncertainties on the direction in comparison to simulations are due to the larger uncertainties I chose for the pulse arrival times of measurements.

The electromagnetic energies I reconstruct for the six GP300 event candidates all lie within the expected energy range for the detector. However, there are caveats limiting the level of confidence in the values of the reconstruct electromagnetic energies. On the one hand, the narrow-band-RFI-filtered traces lead to a small decrease in total power and possibly impact the energy fluence determined by summing over the reconstructed electric field trace. Ideally, one uses unfiltered traces for all three channels. On the other hand, the low-energy bias of the electric-field reconstruction likely significantly impacts the energy fluence at many of the triggered DUs, and, consequently, the reconstructed electromagnetic energy.

Furthermore, full information about the activity status of the deployed DUs at the time of measurement is not available. Whether an active DU on the Cherenkov ring triggers during a measured event is a powerful indicator. As such, this information is critical for the confidence level of an event candidate as a cosmic-ray air-shower. All three of these issues need to be addressed for a high-confidence reconstruction of the electromagnetic energy for future measurements. Additionally, for a more accurate energy reconstruction independent of these factors, a new set of air-shower simulations would be beneficial. This set should more accurately reflect the GP300 array by using the exact altitudes of the deployed DUs.

It is important to note that the LDF fit is only a reliable method to determine whether a measured event is a real cosmic-ray air-shower in the case of many signal DUs following a clear lateral profile. A well-performing LDF fit to a small number

of signal DUs, forming a clear lateral fluence distribution, can serve as an indicator for the presence of an air-shower, but it is not a sufficient criterion. On the contrary, air-showers often have a poorly performing fit in the presence of noise or few signal antennas, as demonstrated by the many simulated events I flag due to quality criteria during the performance studies. However, a more accurate uncertainty model for the energy fluence will strengthen the goodness-of-fit of the LDF fit as an indicator, also in the case of few signal DUs.

The successful application of the reconstruction to real measured data shows its viability for continued use for measurements of GP300, and any future GRAND detectors. While one needs to retune the model parameters for each new site, I expect no change in the model itself to be necessary for this purpose.

9.6 Detector performance of GP300 and GRAND10k

I study the detection efficiency, aperture, and exposure of GP300 and GRAND10k with the same data as the reconstruction performance study under realistic measurement conditions. Since I choose the energy and zenith binning so that each bin has approximately the same number of events, the total efficiency shows the overall efficiency for the covered parameter space. GP300 and GRAND10k, respectively, have 71.8% and 73.7% detection efficiency for air-showers with primary energy between 10^{17} and 10^{20} eV and zenith angles between 65 and 85°.

The maximum geometrical apertures for GP300 and GRAND10k for this range of zenith angles are 107 km^2 sr and 4325 km^2 sr, respectively. For GRAND10k, I reduced the total array area for the aperture calculation by $\sim$ 20% due to the nature of the simulated core distribution. Neither detector reaches its ideal aperture for any energy range. Utilising their full aperture, GP300 and GRAND10k, respectively, expect to detect about $35{,}200^{+7900}_{-4300}$ and $1{,}330{,}000^{+470{,}000}_{-170{,}000}$ cosmic-ray events above $E_{\mathrm{thr}} = 10^{17}$ eV within one year of exposure. However, measurements with an effective aperture $>$ 50% are only possible for energies $> 10^{18}$ eV due to low efficiency at low zenith angles. Above this energy, the expected number of events is not as dependent on trigger thresholds and background noise level. For this threshold, GP300 and GRAND10k expect to detect $\sim$2000 and $\sim$85,000 events, respectively. Perhaps an even better illustration of the difference between the array layouts is the number of UHE cosmic rays with energies $> 10^{19}$ eV. The expected amount of events for GP300 above this energy is 26. GRAND10k expects to detect 1115 events above this energy, and at least ten events for the highest energy bin. In addition, when considering the full area of GRAND10k, it expects to detect 24% more events at all levels of energy.

Another study of the exposure of GP300 [91] predicts 130 events detected per day for energies $> 10^{17}$ eV. This study also used the GP300 simulation set I created for this work. The exposure study I describe in this work predicts 96 detected air-shower events for the same exposure time of one day for GP300. Both results are of the same order of magnitude. The results are compatible with each other since I apply more conservative quality criteria to determine whether a triggered antenna counts as a signal antenna. In addition, due to the high particle flux at these low energies, small differences in detection efficiency strongly influence the predicted event rates.

The best point of reference for the performance of GRAND10k is a study of the detector performance of the Radio Detector (RD) of the Pierre Auger Observatory for inclined air-showers [134, 135]. For RD, the detection criteria for an event are three triggered antenna stations with SNR$>$ 10. For the same zenith angle range between

65 and 85° and a total detection area of 3000 km^2, RD expects to detect between 3000 and 4000 cosmic rays with energy $> 10^{19}$ eV within ten years of exposure time. To compare, I scale up the expected detections for GRAND10k for the same energy threshold by a factor of ten to match the exposure. As such, GRAND10k expects to detect ∼11,000 such events for ten years of exposure. Naturally, GRAND10k has more conservative detection criteria since GRAND can only rely on radio measurements, and requires a limited rate of data. However, a large increase is still expected since the GRAND10k array I simulate has a much larger detection area. However, one has to note that the RD is deployed and taking data, while GRAND still has many challenges to overcome before GRAND10k can be built. The most significant challenge is the development of the fully efficient, high-purity autonomous radio trigger. The development of such a trigger has been attempted in the past, but has not yet succeeded.

Overall, the reconstruction performance and detection efficiency is remarkably similar between the array layouts of GP300 and GRAND10k. I expect significant differences between the two arrays at low energies, low zenith angles, and the highest zenith angles. For low energies and zenith angles, I expect GP300 to perform better due to its in-fill providing more antennas for the fit. This, I verify in terms of detector efficiency. I find no difference in terms of the reconstruction performance for air-showers with low zenith angles. For these events, the presence of noise and, under measurement conditions, the electric-field reconstruction bias dominate the reconstruction performance. At the highest zenith angles, I observe GRAND10k to have a higher detection efficiency. This is in line with expectations due to its large detection area capable of fully containing the large radio footprint of strongly inclined showers. The reconstruction performance for high zenith angles shows no deviation in quality between the arrays. Here, the general degradation of the reconstruction performance at the highest zenith angles appears to be a more dominant effect. There is no significant difference in energy resolution or reconstruction bias for any other energy or zenith angle range unaffected by universal biases.

9.7 Applicability to neutrino-induced air-showers

The main science goal of GRAND invites the question of whether the signal model can also be used to reconstruct the electromagnetic energy of air-showers induced by ultra-high-energy neutrinos. For atmosphere-skimming neutrinos, only traversing and interacting in air, I expect it to be possible, in principle. Such air-showers would be identifiable by their near-horizontal zenith angles, and, relatively, small $d_{\max}$ due to the much deeper penetration depth of neutrinos. As such, the footprint of such an event would be much smaller than that of any cosmic-ray event with the same zenith angle. At the very least, however, the model parameters would need to be retuned for the different properties of such air-showers. For Earth-skimming neutrinos, I do not expect the model to be easily compatible due to the entirely different geometry, and the development of the shower in a much denser region of the atmosphere. In addition, the varying particles from neutrino interactions and their decay products that can induce electromagnetic cascades in either case also introduce more inconsistency to the resulting air-showers. As such, the electromagnetic energy, as well as other shower parameters, like the penetration depth, are not as universal for neutrinos as they are for cosmic-ray events.

Chapter 10

Summary

I have successfully adapted the signal model by Schlüter and Huege [9] for the radio emission of inclined cosmic ray air-showers for the 50–200 MHz frequency band for both GRAND@Auger, located at the Pierre Auger Observatory in Argentina, and the GRANDProto300 (GP300) site in China. For this purpose, I have used air-shower simulations with primary energies between 10^{18} and $10^{20.2}$ eV, and zenith angles between 65 and 85°. I have found new parametrisations of the charge-excess fraction for the higher frequency band. I have used the charge excess fraction to accurately describe the geomagnetic energy fluence with only the energy fluence component polarised in the $\vec{v} \times \vec{B}$ direction. I have modified the geomagnetic energy fluence lateral distribution function (LDF) to account for the emission properties in the wider and higher frequency band. The modifications are generalised and make the model applicable to both higher and lower frequencies. For the low magnetic field strength in Argentina, these changes are sufficient for an accurate signal model. For China, the almost three times as strong magnetic field leads to a loss of signal coherence in the radio emission at high zenith angles. To address this, I have extended the density correction, used to calculate the corrected radiation energy S_{geo}, with additional parameters. With one of the new parameter, I have also been able to further improve the reconstruction performance for GRAND@Auger. For both sites, I have found excellent intrinsic energy resolutions of $\sim 3\%$ with vanishing biases. This matches the intrinsic resolution of the low-frequency model. This result indicates that the model is applicable to any magnetic field configuration. With the successful application of the model, I have also verified the viability of the model for different frequency bands and sites. Further, I anticipate only revisions of the explicit parametrisations to be necessary to adapt the model to additional sites and frequency bands, and no further modifications of the model itself.

I have used multiple CORSIKA air-shower simulation libraries during the course of this project. I have used the RdStar library, originally generated for the low-frequency model, to adapt the model for the 50–200 MHz frequency band for the GRAND@Auger site. For the GP300 site, I have created three simulation libraries myself: the GRAND star-shape library to adapt the model and tune its parameters to the site of GP300, and two libraries for realistic, sparse array layouts to evaluate the reconstruction performance of the model. These layouts are planned final layout of GP300, and a possible layout for GRAND10k, the next stage of GRAND with a detection area of 10,000 km^2.

With these two libraries, I have shown that the LDF fit reconstruction of the electromagnetic shower energy performs exceptionally well for both simulated GRAND detectors under fully realistic measurement conditions. To illustrate the progress of my work over the course of the project, I have shown the reconstruction performance in multiple iterations, each showing a higher level of realism. I have discussed each

iteration, as well as the impact which each element of realism—sparse antenna layouts, the presence of background noise, the reconstruction of all shower parameters, and realistic effects of the detector hardware—have on the reconstruction performance across a wide parameter space. As such, I have provided the first end-to-end reconstruction of the electromagnetic shower energy for GRAND, including the reconstruction of the electric field from measured ADC traces.

Under realistic measurement conditions, the reconstruction achieves an energy resolution of 7% and a bias consistent with zero for the fraction of the parameter space unaffected by systematic biases. The reconstruction shows no inherent dependence on the primary particle initiating the air-shower. At low energies, the effects of noise and a bias present in the electric field reconstruction dominate. At the highest energies, saturated measurements impact the reconstruction performance under measurement conditions. However, the accuracy of the reconstruction generally increases with energy since the presence of noise becomes less relevant. At high zenith angles, I have found that the model accuracy appears to slightly degrade due to large differences small changes in zenith angle induce at the ground level. I have also shown the model to be applicable for primary energies down to 10^{17} eV. These results apply to both array layouts.

I have successfully applied the signal model and energy reconstruction to real data of cosmic-ray event candidates, measured by a partial configuration of GP300. I have presented the reconstruction results for six event candidates which I consider to have high-confidence as real cosmic-ray events. I have discussed that these values of the reconstructed electromagnetic energy are likely affected by the electric-field reconstruction bias as well as other measurement details such as filtered traces and a slight mismatch in observation altitude. Further, I have proposed solutions to these problems. I have discussed that independent energy reconstruction methods within GRAND find compatible results for the electromagnetic energy of the six candidates. As such, I have established a viable, and, under the right conditions, accurate energy reconstruction method for GP300, as well as future GRAND detectors going forward. I have done so timely since reconstruction results of the first cosmic-ray event candidates from GP300 were ready to be published at ICRC 2025.

Furthermore, I have studied the detection efficiency of GP300 and GRAND10k with the simulation libraries I created. I have found GP300 and GRAND10k, over the entire simulated parameter space, to be, respectively, 71.8% and 73.7% efficient. I have calculated the effective aperture, and exposure for both detectors. I have discussed the advantages and disadvantages of each layout, which influence these attributes. Accordingly, I have estimated that GP300 and GRAND10k will detect $\sim$2000 and $\sim$85,000 cosmic-ray events with energies $> 10^{18}$ eV within one year of exposure time. The results for GP300 are compatible with a study carried out independently by colleagues within the GRAND collaboration. Further, I have shown the potential of GRAND10k as a powerful detector for ultra-high-energy cosmic rays. Due to its large detection area, GRAND10k will detect of the order of 1000 events with primary energy $> 10^{19}$ eV, and at least 10 events with energy $> 10^{19.75}$ eV for the same exposure time of one year. For such a detector, my work provides an excellent and reliable energy reconstruction as a basis for measurements of the cosmic-ray energy spectrum at the highest energies.

Acknowledgements

First, and most of all, I am deeply grateful to my parents, Adele and Hans-Georg, and my sister, Hannah, for their truly unconditional and unrelenting support during my physics studies and PhD. I would never take it for granted, and I love you very much. I would also like to thank my aunt, Maggy, for her support and for encouraging me to start baking in 2022, which became one of my favourite hobbies and outlets for stress. I am thankful to my supervisor, Tim Huege, for daily advice, when necessary, and feedback for the whole duration of my doctoral project. I would like to thank my first referee, Ralph Engel, for regular, useful feedback meetings during the final year of my PhD, as well as for the mug, which he gifted me for successfully reconstructing the first cosmic-ray event candidates from GP300. I would like to thank my second referee, Olivier Martineau, for agreeing to the role, and for feedback on my work during the NUTRIG meetings. I am also grateful to the other members of the NUTRIG group for the great workshops in Paris and Karlsruhe, and, especially, Markus Roth for additional feedback during meetings at KIT in my final year.

I am also terribly grateful to the many friends who have contributed to the great time I had during most of my PhD, and who have made the stressful last months easier to bear:

Thank you to the best of friends, back in Bielefeld and all over Germany: Romy, Boris, Dustin, Marius, Johanna, Nils, Ferdi, Sandra, Thorben, Luis, and Marco for the countless inside-jokes, hours spent together in person and virtually, as well as great holiday trips. You are all like family to me.

Thank you to my friends and colleagues at IAP, Pranav, Keito, Federico, Jelena, Megha, Simon, Nikos, Tista, Shefali, Berenika, Asil, Marvin, Steffen, Paul, Max, Sara, Tobias, Carmina, Ezequiel, Joaquin, Gabi, and many more for, of course, many useful and interesting discussions, but, more importantly, for balcony parties, moral support, honest conversations, movie nights, Schlosspark outings, defense celebrations, office snacks, bike-ride conversations, coffee breaks, "hikes", baking inspiration, spice advice, house plant advice, dinner outings, dancing lessons, and so much amazing food. Thank you to Joris for organising the KIT SC Smash Weekly with me, and to the many friends I made thanks to this wonderful endeavour. Thank you to Natalia for many interesting discussions about mutual interests and a great time in Barcelona. Thank you to Tobi for motivating me to keep going to the gym, even in the final months. Thank you to my friends in London, who I see too rarely in person, Harry, Loren, Ethan, Timi, Eugene, Hamad, and Rohan for the many fun draft leagues, and the collaboration for IUPS which kept me sane in the final months. Thank you to Vova for many pieces of useful advice, both professional and personal. Thank you to my friends in Karlsruhe, Max, Olli, Kilian, and Alex for the Tuesday dinners, and gaming sessions.

I would like to thank the GRAND members for the collaborative efforts during my PhD, and especially the members in Nijmegen, Netherlands and Nanjing, China for hosting the GRAND collaboration meetings in 2023 and 2024 at which I enjoyed myself immensely. Special thanks to Chao Zhang for useful discussions early on in my PhD, and also for much of his time during the Nanjing collaboration meeting where he acted as our guide and showed us many wonderful places around the city. I am grateful to Sabine Bucher and Doris Wochele at IAP for swiftly overcoming any logistical and IT problems I presented them with. I am immensely grateful to Kewen Zhang for allowing me access to her electric-field reconstruction method before it was published, greatly accelerating my progress in the final year of my project. I would like to thank Marius and Natalia again for useful comments on my thesis

introduction. I would like to thank Mauricio Bustamante for his helpful comments on my GRAND chapter, as well as for the excellent coordination during the cosmic-ray search and reconstruction efforts in the lead-up to ICRC 2025. I would like to thank Simon Strähnz again for his thoughtful comments on my methods chapters. I am grateful to Felix Schlüter for introducing me to and helping me with the signal model in the early months of my PhD. I would also like to thank Liam Becker, who I supervised as part of a RISE internship at KIT, for collaborating with me while investigating the loss of coherence and the clover-leaf pattern.

This work is part of the NUTRIG project, supported by the Agence Nationale de la Recherche (ANR-21-CE31-0025; France) and the Deutsche Forschungsgemeinschaft (DFG; Projektnummer 490843803; Germany). The author gratefully acknowledges the computing time provided on the high-performance computer HoreKa by the National High-Performance Computing Center at KIT (NHR@KIT). This center is jointly supported by the Federal Ministry of Education and Research and the Ministry of Science, Research and the Arts of Baden-Württemberg, as part of the National High-Performance Computing (NHR) joint funding program. HoreKa is partly funded by the German Research Foundation.

Bibliography

[1] Victor F. Hess. "Über Beobachtungen der durchdringenden Strahlung bei sieben Freiballonfahrten". In: *Phys. Z.* 13 (1912), pp. 1084–1091.

[2] D. J. Bird et al. "Detection of a cosmic ray with measured energy well beyond the expected spectral cutoff due to cosmic microwave radiation". In: *Astrophys. J.* 441 (1995), pp. 144–150. DOI: 10.1086/175344. arXiv: astro-ph/9410067.

[3] R. U. Abbasi et al. "An extremely energetic cosmic ray observed by a surface detector array". In: *Science* 382.6673 (2023), abo5095. DOI: 10.1126/science.abo5095. arXiv: 2311.14231 [astro-ph.HE].

[4] Thomas K. Gaisser, Ralph Engel, and Elisa Resconi. *Cosmic Rays and Particle Physics: 2nd Edition*. Cambridge University Press, June 2016. ISBN: 978-0-521-01646-9.

[5] Alexander Aab et al. "The Pierre Auger Cosmic Ray Observatory". In: *Nucl. Instrum. Meth. A* 798 (2015), pp. 172–213. DOI: 10.1016/j.nima.2015.06.058. arXiv: 1502.01323 [astro-ph.IM].

[6] H. Kawai et al. "Telescope array experiment". In: *Nucl. Phys. B Proc. Suppl.* 175-176 (2008). Ed. by Kwong Sang Cheng et al., pp. 221–226. DOI: 10.1016/j.nuclphysbps.2007.11.002.

[7] Jaime Álvarez-Muñiz et al. "The Giant Radio Array for Neutrino Detection (GRAND): Science and Design". In: *Sci. China Phys. Mech. Astron.* 63.1 (2020), p. 219501. DOI: 10.1007/s11433-018-9385-7. arXiv: 1810.09994 [astro-ph.HE].

[8] Markus Ahlers and Francis Halzen. "Opening a New Window onto the Universe with IceCube". In: *Prog. Part. Nucl. Phys.* 102 (2018), pp. 73–88. DOI: 10.1016/j.ppnp.2018.05.001. arXiv: 1805.11112 [astro-ph.HE].

[9] F. Schlüter and T. Huege. "Signal model and event reconstruction for the radio detection of inclined air showers". In: *JCAP* 2023.1, 008 (Jan. 2023), p. 008. DOI: 10.1088/1475-7516/2023/01/008. arXiv: 2203.04364 [astro-ph.HE].

[10] Jaime Álvarez-Muniz et al. "Towards the Giant Radio Array for Neutrino Detection (GRAND): the GRANDProto300 and GRAND@Auger prototypes". In: (Sept. 2025). arXiv: 2509.21306 [astro-ph.IM].

[11] Beatriz de Errico, João R. T. de Mello Neto, and Charles Timmermans. "The GRAND@Auger Prototype for the Giant Radio Array for Neutrino Detection". In: *39th International Cosmic Ray Conference*. July 2025. arXiv: 2507.07407 [astro-ph.IM].

[12] Pengxiong Ma et al. "Progress of the GRANDProto300 Project". In: *39th International Cosmic Ray Conference*. July 2025. arXiv: 2507.05915 [astro-ph.HE].

[13] Simon Chiche et al. "Loss of Coherence and Change in Emission Physics for Radio Emission from Very Inclined Cosmic-Ray Air Showers". In: *PRL* 132.23, 231001 (June 2024), p. 231001. DOI: 10.1103/PhysRevLett.132.231001. arXiv: 2404.14541 [astro-ph.HE].

[14] T. Huege, M. Ludwig, and C. W. James. "Simulating radio emission from air showers with CoREAS". In: *AIP Conf. Proc.* 1535.1 (2013). Ed. by Robert Lahmann et al., p. 128. DOI: 10.1063/1.4807534. arXiv: 1301.2132 [astro-ph.HE].

[15] A. C. Cummings et al. "Galactic Cosmic Rays in the Local Interstellar Medium: Voyager 1 Observations and Model Results". In: *Astrophys. J.* 831.1 (2016), p. 18. DOI: 10.3847/0004-637X/831/1/18.

[16] S. Navas et al. "Review of particle physics". In: *Phys. Rev. D* 110.3 (2024), p. 030001. DOI: 10.1103/PhysRevD.110.030001.

[17] Rainer Beck et al. "Synthesizing Observations and Theory to Understand Galactic Magnetic Fields: Progress and Challenges". In: *Galaxies* 8.1 (2019), p. 4. DOI: 10.3390/galaxies8010004. arXiv: 1912.08962 [astro-ph.GA].

[18] Theodore Dunham. "The Material of Interstellar Space". In: *Proceedings of the American Philosophical Society* 81.2 (1939), pp. 277–293. ISSN: 0003049X. URL: http://www.jstor.org/stable/984986 (visited on 07/29/2025).

[19] Philip F. Hopkins et al. "Effects of Different Cosmic Ray Transport Models on Galaxy Formation". In: *Mon. Not. Roy. Astron. Soc.* 501.3 (2021), pp. 3663–3669. DOI: 10.1093/mnras/staa3692. arXiv: 2004.02897 [astro-ph.GA].

[20] Christine M. Simpson et al. "How cosmic rays mediate the evolution of the interstellar medium". In: *Mon. Not. Roy. Astron. Soc.* 520.3 (2023), pp. 4621–4645. DOI: 10.1093/mnras/stac3601. arXiv: 2204.02410 [astro-ph.GA].

[21] Carmelo Evoli. *The Cosmic-Ray Energy Spectrum*. Dec. 2020. DOI: 10.5281/zenodo.4396125. URL: https://doi.org/10.5281/zenodo.4396125.

[22] David Maurin et al. "A cosmic-ray database update: CRDB v4.1". In: *Eur. Phys. J. C* 83.10 (2023), p. 971. DOI: 10.1140/epjc/s10052-023-12092-8. arXiv: 2306.08901 [astro-ph.HE].

[23] E. Roulet. "Large-scale cosmic-ray anisotropies measured by the Pierre Auger Observatory". In: *PoS* UHECR2024 (2025), p. 008. DOI: 10.22323/1.484.0008.

[24] Kenneth Greisen. "End to the cosmic ray spectrum?" In: *Phys. Rev. Lett.* 16 (1966), pp. 748–750. DOI: 10.1103/PhysRevLett.16.748.

[25] G. T. Zatsepin and V. A. Kuz'min. "Upper Limit of the Spectrum of Cosmic Rays". In: *Soviet Journal of Experimental and Theoretical Physics Letters* 4 (Aug. 1966), p. 78.

[26] Alexander Aab et al. "Features of the Energy Spectrum of Cosmic Rays above 2.5×10^{18} eV Using the Pierre Auger Observatory". In: *Phys. Rev. Lett.* 125.12 (2020), p. 121106. DOI: 10.1103/PhysRevLett.125.121106. arXiv: 2008.06488 [astro-ph.HE].

[27] Alexander Aab et al. "Measurement of the cosmic-ray energy spectrum above 2.5×10^{18} eV using the Pierre Auger Observatory". In: *Phys. Rev. D* 102.6 (2020), p. 062005. DOI: 10.1103/PhysRevD.102.062005. arXiv: 2008.06486 [astro-ph.HE].

[28] Diego Ravignani. "Measurement of the cosmic-ray energy spectrum above 2.5 EeV using 19 years of operation of the Pierre Auger Observatory". In: *39th International Cosmic Ray Conference*. July 2025. arXiv: 2507.08573 [astro-ph.HE].

[29] A. M. Hillas. "The Origin of Ultrahigh-Energy Cosmic Rays". In: *Ann. Rev. Astron. Astrophys.* 22 (1984), pp. 425–444. DOI: 10.1146/annurev.aa.22.090184.002233.

[30] Kseniya V. Ptitsyna and Sergei V. Troitsky. "Physical conditions in potential sources of ultra-high-energy cosmic rays. I. Updated Hillas plot and radiation-loss constraints". In: *Phys. Usp.* 53 (2010), pp. 691–701. DOI: 10.3367/UFNe.0180.201007c.0723. arXiv: 0808.0367 [astro-ph].

[31] M. G. Aartsen et al. "First observation of PeV-energy neutrinos with IceCube". In: *Phys. Rev. Lett.* 111 (2013), p. 021103. DOI: 10.1103/PhysRevLett.111.021103. arXiv: 1304.5356 [astro-ph.HE].

[32] M. G. Aartsen et al. "Evidence for High-Energy Extraterrestrial Neutrinos at the IceCube Detector". In: *Science* 342 (2013), p. 1242856. DOI: 10.1126/science.1242856. arXiv: 1311.5238 [astro-ph.HE].

[33] S. Adrian-Martinez et al. "Letter of intent for KM3NeT 2.0". In: *J. Phys. G* 43.8 (2016), p. 084001. DOI: 10.1088/0954-3899/43/8/084001. arXiv: 1601.07459 [astro-ph.IM].

[34] Y. Fukuda et al. "The Super-Kamiokande detector". In: *Nucl. Instrum. Meth. A* 501 (2003). Ed. by V. A. Ilyin, V. V. Korenkov, and D. Perret-Gallix, pp. 418–462. DOI: 10.1016/S0168-9002(03)00425-X.

[35] Yoichiro Suzuki. "The Super-Kamiokande experiment". In: *Eur. Phys. J. C* 79.4 (2019), p. 298. DOI: 10.1140/epjc/s10052-019-6796-2.

[36] S. Aiello et al. "Observation of an ultra-high-energy cosmic neutrino with KM3NeT". In: *Nature* 638.8050 (2025). [Erratum: Nature 640, E3 (2025)], pp. 376–382. DOI: 10.1038/s41586-024-08543-1.

[37] J. A. Aguilar et al. "Design and Sensitivity of the Radio Neutrino Observatory in Greenland (RNO-G)". In: *JINST* 16.03 (2021). [Erratum: JINST 18, E03001 (2023)], P03025. DOI: 10.1088/1748-0221/16/03/P03025. arXiv: 2010.12279 [astro-ph.IM].

[38] Ariel Bridgeman. "Determining the Mass Composition of Ultra-high Energy Cosmic Rays Using Air Shower Universality". PhD thesis. Karlsruhe U., 2018.

[39] Johannes Albrecht et al. "The Muon Puzzle in cosmic-ray induced air showers and its connection to the Large Hadron Collider". In: *Astrophys. Space Sci.* 367.3 (2022), p. 27. DOI: 10.1007/s10509-022-04054-5. arXiv: 2105.06148 [astro-ph.HE].

[40] D. Heck et al. "CORSIKA: A Monte Carlo code to simulate extensive air showers". In: (Feb. 1998).

[41] W. Heitler. *The quantum theory of radiation*. Vol. 5. International Series of Monographs on Physics. Oxford: Oxford University Press, 1936.

[42] J. Matthews. "A Heitler model of extensive air showers". In: *Astropart. Phys.* 22 (2005), pp. 387–397. DOI: 10.1016/j.astropartphys.2004.09.003.

[43] Ralf Ulrich, Ralph Engel, and Michael Unger. "Hadronic Multiparticle Production at Ultra-High Energies and Extensive Air Showers". In: *Phys. Rev. D* 83 (2011), p. 054026. DOI: 10.1103/PhysRevD.83.054026. arXiv: 1010.4310 [hep-ph].

[44] M. Aguilar et al. "First Result from the Alpha Magnetic Spectrometer on the International Space Station: Precision Measurement of the Positron Fraction in Primary Cosmic Rays of 0.5–350 GeV". In: *Phys. Rev. Lett.* 110 (2013), p. 141102. DOI: 10.1103/PhysRevLett.110.141102.

[45] E. S. Seo et al. "Cosmic Ray Energetics And Mass for the International Space Station (ISS-CREAM)". In: *Adv. Space Res.* 53 (2014). Ed. by Eun-Suk Seo and Igor V. Moskalenko, pp. 1451–1455. DOI: 10.1016/j.asr.2014.01.013.

[46] O. Adriani et al. "Ten years of PAMELA in space". In: *Riv. Nuovo Cim.* 40.10 (2017), pp. 473–522. DOI: 10.1393/ncr/i2017-10140-x. arXiv: 1801.10310 [astro-ph.HE].

[47] W. B. Atwood et al. "The Large Area Telescope on the Fermi Gamma-ray Space Telescope Mission". In: *Astrophys. J.* 697 (2009), pp. 1071–1102. DOI: 10.1088/0004-637X/697/2/1071. arXiv: 0902.1089 [astro-ph.IM].

[48] A. Abdul Halim et al. "The Scintillator Surface Detector of the Pierre Auger Observatory". In: (July 2025). arXiv: 2507.07762 [astro-ph.HE].

[49] J. V. Jelley et al. "Radio Pulses from Extensive Cosmic-Ray Air Showers". In: *Nature* 205.4969 (1965), pp. 327–328. DOI: 10.1038/205327a0.

[50] D. Ardouin et al. "Radio-Detection Signature of High Energy Cosmic Rays by the CODALEMA Experiment". In: *Nucl. Instrum. Meth. A* 555 (2005), p. 148. DOI: 10.1016/j.nima.2005.08.096. arXiv: astro-ph/0504297.

[51] H. Falcke et al. "Detection and imaging of atmospheric radio flashes from cosmic ray air showers". In: *Nature* 435 (2005), pp. 313–316. DOI: 10.1038/nature03614. arXiv: astro-ph/0505383.

[52] M. P. van Haarlem et al. "LOFAR: The LOw-Frequency ARray". In: *Astron. Astrophys.* 556 (2013), A2. DOI: 10.1051/0004-6361/201220873. arXiv: 1305.3550 [astro-ph.IM].

[53] P. A. Bezyazeekov et al. "Measurement of cosmic-ray air showers with the Tunka Radio Extension (Tunka-Rex)". In: *Nucl. Instrum. Meth. A* 802 (2015), pp. 89–96. DOI: 10.1016/j.nima.2015.08.061. arXiv: 1509.08624 [astro-ph.IM].

[54] Pedro Abreu et al. "Antennas for the Detection of Radio Emission Pulses from Cosmic-Ray". In: *JINST* 7 (2012), P10011. DOI: 10.1088/1748-0221/7/10/P10011. arXiv: 1209.3840 [astro-ph.IM].

[55] Marvin Gottowik. "Recent Highlights from the Auger Engineering Radio Array". In: *39th International Cosmic Ray Conference*. July 2025. arXiv: 2507.08510 [astro-ph.HE].

[56] Antonella Castellina. "AugerPrime: the Pierre Auger Observatory Upgrade". In: *EPJ Web Conf.* 210 (2019). Ed. by I. Lhenry-Yvon et al., p. 06002. DOI: 10.1051/epjconf/201921006002. arXiv: 1905.04472 [astro-ph.HE].

[57] Simon Strähnz. "Event reconstruction with the Radio detector of the Pierre Auger Observatory". In: *39th International Cosmic Ray Conference*. July 2025. arXiv: 2507.08556 [astro-ph.IM].

[58] T. Huege. "Radio detection of cosmic ray air showers in the digital era". In: *Phys. Rept.* 620 (2016), pp. 1–52. DOI: 10.1016/j.physrep.2016.02.001. arXiv: 1601.07426 [astro-ph.IM].

[59] Frank G. Schröder. "Radio detection of Cosmic-Ray Air Showers and High-Energy Neutrinos". In: *Prog. Part. Nucl. Phys.* 93 (2017), pp. 1–68. DOI: 10.1016/j.ppnp.2016.12.002. arXiv: 1607.08781 [astro-ph.IM].

[60] Christian Glaser et al. "An analytic description of the radio emission of air showers based on its emission mechanisms". In: *EPJ Web Conf.* 216 (2019). Ed. by G. Riccobene et al., p. 03001. DOI: 10.1051/epjconf/201921603001.

[61] Ralph Engel, Dieter Heck, and Tanguy Pierog. "Extensive air showers and hadronic interactions at high energy". In: *Ann. Rev. Nucl. Part. Sci.* 61 (2011), pp. 467–489. DOI: 10.1146/annurev.nucl.012809.104544.

[62] P. Allison et al. "Design and Initial Performance of the Askaryan Radio Array Prototype EeV Neutrino Detector at the South Pole". In: *Astropart. Phys.* 35 (2012), pp. 457–477. DOI: 10.1016/j.astropartphys.2011.11.010. arXiv: 1105.2854 [astro-ph.IM].

[63] Lisa Gerhardt et al. "A prototype station for ARIANNA: a detector for cosmic neutrinos". In: *Nucl. Instrum. Meth. A* 624 (2010), pp. 85–91. DOI: 10.1016/j.nima.2010.09.032. arXiv: 1005.5193 [astro-ph.IM].

[64] Ek Narayan Paudel, Alan Coleman, and Frank G. Schroeder. "Parametrization of the Relative Amplitude of Geomagnetic and Askaryan Radio Emission from Cosmic-Ray Air Showers using CORSIKA/CoREAS Simulations". In: *PoS* ICRC2021 (2021), p. 429. DOI: 10.22323/1.395.0429. arXiv: 2108.06336 [astro-ph.HE].

[65] Marianne Ludwig and Tim Huege. "REAS3: Monte Carlo simulations of radio emission from cosmic ray air showers using an 'end-point' formalism". In: *Astropart. Phys.* 34 (2011), pp. 438–446. DOI: 10.1016/j.astropartphys.2010.10.012. arXiv: 1010.5343 [astro-ph.HE].

[66] Clancy W. James et al. "General description of electromagnetic radiation processes based on instantaneous charge acceleration in 'endpoints'". In: *Phys. Rev. E* 84 (2011), p. 056602. DOI: 10.1103/PhysRevE.84.056602. arXiv: 1007.4146 [physics.class-ph].

[67] E. Zas, F. Halzen, and T. Stanev. "Electromagnetic pulses from high-energy showers: Implications for neutrino detection". In: *Phys. Rev. D* 45 (1992), pp. 362–376. DOI: 10.1103/PhysRevD.45.362.

[68] Jaime Alvarez-Muniz, Andres Romero-Wolf, and Enrique Zas. "Cherenkov radio pulses from electromagnetic showers in the time-domain". In: *Phys. Rev. D* 81 (2010), p. 123009. DOI: 10.1103/PhysRevD.81.123009. arXiv: 1002.3873 [astro-ph.HE].

[69] Clancy W. James. "Nature of radio-wave radiation from particle cascades". In: *Phys. Rev. D* 105.2 (2022), p. 023014. DOI: 10.1103/PhysRevD.105.023014. arXiv: 2201.01298 [astro-ph.HE].

[70] Konstantin Belov. "Radio emission from Air Showers. Comparison of theoretical approaches". In: *AIP Conf. Proc.* 1535.1 (2013). Ed. by Robert Lahmann et al., p. 157. DOI: 10.1063/1.4807540. arXiv: 1303.3313 [astro-ph.HE].

[71] K. Bechtol et al. "SLAC T-510 experiment for radio emission from particle showers: Detailed simulation study and interpretation". In: *Phys. Rev. D* 105.6 (2022), p. 063025. DOI: 10.1103/PhysRevD.105.063025. arXiv: 2111.04334 [astro-ph.IM].

[72] J. M. Alameddine et al. "Simulating radio emission from particle cascades with CORSIKA 8". In: *Astropart. Phys.* 166 (2025), p. 103072. DOI: 10.1016/j.astropartphys.2024.103072. arXiv: 2409.15999 [astro-ph.HE].

[73] M. Kobal. "A thinning method using weight limitation for air-shower simulations". In: *Astropart. Phys.* 15 (2001), pp. 259–273. DOI: 10.1016/S0927-6505(00)00158-4.

[74] O. Scholten, K. Werner, and F. Rusydi. "A Macroscopic Description of Coherent Geo-Magnetic Radiation from Cosmic Ray Air Showers". In: *Astropart. Phys.* 29 (2008), pp. 94–103. DOI: 10.1016/j.astropartphys.2007.11.012. arXiv: 0709.2872 [astro-ph].

[75] K. D. de Vries et al. "Coherent Cherenkov Radiation from Cosmic-Ray-Induced Air Showers". In: *Phys. Rev. Lett.* 107 (2011), p. 061101. DOI: 10.1103/PhysRevLett.107.061101. arXiv: 1107.0665 [astro-ph.HE].

[76] Christian Glaser et al. "An analytic description of the radio emission of air showers based on its emission mechanisms". In: *Astropart. Phys.* 104 (2019), pp. 64–77. DOI: 10.1016/j.astropartphys.2018.08.004. arXiv: 1806.03620 [astro-ph.HE].

[77] G. A. Askar'yan. "Excess Negative Charge of an Electron-Photon Shower and its Coherent Radio Emission". In: *Zh. Eksp. Teor. Fiz.* 41 (1961), pp. 616–618.

[78] CORSIKA Project. *CORSIKA 7*. Accessed: 22/07/2025. URL: https://www.iap.kit.edu/corsika/.

[79] Rafael Alves Batista et al. "GRANDlib: A simulation pipeline for the Giant Radio Array for Neutrino Detection (GRAND)". In: *Comput. Phys. Commun.* 308 (2025), p. 109461. DOI: 10.1016/j.cpc.2024.109461. arXiv: 2408.10926 [astro-ph.IM].

[80] Roshan Mammen Abraham et al. "Tau neutrinos in the next decade: from GeV to EeV". In: *J. Phys. G* 49.11 (2022), p. 110501. DOI: 10.1088/1361-6471/ac89d2. arXiv: 2203.05591 [hep-ph].

[81] Markus Ackermann et al. "High-energy and ultra-high-energy neutrinos: A Snowmass white paper". In: *JHEAp* 36 (2022), pp. 55–110. DOI: 10.1016/j.jheap.2022.08.001. arXiv: 2203.08096 [hep-ph].

[82] Claire Guépin, Kumiko Kotera, and Foteini Oikonomou. "Author Correction: High-energy neutrino transients and the future of multi-messenger astronomy [doi: 10.1038/s42254-022-00504-9]". In: *Nature Rev. Phys.* 4.11 (2022), pp. 697–712. DOI: 10.1038/s42254-024-00801-5. arXiv: 2207.12205 [astro-ph.HE].

[83] M. G. Aartsen et al. "IceCube-Gen2: the window to the extreme Universe". In: *J. Phys. G* 48.6 (2021), p. 060501. DOI: 10.1088/1361-6471/abbd48. arXiv: 2008.04323 [astro-ph.HE].

[84] Mauricio Bustamante and Amy Connolly. "Extracting the Energy-Dependent Neutrino-Nucleon Cross Section above 10 TeV Using IceCube Showers". In: *Phys. Rev. Lett.* 122.4 (2019), p. 041101. DOI: 10.1103/PhysRevLett.122.041101. arXiv: 1711.11043 [astro-ph.HE].

[85] Raj Gandhi et al. "Neutrino interactions at ultrahigh-energies". In: *Phys. Rev. D* 58 (1998), p. 093009. DOI: 10.1103/PhysRevD.58.093009. arXiv: hep-ph/9807264.

[86] Olivier Martineau-Huynh. "The path towards the Giant Radio Array for Neutrino Detection". PhD thesis. Paris U., VI-VII, 2021.

[87] Victor Branco Valera, Mauricio Bustamante, and Christian Glaser. "Near-future discovery of the diffuse flux of ultrahigh-energy cosmic neutrinos". In: *Phys. Rev. D* 107.4 (2023), p. 043019. DOI: 10.1103/PhysRevD.107.043019. arXiv: 2210.03756 [astro-ph.HE].

[88] Kumiko Kotera et al. "Observational strategies for ultrahigh-energy neutrinos: the importance of deep sensitivity for detection and astronomy". In: (Apr. 2025). arXiv: 2504.08973 [astro-ph.IM].

[89] Olivier Martineau-Huynh. "Status of the GRAND project". In: *39th International Cosmic Ray Conference*. July 2025. arXiv: 2507.07260 [astro-ph.IM].

[90] Pablo Correa. "NUTRIG: Towards an Autonomous Radio Trigger for GRAND". In: *PoS* ICRC2023 (2023), p. 990. DOI: 10.22323/1.444.0990. arXiv: 2307.09462 [astro-ph.IM].

[91] Sei Kato, Clément Prévotat, and Rafael Alves Batista. "Calculation of the exposure of GRANDProto300 to cosmic rays". In: *39th International Cosmic Ray Conference*. July 2025. arXiv: 2507.06629 [astro-ph.IM].

[92] Jolan Lavoisier et al. "Search for cosmic rays in GRANDProto300". In: *39th International Cosmic Ray Conference*. July 2025. arXiv: 2507.06695 [astro-ph.IM].

[93] J. Abraham et al. "The Fluorescence Detector of the Pierre Auger Observatory". In: *Nucl. Instrum. Meth. A* 620 (2010), pp. 227–251. DOI: 10.1016/j.nima.2010.04.023. arXiv: 0907.4282 [astro-ph.IM].

[94] Klaes Møller, Peter B. Denton, and Irene Tamborra. "Cosmogenic Neutrinos Through the GRAND Lens Unveil the Nature of Cosmic Accelerators". In: *JCAP* 05 (2019), p. 047. DOI: 10.1088/1475-7516/2019/05/047. arXiv: 1809.04866 [astro-ph.HE].

[95] Clarisse Aujoux, Kumiko Kotera, and Odile Blanchard. "Estimating the carbon footprint of the GRAND Project, a multi-decade astrophysics experiment". In: *Astropart. Phys.* 131 (2021), p. 102587. DOI: 10.1016/j.astropartphys.2021.102587. arXiv: 2101.02049 [astro-ph.IM].

[96] Christopher C. Finlay et al. "The CHAOS-7 geomagnetic field model and observed changes in the South Atlantic Anomaly". In: *Earth, Planets and Space* 72.1, 156 (Dec. 2020), p. 156. DOI: 10.1186/s40623-020-01252-9. arXiv: 2010.11313 [physics.geo-ph].

[97] Pablo Correa and Jelena Köhler. "NUTRIG: Development of a Novel Radio Self-Trigger for GRAND". In: *39th International Cosmic Ray Conference*. July 2025. arXiv: 2507.04339 [astro-ph.IM].

[98] Christian Glaser et al. "Simulation of radiation energy release in air showers". In: *JCAP* 2016.9, 024 (Sept. 2016), p. 024. DOI: 10.1088/1475-7516/2016/09/024. arXiv: 1606.01641 [astro-ph.HE].

[99] Harm Schoorlemmer and Washington R. Carvalho. "Radio interferometry applied to the observation of cosmic-ray induced extensive air showers". In: *Eur. Phys. J. C* 81.12 (2021), p. 1120. DOI: 10.1140/epjc/s10052-021-09925-9. arXiv: 2006.10348 [astro-ph.HE].

[100] Felix Andreas Schlüter. "Expected sensitivity of the AugerPrime Radio Detector to the masses of ultra-high-energy cosmic rays using inclined air showers". PhD thesis. KIT, Karlsruhe, IAP, 2022. DOI: 10.5445/IR/1000149113.

[101] Valentin Decoene, Olivier Martineau-Huynh, and Matias Tueros. "Radio wavefront of very inclined extensive air-showers: A simulation study for extended and sparse radio arrays". In: *Astroparticle Physics* 145 (Mar. 2023), p. 102779. ISSN: 0927-6505. DOI: 10.1016/j.astropartphys.2022.102779. URL: http://dx.doi.org/10.1016/j.astropartphys.2022.102779.

[102] Tim Huege, Lukas Brenk, and Felix Schlüter. "A Rotationally Symmetric Lateral Distribution Function for Radio Emission from Inclined Air Showers". In: *EPJ Web Conf.* 216 (2019). Ed. by G. Riccobene et al., p. 03009. DOI: 10.1051/epjconf/201921603009. arXiv: 1808.00729 [astro-ph.IM].

[103] O. Scholten et al. "Measurement of the circular polarization in radio emission from extensive air showers confirms emission mechanisms". In: *Phys. Rev. D* 94.10 (2016), p. 103010. DOI: 10.1103/PhysRevD.94.103010. arXiv: 1611.00758 [astro-ph.IM].

[104] Jordan C. Hanson and Amy L. Connolly. "Complex Analysis of Askaryan Radiation: A Fully Analytic Treatment including the LPM effect and Cascade Form Factor". In: *Astropart. Phys.* 91 (2017), pp. 75–89. DOI: 10.1016/j.astropartphys.2017.03.008. arXiv: 1605.04975 [astro-ph.HE].

[105] P. Schellart et al. "Polarized radio emission from extensive air showers measured with LOFAR". In: *JCAP* 2014.10 (Oct. 2014), pp. 014–014. DOI: 10.1088/1475-7516/2014/10/014. arXiv: 1406.1355 [astro-ph.HE].

[106] Felix Schlüter et al. "Refractive displacement of the radio-emission footprint of inclined air showers simulated with CoREAS". In: *Eur. Phys. J. C* 80.7 (2020), p. 643. DOI: 10.1140/epjc/s10052-020-8216-z. arXiv: 2005.06775 [astro-ph.IM].

[107] Christian Glaser et al. "NuRadioReco: a reconstruction framework for radio neutrino detectors". In: *The European Physical Journal C* 79.6 (June 2019). ISSN: 1434-6052. DOI: 10.1140/epjc/s10052-019-6971-5. URL: http://dx.doi.org/10.1140/epjc/s10052-019-6971-5.

[108] Chao Zhang. Private Communication. Karlsruhe Institute of Technology, Germany, 2022.

[109] John D. Hunter. "Matplotlib: A 2D Graphics Environment". In: *Computing in Science & Engineering* 9.3 (2007), pp. 90–95. DOI: 10.1109/MCSE.2007.55.

[110] Felix Riehn et al. "Hadronic interaction model Sibyll 2.3d and extensive air showers". In: *Phys. Rev. D* 102.6 (2020), p. 063002. DOI: 10.1103/PhysRevD.102.063002. arXiv: 1912.03300 [hep-ph].

[111] S. A. Bass et al. "Microscopic models for ultrarelativistic heavy ion collisions". In: *Prog. Part. Nucl. Phys.* 41 (1998), pp. 255–369. DOI: 10.1016/S0146-6410(98)00058-1. arXiv: nucl-th/9803035.

[112] M. Bleicher et al. "Relativistic hadron hadron collisions in the ultrarelativistic quantum molecular dynamics model". In: *J. Phys. G* 25 (1999), pp. 1859–1896. DOI: 10.1088/0954-3899/25/9/308. arXiv: hep-ph/9909407.

[113] Sergey Ostapchenko. "Monte Carlo treatment of hadronic interactions in enhanced Pomeron scheme: I. QGSJET-II model". In: *Phys. Rev. D* 83 (2011), p. 014018. DOI: 10.1103/PhysRevD.83.014018. arXiv: 1010.1869 [hep-ph].

[114] Sara Martinelli, Felix Schlueter, and Tim Huege. "Parameterization of the frequency spectrum in the 30-80 MHz of radio emission from inclined air showers". In: *PoS* ARENA2022 (2023), p. 036. DOI: 10.22323/1.424.0036. arXiv: 2407.18662 [astro-ph.IM].

[115] Matthew Newville et al. *LMFIT: Non-Linear Least-Square Minimization and Curve-Fitting for Python*. Version 0.8.0. Sept. 2014. DOI: 10.5281/zenodo.11813.

[116] Hans Dembinski et al. *iminuit: Jupyter-friendly Python interface for C++ MINUIT2*. Astrophysics Source Code Library, record ascl:2108.024. Aug. 2021.

[117] S. Argiro et al. "The Offline Software Framework of the Pierre Auger Observatory". In: *Nucl. Instrum. Meth. A* 580 (2007), pp. 1485–1496. DOI: 10.1016/j.nima.2007.07.010. arXiv: 0707.1652 [astro-ph].

[118] Jens Christian Glaser. "Absolute energy calibration of the Pierre Auger observatory using radio emission of extensive air showers". PhD thesis. RWTH Aachen U., 2017. DOI: 10.18154/RWTH-2017-02960.

[119] Arsène Ferrière et al. "Analytical planar wavefront reconstruction and error estimates for radio detection of extensive air showers". In: *Nucl. Instrum. Meth. A* 1072 (2025), p. 170178. DOI: 10.1016/j.nima.2024.170178. arXiv: 2408.15677 [astro-ph.IM].

[120] Kewen Zhang et al. "Electric field reconstruction with three polarizations for the radio detection of ultra-high energy particles". In: *JCAP* 08 (2025), p. 027. DOI: 10.1088/1475-7516/2025/08/027. arXiv: 2501.12614 [astro-ph.IM].

[121] Kewen Zhang et al. "Electric-Field Reconstruction for Radio Detection of Inclined Air Showers in Three Polarizations". In: *39th International Cosmic Ray Conference*. July 2025. arXiv: 2507.06874 [astro-ph.IM].

[122] Simon Chiche et al. "Polarisation signatures in radio for inclined cosmic-ray induced air-shower identification". In: *Astropart. Phys.* 139 (2022), p. 102696. DOI: 10.1016/j.astropartphys.2022.102696. arXiv: 2202.06846 [astro-ph.HE].

[123] Marion Guelfand et al. "Reconstruction of inclined extensive air showers using radio signals: From arrival times and amplitudes to direction and energy". In: *Astropart. Phys.* 171 (2025), p. 103120. DOI: 10.1016/j.astropartphys.2025.103120. arXiv: 2504.18257 [astro-ph.HE].

[124] Marion Guelfand et al. "Reconstruction of inclined cosmic-ray properties with GRAND data". In: *39th International Cosmic Ray Conference*. July 2025. arXiv: 2507.04324 [astro-ph.IM].

[125] Arsène Ferrière and Aurélien Benoit-Lévy. "Reconstruction of cosmic-ray properties with GNN in GRAND". In: *39th International Cosmic Ray Conference*. July 2025. arXiv: 2507.07541 [astro-ph.IM].

[126] Vladimir Lenok. "Measurement of the cosmic-ray energy spectrum using a novel approach to model the aperture of radio arrays". PhD thesis. KIT, Karlsruhe, 2022. DOI: 10.5445/IR/1000143479.

[127] Vladimir Lenok and Frank G. Schröder. "A probabilistic model for the efficiency of cosmic-ray radio arrays". In: *JCAP* 06 (2023), p. 014. DOI: 10.1088/1475-7516/2023/06/014. arXiv: 2208.07233 [astro-ph.IM].

[128] P. Abreu et al. "The energy spectrum of cosmic rays beyond the turn-down around 10^{17} eV as measured with the surface detector of the Pierre Auger Observatory". In: *Eur. Phys. J. C* 81.11 (2021), p. 966. DOI: 10.1140/epjc/s10052-021-09700-w. arXiv: 2109.13400 [astro-ph.HE].

[129] Pedro Abreu et al. "Expected performance of the AugerPrime Radio Detector". In: *PoS* ICRC2021 (2021), p. 262. DOI: 10.22323/1.395.0262.

[130] Tim Huege. "Air-Shower Radio Simulations - Where we stand and where we go". In: *PoS* ARENA2022 (2023), p. 053. DOI: 10.22323/1.424.0053. arXiv: 2305.10100 [astro-ph.IM].

[131] Sara Martinelli et al. "Quantifying energy fluence and its uncertainty for radio emission from particle cascades in the presence of noise". In: *Astropart. Phys.* 168 (2025), p. 103091. DOI: 10.1016/j.astropartphys.2025.103091. arXiv: 2407.18654 [astro-ph.IM].

[132] Martin Ravn et al. "Likelihood reconstruction of radio signals of neutrinos and cosmic rays". In: *10th International Workshop on Acoustic and Radio EeV Neutrino Detection Activities*. Sept. 2024. arXiv: 2409.11888 [astro-ph.IM].

[133] Alexander Aab et al. "Energy Estimation of Cosmic Rays with the Engineering Radio Array of the Pierre Auger Observatory". In: *Phys. Rev. D* 93.12 (2016), p. 122005. DOI: 10.1103/PhysRevD.93.122005. arXiv: 1508.04267 [astro-ph.HE].

[134] Tim Huege. "The Radio Detector of the Pierre Auger Observatory – status and expected performance". In: *EPJ Web Conf.* 283 (2023), p. 06002. DOI: 10.1051/epjconf/202328306002. arXiv: 2305.10104 [astro-ph.IM].

[135] Mohit Saharan. "Status and Performance of the Radio Detector of the Pierre Auger Observatory". In: *J. Phys. Conf. Ser.* 3053.1 (2025), p. 012010. DOI: 10.1088/1742-6596/3053/1/012010.